UNIVERSIDAD DE GRANADA

PROGRAMA DE DOCTORADO EN FÍSICA Y CIENCIAS DEL ESPACIO

THE ROLE OF STARBURSTS IN GALAXY EVOLUTION

Antonio Arroyo Polonio

Supervisors: Dr. Jorge Iglesias Páramo
Dr. Carolina Kehrig

INSTITUTO DE ASTROFÍSICA DE ANDALUCÍA
CONSEJO SUPERIOR DE INVESTIGACIONES CIENTÍFICAS

Granada, Junio 2024

Qué bueno que la naturaleza haga siempre lo que tiene que hacer a pesar de nuestras expectativas.

Agradecimientos

Soy una persona que cree que ante cualquier experiencia vital siempre se presentan dos alternativas: agradecer o culpar. Dependiendo de lo agradable que sea la experiencia, en un primer momento resulta más natural sentirse agradecido o recurrir a la queja. Sin embargo, con tiempo y esfuerzo, se puede transitar poco a poco por el camino del agradecimiento, el cual engrandece a la persona y la lleva a ser feliz. Se trata, algunas veces, de un ejercicio colosal; otras, no requiere de esfuerzo ninguno; pero pienso que siempre vale la pena. Ahora voy a tratar con el mayor cuidado y sinceridad posibles realizar este ejercicio primero en relación a mi desarrollo en el estudio de una ciencia tan apasionante como es la astrofísica y en general, a mi vida.

Me gustaría, si me lo permitís, empezar agradeciendo a los que considero el núcleo responsable de mi desarrollo como científico; Pepe, Jorge y Carolina. Gracias a Pepe por introducirme en el ámbito de la astrofísica, por tener paciencia conmigo y por cuidar de mí. Tu pasión tan genuina por la ciencia me ha inspirado a lo largo de este camino. Gracias a Jorge por haberme ayudado y guiado en todo lo que has podido estos años. Gracias por preocuparte por mí cuando no veía cómo avanzar y por todo el tiempo que me has dedicado a pesar de la distancia. Gracias Carolina por no rendirte conmigo, gracias al tiempo y la paciencia las semillas que un día se plantaron han dado su fruto. Os deseo de corazón una vida sana y completa.

Gracias a todos los demás que me estáis acompañando en un camino similar. A Borja, por tu apoyo, paciencia conmigo, por nuestro intercambio de ideas y sobre todo por ser mi amigo. A Ricardo, que a pesar de tener tantos frentes abiertos me ha dedicado su tiempo e interés. A Enrique, por todas nuestras agradables conversaciones y su gran calidad como científico que siempre se ha reflejado en los trabajos donde me ha acompañado. A Salva, por introducirme a tantos en el instituto, por tu paciencia enseñandome a programar y por tu gran corazón. A Antonio por saber escucharme y ser tan cercano a mí. A Miguel y Belén por todo el esfuerzo dedicado en el parque y vuestra constancia. A Guille, por ser como un tótem al que aferrarme en el despacho. Tu ejemplo de esfuerzo y constancia en el trabajo es admirable. A todos los demás pre-docs que me han acompañado; Julios, Teresa, Ana, Florín, Borja, Roberto, Juan, Anthony, Alberto, Javi, Valentin, Ginés, Marianna... siento mi usual ausencia, gracias por estar ahí. Al grupo de Estallidos que siempre se ha sentido como una familia donde nos dedicamos tiempo a conocernos y acogernos.

A los profesores y compañeros que he tenido antes de empezar mi tesis durante el máster, carrera, instituto y colegio. A Bert por inspirarme con tu indiscutible calidad como científico, tu tiempo y cercanía. A Ute, por ver mi potencial, preocuparse por mí y enlazarme con Pepe. A Almudena, con tu paciencia y templanza me ayudaste a asentar bases para lo que se venía. A Enrique Arriola, por hacer que el resto de asignaturas del máster parecieran fáciles. A Adrián y Jose por mantener la amistad y por el apoyo mutuo. A Antonio Sarsa y Jose Ignacio, los padrinos de mi carrera. Gracias por inspirarme a aprender y sacar lo mejor de mí. Vuestro compromiso con la enseñanza y cercanía con el alumnado es ejemplar. A Jorge Pretel por seguir presente en mi vida. A Miguel Ulloa por tus abrazos y tu amistad. A Fran por seguir en contacto conmigo a pesar de la distancia. Al resto de compañeros de la carrera, Coral, Mila, Mari, Porras, Manuel, Dani, Laura, Julio, Fátima, Vicente, Edu, Nicola, Antonios... atesoro vuestros recuerdos a pesar de la distancia. Con respecto a mis años mas tiernos, quiero agradecer a Juan Moyano. Me enseñaste con gran calidad la física fundamental que, en buena parte, gracias a ti ha quedado grabada a fuego en mi mente. Además de a Antonio, me inspiraste a leer sobre Richard Feynman que en última instancia determinó mi mente a estudiar la carrera de física, decisión que siempre agradeceré.

Quiero agradecer a mi familia. A mis padres, por inculcarme valores como la honestidad, el esfuerzo y el entendimiento, valores que todavía van forjando mi ser. Aunque sobre todo gracias por cuidarme y quererme. A mi hermano, eres una inspiración para seguir creciendo en todos los aspectos de mi vida. Gracias por haberme abierto a tu vida, contigo es más fácil sentirse en casa. A Miri, por dedicarme tanto cariño, amor y ternura todos estos años. Contigo la vida tiene mas color y el mundo es más bonito. Gracias también a tu familia y amigos por acogerme como uno más. Al resto de mi familia, abuelos que ya no están, titos y primos. Gracias a vosotros los recuerdos de la infancia se hacen más cercanos, os deseo lo mejor. A todos mis amigos. A Víctor por tantas hostias y risas, pero sobre todo por ese entendimiento tácito tan duradero. A Juanlu por ser un ejemplo de esfuerzo y constancia. Contigo me es fácil hablar sobre los aspectos más duros de la vida y eso lo valoro mucho. A Pérez, gracias por ser tú, por cuidar a los tuyos, por ser tan bueno y por sorprendernos siempre. Gracias a Juan Andrés, Rafa, Joses, Poye, Nano, Jorge, Sergio, Ana, Marta, Paulo, Edu, Ici, Puli, Fernandez, Elias... gracias por ser mis amigos y seguir en mi vida. Me alegro de haberos conocido y os deseo lo mejor.

Por último, me queda agradecer no solamente los lazos que me unen a tantos sino también los lazos que os unen entre vosotros y con otros. Todo por un mundo unido donde se fomente el amor y el entendimiento. Todos somos en el fondo representaciones de una misma cosa, la naturaleza.

Resumen

Las Galaxias con Líneas de Emisión Extrema (EELGs, por sus siglas en inglés) se caracterizan por tener intensos brotes de formación estelar reciente, donde abundan estrellas muy masivas; estas emiten una radiación electromagnética capaz de ionizar el medio interestelar que las rodea. El gas ionizado reemite la radiación en forma de líneas de emisión, que son características en los espectros de estas galaxias. Las EELGs suelen exhibir baja masa, apariencia compacta, baja metalicidad y altas tasas de formación estelar (SFR) en comparación con galaxias de otros tipos. Son más comunes en altos desplazamientos al rojo y juegan un papel clave en la reionización del Universo.

La primera parte de este trabajo se ha centrado en la búsqueda de EELGs utilizando datos del proyecto J-PAS. Por su diseño instrumental, este proyecto es ideal para detectar líneas de emisión en varios objetos astronómicos. Hasta la fecha, J-PAS ha completado dos estudios piloto, miniJPAS y J-NEP, que cubren 1 y 0.25 grados cuadrados respectivamente. Estos son una preparación para el estudio final, que cubrirá 8500 grados cuadrados del cielo. Nuestra búsqueda de EELGs en los campos de miniJPAS y J-NEP arrojó un total de 19 candidatos a EELG, lo que nos permitió estimar la densidad espacial de estos objetos en función del desplazamiento al rojo hasta $z = 1.4$.

En la segunda parte de este trabajo se estudió la distribución espacial de las propiedades del gas ionizado en una subcategoría de EELGs llamadas galaxias Green Pea (GPs). Se analizó una muestra de 24 galaxias GP observadas con el Explorador Espectroscópico Multi-Unidad (MUSE) en el Very Large Telescope (VLT). Las observaciones muestran que la mayor parte del brillo de la galaxia está dominado por la emisión central de la región de formación estelar, con gas ionizado extendiéndose varios kpc más allá del centro galáctico. El estudio incluye información detallada sobre la distribución espacial de la estructura de ionización y la cinemática, proporcionando pistas sobre posibles canales a través de los cuales los fotones de alta energía podrían escapar al medio intergaláctico.

Por último, se estudió la cinemática del gas ionizado en la galaxia IZw18 utilizando el instrumento MEGARA en el Gran Telescopio Canarias (GTC). IZw18, es una EELG conocida por su extremadamente baja metalicidad e intensa formación estelar. Las observaciones, basadas en el análisis de la linea Hα, revelaron unas características cinemáticas mucho más

complejas de las que se habían visto en esta galaxia hasta la fecha. Destaca la presencia de una componente muy ancha, además de perfiles estrechos con una alta complejidad y variación espacial. La interpretación física de estos resultados no es trivial, pudiendo corresponderse con una intrincada interacción entre fuerzas gravitacionales, mecanismos de retroalimentación estelar y gradientes de densidad en la línea de visión.

Abstract

EELGs are characterized by intense recent star formation bursts, where very massive stars are present, emitting powerful electromagnetic radiation that ionizes the surrounding interstellar medium (ISM). The ionized gas re-emits the radiation in the form of emission lines, characteristic of the spectra of these galaxies. EELGs typically exhibit low mass, compact appearance, low metallicity, and high SFRs compared to other types of galaxies. They are more common at high redshifts and play a key role in the reionization of the Universe.

The first part of this work consists in searching for EELGs by using data from the J-PAS project. Due to its instrumental design, this project is ideal for detecting emission lines in various astronomical objects. To date, J-PAS has completed two pilot surveys, miniJPAS and J-NEP, covering 1 and 0.25 square degrees, respectively. These pilot surveys serve as a preparation for the final survey, which will cover 8500 square degrees of the sky. Our search in miniJPAS and J-NEP yielded a total of 19 EELG candidates, allowing us to estimate the spatial density of these objects as a function of redshift up to $z = 1.4$.

In the second part of this work, the spatial distribution of ionized gas properties in a subcategory of EELGs called GPs was studied. A sample of 24 GP galaxies observed with MUSE at the VLT was analyzed. Observations show that most of the brightness of the galaxy is dominated by central emission from the starburst region, with ionized gas extending several kpc beyond the galactic center. The study includes detailed information on the spatial distribution of ionization structure and kinematics, providing clues about possible channels through which high-energy photons could escape into the intergalactic medium (IGM).

Lastly, the kinematics of the ionized gas in the galaxy IZw18 were studied using the MEGARA instrument on the GTC. IZw18 is an EELG known for its extremely low metallicity and intense star formation. Observations, based on the analysis of the Hα line, revealed much more complex kinematic features than previously seen in this galaxy. We highlight the presence of a very broad component, in addition to narrow profiles with high complexity and spatial variation. The physical interpretation of these results is not trivial, possibly corresponding to an intricate interaction between gravitational forces, stellar feedback mechanisms, and density gradients along the line of sight.

Contents

List of Figures

List of Tables

Chapter 1

Introduction

1.1 From the Big Bang to the Cosmic Dawn

The Big Bang theory and the expansion of the Universe were first proposed by the Belgian astronomer Georges Lemaître in the 1920s (Lemaître 1927). He suggested that the Universe is expanding and that it has a finite age. In the late 1920s, American astronomer Edwin Hubble confirmed the predictions of Lemaître by observing that galaxies were moving away from each other, implying that the Universe was indeed expanding (Hubble 1929). This provided strong evidence for the Big Bang theory, which posits that the Universe began as a singularity approximately 13.8 billion years ago and has been expanding and cooling ever since (more information about cosmology and the origin of the Universe can be found in e.g. Peebles (1993); Kolb & Turner (2018); Weinberg (2008)). The discovery of the expansion of the Universe by Lemaître and Hubble marked a major turning point in our understanding of it and remains one of the most important discoveries in modern astronomy.

Just a fraction of a second after the Big Bang, the average energy of particle interactions had dropped below the binding energy of quarks, initiating a phase transition in the Universe where these particles were confined within hadrons. Approximately ten seconds later, primordial nucleosynthesis took place. This process happened as the Universe expanded and cooled, enabling protons and neutrons to combine and form more diverse atomic nuclei. The temperature and density during this stage were ideal for protons and neutrons to collide and bind together, similar to how it happens in the core of stars, creating the first light chemical elements (e.g. Wagoner 1973). This synthesis of light elements from primordial material became the foundation for the formation of the first stars and galaxies. The quantity of these light elements, particularly helium, is a crucial factor in determining models of the early Universe and the conditions that existed during that time.

The primordial nucleosynthesis lasted about 20 minutes, leading to the plasma era of the Universe (that would be the first ionization of the Universe). During this time, the Universe consisted of a hot, dense plasma of ionized particles, similar to the inner part of stars but without significant nuclear reactions. As the Universe expanded and cooled, temperatures dropped from billions of Kelvin (K) to a few thousand K. The plasma era persisted until approximately 380,000 years after the Big Bang, during which the Universe remained opaque due to constant interactions between photons and free electrons. After the plasma era, the Universe cooled to about 3000 K, allowing protons and electrons to combine (for the very first time) and form neutral hydrogen atoms in a process known as recombination. This marked the transition from an opaque to a transparent Universe, as photons could now travel freely, giving rise to the Cosmic Microwave Background (CMB). The CMB is the afterglow of the Big Bang (e.g. Dodelson & Schmidt 2020). As the oldest observable light, it was initially emitted mostly as infrared light due to the temperatures at this stage of the Universe ($\sim$ 3000 K) (e.g. Ryden 2017), the peak emission of the CMB had a wavelength of around 9660 Å. This characteristic wavelength allowed the photons to travel without interacting with the newly formed neutral hydrogen, as their energy was not sufficient to ionize hydrogen atoms. Over time, the expansion of the Universe has redshifted these photons to the microwave region, making the CMB a homogeneous and isotropic microwave radiation background. At this point, the Dark Ages began with the formation of neutral hydrogen and lasted until the first stars and galaxies emerged. This period was characterized by a lack of significant sources of light or heat, although small density fluctuations began to grow under the influence of gravity. These fluctuations eventually led to the formation of the first luminous objects, marking the end of the Dark Ages and the onset of the Cosmic Dawn. This period remains one of the least understood and most challenging eras in cosmological history to study and marks the origin of stars and galaxies (e.g. Barkana & Loeb 2001). In figures 1.1 and 1.2 a representation of the evolution of the Universe and the particles in their first stages are shown.

1.2 From the Cosmic Dawn to the present

In the dark ages, as the Universe continued to expand and cool, gravitation began to play a major role producing small density fluctuations (e.g., Peebles & Yu 1970). These grew under the influence of gravity, changing the homogeneity and isotropy of the Universe to a much bigger scale, and eventually leading to the formation of the first self-gravitational light sources in the Universe (e.g., Springel et al. 2005). These were the first objects that were

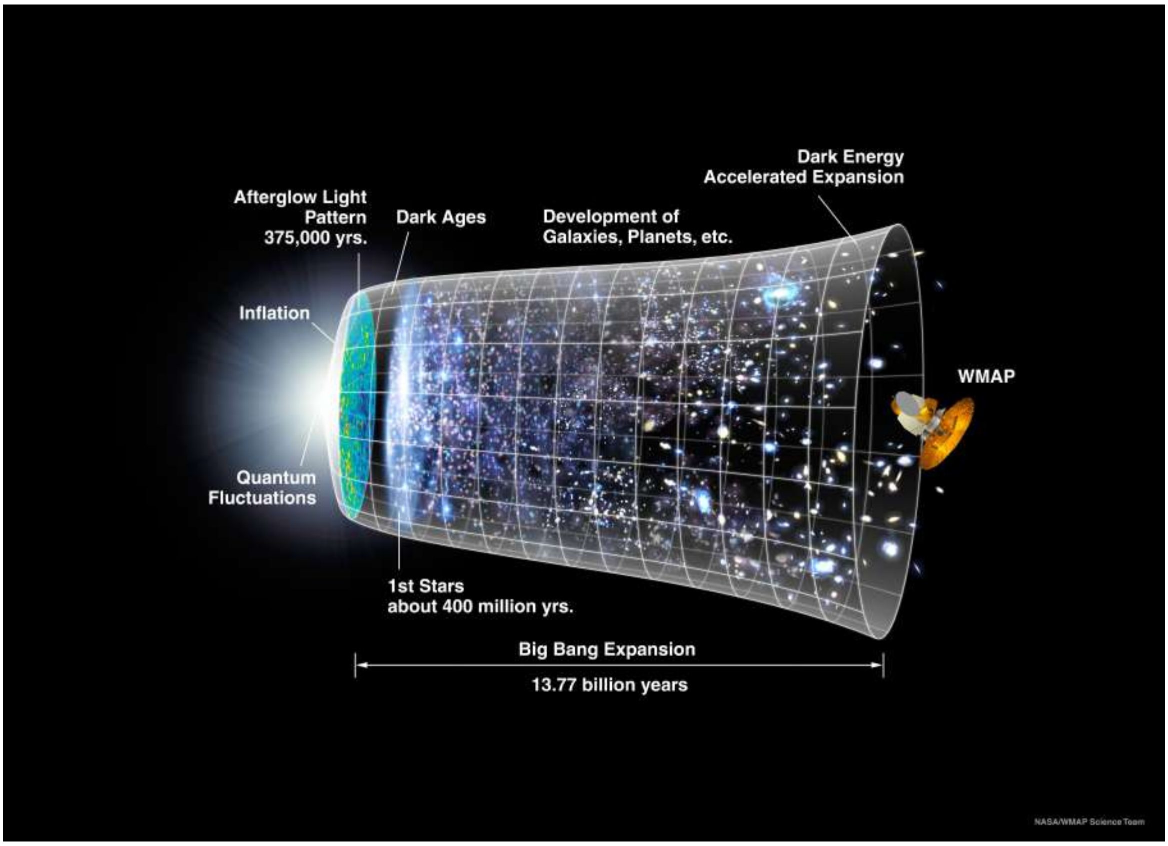

Figure 1.1 Time-line representation of the Universe. Credit to NASA/WMAP science team (https://map.gsfc.nasa.gov/media/060915/)

massive enough to overcome the pressure of surrounding gas, and to ignite nuclear fusion reactions in their cores, thus producing light and heat (e.g., Bromm & Larson 2004).

The formation of these first luminous objects was a pivotal moment in the cosmic timeline, marking the end of the cosmic dark ages and heralding the onset of the Cosmic Dawn. This period occurred between 150 million years and one Gyr after the Big Bang, corresponding to redshifts of about 20 to 6 (e.g., Singh et al. 2022). This era, characterized by the emergence of the first stars and galaxies, was shaped by the interplay of gravitational forces and gas dynamics. Gravity encouraged the agglomeration of matter into dense regions, precursors to stars and galaxies, while gas pressure countered gravitational collapse, regulating the formation of these celestial structures (Haemmerlé et al. 2020). Complementing this dynamic was the enigmatic role of dark matter, an invisible yet omnipresent component that contributes to $\sim 85\%$ of the total mass of the Universe. Its gravitational influence, manifest in the rotational patterns of galaxies (e.g., Prada et al. 2003) and the bending of light in gravitational lenses. Dark matter also played a pivotal role in sculpting the large-scale structure of the Universe, thereby laying the groundwork for the genesis of the first stars and galaxies.

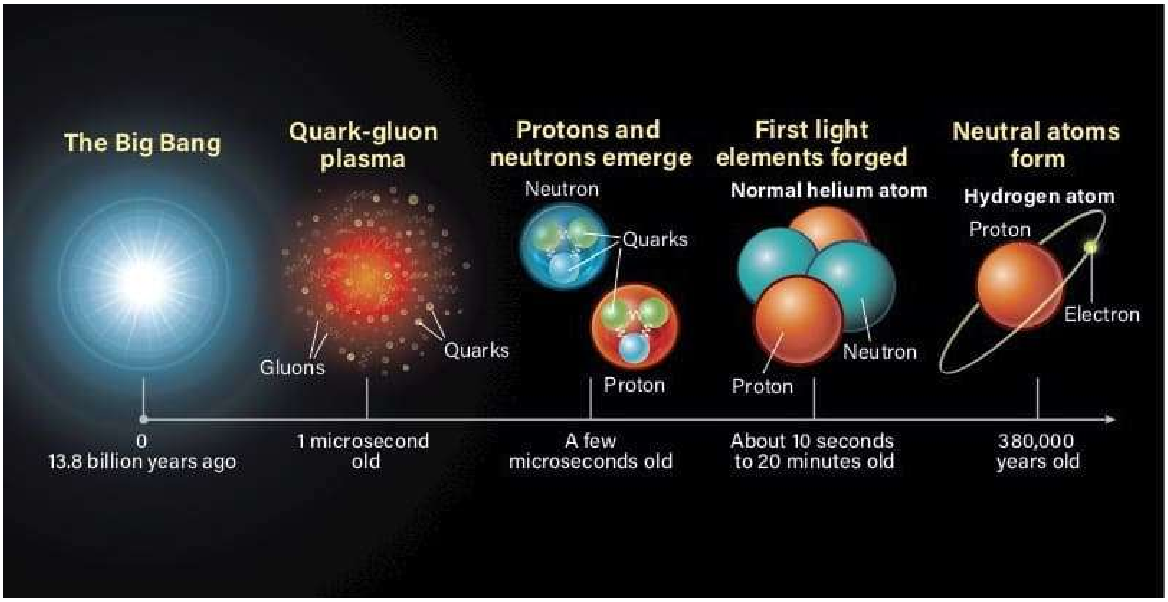

Figure 1.2 Evolution of the particles in the Universe from the Big Bang to the recombination era. (https://www.astronomy.com/science/the-beginning-to-the-end-of-the-Universe-the-emergence-of-matter/)

The cooling of gas is a pivotal mechanism driving the contraction of gas clouds through radiative energy loss and enabling gravitational collapse for star formation. In this primordial environment, dominated by hydrogen and helium, the absence of heavier elements restricted cooling pathways. However, molecular hydrogen (H_2) emerged as a crucial coolant in these metal-free clouds (e.g., Greif et al. 2008). Despite its simplicity, H_2 facilitated effective energy dissipation through rotational and vibrational transitions, emitting photons and reducing the kinetic energy of the gas. This process was vital for cooling the primordial gas to the point where it could condense into the first stars. In contrast, in the present Universe it is usual to see regions enriched with metals and dust. Thus, the cooling processes are now significantly enhanced. Metals, with their complex electronic structures, and dust particles (beeing more complex than any atom), getting closer to black-body radiation, provide more efficient cooling mechanisms, accelerating the contraction and formation of celestial structures (e.g., Choi & Nagamine 2009; Vogelsberger et al. 2019).

Within this intricate cosmic framework, the very first stars of the Universe, the Population III stars, emerged. Forged from the primordial gas, a nearly pure mixture of hydrogen and helium from the aftermath of primordial nucleosynthesis, these stars were markedly different from those we see today (e.g., Johnson 2010). Notably, Population III stars are believed to have the potential to be much more massive, often exceeding several hundred solar masses, which led to greater luminosities and higher surface temperatures compared to their current counterparts (e.g., Nakamura & Umemura 2001). Those stars were not only the first points of light in the dark cosmos but also the forges in which the first heavy elements were created, seeding the Universe with the building blocks for more complex cosmic structures. The most massive ones had a brief but intense lifespans, leading to supernova endings and thus creating and dispersing heavier chemical elements through the Universe. This enriched for the very first time the ISM paving the way for the next generations of stars forged with these elements (e.g., Maio et al. 2010). At the same time as the emergence of Population III stars, the cosmic landscape began to further differentiate through gravitational collapses occurring at various scales. These collapses not only facilitated the formation of the first stars but also led to their clustering (along the gas), resulting in the formation of the earliest galaxies. These primordial galaxies began to carve out their distinct identities within the vast expanse of the Universe (e.g., Bromm & Yoshida 2011).

As the first stars and galaxies began to form and grow, they emitted a tremendous amount of energy in form of light. Most of it with wavelengths from the near infrared (NIR) to the ultraviolet (UV), where energies are high enough to ionize the surrounding gas. This ionization of the gas (specially in the IGM) is a process called the reionization of the Universe, which started alongside the Cosmic Dawn (e.g., Djorgovski et al. 2001).

Apart from the formation of Pop III stars, there exist alternative scenarios in which stars can produce significant amounts of UV radiation, contributing to the reionization of the Universe. For instance, binary star systems (which are very likely expected for high mass stars) can emit strong UV radiation when one star is stripped of its outer layers by the other companion (e.g., Götberg et al. 2019). This process, called mass transfer, generates powerful radiation from the stripped star as it reveals its inner region.

Active Galactic Nuclei (AGNs) are another contributor to the reionization of the Universe. These are extremely bright, compact regions at the centers of some galaxies that are powered by the accretion of matter onto a supermassive BH. The accretion process releases a tremendous amount of energy, which can ionize the surrounding gas and produce intense radiation. This radiation can escape the host galaxy and contribute to the reionization of the Universe (e.g., Smith et al. 2020).

However, not all of the UV photons were able to escape their host galaxies and ionize the surrounding IGM (e.g., Siana et al. 2007; Cen & Kimm 2015). This was due to the absorption of this high energy emission by gas and dust within the galaxy itself. Most of the gas is composed by Hydrogen atoms that can efficiently absorb photons at specific wavelengths corresponding to electronic transitions, such as those in the Lyman series. However, for photon energies above the Lyman limit (912 Å), hydrogen atoms can potentially absorb photons of any energy higher than the ionization threshold (e.g., Giavalisco 2002), with the excess energy beyond ionization imparted as kinetic energy to the ejected electron. This absorption processes make gas and dust to play a complex role in the interaction between radiation from the galaxy and the ionization of the IGM.

In the reionization, as the first galaxies continued to form, their intense radiation ionized increasing portions of the IGM, mostly composed by Hidrogen atoms (e.g., Zaroubi 2012). This era marks a major milestone in the evolution of the Universe because it is the point at which the IGM becomes transparent to UV radiation. Reionization is complex and still not completely understood. However, it is clear that the first stars and AGN played critical roles in this process. Some studies suggest that star-forming galaxies might dominate the ionizing photon budget during the earlier stages of reionization, while AGNs might become increasingly important at later stages (Smith et al. 2020).

During the Cosmic Dawn, these nascent galaxies, emerging from the primordial soup of the early Universe, represent the fundamental building blocks from which the rich tapestry of the contemporary cosmos has been woven (e.g., Kroupa 2004). The birth of these first galaxies marks not just a milestone in the evolution of the Universe but also the beginning of a complex process of transformation and maturation that spans billions of years.

The early galaxies were small, often irregular in shape, and predominantly composed of young, massive stars that blazed fiercely, illuminating the Universe and playing a crucial role in the reionization epoch (e.g., Bromm & Yoshida 2011). These galaxies were the crucibles in which the first heavy elements were forged, setting the stage for the chemical complexity necessary for life as we know it (e.g., Frebel & Bromm 2012). As the Universe continued to evolve, these early structures underwent numerous transformation through processes such as mergers and accretion, they grew in size and complexity, giving rise to the variety of galaxy forms observed today: irregular dwarfs, spirals like our Milky Way (MW), massive ellipticals that dominate galaxy clusters, among others (e.g., Bundy et al. 2004; Conselice et al. 2009; Nadler et al. 2023).

In this light, the study of galaxy formation and evolution bridges the gap between the earliest moments of cosmic history and the rich, diverse Universe we inhabit. It underscores the profound connection between the macroscopic structures of the cosmos and the complex microscopic processes involving particle interactions. As we continue to explore the depths of the Universe, each discovery adds a piece to the puzzle, gradually unveiling the grand narrative of cosmic evolution from the Big Bang to the vibrant Universe we see around us today.

1.3 Role of local analogues to high redshift galaxies

The finite velocity of light allows us observe at any time in the past by observing far away enough. So although direct observations of primeval galaxies are possible, such observations present significant challenges. The vast distances separating us from these primeval structures introduce two major observational constraints: the diminished flux and angular size of distant galaxies. The flux (F) from an astronomical object is inversely proportional to the square of the distance (d) from the observer ($F \propto d^{-2}$). The angular size (θ) of an object is inversely proportional to its distance ($\theta \propto d^{-1}$) at low redshifts, but this relationship changes at higher redshifts. Specifically, the angular size decreases with increasing redshift up to a certain point (approximately at $z \simeq$ 1.5-2), beyond which the angular size begins to increase with further increases in redshift (e.g., Melia & Yennapureddy 2018). These relationships mean that the farther away a galaxy is, the fainter it appears to us and the lower (up to $z \simeq$ 1.5-2) is the power to spatially resolve it.

Due to these intrinsic limitations, only the brightest galaxies in the early Universe are observable with current astronomical technology. These distant luminaries, despite their inherent brilliance, often appear to us as mere dim point-like sources, severely limiting our ability to discern their structure or the finer details of their formation and evolution. The James Webb Space Telescope (JWST) marks a significant advancement in the exploration of the early Universe. With its 6.5-meter primary mirror and ability to observe in infrared wavelengths (0.6 to 28 micrometers), JWST surpasses previous telescopes in both scale and capability (e.g., Pontoppidan et al. 2022). Its design allows for the observation of high-redshift galaxies, making it possible to study the very first galaxies with unprecedented clarity. Since its deployment, the JWST has discovered several galaxies at redshifts greater than 10, setting new records in the observation of the early Universe. Among these discoveries, the galaxy JADES-GS-z13-0 stands out with a record-breaking (up to this date) redshift of 13.2 (Curtis-Lake et al. 2023), pushing the boundaries of our understanding of the infancy of the cosmos.

Taking into account the restrictions that we have when observing the very first galaxies, the study of local analogues to high-redshift galaxies has emerged as a pivotal method for understanding the evolution of galaxies since their beginning (e.g., Schaerer et al. 2022; Chen et al. 2023). These local analogues are galaxies in the nearby Universe that exhibit characteristics similar to those expected in the infant cosmos (such as high SFRs, low metallicity, and compact size). They serve as more accessible laboratories for studying the conditions prevalent in the early stages of galaxy evolution. This allows us to understand in detail processes and properties (like star formation, feedback mechanisms, and chemical composition) that are less accessible in distant, faint primeval galaxies. By comparing these nearby galaxies with their early Universe counterparts, researchers bridge the theoretical and observational division, enhancing our knowledge of galaxy evolution.

A common trait linking high-redshift galaxies with their local analogues is the presence of high-mass stars indicative of starburst events or periods of intense star formation. These stars emit high-energy photons, predominantly in the UV range, that ionize the interstellar gas clouds present in galaxies. This ionization process leads to the production of emission lines from electronic transitions in gas atoms, which are prominently visible in the spectra of galaxies in all ranges of wavelengths. Galaxies known for their vivid emission lines (usually lines with equivalent width (EW) > few 100 Å), are classified as EELGs (e.g., Iglesias-Páramo et al. 2022). These emission lines are crucial for identifying these galaxies, offering a practical marker of their presence. However, it is essential to differentiate between ionization caused by star formation and that produced by AGNs, as both can generate emission lines in the spectra. This distinction is vital for accurately understanding the mechanisms driving the ionization and the nature of the galaxies in question.

The study of EELGs encompasses various subclasses, each characterized by distinctive features and historical discovery contexts:

- **HII galaxies**, identified in the 1970s as extragalactic counterparts to the HII regions of the MW, known for their intense ionized hydrogen emission lines. This classification underscored the starburst nature of galaxies, a concept further elaborated by Terlevich & Melnick (1981), who investigated the burst of star formation in luminous galaxies.

- **Wolf-Rayet (WR) galaxies**, recognized in the 1980s, exhibit broad emission lines in their spectra indicative of WR stars. WR stars are a rare and evolved class of massive stars, typically having initial masses greater than 20 solar masses. These stars are known for their extremely high temperatures, often exceeding 30,000 K, and can reach up to 200,000 K. These features highlight the active star-forming regions of galaxies, where the presence of these stars signifies intense starburst activity (e.g., Conti 1991).

- **Blue Compact Dwarf (BCD) galaxies**, gaining attention in the same era, are characterized by their proximity, compact size, low metallicity, intense star formation, and blue colours (e.g., Thuan & Martin 1981).

- **Lyman-α (Lyα) Emitters** emerged as a distinct category in the late 1990s, identified through deep field observations enabled by advances in spectroscopy. Cowie & Hu (1998) discussed the significance of these galaxies, noting their role as a new class of star-forming galaxies observable at higher redshifts ($z \gtrsim 3$).

- **GPs**, discovered through the Galaxy Zoo citizen science project in the late 2000s, represent a class of compact, extremely star-forming galaxies at $z \sim 0.25$. Cardamone et al. (2009) introduced GPs, highlighting their unique characteristics and the contribution of citizen science to astronomical discoveries.

- **Blueberries**, similar to BCDs, describes local ($z < 0.05$), ultra-compact, highly star-forming galaxies identified in the 2010s as a subset of EELGs with extreme properties. Yang et al. (2017c) detailed the discovery and characteristics of Blueberries, underscoring their significance in the study of young starbursts.

  These varied classifications reflect the diverse observational and theoretical frameworks used to understand the myriad processes underlying galaxy evolution, emphasizing the role of intense star formation and the physical conditions in the early Universe.

1.4 Emission line spectroscopic study

The study of emission lines through spectroscopy offers a window into the physical processes governing galaxies, particularly those undergoing intense star formation, known as starburst events. At the heart of these phenomena there is the ionization source (stars, AGNs, shocks...), that produce photons with distinctive spectral energy distributions (SEDs). These photons interact with interstellar gas (or the ISM in general), which is dispersed over larger volumes and characterized by specific densities, temperatures and chemical compositions. This interaction is a reflection of the physical conditions and processes that drive galactic evolution and starburst activity.

1.4.1 Nebulae. On the firsts detections of emission lines

The journey into understanding the evolution of galaxies took a significant leap with the first historical detection of emission lines. In the mid-19th century, William Huggins pioneered the use of spectroscopy in astronomy, leading to the discovery that many celestial objects known as nebulae exhibited emission lines in their spectra. In Huggins (1864) it is first observed the distinct emission lines in the Cat's Eye Nebula (see Fig. 1.3), identifying them as evidence of gaseous composition. This breakthrough marked a departure from the previous belief that all nebulae were unresolved clusters of stars, fundamentally altering our understanding of the composition of the Universe.

The word "nebula" comes from Latin, meaning "cloud" or "mist". Ancient astronomers, observing the night sky with the naked eye, used it to describe any diffuse, cloudy object they could not resolve into individual stars. The spectroscopic studies by Huggins (1864)

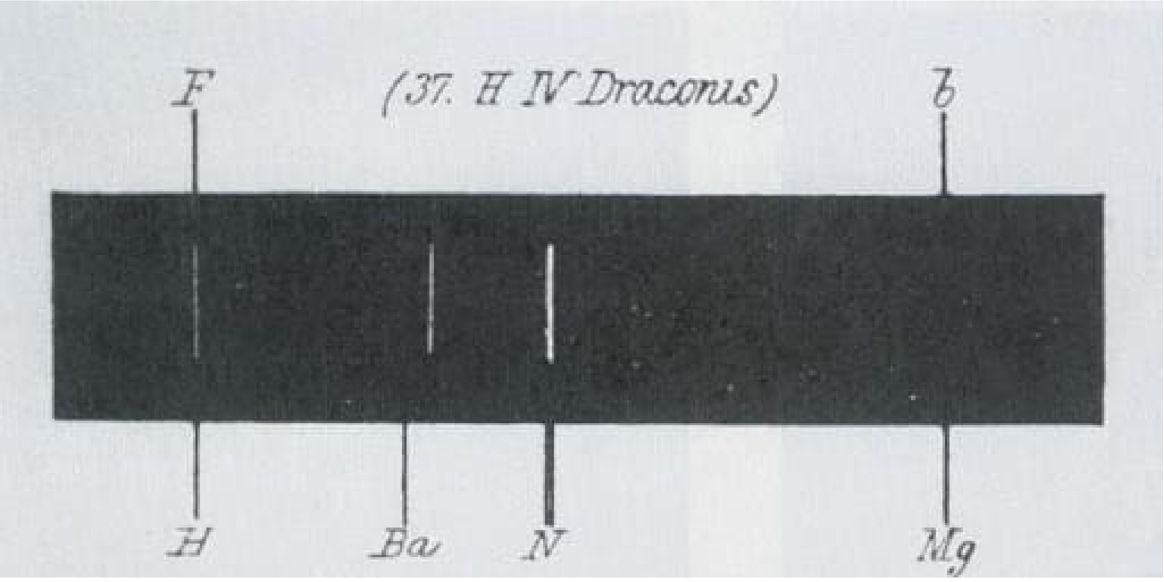

Figure 1.3 Spectrum image of the Cat's eye nebula in Huggins (1864). Hβ and the [Oiii]$\lambda\lambda$4959,5007 Å doublet are clearly distinguished.

laid the groundwork for understanding nebulae as regions where ionized gas is emitting a very specific kind of radiation (mostly in form of emission lines). As spectroscopy advanced, it became clear that nebulae were not merely localized regions of ionized gas within our galaxy but could also exist as part of the emission in independent galaxies themselves. This realization was cemented by the work of Edwin Hubble in the early 20th century, who used Cepheid variable stars to determine the distance to the Andromeda Nebula, proving it was far outside the MW and indeed a galaxy in its own right (Hubble 1926, 1929).

The concept of nebulae evolved from localized regions of ionized gas in the MW to encompass vast, extragalactic systems capable of hosting their star-forming regions (in some cases being much more "bursty" than our MW). This shift not only expanded the scale of the observable Universe but also enriched the study of galaxies and their formation, highlighting the universality of physical processes such as ionization and starburst phenomena across the cosmos.

1.4.2 Ionization sources

The sources of ionization within galaxies are diverse, including stars, AGNs, and shock waves, each contributing in varying proportions to the ionization of the different ionized regions in galaxies. Importantly, each ionization source presents its own SED and can occupy distinct spatial locations.

- **Stars**: Stars are fundamental celestial bodies that serve as fundamental building blocks of galaxies. They are massive, luminous spheres of plasma held together by their own gravity, generating energy through nuclear fusion reactions at their cores. This energy production is the source of the light and heat that stars emit, making them visible across vast cosmic distances. The life cycle of a star, from its formation in dense regions of interstellar gas and dust to its eventual death, plays a critical role in the evolution of the Universe, influencing the formation of planets, the synthesis of heavy elements, and the dynamics of galaxy evolution.

  The SED of stars is a vital tool for understanding these celestial objects, providing insights into their physical properties and the mechanisms by which they interact with their surroundings. The SED of a star is influenced by several factors, including its total mass, age, and metallicity. Young, massive stars are particularly notable for their emission of copious amounts of UV light, which plays a significant role in the ionization of interstellar gas.

  In astrophysics, the SED of an individual star is often approximated by that of a black body, a theoretical model that assumes a perfect absorber and re-emitter of all incident radiation. This approximation is supported by the observation that stars emit a mostly continuous spectrum of radiation (with some absorption lines) across a broad range of wavelengths. According to Planck's law, the shape of a black body SED corresponds to a specific temperature. Therefore, we can define a temperature of a star by identifying the black body SED that best matches the spectrum of the star.

- **AGNs**: They represent some of the most energetic and dynamic environments in the Universe. They are powered by supermassive BHs usually located at the centers of massive galaxies, which accrete matter from their surroundings at extraordinarily high rates. This accretion process releases vast amounts of energy through the friction of the gas spiraling towards the central BH. This emits light across the whole electromagnetic spectrum, from radio waves to gamma rays, making AGNs among the brightest objects in the cosmos. AGNs are key to understanding the growth and evolution of galaxies, as the energy they emit can have profound effects on their host galaxies, influencing SFRs and the distribution of interstellar matter.

  The SED of an AGN is intricately linked to the mass of the central supermassive BH, the rate at which it accretes material and its orientation (i.e. its emission is anisotropical). These factors determine the intensity and range of the electromagnetic radiation emitted by the AGN, including extremely energetic photons capable of ionizing gas across vast distances. Thus, the radiation from AGNs can affect regions far beyond their immediate vicinity, altering the physical state of the ISM and impacting the overall evolution of their host galaxies and beyond.

- **Shock Waves**: The physical process behind shock waves (or shocks) emission is fundamentally the same as AGNs; thermal motion of the gas through friction/collision, but the scenario in which it occurs is different. Shocks are dynamic phenomena occurring within the ISM itself, arising at the boundaries where gas clouds with differing properties and velocities collide, heating the gas. Feedback mechanism like supernovae explosions create optimal conditions for shocks to arise in the form of shells-like structures around the central feedback source. The SED of regions affected by shocks is largely determined by the relative velocity between these colliding gas clouds and their chemical composition. As the gas is compressed and heated by the shock, it can emit radiation across a wide spectrum, going up to X-rays of even gamma rays if the relative velocity of the clouds is high enough. Similar to AGNs, the emission lines produced in these environments usually comes from high ionization energy ions due to the high temperature that can be produced in this physical process.

1.4.3 ISM

Having explored the diverse sources of ionization within galaxies, now we turn our attention to the gas itself. The gas in the ISM exists in a variety of phases, each characterized by its unique density, temperature, and composition. Understanding these phases is crucial as they play a central role in star formation, galaxy evolution, and the interaction with ionizing radiation.

- **Hot, Highly Ionized Gas (Coronae and Filaments):** This gas resides in the halo of the galaxy and coronae of star-forming regions. It is the least dense (10^{-4} - 10^{-1} cm^{-3}) and hottest (10^{6} - 10^{8} K) phase.
- **Warm Ionized Gas (HII Regions):** Colder (10^{4} K) and denser (10 - 100 cm^{-3}) than the corona, HII regions are ionized nebulae surrounding hot, young stars. The intense UV radiation from these stars strips electrons from surrounding hydrogen atoms, creating a region of ionized gas.
- **Warm Neutral Medium (WNM):** This relatively warm (several thousand K) and diffuse (0.5 - 1 cm^{-3}) phase is composed primarily of neutral hydrogen. The WNM occupies a significant volume of the ISM and is the source material for star formation.

- **Cold Neutral Medium (CNM):** Denser (20 - 500 cm^{-3}) and cooler (around 100 K) than the WNM, the CNM is another major reservoir of neutral hydrogen in the ISM. This phase plays a crucial role in star formation as gravitational collapse within the CNM can initiate the birth of new stars.

- **Molecular Clouds:** The densest (100 - 10^6 cm^{-3}) and coldest (10 - 50 K) phase of the ISM, molecular clouds are composed primarily of H_2 and other molecules like CO. Dust grains are also abundant in these regions. Shielded from UV radiation by their outer layers, molecular clouds are the birthplaces of stars and planetary systems.

As gas in the ISM cools and condenses, it transitions from the atomic to the molecular phase, reaching a point in which it forms dust. Interstellar dust, composed of silicates, carbonaceous materials, and polycyclic aromatic hydrocarbons (PAHs), plays a crucial role in the thermal and chemical processes of the ISM. These grains, ranging from a few nanometers to several micrometers, undergo dynamic changes in composition and size due to accretion, erosion, and shattering, illustrating the evolving nature of the ISM (e.g., Nozawa et al. 2006). Dust causes extinction by absorbing and scattering light, altering the color and brightness of sources behind dust regions (e.g., Mathis 1990). Dust grains emit thermal radiation akin to black bodies, with temperatures ranging from 10 to 1000 K, which is pivotal for understanding the energy dynamics within the ISM (e.g., Zucconi et al. 2001; Bernard et al. 2010; Ma et al. 2019). This dynamic interplay between dust, gas, and radiation shapes galaxy evolution and star formation.

After discussing the phases of the ISM and the pivotal role of interstellar dust, it is imperative to delve deeper into the chemical composition of the atomic gas. The elements found in the ISM are not uniformly distributed; their abundances and origins vary significantly, painting a complex picture of chemical evolution in the Universe.

The atomic gas in galaxies, encompasses a vast array of elements, each tracing back to distinct cosmic phenomena. These origins fall into two primary categories: primordial nucleosynthesis, responsible for the formation of the lightest elements like hydrogen and helium in the nascent Universe shortly after the Big Bang (see Fig. 1.4), and stellar nucleosynthesis, a complex array of processes that forge heavier elements within the cores of stars or in their tumultuous demise.

Stellar nucleosynthesis itself encompasses several mechanisms, reflective of the life cycles and endpoints of stars of varying masses and compositions. Dying low-mass stars, such as red giants, contribute to the ISM through planetary nebulae, enriching it with elements like carbon and nitrogen. In contrast, exploding massive stars, or supernovae, are key sources of oxygen, silicon, and iron, among others, catalyzing the rapid nucleosynthesis that occurs during their explosive final moments. Meanwhile, merging neutron stars, in their cataclysmic collisions, produce a wealth of heavy, neutron-rich elements like gold and platinum in a process known as the r-process. Exploding white dwarfs, often in type Ia supernovae, primarily contribute to the synthesis of intermediate-mass elements such as silicon and iron (see Fig. 1.4).

Beyond these natural stellar processes, more exotic mechanisms like cosmic ray fission also play a role in the cosmic ballet of element formation, albeit on a much smaller scale. These high-energy particles can split nuclei into lighter elements as they traverse the galaxy. Additionally, human synthesis, while not contributing significantly to the cosmos at large, has expanded our understanding of chemical elements, creating unstable isotopes that exist momentarily before decaying (see Fig. 1.4).

Each of these processes underscores the complexity and dynamism of chemical evolution in the Universe, painting a picture of an ever-changing cosmic landscape where elements are continuously recycled and reformed, driving the engine of stellar life and death.

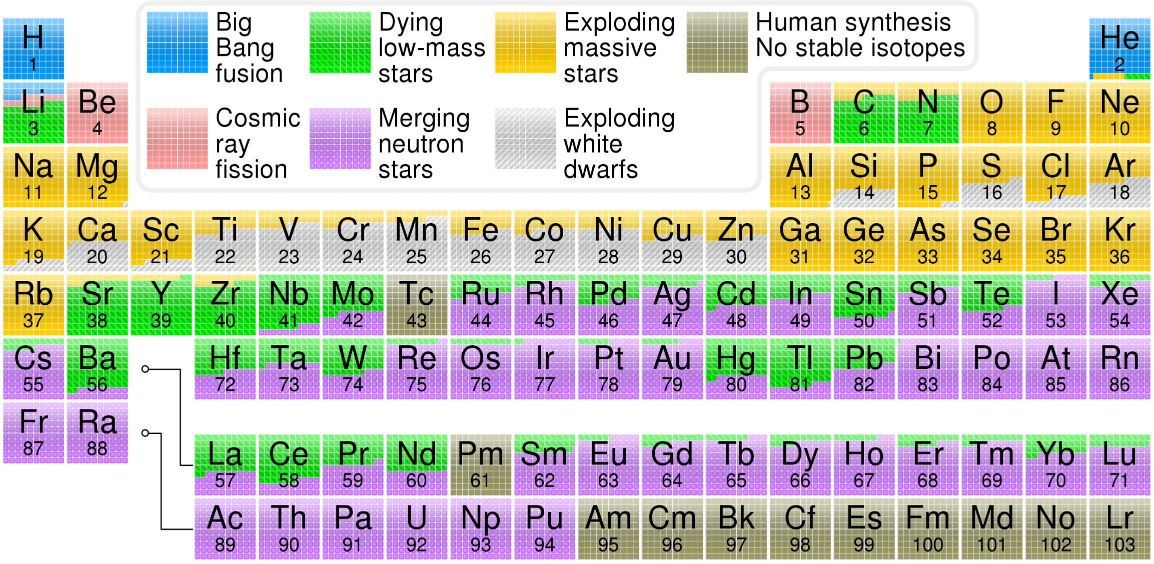

Figure 1.4 Periodic table showing the cosmological origins of the elements in the Solar System. See in https://commons.wikimedia.org/wiki/File:Nucleosynthesis_periodic_table.svg

As a proxy to understand the diverse abundances of each element, we can use the MW, whose chemical composition has been extensively studied and documented. This detailed analysis serves as a valuable benchmark for comparing elemental abundances across different cosmic environments.

In table 1.1 we can see the abundances of the main elements in the MW by Croswell (1996). Hydrogen and helium, the most abundant elements, highlight the primordial nucleosynthesis aftermath. Meanwhile, the presence and ratios of elements like oxygen, carbon and nitrogen are testament to the dynamic life cycle of the galaxy, revealing the history of star formation and the types of stars that have contributed to the enrichment of the ISM. This complex tapestry of elemental abundance, detailed in the MW, serves as a foundational observation of chemical abundances.

Table 1.1 Fractional abundances of the ten most common elements in the MW, estimated spectroscopically by Croswell (1996).

Z (1)	**Element** (2)	**Mass fraction** (3)
1	Hydrogen	739,000
2	Helium	240,000
8	Oxygen	10,400
6	Carbon	4,600
10	Neon	1,340
26	Iron	1,090
7	Nitrogen	960
14	Silicon	650
12	Magnesium	580
16	Sulfur	440
	Total	999,060

Column (1): Atomic number of the element. Column (2): Name of the element. Column (3): Mass fraction, being 1,000,000 the total amount.

The atomic composition of the Universe is not static but in perpetual motion, intricately linked to the lifecycle of stars. This cycle of star formation and subsequent demise serves as a cosmic forge, transmuting simple elements into increasingly complex ones. Over the vast canvas of cosmic time, there emerges a discernible trend in this process: a gradual shift towards elements that exhibit lower binding energy per nucleon. Central to this narrative is iron-56 (^{56}Fe), which stands as a pivotal benchmark in nuclear stability (see Fig. 1.5).

The accompanying graph (Fig. 1.5) underscores the binding energy per nucleon, highlighting the paramount role of ^{56}Fe. Its prominence is rooted in its peak position on the curve, denoting the point at which nuclear reactions no longer release energy through fusion or fission. This hallmark of stability marks ^{56}Fe as a significant terminus in the process of stellar nucleosynthesis, where elements strive for greater stability.

While the atomic composition of the Universe undergoes continuous transformation, driven by the cycle of star formation and destruction, a broader perspective reveals a Universe

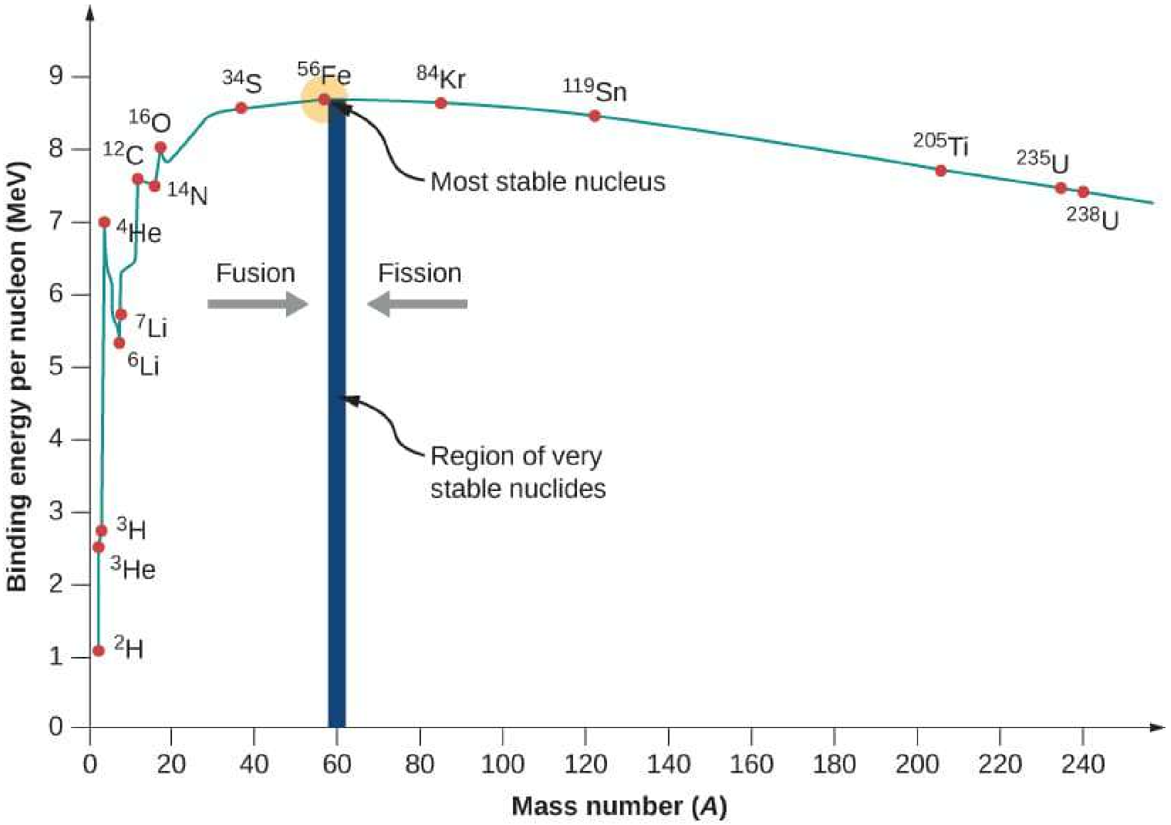

Figure 1.5 Graph of binding energy per nucleon for stable nuclei. See in https://phys.libretexts.org/Bookshelves/University_Physics.

that remains chemically immature. Despite the natural tendency of atomic nuclei to evolve towards configurations with lower binding energy per nucleon, hydrogen (the simplest and most primordial of element) continues to predominate, as much as it did in the immediate aftermath of primordial nucleosynthesis.

At the dawn of the Universe, following the epoch of primordial nucleosynthesis, hydrogen constituted approximately 75% of all baryonic matter by mass, with helium accounting for nearly all of the remaining 25% (e.g., Olive et al. 2000). This initial abundance set the stage for the long-term evolution of the Universe. Today, despite billions of years of stellar activity and the production of heavier elements, hydrogen remains the most abundant element, constituting roughly 74% (e.g., Croswell 1996) of the baryonic mass in the Universe. This slight decrease is testament to the ongoing process of stellar nucleosynthesis yet underscores the slow pace of chemical maturation on a cosmic scale.

This enduring dominance of hydrogen suggests that the Universe is still in a relatively early stage of its chemical evolution. Stars continue to form and fuse hydrogen into helium and other heavier elements, a process that could persist for trillions of years. Another explanation for such a high hydrogen dominance in the local Universe ISM, is the fact that a portion of the heavy elements created in the Universe are confined in what we could call the heavy elements graveyards (BHs, neutron stars, brown dwarfs and even planets). A fraction of the metals produced in stars never gets to be released and remain imprisoned in these kind of structures. The accreting gas around AGNs is known for presenting high metallicity (e.g., King 2005), this gas is being trapped in the central BH. Constraining the portion of heavy elements confined in these regions is not trivial, but it should contribute to explaining the hydrogen dominance in the local Universe. Anyway, the eventual fate of star formation, and indeed the chemical maturation of the Universe, may be influenced not by a depletion of hydrogen, but rather by the cosmic expansion (e.g., Briscese et al. 2007; Yurov et al. 2008). As the Universe expands, the increased distances and recession velocities between objects could slow down and eventually halt the process of star formation, leading to a cooling and quieting of the cosmos.

Still, the future of the Universe (specially in terms of the balance between gravity and the dark energy expansion) is unknown. Yet, in term of chemical abundances, hydrogen will continue to serve as the primary building block for stars, underscoring the ongoing chemical youth of the Universe and its potential for continued stellar activity.

1.4.4 Interplay between ionization sources and gas

In the diverse and dynamic environments of galaxies, the interplay between ionization sources and the interstellar gas they encounter is a fundamental aspect of astrophysical phenomena. When the high-energy photons emitted by these sources encounter interstellar gas, they ionize the gas by stripping electrons from atoms. This ionization process is not merely a one-step event but acts as a catalyst for a series of subsequent reactions within the gas. As electrons recombine with ions, they transition between different energy levels. Each of these transitions results in the emission of photons at specific wavelengths, characteristic of the electronic structure of the atom. These photons manifest as emission lines in the spectra of galaxies, serving as luminous fingerprints of the underlying atomic processes.

The interaction between light and gas within a galaxy is a sophisticated "dance" between photons, electrons, and various atomic nuclei, unfolding in regions often much larger in volume than the ionization sources themselves and involving a myriad of processes:

- **Photoionization**: This process occurs when high-energy photons eject electrons from atoms. It depends on the energy of the photon surpassing the ionization threshold (or ionization energies) of the atom. For instance, hydrogen requires 13.6 eV to ionize, while the ionization energies of the helium are 24.6 eV (to HeII) and 54.4 eV (to HeIII).

Elements like oxygen and iron have their specific thresholds, with oxygen needing almost the same as H (around 13.6 eV) and iron about 7.9 eV for the first ionization (the first ionization energy of some elements can be seen in Fig. 1.6). As of in the case of He, each ionization of a second, third... electron tends to require more energy each time.

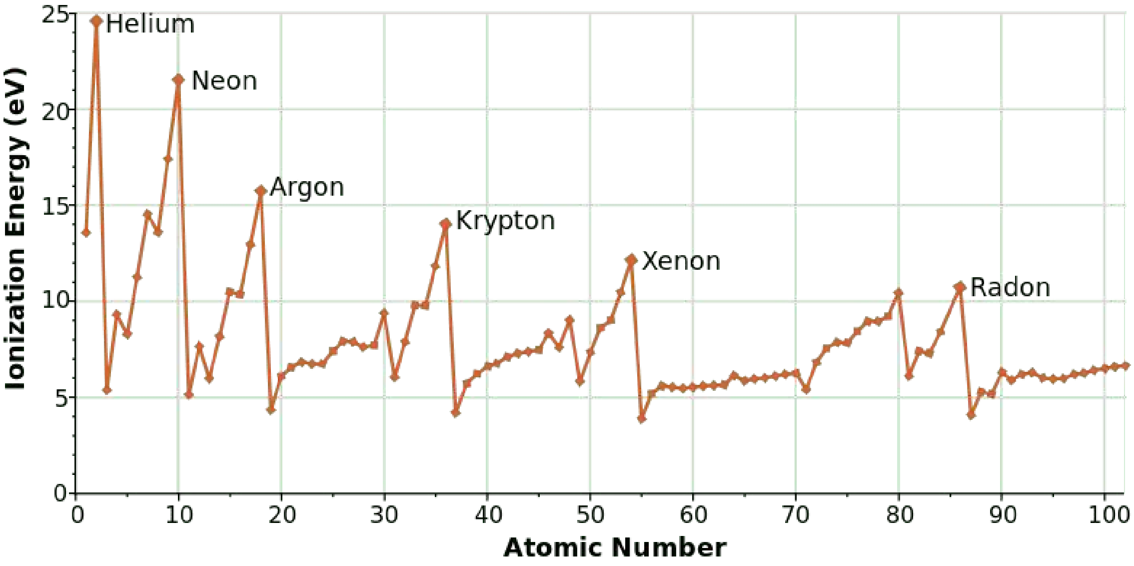

Figure 1.6 First ionization energy of some chemical elements. See in https://chemistrytalk.org/ionization-energy-trend/.

When the energy of the photon is the same as the ionization energy the absorption cross section (or the probability of the process to occur) reaches its peak. The photoionization can still happen if the energy of the photon is above the ionization energy, leading to an increment of the kinetic energy of the system (influencing the dynamics of the ISM) but the absortion cross section drops to zero as the difference of energies increases (Osterbrock & Ferland 2006).

A similar process happens when the electron have less energy that the ionization energy but matches the difference of energy between two electronic states. If the electron is in the state with less energy it can absorb the photon by reaching the higher level. This can be simply called electron photo-excitation.

- **Recombination**: This process is the inverse (in time) of the photoionization. Recombination describes the capture of a free electron by an ionized atom, leading to the emission of one or several photons as the electron in the atom returns to a lower energy state. This process has different probabilistic outcomes than the photoionization. For instance, the direct transition of an electron to the ground state during recombination is less probable compared to a cascading process, where the electron sequentially transitions through excited states, releasing a photon with a very concrete energy at each step. This cascade effect is fundamental for producing emission lines that are characteristic of each element in the ISM.

The probabilistic nature of these processes has significant implications for the spectral characteristics of light. For example, photoionization often occurs due to the absorption of an UV photon; while the release back of this UV photon due to a subsequent recombination is possible, but not likely. Rather it is more probable that in the recombination, the energy of the UV photon is reconverted into several photons with lower energies resulting from an electron cascade. This phenomenon, where high energy light is spread among low energy light, can be interpreted as an increase in the entropy of the light itself.

Nevertheless, there exist processes characterized by equal probabilities of occurring in either direction, these are called resonant processes. As an example, the photo-excitation of an electron from the ground state to the first excited state is followed by its inevitable return to the ground state (if undisturbed). A prime example is the Lyα resonance in hydrogen (Brasken & Kyrola 1998), where photons with a specific energy are scattered in random directions by neutral hydrogen. This scattering contributes to the diffuse nature of certain spectral lines observed in astronomical phenomena.

- **Collisional Excitation/Ionization**: Occurs when a particle, such as a free electron, collides with an atom or ion, transferring part of its kinetic energy to the atom. This transfer can result in an electron bound to the atom being excited to a higher energy level or even ejected from the atom, leading to ionization. This dual process is prevalent in hot, dense astrophysical environments, where electrons with sufficient kinetic energy are abundant. The occurrence of collisional excitation/ionization depends on several key factors.

  The efficiency of collisional excitation and ionization is influenced by a combination of factors including the density of particles, the temperature of the gas, and the specific energy levels of the atom involving excitation and ionization, which vary across different elements. High particle densities increase the likelihood of collisions, facilitating excitation and ionization processes. Similarly, higher temperatures equate to greater kinetic energies for particles, enabling them to overcome the excitation energy thresholds and ionization potentials of atoms more readily. This is particularly evident in environments ranging from a few thousand to 25,000 K, where collisional excitation is pronounced, especially for atoms and ions with lower excitation thresholds. Such conditions are characteristic of HII regions surrounding young stars.

In extremely hot environments, such as the coronae of stars or the hot ISM where temperatures exceed 10^6 K, collisional ionization becomes dominant. For example, at a temperature of 10^6 K, approximately 95.71% of electrons in a plasma in thermal equilibrium have sufficient energy to ionize hydrogen (according to the Maxwell-Boltzmann distribution). This vast proportion of high-energy particles at elevated temperatures significantly alters the ionization balance and contributes to the X-ray emissions observed from these regions. Conversely, at lower temperatures, such as 10,000 K, only a minuscule fraction (about 0.0000646%) of electrons can ionize hydrogen, highlighting the dramatic effect of temperature on ionization processes within astrophysical plasmas.

Interestingly, the phenomena of shocks and AGNs in galaxies illuminate the versatility of collisional excitation/ionization. Shocks, resulting from the supersonic collision of gas clouds, generate rapid compressions and heating of the gas, transforming collimated kinetic energy into thermal energy of the gas at the boundaries. The average relative velocities of the clouds within such shocks, usually range from 50 km s^{-1} to 2000 km s^{-1}. Considering that most particles whitin these gases have the mass of Hydrogen, the impact would generate temperatures approximately between 25,000 K and 60 millions K. For this calculation, we use the relationship between the mean square velocity (i.e. the speed of a particle with average kinetic energy) of particles and the temperature of the gas that can be described by the equation:

$$v_{rms} = \sqrt{3/2}\sqrt{\frac{2kT}{m}}$$

known as the thermal velocity formula (derived from the Maxwell-Boltzmann distribution). In this equation, v_{rms} represents the mean square velocity of the particle, k is the Boltzmann constant (1.380649×10^{23} m^2 kg s^2 K^1), T is the temperature and m is the mass of the particle. This equation crucially links the microscopic kinetic energy of particles to macroscopic thermal properties of the gas. Regarding AGNs, the emission of light is primarily due to gas that accelerates as it spirals towards a central supermassive BH. This spiraling process generates significant friction among the gas particles, mirroring the shock phenomena by transforming collimated kinetic energy into thermal energy. The friction not only heats the gas to extreme temperatures but also triggers a wide spectrum of electromagnetic radiation, from radio waves to X-rays or even gamma-rays, effectively making AGNs some of the most luminous and powerful objects in the Universe. All this underline the extreme conditions under which collisional excitation/ionization occurs, further illustrating the transformative power of shock and AGNs events in galactic environments.

- **Collisional De-excitation**: The inverse of collisional excitation, this process involves an excited atom colliding with another particle, leading to a transfer of energy from the atom to the particle and resulting in the electron within the atom returning to a lower energy state. Collisional de-excitation redistributes energy within the gas, contributing to its thermal energy balance. This process is more likely in high-density environments where particle collisions are frequent.

The interplay between collisional excitation, ionization, and de-excitation is pivotal for understanding the thermal and ionization states of the ISM. Their rates, governed by environmental conditions such as temperature and density, offer tools to diagnose the physical conditions within stars, galaxies, and nebulae, shedding light on the complex dynamics that govern the Universe.

Connecting the processes of collisional de-excitation and radiative de-excitation of electrons (i.e. when the electron in an excited state goes to a lower state releasing a photon) arises the concept of critical density (n_{crit}). The critical density is a key parameter in astrophysics, especially in the study of emission lines from gases in various astrophysical environments. It refers to the density of collision partners (usually electrons) at which the rate of collisional de-excitation of an excited atomic or molecular state equals the rate of radiative de-excitation. At densities below the critical density, radiative processes dominate, whereas at densities above it, collisional processes are more significant.

To grasp the concept more concretely, consider a gas of atoms in thermal equilibrium that exists primarily in two electronic configurations: a base or ground state (0) and an elevated or excited state (1). Transitions between these states are facilitated either through the emission of photons or via direct collisions with other particles. In essence, the atom shifting from its excited state back to its ground state can occur spontaneously, emitting a photon in the process (radiative de-excitation), or through collisional encounters (collisional de-excitation) that directly impart kinetic energy. If the gas is also in ionizing equilibrium that means that the density of the excited state (n_1) follows the next relation:

$$0 = \frac{dn_1}{dt} = -A_{10}n_1 - k_{10}n_1n + k_{01}n_0n$$

where n_0 is the density of the ground state, n is the total density ($n = n_0 + n_1$), A_{10} is the Einstein coefficient from state 1 to ground state and k_{10} and k_{01} are the collisional coefficients from state 1 to ground state and from ground state to state 1 respectively. Now, taking into account that the gas follows the Maxwell-Boltzmann distribution, the ground state density follows the next relation

$$n_0 = n/Z$$

where Z is the partition function following the next equation:

$$Z = 1 + e^{-\frac{E}{KT}}$$

where E is the diference of the energies between the 1 state and the ground state, K is again the Boltzmann constant and T is the temperature. Unfolding all this we arrive to the next relation between densities:

$$\frac{n_1}{n_0} = \frac{e^{-\frac{E}{KT}}}{1 + \frac{n_{crit}}{n}}, \quad n_{crit} = \frac{A_{10}}{k_{10}}$$

Now that we have come to the final expression of the n_{crit} we are going to delve into what happens at different values of n. As n becomes much greater than the n_{crit} ($n >> n_{crit}$), collisional de-excitation predominates. This dominance of collisional processes implies that even though the number of atoms in the excited state increases, the likelihood of these atoms returning to the ground state via photon emission decreases, favoring non-radiative energy transfers. Conversely, when $n << n_{crit}$, radiative de-excitation takes precedence, meaning that atoms in the excited state primarily return to the ground state by emitting photons, contributing to the emission of spectral lines in the spectrum of the gas. Thus, it is important to recognize that in this regime, the process of cooling the gas through radiation is happening.

At around the n_{crit}, the emission of photons corresponding to the transition from the excited state to the ground state (emission line) reaches its peak for a given volume. This phenomenon occurs because, at densities lower than n_{crit}, increasing the density boosts the emission of photons due to the higher number of atoms capable of undergoing radiative transitions. However, as the density surpasses n_{crit}, collisional de-excitation begins to overshadow radiative processes, leading to a decline in photon emission despite the higher density. This dynamic creates an optimal point for the emission intensity of specific transitions.

Regarding typical critical densities, for hydrogen and double-ionized oxygen (OIII), the values can vary based on the specific transitions and conditions. However, as a general guideline:

- Hydrogen critical densities are typically in the range of 10^3 to 10^5 cm^{-3} for transitions relevant in astrophysical contexts, particularly in the visible spectrum such as the Balmer series.

- O III transitions, often observed in nebulae and indicative of high-temperature regions, have critical densities that can go up to 10^5 to 10^6 cm^{-3}.

These critical densities offer invaluable insights into the physical conditions of astrophysical gases, guiding the interpretation of their emission spectra and enhancing our understanding of the environments where these gases reside.

1.4.5 Physical - chemical properties derived from emission lines

Emission lines are observed across all wavelength ranges and provide critical insights into the physical conditions within galaxies. They reveal not only the chemical composition of the ISM but also the density, temperature, ionization state and kinematics of the gas. Furthermore, the presence and intensity of specific emission lines can elucidate the mechanisms driving the ionization.

Ionization source

Each ionization source imprints its signature on the gas it interacts with, altering the physical state of the ISM. The resulting emission lines serve as a diagnostic tool, allowing us to decipher the conditions within galaxies, from the ages of their stars to the presence of AGNs and the impact of dynamic processes like shocks. Through the analysis of these spectral fingerprints, we gain insights into the complex interplay between light sources and the vast clouds of gas that populate the cosmos, offering clues to the life cycles of galaxies and the universal processes that govern their evolution. We now focus on differentiating the ionization sources within galaxies.

One of the initial steps in this exploration is the application of the Baldwin, Phillips & Terlevich (BPT) diagram (Baldwin et al. 1981; Kauffmann et al. 2003; Kewley et al. 2006), a cornerstone in the field of astrophysics for discerning the dominant ionization mechanisms within galaxies. By comparing the ratios of specific emission lines: [O III]λ5007 Å/Hβ (hereafter [O III]/Hβ) vs [N II]λ6584 Å/Hα (hereafter [N II]/Hα), [S II]$\lambda\lambda$6717,6731 Å/Hα (hereafter [S II]/Hα), or [O I]λ6300 Å/Hα (hereafter [O I]/Hα), the BPT diagram categorizes galaxies into those with star formation-dominated ionization, those influenced by AGNs, and those affected by shock ionization.

The BPT diagram is an essential yet simplified tool for galaxy classification that does not account for the complexity introduced by the nitrogen-to-oxygen ratio (N/O). This ratio, shaped by the star formation history of a galaxy, affects the diagram position independently of the underlying ionization mechanism. Specifically, variations in the N/O ratio (reflecting the relative contributions of low and high mass stars to nitrogen and oxygen production) can shift the placement within the BPT diagram ([OIII]/Hβ vs [NII]/Hα) in a particular galaxy. Such shifts are not indicative of changes in the ionization source but rather highlight the N/O ratio as an additional parameter that must be considered.

Additionally, the complexity of ionization sources is further exemplified by shock models in galaxy diagnostics. These models demonstrate that by adjusting parameters like shock velocity and the N/O ratio, it is possible to replicate the emission line ratios associated with both AGNs and star-forming regions, spanning the entirety of the BPT diagram. This underscores the limitations of the diagram and the necessity for a more sophisticated analysis to resolve the ambiguities in emission line diagnostics and accurately identify ionization mechanisms.

Electronic temperature

Following the discussion of the BPT diagram and the nuances of ionization mechanisms within galaxies, we delve into the methods of determining the physical conditions of the ISM, specifically focusing on the temperature and density of the gas. These parameters are crucial for understanding the energetic and dynamic state of the gas in galaxies.

The temperature of the gas is determined by the electronic temperature. This is based on the principle that the low mass of the electrons allows for a rapid distribution of kinetic energy throughout the gas. To determine the electronic temperature, we rely on line ratios of specific emission lines, such as the ratio of [OIII]λ4363 Å to [OIII]λ5007 Å. The underlying physics is that a higher electronic temperature results in greater kinetic energy of free electrons, enabling them to excite electrons within the oxygen ions to higher energy states. For instance, the emission of [OIII]λ4363 Å requires electrons to occupy a higher energy level ($^1S_0$ see Fig. 1.7) compared to the lower energy state ($^1D_2$ see Fig. 1.7) necessary for the emission of [OIII]λ5007 Å. Therefore, an increase in electron temperature leads to a higher ratio of [OIII]λ4363 Å to [OIII]λ5007 Å because a greater proportion of electrons possess the requisite energy to transition to the $^1S_0$ state. For example, in an HII region with a temperature of 10890 K / 19770 K (acording to the Maxwell-Boltzmann distribution), approximately 1% / 10% of electrons have enough energy to excite to the $^1S_0$ state (see Fig. 1.8), producing the [OIII]λ4363 Å emission, while about 15% / 41 % can achieve the $^1D_2$ state, allowing for the emission of [OIII]λ5007 Å. Thus for a temperature of 10890 K / 19770 K the fraction of electrons able to produce the [OIII]λ4363 Å emission divided by the fraction of electrons able to produce the [OIII]λ5007 Å emission is ~ 7% / ~ 24%. In conclusion, the higher the temperature the higher will be the [OIII]λ4363 Å/[OIII]λ5007 Å value.

Just as the ratio of [OIII]λ4363 Å to [OIII]λ5007 Å emission lines is utilized to calculate the electronic temperature in galaxies, similar methodologies apply to other ions like NII.

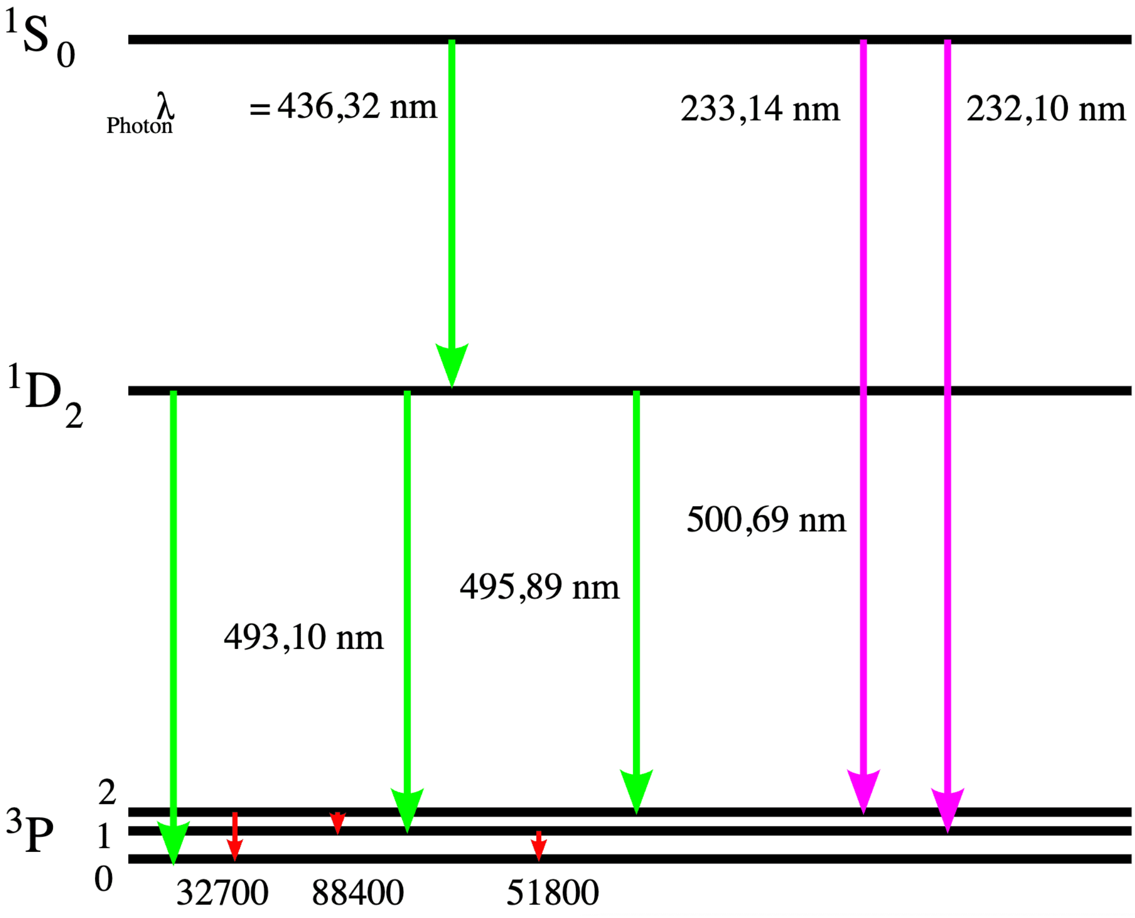

Figure 1.7 Energy levels of the electron in the OIII ion. See in https://commons.wikimedia.org/wiki/File:Oiii-linesp.svg.

This is thanks to their analogous electronic structures, since both ions have the same number of electrons. Thus OIII and NII ions exhibit proportional electronic energy levels, with the proportionality constant varying based on the charge of the atomic nuclei. This similarity allows to use specific NII line ratios ([NII]λ5755 to [NII]λ6584 ratio), analogous to the OIII lines, for electronic temperature determinations, offering an alternative method that can be particularly useful in different regions of a galaxy.

Furthermore, ions such as SIII, SII and OII are also valuable for assessing electronic temperatures, each with unique electronic levels that contribute to a broader understanding of the conditions of the ISM. The spatial distribution of these ions within a galaxy (e.g. OIII often found in highly ionized regions close to ionization sources, and NII in less ionized, outer regions of HII regions) enables the mapping of temperature gradients across the galaxy. By measuring the emission lines attributed to different ions, we can infer varying

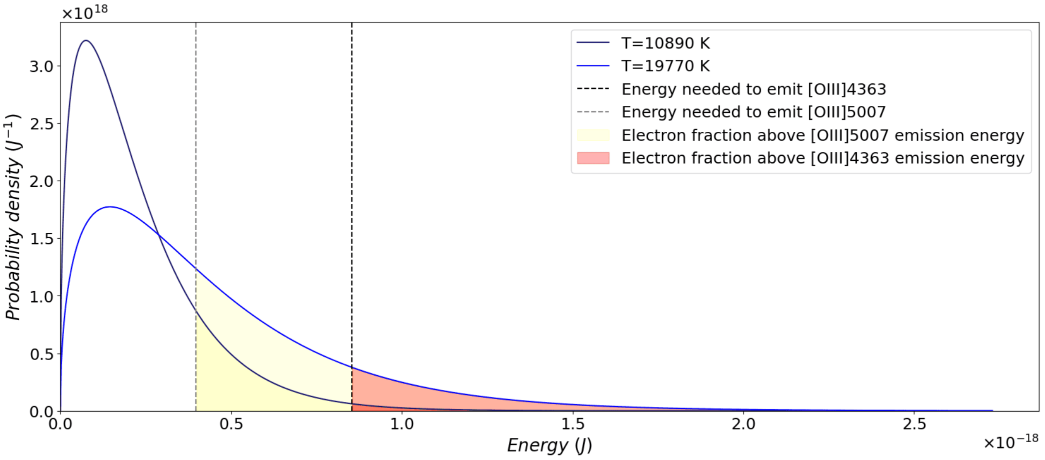

Figure 1.8 Maxwell-boltzmann distribution for temperatures of 10890 K and 19770 K. The yellow area indicate the fraction of electrons that have enough energy to excite the OIII to its $^1D_2$ state. The red area indicate the fraction of electrons that have enough energy to excite the OIII to its $^1S_0$ state. Gray vertical line indicates the energy of the $^1D_2$ state. Black vertical line indicates the energy of the $^1S_0$ state.

electronic temperatures, providing insights into the physical state of the gas in distinct galactic environments.

Electronic density

Building on the methodologies for determining electronic temperatures in galaxies, electronic density is another fundamental parameter that can be assessed through the analysis of emission lines. The density of electrons within the ionized regions of a galaxy influences the intensity and ratios of specific emission lines, serving as a key diagnostic tool for understanding the conditions of the ISM.

The analysis of specific diagnostic line ratios offers insights into the electronic density. Among these, the forbidden lines of singly ionized sulfur, [SII]λ6716 Å and [SII]λ6731 Å, serve as key indicators (see Fig. 1.9). These lines originate from closely spaced energy levels, which minimize temperature effects on their emission (contrary to what we are looking for in temperature diagnostic). The fact that these lines are forbidden means collisions with free electrons (rather than photon absorption) are the primary mechanism for electron excitation to these higher levels.

The electrons in the lower energy level of the Sɪɪ can be excited to higher levels (3/2 or 5/2) through collisions (see Fig. 1.9). Given the energy proximity of these levels, collisions have a roughly equal probability of exciting an electron to either level. However, differences in the statistical weight between the two levels introduce nuances in their population dynamics. Specifically, the 5/2 level, with a statistical weight of 6, can hold more electrons than the 3/2 level, which has a weight of 4. This means that the probability of populating the 5/2 level is 60% meanwhile the 3/2 level has a 40% chance. Moreover, the lifetimes of electrons in these levels are significantly different: 3846 seconds for the 5/2 level and 1136 seconds for the 3/2 level, such long times reflect the forbidden nature of the lines.

The density and temperature of the gas influence the frequency of collisions, affecting the excitation and de-excitation processes. At very low densities ($n << n_{crit}$), below about 100 cm^{-3}, collisions are infrequent, allowing most collisionally excited electrons to emit photons before another collision occurs. In this regime, the [Sɪɪ]λ6716 Å/[Sɪɪ]λ6731 Å value reflects the ratio of statistical weights (6/4 = 1.5) (see Fig. 1.10), with lifetimes playing a negligible role. Conversely, at high densities ($n >> n_{crit}$), above about 10,000 cm^{-3}, colisional de-excitation dominates and the line ratio converges to a value determined by both statistical weights and lifetimes (6 × 1136 s / 4 × 3846 s = 0.44) (see Fig. 1.10). The significance of lifetime becomes evident, as shorter-lived levels tend to emit more strongly when collisional de-excitation dominates.

The utility of the measurement of the line ratio lies in its ability to gauge the gas density within the nebula. The observed [Sɪɪ]λ6716 Å/[Sɪɪ]λ6731 Å value varies when density moves between the low and high extremes previously mentioned, providing a sensitive diagnostic tool (see Fig. 1.10). As density increases from the lower limit, the relative lifetimes of the two levels influence the ratio due to escalating collision frequencies. The advantage shifts towards the shorter-lived 3/2 level, enhancing the [Sɪɪ]λ6731 Å line relative to [Sɪɪ]λ6716 Å. This trend persists until reaching a density threshold where the lifetime advantage stabilizes, and the ratio no longer changes, marking a transition in the diagnostic utility of these line ratios for probing electronic densities in galaxies.

This method is widely applicable across a range of astrophysical contexts, from nebulae in our own galaxy to distant extragalactic HII regions and AGNs, where understanding the density of the ISM provides insights into the physical processes driving galaxy evolution.

Other ions, such as [Oɪɪ] (see Fig. 1.9) and [Arɪᴠ], also provide pairs of emission lines suitable for density diagnostics, each one sensitive to a particular range of electron densities. This allows for cross-verification of density estimates and the exploration of density variations within different ionization zones of a galaxy, offering a nuanced understanding of the ISM.

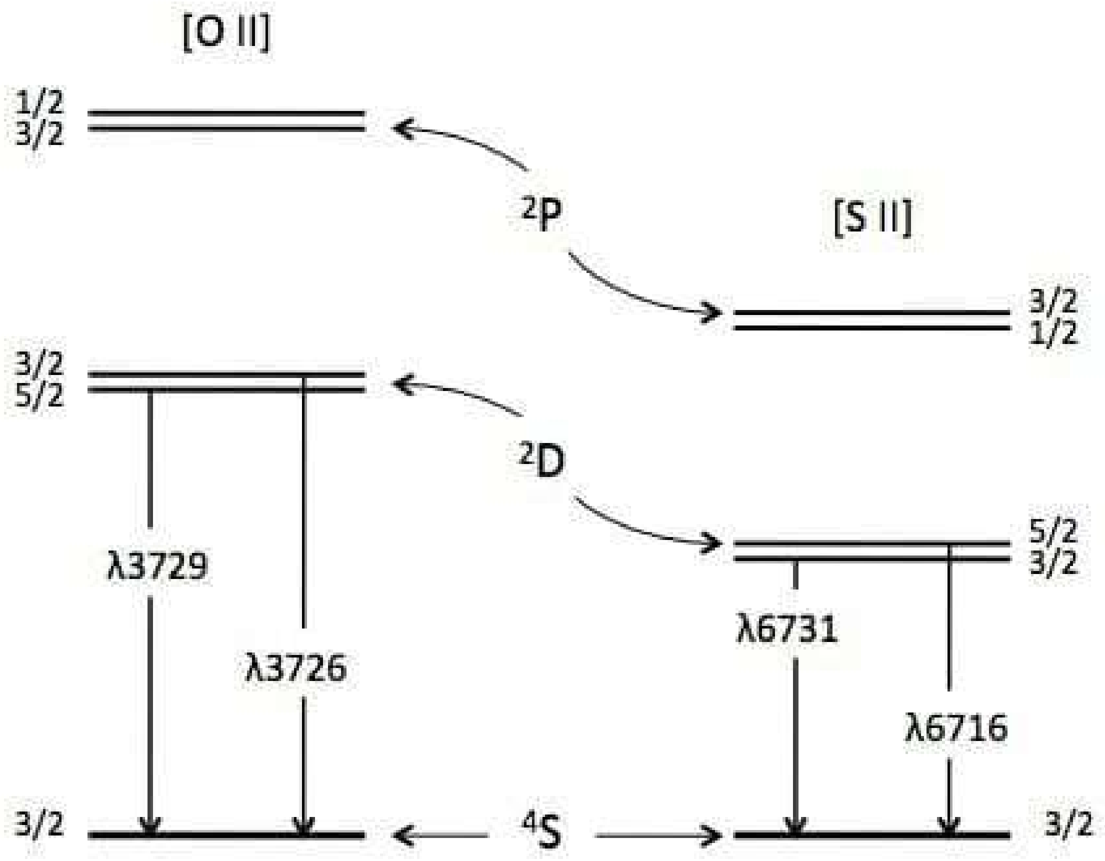

Figure 1.9 Energy levels of the electron in the OII ion and the SII ion. See in https://www.researchgate.net/figure/Energy-level-diagrams-of-the-2p-3-ground-configuration-of-OII-and-3p-3-ground_fig8_47702644

Kinematics of the gas

The characterization of gas kinematics within galaxies is a cornerstone of astrophysical research, providing essential insights into the dynamics of the galaxy such as the presence of a plane of rotation, stellar feedback processes and the influence of phenomena such as BHs and dark matter. At the heart of this analysis lies the Doppler effect, a principle that describes how the observed frequency of light waves changes relative to the motion of the source and the observer. When the relative motion happens in the line of sight this effect can be described as follows:

$$v = c\frac{(\lambda/\lambda_0)^2 - 1}{(\lambda/\lambda_0)^2 + 1}$$

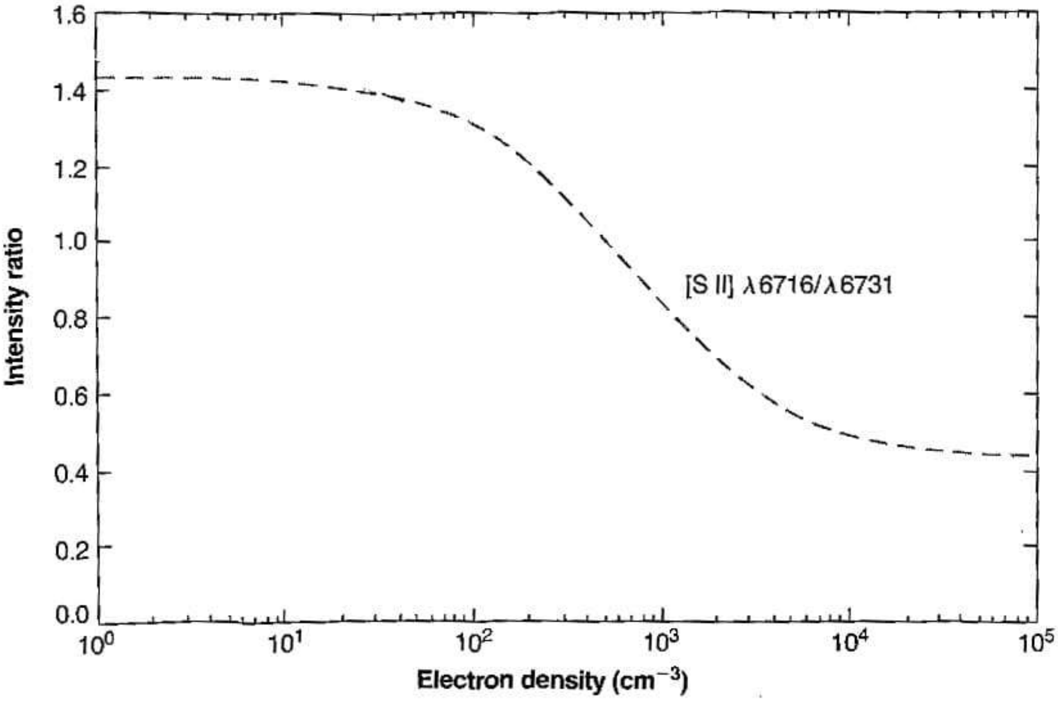

Figure 1.10 [SII]λ6716 Å / [SII]λ6731 Å value dependence on electronic density. See in https://web.williams.edu/Astronomy/research/PN/nebulae/exercise3.php.

where v is the relative velocity, c is the speed of light, λ is the observed wavelength, and λ_0 is the rest wavelength. In this way, when v is positive (source and observer moving away from each other) the wavelength of the light gets redshifted. Otherwise if v is negative (source and observer moving towards each other) the wavelength of the light gets blueshifted.

To determine the velocity of gas within different regions in the field of view (FoV) of a galaxy, we can measure the wavelengths of known spectral lines in the spectra of each region of the galaxy. Then, we compare these to their rest wavelengths (i.e., the wavelengths of these lines when observed in a laboratory setting). The shift from the rest wavelength offers a precise measurement of the radial velocity of the gas along the line of sight. If the spectral resolution is high enough and the galaxy presents complex kinematics (i.e. the line profile presents asymmetry, broadening or even several peaks), the analysis can be performed using various components (see Fig. 1.11). This allows to distinguish different regions along the line of sight with different kinematic properties. In this way, the velocity field generated help us to interpret the collimated motion of the gas in galaxies (see Fig. 1.12), that in several cases reveals the existence of a plane of rotation in the galaxy. If the rotation is present, the knowledge of how the velocity changes respect to the distance to the axis of rotation allows to estimate the mass of the galaxy as a function of this distance.

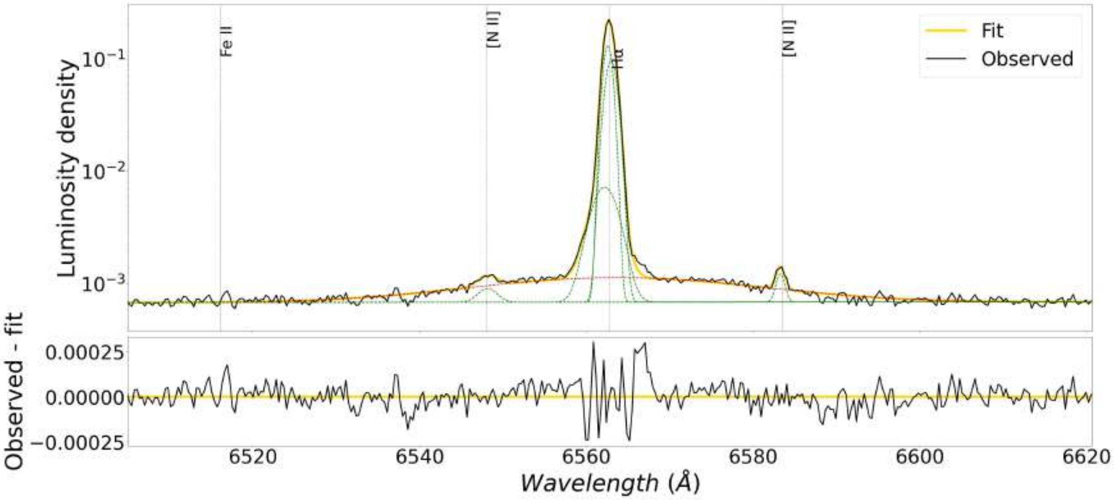

Figure 1.11 Hα line of the galaxy IZw18. In black it is represented the observed spectrum and in yellow the multi-gaussian fit. In green we can see the continuum plus the individual gaussians. In red it is represented the gaussian with high standard deviation (σ>10 Å).

The velocity dispersion is another critical concept in gas kinematics. It refers to the range of velocities around a mean velocity within a given area of the FoV. The velocity dispersion reflects the temperature, turbulence and even spatially unresolved collimated motions of the gas. It is measured through the broadening of spectral lines, a phenomenon that arises because the gas (within a particular area or spaxel in the FoV) is not moving at a single velocity but exhibits a distribution of velocities. The broader the spectral line, the greater the velocity dispersion, indicating a more significant spread in the velocities of the gas particles. The analysis of velocity dispersion is pivotal for understanding the energetic processes within galaxies. It can reveal the presence of gravitational disturbances, such as those caused by interactions with other galaxies, the influence of central supermassive BHs, or the dynamics of star formation regions. A high velocity dispersion in the gas around a galactic nucleus may suggest the presence of a supermassive BH whose gravitational forces induce high velocities in the surrounding gas. Furthermore, a high velocity dispersion in the gas near a star forming region could indicate the presence of stellar feedback in form of outflows. These outflows can even make holes in the ISM where Lyman continuum (LyC) photons may escape, connecting high velocity dispersion with escape fraction of LyC (Amorín et al. 2024).

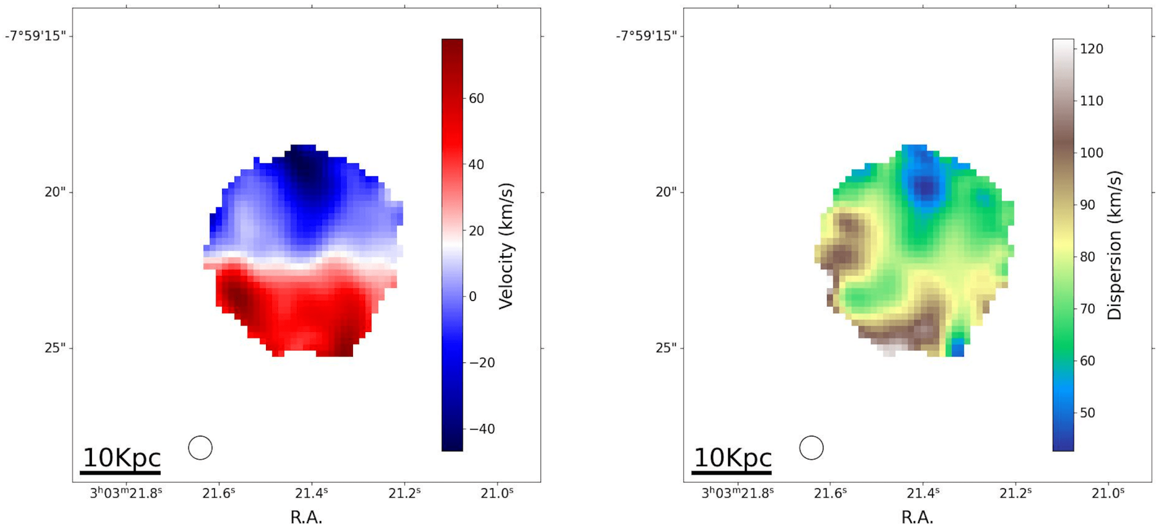

Figure 1.12 Velocity (left) and velocity dispersion (right) fields of the ionized gas in a GP.

1.5 This thesis

The aim of this thesis is to better understand the physical processes occurring in primeval galaxies through the observation of their local analogues, with a particular emphasis on extreme star formation events, or starbursts.

The structure of the thesis is methodically designed to narrow its focus from a broad analysis of potential starburst galaxies to a detailed study of specific cases with high-quality data. It begins with an exploration within J-PAS, where we shift through photometric spectra of approximately 60,000 objects. The goal of the first chapter is to identify EELGs indicative of starburst phenomena. This identification process involves detecting peaks in the photometric spectra to approximate redshifts and differentiate these galaxies from other astronomical bodies present in the survey.

The second chapter delves into an in-depth analysis of 24 GPs, utilizing data from MUSE/VLT. This phase of the research characterizes the ISM in a spatially resolved manner, assessing various parameters such as extinction, continuum versus gas morphology, excitation levels, density-bounded tracers, electron density and temperature, chemical abundances and gas kinematics.

In the final chapter, the thesis culminates in a study of the local extreme metal-poor galaxy (XMP) IZw18, employing the high spectral resolution data from MEGARA/GTC. This detailed examination allows for a comprehensive characterization of the gas kinematics within the galaxy through the analysis of the Hα line. The creation of luminosity, velocity, and velocity dispersion maps under both single-component and double-component models, alongside a multi-gaussian fit to the integrated spectra, reveals a very complex kinematical picture never seen before in this galaxy.

Overall, this thesis systematically narrows its lens from a wide-field survey to a focused study of individual galaxies, illuminating local extreme star-forming conditions that mirror those of the early Universe. Through this rigorous approach, we contribute to a deeper understanding of the universal mechanisms of star formation and galactic evolution, offering insights into the past through the lens of the present.

Chapter 2

Searching for EELGs in J-PAS

This chapter is based on the publication:

"The miniJPAS survey: A search for extreme emission-line galaxies"
by Jorge Iglesias-Páramo, Antonio Arroyo-Polonio et al.
Published in A&A, 665, A95 (2022).

https://doi.org/10.1051/0004-6361/202243931

2.1 Introduction

Understanding the evolution of the Universe relies on studying galaxies that experience intense bursts of star formation, which serve as the building blocks for more massive galaxies (e.g. Ono et al. 2010). Such galaxies may also be significant sources of the UV photons needed for the re-ionization of the Universe (e.g. Salvaterra et al. 2011; Dressler et al. 2015; Erb et al. 2016; Yang et al. 2017c; Sobral et al. 2018a; Naidu et al. 2022a; Matthee et al. 2022).

Galaxies with intense emission lines result from the ionization of gas surrounding young stellar complexes. This ionized gas accounts for a significant fraction of the energy radiated away. EELGs cover different categories depending on the selection method and their redshifts, including HII galaxies (Terlevich et al. 1991), BCDs (Kunth & Sargent (1986); Cairós et al. (2001)), GPs (Cardamone et al. 2009; Amorín et al. 2010), blueberry galaxies (Yang et al. 2017c), and ELdots (Bekki 2015). Even more, several studies report the detection of galaxies with strong emission lines with Spitzer/IRAC data using the color excess in one of the IRAC bands as a proxy for the EW (Labbé et al. 2013; Smit et al. 2015; Castellano et al. 2017; De Barros et al. 2019; Endsley et al. 2021). Some EELGs emit intense UV radiation that can double ionize the He and are therefore called HeII emitters (Shirazi & Brinchmann 2012; Cassata et al. 2013; Kehrig et al. 2018). Although such starburst galaxies can be found in the local Universe, they are more frequent at higher redshifts (Endsley et al. 2021; Boyett et al. 2022), where they can be detected by prominent emission in the Lyα line in some cases (e.g. Kunth et al. 2003; Erb et al. 2016; Sobral et al. 2018b; Sobral & Matthee 2019).

In previous studies, various methods were used to investigate EELGs at different redshifts. van der Wel et al. (2011) used broad band photometry to identify around 70 EELGs in the CANDELS fields, while Amorín et al. (2015) characterized nearly 180 of these galaxies from the 20k zCOSMOS bright survey, which were selected based on their high rest-frame EW (EW$_0$). Maseda et al. (2018) estimated the density of EELGs through an automated line search technique for slitless spectroscopic data from the 3D-HST survey, also using a high EW$_0$([OIII]). These studies indicate that EELGs have stellar masses in the range of $6.5 \leq \log(M_*/M_\odot) \leq 10$, are compact with $r_{50} < 2$ kpc, and have oxygen abundances of $12+\log(\mathrm{O/H}) \lesssim 8.16$. Additionally, Khostovan et al. (2016) explored the properties of approximately 7000 galaxies from the HiZELS survey with strong emission in the Hβ+[OIII]λ5007 Å (hereafter [OIII]) and [OII]$\lambda\lambda$3727,3729 Å (hereafter [OII]) emission lines in the redshift range of $0.8 \leq z \leq 5$ and found EW$_0$ between 10 Å $\leq$ EW$_0$ $\leq 10^5$ Å.

The minimum required EW$_0$ to classify a galaxy as an EELG is usually a few hundreds Å. Some BCDs show Hα EW$_0$ > 500 Å (e.g., IZw18, Moustakas & Kennicutt Jr 2006), and typical values of [OIII] EW$_0$ are > 500 Å (e.g Sobral et al. 2013; Brunker et al. 2020). In general, the EW_0 increases with redshift due to increased ionization efficiency (Sobral et al. 2014; Khostovan et al. 2016). Moreover, Lumbreras-Calle et al. (2021) identified a sample of EELGs at $z \leq 0.06$ with [OIII] $EW_0 > 300$ Å using 2000 deg^2 of the J-PLUS survey (Cenarro et al. 2019).

An exhaustive study regarding the number density of EELGs across a broad range of redshifts remains a challenge in observational astronomy. A comprehensive investigation of their fundamental characteristics at varying redshifts is vital due to their importance as high-redshift extreme emitters analogs. Therefore, a combination of large-scale surveying and advanced instrument design, which is sensitive to high EW emission features, represents an ideal approach to tackle this issue.

JPAS is a survey that will cover an area of approximately 8500 deg^2 with 56 contiguous narrow-band filters, each approximately 120 Å wide, spanning the range from 3800 Å to 9100 Å (Benítez et al. 2009; Benitez et al. 2014). J-PAS design has been shown to be effective in identifying normal emission line galaxies and measuring their fluxes (e.g. Martínez-Solaeche et al. 2021, 2022) and characterizing galaxy populations (Delgado et al. 2021). This instrumental setup is ideal for detecting objects showing an important excess of flux in one single band compared to the flux detected in the adjacent bands.

In this work, we present a methodology designed to select EELGs using the miniJPAS (Bonoli et al. 2021) and J-NEP datasets, both of which have the same filter setup and observational strategy as the larger J-PAS survey. These datasets were obtained using JPCam, the instrument of the 2.5 m Javalambre Survey Telescope (JST250) at the Javalambre Astrophysical Observatory (OAJ). The miniJPAS data was released in December 2019, while the J-NEP data was released in July 2021. Regarding the sky coverage, the miniJPAS data cover 1 deg^2 overlapping with the AEGIS fields, while the J-NEP field covers 0.25 deg^2. This pilot study aims to demonstrate the feasibility of our approach for detecting EELGs over a large area of the sky, and we focus on galaxies with EW_0 of at least 300 Å in the emission lines [OII], [OIII] or Hα.

2.2 Data and EELGs selection procedure

The miniJPAS Public Data Release (miniJPAS-PDR201912[1], December 2019), which covers four AEGIS fields with 60 visible filters and a field of view of ≈ 1 deg^2, was used in this study. The observations, telescope, and instrumental setup are described in detail in Bonoli et al. (2021). Additionally, we also use data from the J-NEP field, which has the same filter setup and observational strategy as miniJPAS and covers a field of view of ≈ 0.25 deg^2.

---

[1] http://archive.cefca.es/catalogues/minijpas-pdr201912/

EELGs are defined in this study as objects that exhibit an emission line with an EW_0 greater than or equal to 300 Å. To avoid potential biases in the underlying continuum, we limit our analysis to the J-PAS filter dataset covering the wavelength range between 4000 Å (filter J0400) and 9000 Å (filter J0900). Our focus is on detecting star-forming EELGs, which are most readily identified by prominent optical emission lines such as [OII], [OIII], and Hα. It should be noted that quasi-stellar objects (QSOs) may also display strong emission features in Lyα (1216 Å), CIV (1549 Å), CIII] (1909 Å), and MgII (2800 Å) that may appear in the optical range due to their usually high redshift ($z \gtrsim 2$).

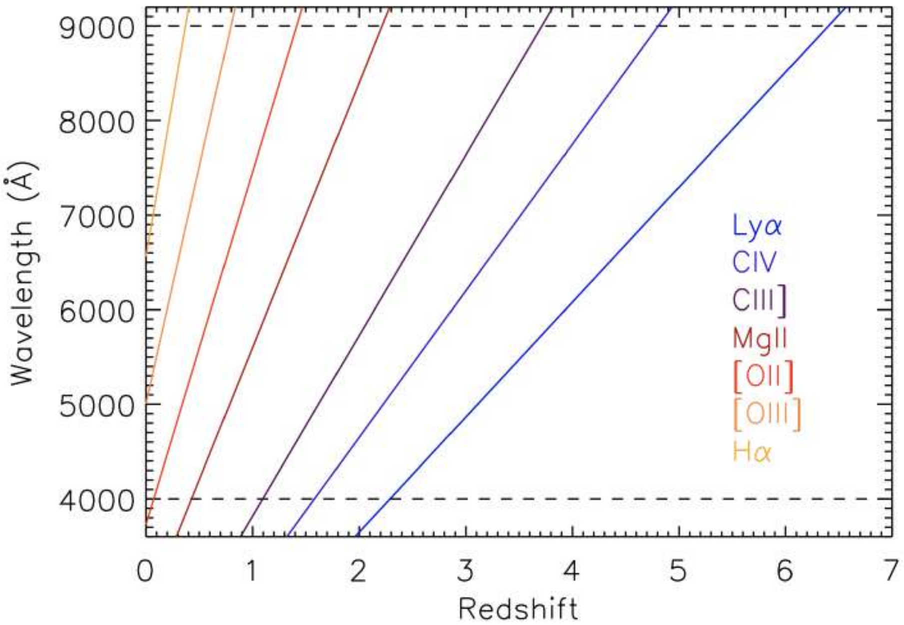

Figure 2.1 Redshift dependence of the most prominent emission lines in star-forming galaxies and QSOs within the wavelength range studied in this work ([4000,9000] Å).

Figure 2.1 displays the redshifted wavelengths of the emission lines of interest as a function of redshift, within the considered wavelength range. The emission lines [OII], [OIII], and Hα are detectable within our wavelength range up to redshifts of $z < 1.4$, $z < 0.8$, and $z < 0.4$, respectively. Therefore, our selection method would include all EELGs with EW_0 of at least 300 Å in these lines at these redshifts.

The first step in the analysis involves examining the information provided by the miniJPAS and J-NEP catalogs generated using Sextractor (Bertin & Arnouts 1996), including basic properties such as coordinates and fluxes. Sextractor operates in two modes: a single mode where sources are detected and measured on individual images, and a dual mode where sources are detected in the r_{SDSS} image and measured at the same position using the same criteria in the remaining filters. In this study, we start by using the dual catalog containing the fluxes in all miniJPAS and J-NEP images of the selected sources extracted from the r_{SDSS} image. Our detection procedure is based on the observable $(F_l - F_c)/F_l$, referred to as `Contrast` hereafter, where F_l and F_c represent the flux density in the image containing the emission line and the underlying continuum, respectively. As the emission lines of the EELGs are much narrower than the throughput curve of the narrow-band J-PAS filters, this ensures that in most cases all the flux of the emission lines is captured by the filter. The `Contrast` observable is similar to the observed EW, but is more stable for sources with very low continuum levels, which is common for EELGs. The relationship between this observable and the observed EW is given by:

$$\frac{F_l - F_c}{F_l} = \frac{\mathrm{EW}}{\mathrm{EW} + W_n/T_{peak,n}}, \tag{2.1}$$

where W_n is the total area under the throughput curve of filter n containing the emission feature, and $T_{peak,n}$ is the peak throughput of filter n. Thus, $W_n/T_{peak,n}$ represents the effective width of the filter.

Our objective is to identify galaxies with $\mathrm{EW}_0 \geq 300$ Å. Since EW_0 is always lower than the observed EW, we start by setting a limiting value on the `Contrast` equivalent to EW = 300 Å. This allows us to retain only those sources with $\mathrm{EW}_0 \geq 300$ Å after estimating their redshifts. Given that the throughput of the medium-band filters are not identical, the limiting value for the `Contrast` slightly varies from filter to filter. For the sake of simplicity, we adopt an average value of 0.674.

In order to evaluate the effectiveness of our method to select EELGs from the miniJPAS and J-NEP data, we first confirmed that it identifies known EELGs by comparing our results to SDSS-DR16 (Ahumada et al. 2020) data. We selected all galaxies from SDSS-DR16 with observed EW ≥ 300 Å in [Oɪɪ], [Oɪɪɪ] or Hα that were also present in the miniJPAS and J-NEP images. The EWs of these galaxies were determined by fitting Gaussian functions to the emission lines. All the selected galaxies were found in the miniJPAS field (there were no galaxies in the J-NEP field), none had observed EW ≥ 300 Å in [Oɪɪ], six had observed EW ≥ 300 Å in [Oɪɪɪ], and one had observed EW ≥ 300 Å in Hα. We then calculated the `Contrast` for each of these galaxies using the flux density measured in the narrow-band filter n, whose central wavelength is closest to that of the emission line, as F_l. To estimate the continuum flux density F_c, we performed a linear fit of the flux densities in the dual catalogue for filters with 100 Å $\leq| \lambda_i^{cen} - \lambda_n^{cen} |\leq$ 1000 Å, excluding the filter n and its two adjacent filters from the fit. This approach avoids including flux densities from filters that could be contaminated by the emission line. We interpolated the fit at the central wavelength of the filter to estimate F_c for each source. Given the faint nature of the EELGs, we defined a baseline of 2000

Å to define a stable continuum flux density. For Hα, the continuum was estimated in the rest-frame spectral region 5563 Å $\leq \lambda \leq$ 7563 Å, excluding the filter containing Hα and its two adjacent filters. The brightest emission lines in this region are [SII]$\lambda\lambda$6717, 6731 Å (hereafter [SII]), which are much fainter than Hα. For [OIII], the continuum was estimated in the rest-frame spectral range 4007 Å $\leq \lambda \leq$ 6007 Å, excluding the filter containing the [OIII] line and its two adjacent filters, which contain the [OIII]λ4959 Å (hereafter [OIII]b) and Hβ lines. There are no other bright lines in this spectral range that could affect the estimation of the continuum. For [OII], the procedure is similar to the previous cases, as there are several fainter emission lines in the spectral range selected to estimate the continuum. In all three cases, there are no bright emission lines in the wavelength range used to estimate the continuum, and we are confident that the derived values for F_c are not biased.

We also derived the continuum flux density underlying the emission line ($f_{c,l}$) and the flux of the emission line (F_λ) from the data using the Sextractor AUTO magnitudes. To estimate $f_{c,l}$, we interpolated a linear fit of the flux densities from the dual catalogue corresponding to filters with 100 Å $\leq\mid \lambda_i^{cen} - \lambda_n^{cen} \mid\leq$ 1000 Å, excluding the filter containing the emission line and its two contiguous filters. The value was derived by interpolating the fit at the wavelength of the emission line. To estimate F_λ, we deconvolved F_l with the profile of the filter n, assuming an infinitely narrow emission line and a value of $f_{c,l}$ for the continuum flux density. We produced 1000 random realizations of the J-spectra [2] of each source to estimate the uncertainties of these quantities. The final uncertainties were taken as half the difference of the percentiles 15.9 and 84.1 of the 1000 derived values for each quantity, assuming that the uncertainties of the fluxes are Gaussian.

Fig. 2.2 presents a comparison of the emission line parameters derived from the miniJPAS and J-NEP data and those measured from the SDSS spectra. The top panel displays the observed EWs obtained from the SDSS spectra as a function of the `Contrast` estimated from the miniJPAS and J-NEP data. The measured `Contrast` values for these sources are larger than the adopted threshold of 0.674, validating the use of this criterion for identifying EELGs. The middle panel shows the miniJPAS and J-NEP flux estimated for the emission lines (F_λ) versus the corresponding SDSS measurements. Although the agreement is generally good, the miniJPAS and J-NEP fluxes for the most intense emission lines are slightly underestimated by approximately 10% compared to the SDSS values, which could be due to the limited aperture of the SDSS fiber. Finally, the bottom panel depicts the continuum flux density underlying the emission lines derived from the miniJPAS and J-NEP data versus the corresponding SDSS values. For the lowest continuum levels, the agreement is reasonable, but the miniJPAS and J-NEP values are again below the SDSS measurements. Out of all the galaxies, only

---

[2] By J-spectra we mean the photo-spectra produced by the J-PAS filters

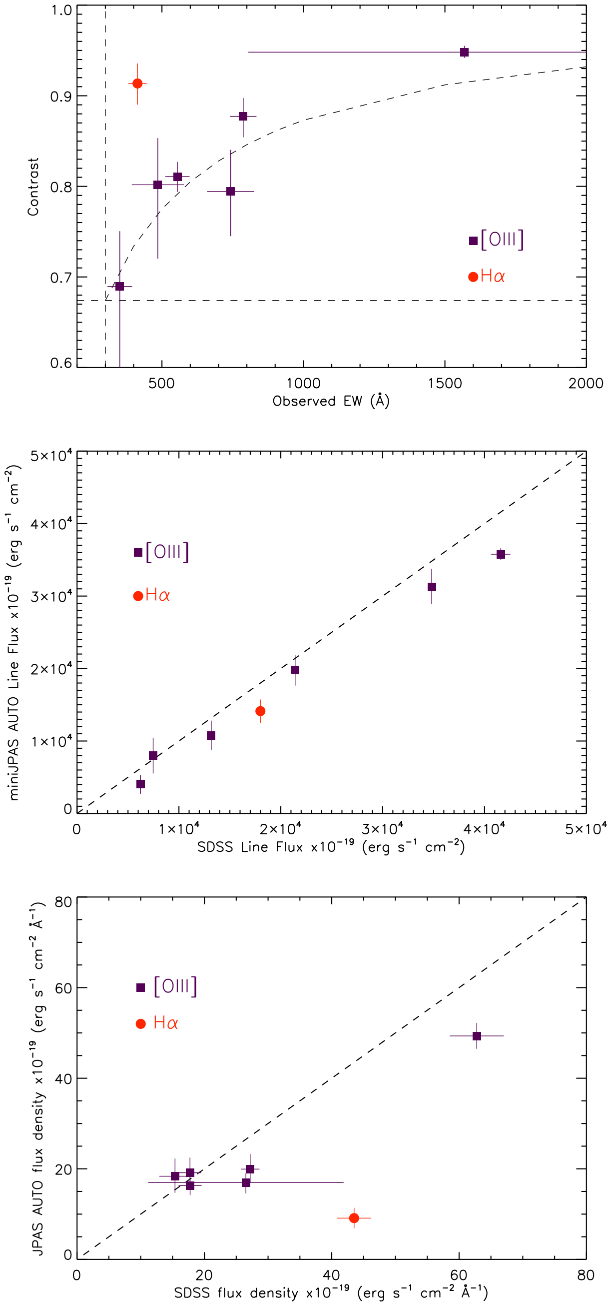

Figure 2.2 Comparing miniJPAS and J-NEP data vs SDSS spectra. Top: Contrast vs observed EW for SDSS galaxies with observed EW > 300 Å. Horizontal and vertical dashed lines indicate lower limits. The curved dashed line corresponds to the theoretical relation between the observed EW and the Contrast. Middle: Emission line flux from miniJPAS and J-NEP data vs SDSS flux. Dashed line shows one-to-one relation. Bottom: Continuum flux density from miniJPAS and J-NEP data vs SDSS flux. Dashed line shows one-to-one relation.

one shows significant discrepancies in the continuum and EW derived from the SDSS and miniJPAS and J-NEP data. This discrepancy is attributed to sky line contamination and the low continuum level of the galaxy, combined with the difficulty in matching the aperture of the SDSS fibre and the miniJPAS and J-NEP data. Overall, the results suggest that this method is useful for identifying EELGs from the J-PAS images, and we proceed to outline the steps followed to produce our list of EELG candidates.

Our selection is based on the dual catalogue extracted from the r_{SDSS} image, which lead to a bias as EELGs not detected in this catalogue are excluded even if they meet other selection criteria described later. We select sources from the dual catalogue [3] of each narrow-band J-PAS filter of interest (from J0400 to J0900) based on the following criteria: (a) $F_n \geq 10^{-17}\mathrm{ergs}^{-1}\mathrm{cm}^{-2}\text{Å}^{-1}$, where F_n is the flux density in filter n; (b) FLAG≤3 and MASK_FLAG≤0, to avoid instrumental artefacts and false detections; (c) $F_{8500}/F_{4300} < 1.2$, to avoid spurious detections of red objects; and (d) having a counterpart in the single catalogue corresponding to filter n, to ensure a real detection in the images.

We estimate F_c for each selected source using the same method as previously explained. Then, we confirm EELG candidates by imposing a minimum `Contrast` condition $(F_n - F_c)/F_n \geq 0.674$, corresponding to observed EW ≥ 300 Å in at least one emission feature. However, some sources may be discarded if their EW_0 is lower than our limiting value of 300 Å once their redshifts are estimated.

One additional condition was added to remove undesirable detections from the EELG candidates. Sources with an intensity peak in filter n lower than $5 \times \sigma$ are discarded, where σ is the standard deviation of the sky of the corresponding image n, as they are too noisy and produce spurious detections. No condition was imposed on the stellarity index of the selected sources since EELGs are known to show a compact appearance (e.g. Amorín et al. 2015). The final list of EELG candidates includes 38 sources with some of them detected in more than one filter.

As mentioned earlier, our EELG sample may be contaminated by high-redshift QSOs. To distinguish between star-forming galaxies and QSOs, we compared the J-spectra of our candidates to a sample of SDSS star-forming galaxies and QSOs from DR16. These spectra cover most of the J-PAS range and are ideal for comparison. We selected SDSS QSO and star-forming spectra from the SDSS-DR16 database based on their prominent emission lines, following the criteria established by Thomas et al. (2013). To cover a wide redshift range up to $z = 1.4$ for star-forming galaxies and up to $z = 6.49$ for QSOs, we shifted each SDSS spectrum (star-forming of QSO) from z-0.05 to z+0.05 in steps of 0.002. Synthetic photometry was performed by convolving the SDSS spectra with the narrow-band J-PAS filters, creating our comparison database of J-spectra. Additionally, synthetic spectra were

---

[3] *FLambdaDualObj* in the database.

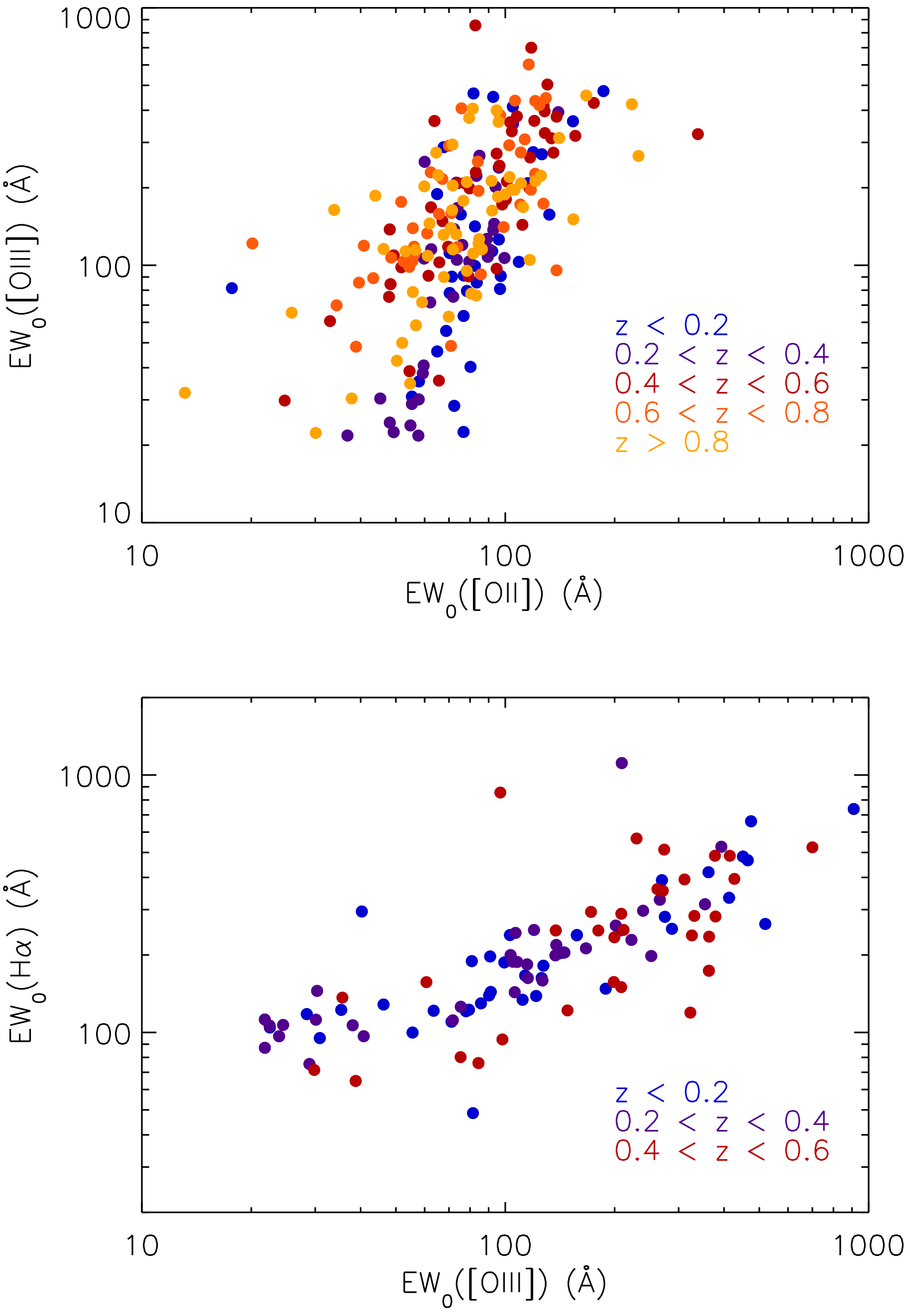

Figure 2.3 Comparison of the EWs of different emission lines for a sample of strong emission-line galaxies from SDSS. Top: EW$_0$([OII]) as a function of EW$_0$([OIII]). Bottom: EW$_0$([OIII]) as a function of EW$_0$(Hα).

generated with two typical continua of strong star-forming galaxies and narrow emission lines ([OII], Hβ, [OIII], [OIII]b, and Hα) following the relations in Fig. 2.3. These synthetic spectra were also convolved with the J-PAS filters and included in the comparison database.

To determine their final redshift and classification (QSO or galaxy), we compared the J-spectrum of each candidate to all the J-spectra in our database, calculating a χ^2 value for each candidate. The spectrum with the minimum χ^2 was used to determine the classification of the candidate. A total of 38 candidates were retrieved from miniJPAS and J-NEP, including 20 star-forming galaxies and 11 QSOs from miniJPAS, and 6 star-forming galaxies and 1 QSO from J-NEP. We checked for consistency in our QSO classification by searching for X-ray counterparts in NED [4]. Out of all our QSOs candidates, six were found to have X-ray counterparts, all of them were classified as QSOs according to NED.

2.3 Properties of the selected candidates

The basic properties of our detected sources are presented in Table A.1, which includes a range of quantities. These consist of coordinates, magnitude, and stellarity index extracted from the J-PAS catalogues, as well as redshift, EW_0, flux, and luminosity of the detected emission lines, which were derived in this work. Whenever available, spectroscopic redshifts from SDSS and DEEP2 or DEEP3 were also included. To ensure consistency across the entire sample, EW_0 were derived using our z estimation for all sources.

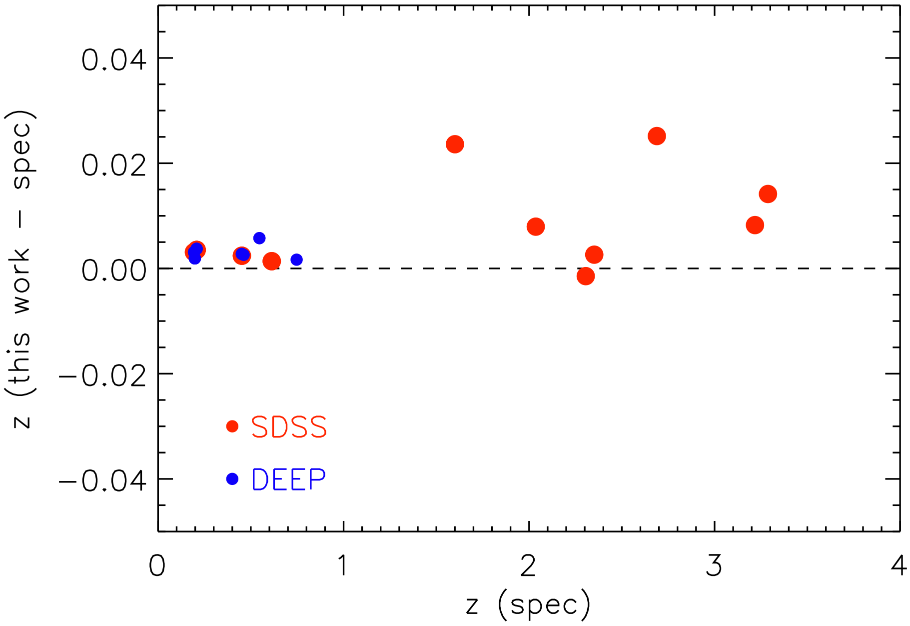

Figure 2.4 Redshift difference as a function of the spectroscopic redshifts from SDSS (red) and DEEP2/3 (blue) for the EELG candidates present in the SDSS and DEEP databases.

---

[4] The NASA/IPAC Extragalactic Database (NED) is operated by the Jet Propulsion Laboratory, California Institute of Technology, under contract with the National Aeronautics and Space Administration.

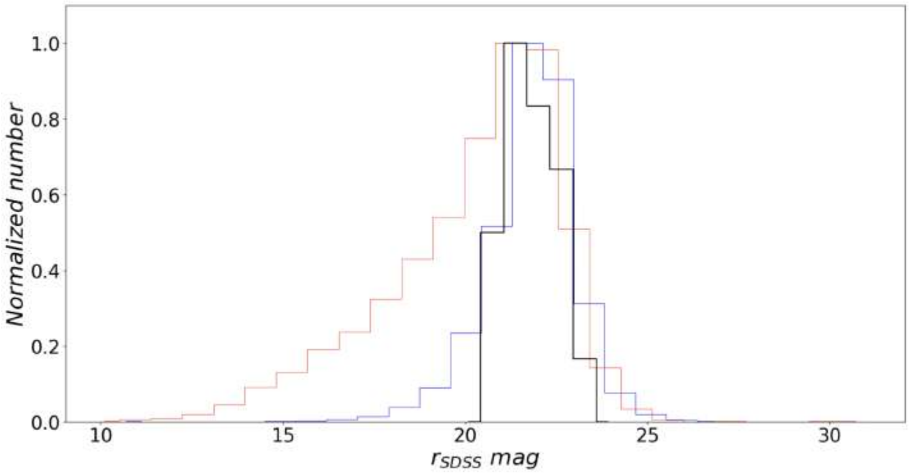

Figure 2.5 The black line in the histogram represents the r_{SDSS} magnitude of the chosen candidates. The blue and red histograms represent the total collection of galaxies and stars in the dual catalog (of miniJPAS and J-NEP), respectively. They are classified based on the stellarity index. Each of the three histograms is scaled to the peak of its distribution.

By utilizing available spectroscopic redshifts from SDSS and DEEP, we are able to evaluate the accuracy of our methodology and the precision of the derived redshifts. This is particularly important for subsequent analyses based on the luminosities of the brightest emission lines of our candidates. After performing a cross-match with a 1 arcsec radius, we identified 11 objects with available spectroscopic redshifts in SDSS and seven objects in DEEP2 or DEEP3, giving a total of 15 objects with a spectroscopic redshift in at least one of these three catalogues. In Fig. 2.4, we present a comparison of the redshifts derived in this work with the spectroscopic redshifts. We find that all the redshifts derived in this work are consistent with the corresponding spectroscopic redshifts, to a level that allows us to unequivocally identify the emission line that was selected as extreme. The only significant deviations occurred for redshifts larger than one, which are classified as QSOs. For all sources, we find $|\Delta z/(1+z_{spec})| \leq 0.01$. We emphasize that our aim is not to provide a detailed redshift analysis, as the methodology used to select EELGs is not optimized for photometric redshift derivation. Our primary goal is to derive redshifts consistent with the spectroscopic redshifts, allowing us to identify the detected emission line and estimate fluxes, luminosities, and EW_0 with reasonable accuracy. Overall, our methodology has demonstrated the required accuracy, although there is a possibility of misidentification in a larger sample.

The histogram of the r_{SDSS} magnitude with the AUTO photometry for the selected objects is presented in Figure 2.5. The peak of the detections falls within the 21 to 22 mag range, with the majority of objects falling within the 20 to 23 mag range. The range of magnitudes covered by our sample highlights the intrinsic difficulty of identifying these objects in broad-band photometric surveys, as compared to samples of other types of galaxies. As indicated in Table A.1, some of the star-forming candidates are classified as stars in the catalogues based on the stellarity indices. Similarly, with respect to the QSOs, all but one are classified as stars based on the same index. The images of the candidates in the filter where they were detected are presented in Figure A.1, which shows that most of them have a compact appearance.

2.4 The confirmed EELGs

In Sect. 2.2, we explained that our selected candidates exhibit an observed EW ≥ 300 Å in at least one emission feature. However, we only consider those candidates classified as galaxies and showing $\mathrm{EW}_0 \geq 300$ Å as confirmed EELGs. To estimate their EW_0s, we first recover the fluxes of the brightest emission lines of our EELG candidates. It is important to note that due to the partial overlap of some contiguous J-PAS filters, some galaxies may exhibit multiple detections of the same emission line in different filters, while more than one emission line may be detected by the same J-PAS filter, depending on the redshift of the source. This is especially common for Hβ, [Oɪɪɪ]b, and [Oɪɪɪ] lines, which are in close proximity to each other. It is even more frequent in the case of [Nɪɪ]λ6548 Å, Hα and [Nɪɪ]λ6583 Å. However, we assume a mean line ratio of [Nɪɪ]λ6583 Å/Hα = 0.05 for all the galaxies as a first approximation, since the intensities of the [Nɪɪ] lines are expected to be much fainter than the Hα line. This ratio is considered typical for galaxies with strong emission lines, according to previous studies (e.g. Pérez-Montero et al. 2011; Amorín et al. 2012a; Kehrig et al. 2020).

In Table A.1, we present the EW_0 values, fluxes, and luminosities of the selected emission features of the EELG candidates, which were derived from the AUTO J-spectra. To obtain the emission line fluxes, we used the J-PAS fluxes and assumed an infinitely narrow emission line at the derived redshift, so that the filter (or filters) where the emission line is detected contains (contain) all the flux from the line. This approximation is reasonable for star-forming galaxies, but it may not hold for QSOs, as their emission lines in the rest-frame UV, which shift into the optical at the redshifts where we detect them, are mostly broad. Therefore, the EW_0 values, fluxes, and luminosities of the QSO emission lines quoted in Table A.1 are approximations that may have significant associated uncertainties.

Out of the sources that satisfy our criterion of $\mathrm{EW}_0 \geq 300$ Å, a total of 19 are classified as star-forming galaxies, making them confirmed EELGs candidates. Among these, 14 are extreme emitters in [Oɪɪɪ], 2 in Hα, and 3 in both [Oɪɪɪ] and Hα. It is worth mentioning that we did not find any EELGs selected in the [Oɪɪ] line in our sample. Although such galaxies do exist, they are rare up to high redshifts (Darvish et al. 2015; Cava et al. 2015; Cedrés et al. 2021). Thus, even though they are absent in our small sample, we expect to detect some of them in the entire J-PAS survey.

2.4.1 Investigating contamination due to Lyα emitters

Within this section, we explore the possibility of some confirmed EELGs being misclassified high-redshift Lyα emitters as lower redshift star-forming galaxies due to potentially inaccurate redshift estimates for sources lacking spectroscopic counterparts. Lyα emitters have already been identified in the J-PLUS survey (Cenarro et al. 2019) at redshifts ranging from $2.2 \leq z \leq 3.3$ (Spinoso et al. 2020). If any such Lyα emitters were present in the J-PAS images, they would be incorrectly classified since our spectral database lacks spectra for star-forming galaxies at $z \geq 1.4$. However, this is not the case for QSOs, as they are included in our database and are classified correctly (see Table A.1).

Star-forming Lyα emitters typically exhibit a flat and dim continuum in rest-frame UV spectra, with a high EW$_0$ Lyα line ($\geq$ 50Å) and additional lower intensity lines, such as C IVλ1550 Å, He IIλ1640 Å, O III]$\lambda\lambda$1661,1667 Å, and C III]λ1909 Å (e.g. Verhamme et al. 2017; Nakajima et al. 2018; Feltre et al. 2020). As a result, a high-redshift, star-forming, Lyα-emitting galaxy would have a faint and flat continuum in the J-spectra, with a peak in one of the narrow-band filters due to the presence of the Lyα line. A closer examination of our selected sample, depicted in Fig. A.1, reveals this to be the case for several sources, despite being classified as [O III] or Hα emitters. This leads to the question of whether these sources could be wrongly identified as star-forming Lyα emitters.

To distinguish between the two possibilities, we use information from the literature. Assuming that all our confirmed EELGs are high-redshift Lyα galaxies, their emission line would be Lyα, and they would have a redshift range of $2.30 \leq z \leq 6.20$, with corresponding Lyα luminosities ranging from $43.79 \leq \log L_{Ly\alpha}/(ergs^{-1}) \leq 44.93$, and an average rest-frame absolute UV magnitude between [1000,2000] Å, ranging from $-25.19 \leq M_{UV,AB} \leq -21.92$[5]. However, the values for these rest-frame UV magnitudes and Lyα luminosities are much brighter than expected at such high redshifts (Khusanova et al. 2020). Sobral et al. (2018b) also suggest that these Lyα luminosity values correspond to the high-luminosity end of the Lyα luminosity function (evaluated between $2.5 \leq z \leq 6$), and that they would be scarce and challenging to detect in a 1 deg^2 survey. Moreover, such high luminosities are typically associated with QSOs, whose Lyα emission is related to AGN activity, and most QSOs

---

[5] The rest-frame UV magnitudes and Lyα luminosities were calculated based on the assumption that the detected emission line is Lyα, and the rest-frame UV continua and line luminosity were estimated from the observed J-spectra.

detected in our study have derived Lyα luminosities within this range, as shown in TableA.1. Additionally, all six sources exhibiting X-ray emission in our sample are classified as QSOs, as expected for their luminosities if their selected line was Lyα. Though our redshift detection algorithm may result in misclassification, these arguments indicate that our confirmed EELG sample is not primarily composed of star-forming galaxies with strong Lyα emission redshifted into the visible range of the spectrum. While star-forming Lyα emitters that meet our EW_0 criteria have been reported (Malhotra & Rhoads 2002; Kerutt et al. 2022), and could be a source of confusion with EELGs at lower redshifts in the overall J-PAS survey, none are present in our sample.

2.4.2 The Hα and [O III] luminosity functions

A noteworthy topic for discussion is the estimation of luminosity ranges observable by J-PAS. To explore this, we compare the luminosities of our confirmed EELGs to luminosity functions reported by Comparat et al. (2016) for the [O III] and Hβ lines at different redshifts. Though these luminosity functions pertain to galaxies with emission lines and are not restricted to EELGs, we use them due to their coverage of our redshift range and their ability to demonstrate how the depth of our sample compares to the values of L_*. The authors derived the luminosity function parameters as a function of redshift using a Schechter function (Schechter 1976). Figure 2.6 portrays the evolution of the characteristic luminosity L_* of the luminosity functions with redshift. As some of our sources were detected in the Hα line, we transformed the Hβ luminosity function given by Comparat et al. (2016) into Hα by assuming a constant Hα/Hβ ratio of 2.78. Our EELG detection in [O III] line indicates sensitivity to luminosities even lower than L_* at redshifts $z \leq 0.5$. Similarly, EELGs detected in Hα are sensitive to luminosities lower than L_* at redshifts $z \leq 0.25$. Otherwise, we only detect galaxies more luminous than L_* in both lines. In summary, assuming that J-PAS is capable of detecting EELGs to a similar depth as miniJPAS and J-NEP, it can probe the low-luminosity regime of the LF for the Hα and [O III] lines at redshifts lower than 0.25 and 0.5, respectively. Moreover, it can offer significant information on the high-luminosity end of the luminosity function for these emission lines at higher redshifts.

2.4.3 Number density of EELGs

Within this section, we discuss the number of detected EELGs concerning reported densities of similar objects in the literature. A comprehensive comparison is challenging as the various samples are selected based on varying criteria and from photometric samples with biases.

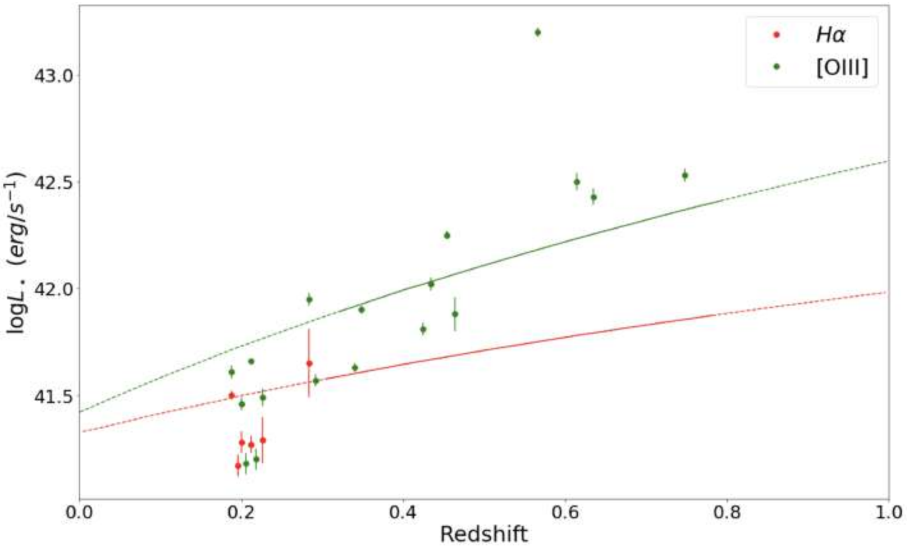

Figure 2.6 Comparat et al. (2016) demonstrates how the characteristic luminosity L_* evolves with redshift for the [OIII] (solid green) and Hα (solid red) lines. The extrapolations for the values of L_* outside the ranges where the estimation was made are represented by dashed lines. Our confirmed EELGs are represented by filled points, using the same color scheme as the two lines mentioned above.

As mentioned earlier, our sample is constructed using the dual catalog generated by Sextractor, which only includes sources selected in the r_{SDSS} images. Additionally, we impose a further constraint on the flux in the narrow-band filter where the galaxies are selected. As a result, there is a bias towards galaxies fainter than a particular r_{SDSS} magnitude whose flux is below our limit (10^{-17}erg s^{-1} cm^{-2}) that will not be detected. Quantifying this bias is difficult because our galaxies are detected across a wide range of wavelengths, and the r_{SDSS} magnitude mimics the continuum in the wavelength range of [6000,7000] Å. For these galaxies, we estimate that we become incomplete at magnitudes fainter than r_{SDSS} $\approx$ 22.3, and this value may differ for galaxies detected at varying wavelengths. To gauge the completeness of our sample, we compare it to samples of similar objects selected using different criteria.

Cardamone et al. (2009) established a spatial density of GPs at ~2 deg^{-2}, by imposing conditions on r_{SDSS}, redshift, optical colours, and morphology. Due to the distinct conditions imposed, comparing their sample with ours is challenging, especially given that our sample includes galaxies much fainter than those in Cardamone et al. (2009). Only 2 of our galaxies exhibits properties almost compatible with the sample of Cardamone et al. (2009) [6], leading

---

[6] r_{SDSS} = 20.8 and r_{SDSS} = 20.6, compared to Cardamone et al. (2009), who considers galaxies with $18 \leq r_{SDSS} \leq 20.5$.

to a spatial density of 1.6 deg^{-2}, indicating that our counts are consistent with those of the GPs.

Yang et al. (2017c) conducted a study of blueberries with $z \leq 0.05$ and EW$_0$([Oiii])$\geq$ 800 Å in the very local Universe, reporting a total of 43 objects in 14,555 deg^2, resulting in a total of ~0.003 deg^{-2}. Similarly, Lumbreras-Calle et al. (2021) identified 466 EELGs with $z \leq 0.06$ and EW$_0$ $\geq$ 300 Å in the J-PLUS survey, covering 2000 deg^2. As we do not detect any objects within these redshift ranges, our results align with those of the two aforementioned studies.

Amorín et al. (2015) conducted a more comprehensive study on the number density of EELGs using spectroscopic data from the zCOSMOS-bright survey, covering $\sim$ 1.7 deg^{-2}. They utilized the 20k-bright sample, consisting of 20,000 galaxies with spectroscopic spectra at $z \leq 2$, down to $I_{AB} \leq 22.5$ as measured from the HST-ACS imaging, and reported a total of 165 EELGs with EW$_0$([Oiii])$\geq$ 100 Å in the redshift range $0.11 \leq z \leq 0.93$. However, their upper limit of $z \approx 0.8$ is beyond the limit where the [Oiii] line is detectable in the J-PAS data, and their limit of EW$_0$([Oiii])$\geq$ 100 Å is lower than our limit for EELGs. Hence, we used their Fig. 2.3 to estimate the number of their galaxies that fulfill our EW$_0$ $\geq$ 300 Å condition, and found 37 galaxies within the redshift range $0.11 \leq z \leq 0.8$, resulting in a density of 21.7 deg^{-2} for the surveyed area. In comparison, our sample contains 17 EELGs with EW$_0$ $\geq$ 300 in the [Oiii] line and within the redshift range $0.11 \leq z \leq 0.8$, leading to a spatial density of 13.6 deg^{-2}, which is slightly lower than the estimations of Amorín et al. (2015). We previously mentioned that the observed discrepancy in estimated EELG densities using different samples could be attributed to differing selection criteria imposed by methodology. Amorín et al. (2015) found a comparable number of EELGs across the entire redshift range examined (up to $z = 0.9$), whereas we only selected EELGs in [Oiii] in the redshift range $0.206 \leq z \leq 0.748$, even though our observational limits enable their detection below $z \leq 0.8$. This difference could stem from limitations in the miniJPAS and J-NEP data, small statistics, or cosmic variance, which can be properly addressed with larger samples.

In summary, the different selection criteria used in each sample prevent precise comparisons with other samples of similar objects. However, our counts are generally consistent (with some slight variations) with the reported counts of other samples of EELGs.

2.5 Conclusions

Using the miniJPAS and J-NEP data covering 1.25 deg^2, we searched for EELGs by applying a method that uses the `Contrast` of emission in one of the J-PAS narrow-band filters compared to the continuum in the adjacent filters. Our sample of EELGs was selected from the miniJPAS and J-NEP catalogs of sources that were previously selected in the r_{SDSS}

images. For our study, we defined EELGs as galaxies exhibiting $\mathrm{EW}_0 \geq 300$ Å in at least one of the emission lines [OII], [OIII], or Hα. The selection process involved applying a minimum `Contrast` that resulted in an observed EW ≥ 300 Å. We identified 38 sources that met our criteria.

We utilized the SDSS-DR16 spectra database to obtain redshifts and classify our sources as either star-forming galaxies or QSOs. After comparing the J-spectra of our sample galaxies with the SDSS data, we identified 26 of our sources as star-forming EELG candidates, while the remaining 12 sources were classified as QSOs. The derived redshifts for our sources were found to be in good agreement with spectroscopic redshifts, with a difference between the derived redshifts and spectroscopic redshifts for all sources following $\Delta z/(1 + z_{spec}) \leq 0.01$.

The majority of the star-forming EELG candidates were identified through detection in the [OIII] emission line, while some were detected in the Hα line, and none were detected in the [OII] line. On the other hand, the QSOs were mainly detected in the Lyα line, with only two of them being identified through detection in the CIV emission line.

In the end, we identified 19 candidates as confirmed EELGs, which are classified as star-forming galaxies and meet the minimum EW_0 requirement in Hα or [OIII]. These confirmed EELGs were detected in the redshift range $0 \leq z \leq 0.748$, with the highest concentration of [OIII] sources in the range of $0.2 \leq z \leq 0.3$.

If J-PAS has a similar depth to miniJPAS and J-NEP, it can investigate the high-luminosity end of the Hα and [OIII] luminosity functions for EELGs at redshifts greater than 0.25 and 0.5, respectively. Moreover, at lower redshifts, J-PAS can detect EELGs with Hα and [OIII] luminosities below their respective L_* values.

While comparing our sample to others is challenging due to the different selection criteria, we observe a reasonable consistency in the number counts of our EELGs compared to those of Cardamone et al. (2009); Yang et al. (2017c); Lumbreras-Calle et al. (2021). However, our count is slightly lower than that of Amorín et al. (2015), who used the zCOSMOS data.

Although our sample is small, this study can be considered a successful pilot, demonstrating the effectiveness of our methodology in detecting EELGs. With the ongoing J-PAS survey covering a much larger area of ~ 8500 deg^2, it is expected that a significant number of such galaxies will be detected. This will enable us to unveil the nature and evolution of EELGs on a larger scale.

To fully assess the validity of the methodology used in this study, it is necessary to conduct a spectroscopic follow-up of the sample. Such an endeavor would allow for the determination of the percentage of false detections (if any), as well as the verification of the precision of the emission-line fluxes measured using the miniJPAS and J-NEP data.

Chapter 3

GPs seen with MUSE/VLT

This chapter is based on the publication:

"A MUSE/VLT spatially resolved study of the emission structure of Green Pea galaxies"
by Antonio Arroyo-Polonio et al.
Published in A&A, 677, A114 (2023).

https://doi.org/10.1051/0004-6361/202346192

3.1 Introduction

The period known as the cosmic dawn, occurring when $6 \lesssim z \lesssim 20$, signifies a pivotal transformation in the Universe. This epoch saw the emergence of the "first light," which included metal-free stars (commonly known as PopIII-stars) and the subsequent creation of numerous low-mass galaxies with extremely low metal content, effectively ending the dark ages of the Universe. Insights into the reionization history provide a glimpse into the characteristics of these initial celestial sources, a subject currently being probed by the JWST (e.g., Curtis-Lake et al. 2022; Robertson et al. 2022; Naidu et al. 2022b). Nonetheless, the precise timing and mechanisms behind the reionization of the Universe continue to be key unanswered questions in contemporary astrophysics, set to be investigated in the coming decades.

A straightforward method to gain insights into the first celestial sources involves studying galaxies at lower redshifts that share characteristics with those in the early Universe (e.g., Schaerer et al. 2022; Chen et al. 2023). Within this category of local analogs, we encounter entities known as GPs, which form a subgroup within the broader category of EELGs (e.g., Pérez-Montero et al. 2021; Breda et al. 2022; Iglesias-Páramo et al. 2022; Lumbreras-Calle et al. 2022). GPs are compact starburst galaxies typically observed at redshift $z \in (0.112, 0.360)$, which corresponds to $2.5-4.3$ Gyr in the past. Their maximum size, as seen in the Hubble Space Telescope (HST) images, is 5 kpc (Yang et al. 2017a). The JWST has already demonstrated the similarities between primeval galaxies ($z \sim 8$) and GPs (Rhoads et al. 2022). The trio of high-redshift galaxies featured in Rhoads et al. (2022) are all potent line emitters, displaying spectra akin to those of nearby GPs. They also exhibit the compact morphologies commonly found in GPs, affirming without question that GPs serve as excellent local proxies for high-redshift galaxies.

On average, a GP galaxy possesses a stellar mass of $M_\star = 1 \times 10^9$ $M_\odot$ and a SFR of 10 $M_\odot$ yr^{-1} (Cardamone et al. 2009; Izotov et al. 2011). As a result, its timescale for doubling mass can fall below 100 Myr. In this context, GPs exhibit intense starburst activity, similar to that observed in high-redshift galaxies (Lofthouse et al. 2017). Additionally, multiple investigations point to hot, massive stars as the primary agents of excitation within GPs, leading to a highly ionized ISM (e.g., Jaskot & Oey 2013).

The spectra of GPs feature optical emission lines with high EW, reaching up to 2000 Å. The most prominent among these lines is [OIII]. In fact, the intense emission of this particular line led to the initial identification of these galaxies in Galaxy Zoo (Lintott et al. 2008). The gas metallicity in GPs is relatively low when compared to typical star-forming galaxies, falling within the range of $12 + \log(O/H) = 7.6$ to 8.4 (e.g., Amorín et al. 2010).

Compared to conventional galaxies, GPs are relatively rare. On average, there are 2 GPs per square degree brighter than 20.5 mag. Additionally, they tend to be isolated, residing in regions $2/3$ less dense than those occupied by regular galaxies (Cardamone et al. 2009). Despite this, the potential for interactions between GPs and nearby galaxies has been examined in Laufman et al. (2022), which concluded that such interactions are not the driving force behind the intense star formation observed in these galaxies. Due to their extraordinarily high SFR, nearly all GPs are Lyα emitters. A considerable portion of their Lyα photons, ranging from 2% to 70%, escape into the IGM (Yang et al. 2016, 2017a; Jaskot et al. 2017; Yang et al. 2017b; Henry et al. 2018; McKinney et al. 2019; Kim et al. 2020; Hayes et al. 2023). Furthermore, at least $\sim 10\%$ of these galaxies are LyC leakers (Yang et al. 2017a). These characteristics underscore the importance of GPs as local counterparts to high-redshift galaxies, making them invaluable for understanding the reionization processes that occurred in the early Universe.

The use of spatially-resolved analysis through integral field spectroscopy (IFS) offers significant advantages over traditional integrated single-aperture or long-slit spectroscopic methods, particularly in enhancing our comprehension of the warm ISM conditions in various systems. This has been well-documented in existing literature (e.g., Kehrig et al. 2008; Cairós et al. 2009; James et al. 2010; Monreal-Ibero et al. 2011; Papaderos et al. 2013; Kehrig et al. 2015; Bae et al. 2017; Herenz et al. 2017). Nonetheless, there has been a limited focus on the spatially-resolved properties of GPs to date (see Lofthouse et al. (2017)). In the current study, we unveil the spatially resolved properties, such as excitation, extinction, ionization and kinematics of a sample of 24 GPs observed using the MUSE integral field unit (IFU) spectrograph. An in-depth bidimensional spectroscopic analysis of our selected GPs is vital for uncovering the ISM characteristics in galaxies within the intermediate to high-redshift range.

The chapter is organized as follows. In Section 3.2, we outline the observations and the procedures for data reduction. Section 3.3 details the flux measurements and the spatial structures of the galaxies. Integrated attributes of each GP are discussed in Section 3.4. The chapter concludes with a summary of key findings in Section 3.6. Throughout this chapter we use physical distances and assume flat ΛCDM cosmology with $H_0 = 70$ km s^{-1} Mpc^{-1}, $\Omega_m = 0.3$ and $\Omega_\Lambda = 0.7$.

3.2 Observations

3.2.1 MUSE data

In this study, we analyze a sample of GPs observed using the MUSE instrument (Bacon et al. 2010) at the VLT, located at the ESO Paranal Observatory in Chile. MUSE is a panoramic IFS that, when operating in its Wide Field Mode (WFM), offers a FoV of $1' \times 1'$ with a spatial sampling of $0.2''$ and a full width half maximum (FWHM) spatial resolution ranging from $0.3'' - 0.4''$. The data were acquired in nominal mode, covering a wavelength range of $\lambda 4750$ Å – $\lambda 9350$ Å, a spectral sampling around 1.07 Å pix^{-1}, and an average resolving power of $R \sim 3000$. The sample was selected based on the criteria of including all Cardamone et al. (2009) GPs with $\delta < +20\,\mathrm{deg}$, ensuring visibility from the Paranal Observatory. The program ID for these observations is $0102.B-0480(A)$, with the PI being Hayes, Matthew.

We obtained fully processed data cubes from the ESO archive. Data reduction was carried out using the MUSE Instrument Pipeline version 1.6.1, employing default settings (Weilbacher et al. 2020). This involved standard procedures like bias subtraction, flat field correction, sky subtraction, wavelength calibration, and flux calibration.

Our sample includes 24 GPs and is an unbiased, representative collection of GP galaxies in terms of stellar masses, redshifts, metallicities, SFR, and [OIII] EWs, as well as line ratios that span the typical ranges for GPs (e.g., Cardamone et al. 2009; Amorín et al. 2010). Details such as the names, positions, and redshifts of the galaxies, along with additional observational information, are provided in Table 4.1. A redshift histogram for the GPs in our sample is depicted in Figure 3.1.

Upon initial examination of the data cubes, most of our GPs appear compact and nearly point-like, with a few exceptions. To confirm the spatial resolution of these galaxies, we measured the FWHM of all sources within the FoV in white light [1]. We verified the identities of stars in the FoV using SDSS DR16 (Ahumada et al. 2020). We then established the stellar-like FWHM ($\mathrm{FWHM}_\star$) as the median FWHM of these stars; if no SDSS stars are present in the FoV, $\mathrm{FWHM}_\star$ is defined as the FWHM of the least extended object within the FoV. A GP is considered extended if its FWHM ($\mathrm{FWHM}_{\mathrm{GP}}$) meets the following condition:

$$\mathrm{FWHM}_{\mathrm{GP}} > \mathrm{FWHM}_\star + 0.1''$$

Upon applying this criterion, 12 out of the 24 GPs in our sample are considered to be extended. The values of $\mathrm{FWHM}_\star$ and $\mathrm{FWHM}_{\mathrm{GP}}$, along with the number of stars in the FoV, are presented in Table 3.2.

---

[1] This corresponds to integrated light across the entire wavelength range of $\lambda 4750$Å – $\lambda 9350$Å

Table 3.1 GPs observational data.

Name (1)	SDSS name (2)	R.A. (deg) (3)	Dec (deg) (4)	Redshift (5)	Exp. time (s) (6)	Seeing (") (7)	Date (8)
GP01	J094458.22-004545.4	146.242675	-0.762983	0.300	5600	0.73	25 Jan 2020
GP02	J130211.15-000516.4	195.546538	-0.087455	0.225	2800	0.94	23 Jan 2020
GP03	J232539.23+004507.2	351.413396	0.751927	0.276	2800	1.06	6 Oct 2019
GP04	J032244.89+004442.3	50.687444	0.745181	0.304	2800	0.81	26 Feb 2020
GP05	J012910.15+145934.6	22.292355	14.993034	0.280	2800	0.93	28 Oct 2019
GP06	J030321.41-075923.2	45.839214	-7.989385	0.164	2800	0.67	17 Nov 2019
GP07	J032613.62-063512.5	51.556553	-6.587215	0.162	2800	1.33	18 Nov 2019
GP08	J033947.79-072541.2	54.949309	-7.427967	0.260	4900	0.83	30 Dec 2019
GP09	J105716.72+023207.0	164.319295	2.535426	0.302	2800	0.45	26 Jan 2020
GP10	J124423.37+021540.4	191.097708	2.261385	0.239	2800	1.01	23 Jan 2020
GP11	J084216.95+033806.6	130.570286	3.634824	0.219	3200	1.21	24 Jan 2020
GP12	J154709.10+033614.0	236.788328	3.604116	0.231	2800	1.11	20 Feb 2020
GP13	J223735.05+133647.0	339.396355	13.612971	0.293	2800	1.68	7 Nov 2019
GP14	J133711.88-022605.4	204.299314	-2.434471	0.273	2800	1.77	11 Feb 2020
GP15	J144231.37-020952.0	220.630418	-2.164616	0.293	2800	1.14	11 Feb 2020
GP16	J103138.93+071556.5	157.912233	7.265419	0.252	2800	0.41	26 Jan 2020
GP17	J124834.63+123402.9	192.144500	12.566958	0.263	2800	0.68	28 Jan 2020
GP18	J160436.66+081959.1	241.152495	8.333018	0.312	2800	1.45	20 Feb 2020
GP19	J155925.97+084119.1	239.858999	8.688758	0.297	2800	0.54	21 Feb 2020
GP20	J101157.08+130822.0	152.988016	13.139831	0.143	2800	0.69	28 Jan 2020
GP21	J163719.30+143904.9	249.330324	14.650662	0.292	2800	1.78	26 Feb 2020
GP22	J092532.36+140313.1	141.384720	14.053597	0.301	2800	0.64	28 Jan 2020
GP23	J161306.31+092949.1	243.276809	9.496739	0.299	2800	1.33	14 Mar 2020
GP24	J080518.06+092533.3	121.325130	9.425853	0.330	2800	1.12	24 Jan 2020

Column (1): Names used in this study. Column (2): SDSS name. Columns (3) and (4): Position of each galaxy. Column (5): Redshift. Column (6): Exposure time. Column (7): Seeing in the night of observation. Column (8): Date of observation.

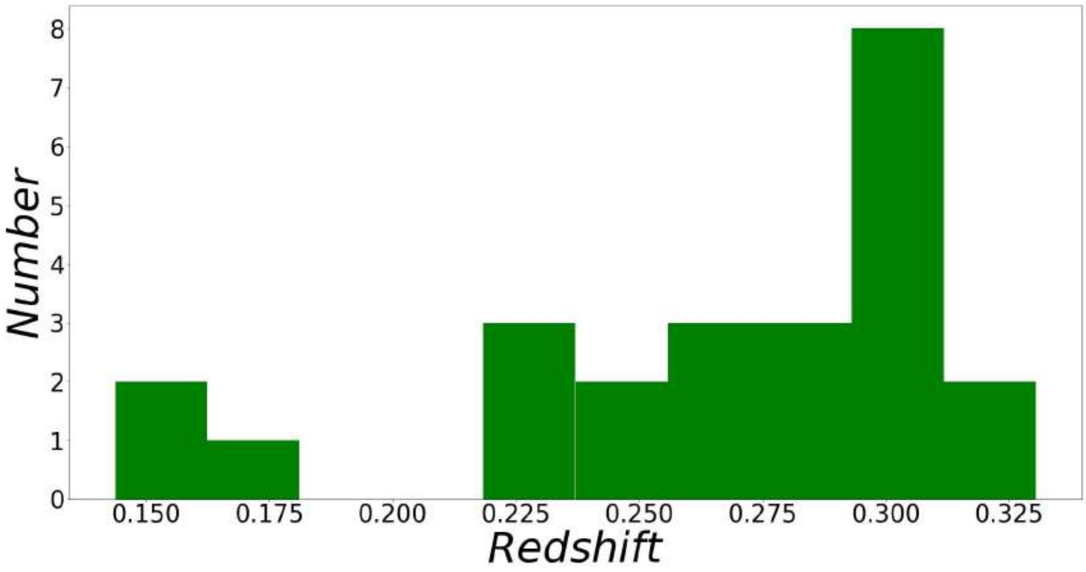

Figure 3.1 Redshift histogram of the 24 GPs in our sample.

This initial analysis helps us identify galaxies with a resolved core. However, the exceptional sensitivity of MUSE/VLT also allows us to examine the extended nature of these galaxies in regions of low surface brightness. To this end, we conducted a parallel analysis using the full width at $\frac{1}{10}$ of the maximum (FW$\frac{1}{10}$M) and the full width at $\frac{1}{100}$ of the maximum (FW$\frac{1}{100}$M). These metrics indicate the extension of the object in areas of lower surface brightness. A GP is deemed to be extended in low surface brightness regions if it meets either of the following conditions:

$$\mathrm{FW}\tfrac{1}{10}\mathrm{M_{GP}} > \mathrm{FW}\tfrac{1}{10}\mathrm{M}_{\star} + 0.3''$$

,

$$\mathrm{FW}\tfrac{1}{100}\mathrm{M_{GP}} > \mathrm{FW}\tfrac{1}{100}\mathrm{M}_{\star} + 0.5''$$

After implementing these criteria, 11 of the 24 GPs are considered to be extended in areas of low surface brightness. The values for FW$\frac{1}{10}$M and FW$\frac{1}{100}$M for both stellar-like sources and GPs are also included in Table 3.2.

Due to the redshift distribution within the GP sample, the spectral coverage of MUSE captures most of the optical emission lines. In particular, for all GPs, emission lines from $H\delta$ to $[S\,\textsc{ii}]\lambda6731$Å are available. For 13 of these galaxies, the coverage even extends to the $[O\textsc{ii}]\lambda3727$Å line.

The earth atmosphere cause the dispersion of light through Rayleigh scattering which depends on wavelength. As a result, the spatial extent of emission line maps at significantly different wavelengths (e.g., Hα vs Hβ and [O III] vs [O II]) could be affected. To adjust for this effect, a detailed analysis was conducted, measuring the FWHM for all sources within each GP FoV across the entire wavelength range. This analysis shows that blue images in the cubes have lower spatial resolution compared to red images. A decrease in the FWHM of the sources was observed, ranging from 2.25×10^{-5} arcsec Å^{-1} to 1.15×10^{-4} arcsec Å^{-1}. This information enables the application of the appropriate Gaussian kernel to red images for a fair comparison with blue images.

The MUSE pipeline accounts for the effects of Atmospheric Differential Refraction. As an additional verification, the centers of all objects detected in the cubes were measured within the spectral ranges [4900, 5100] Å and [8950, 9150] Å. A mean difference of only 0.07″ was found (Weilbacher et al. 2020).

Table 3.2 Extension of stellar-like sources and GPs.

Name (1)	Number of stars (2)	FWHM$_\star$ (”) (3)	FW$\frac{1}{10}$M$_\star$ (”) (4)	FW$\frac{1}{100}$M$_\star$ (”) (5)	FWHM$_{\rm GP}$ (”) (6)	FW$\frac{1}{10}$M$_{\rm GP}$ (”) (7)	FW$\frac{1}{100}$M$_{\rm GP}$ (”) (8)
GP01	1	0.825	1.82	3.498	1.011	2.44	5.489
GP02	0	1.232	2.261	3.229	1.232	2.261	3.229
GP03	0	1.04	2.31	4.485	1.04	2.31	4.485
GP04	1	0.821	1.782	3.325	0.902	1.972	3.725
GP05	1	0.862	1.852	3.397	1.105	2.371	4.342
GP06	0	0.692	1.265	1.797	0.795	1.648	2.844
GP07	1	1.338	3.476	8.435	1.559	3.76	8.435
GP08	1	0.792	1.735	3.291	0.94	1.998	3.604
GP09	1	0.924	1.794	2.792	0.936	2.038	3.82
GP10	3	0.977	2.095	3.813	1.116	2.54	5.148
GP11	1	1.126	2.681	4.857	1.257	2.681	4.857
GP12	3	1.309	2.711	4.22	1.395	2.711	4.22
GP13	1	1.313	3.026	6.265	1.529	3.355	6.383
GP14	1	1.269	2.707	4.906	1.44	3.042	5.425
GP15	1	1.275	2.718	4.921	1.345	2.917	5.44
GP16	1	0.696	1.339	2.049	0.76	1.656	3.118
GP17	1	0.768	1.601	2.791	0.878	1.759	2.873
GP18	1	1.643	3.335	5.564	1.643	3.335	5.564
GP19	2	0.86	1.813	3.22	0.926	1.934	3.382
GP20	0	0.903	1.839	3.088	0.903	1.839	3.088
GP21	4	1.546	3.39	6.36	1.705	3.675	6.782
GP22	2	0.717	1.491	2.421	0.747	1.491	2.421
GP23	4	1.144	2.545	4.961	1.324	2.941	5.707
GP24	2	1.064	2.179	3.7	1.1	2.374	4.387

Column (1): name of the galaxy, bolded text indicates that the galaxy satisfies the extension criteria. Column (2): number of SDSS-stars in the FoV. Column (3): FWHM of stellar-like source. Column (4): FW$\frac{1}{10}$M of stellar-like source. Column (5): FW$\frac{1}{100}$M of stellar-like source. Column (6): FWHM of the GP. Column (7): FW$\frac{1}{10}$M of the GP. Column (8): FW$\frac{1}{100}$M of of the GP.

3.2.2 SDSS spectra

Integrated spectra from SDSS-DR16 (Ahumada et al. 2020) have been obtained for all the GPs in the study. The SDSS fiber diameter is 3”. The wavelength range covered is from 3800 to 9200 Å. Spectral resolution starts at 1500 at 3800 Å and goes up to 2500 at 9000 Å. The pixel spacing in log-wavelength is 10^{-4} dex, and exposure times vary between 2800 s and 8500 s.

3.3 Flux measurements and spatially resolved structure

This section outlines the approach used to quantify the flux of the emission lines in the galaxies. We also introduce the spatially resolved maps, which were produced using spaxel-to-spaxel measurements of emission line fluxes and the continuum at different wavelengths. Alongside, we discuss the BPT diagrams as described by (Baldwin et al. 1981; Kewley et al. 2006).

3.3.1 Emission line and continuum maps

For each spaxel the fluxes of the most conspicuous emission lines were estimated by fitting a Gaussian to the spectral profiles. Flux errors were estimated through the bootstrap method (Efron & Tibshirani 1985). By combining these fluxes with the sky positions of the fibers, the emission line maps discussed in this chapter were generated.

For illustration, the emission line maps for galaxy GP06 can be seen in Fig. 3.2. This galaxy was chosen since it shows intricate features and rich structure in all the maps. Even faint lines like [SII]λ6716 Å and [SII]λ6731 Å (hereafter [SII]) reveal a minor protrusion in the south-western position relative to the central burst. This galaxy also features the most intense HeIIλ4686 Å(hereafter HeII line) nebular emission in the sample; this line was also detected in GP20 and GP15. The presence of this emission indicates the presence of high-energy photons (E > 4 Ry) that substantially ionize the gas and elevate the electron temperature (e.g., Kehrig et al. 2015). The emission line maps for the remaining galaxies are included in Appendix B.1.

The peaks of the emission line maps for all the GPs coincide with the galaxy center, this means that the total luminosity is governed by a compact area containing the ionization sources. This central region is slightly resolved in only a few cases, such as GP13 (see Fig. B.12). Only four of our GPs (GP06, GP13, GP07, and to a lesser extent GP01) show non-circular symmetry in low surface brightness areas (see Figs. 3.2, B.12, B.6, and B.1). The most extended structures visible in the maps correspond to the [OIII] line and, to a lesser extent, the Hα line. Their high intensity helps to map the low surface brightness regions of ionized gas in the outskirts of the galaxy. Fainter emission lines like Hβ, [Nii], [Sii], [Oi]λ6300 Å (hereafter [Oi]) and [Oiii]λ4363 Å display less extension and greater circular symmetry.

To construct the continuum maps, a common rest-frame spectral range was identified for all galaxies for the purpose of integrating the continuum. Given the different redshifts of each galaxy, each has its own rest-frame spectral range. The intersection of these ranges defines the rest-frame spectral range used for the continuum, which is between 4154 Å and 7026 Å, closely mirroring the spectral range of the human eye. The continuum at each spaxel was estimated by integrating the spectrum along the common rest-frame range, after removing the emission lines. Figure 3.3 displays the continuum map for GP06, while the continuum maps for all GPs can be found in Fig. B.48.

In these maps, it is apparent that all galaxies exhibit more complex structures than those seen in the emission line maps. One reason for this could be the broader collection of light, as the selected rest-frame spectral range spans 2872 Å. To collect a similar amount of light from a line, its EW would need to be comparable, yet the EW values observed are up to 2000 Å. The continuum maps often show additional features adjacent to the central regions of the galaxies, such as in GP03, GP06, GP13, and GP15. These irregularities in the continuum morphologies may suggest a dispersion in the underlying stellar populations, potentially due to recent merger events (Lofthouse et al. 2017).

While the continuum captures more light than the emission lines, the galaxies appear more compact in the continuum maps compared to the [Oiii] emission line maps. This could suggest that the ionized gas in the outer parts of the galaxies is being traced, given that the underlying stellar population is not as extended as the ionized gas. Specifically, GP06 features two areas on its north-east and north-west side (relative to the Hα peak) where the [Oiii] emission line extends significantly further (up to 10 kpc) than the continuum (see Figs. 3.2 & 3.3). In these galactic areas, there is almost no extinction (Hα/Hβ ~ 2.86), and the gas exhibits higher excitation (log([Oiii]/Hβ) ~ 0.7) compared to other outer regions where log([Oiii]/Hβ) ~ 0.45 (refer to Section 3.3, Figs. 3.4 and 3.6). Similar observations were made for the galaxy SBS 0335–052E, which has [Oiii] and Hα filaments with low Hα/H β ratios (Herenz et al. 2023). These findings indicate that these areas could serve as channels for the escape of LyC photons.

Particularly in the case of GP06, the galaxy exhibits an optically thick, neutral outflow along the line of sight (Jaskot & Oey 2014), complicating the escape of high-energy photons in that specific direction (with f_{esc}(Lyα) = 0.05, as identified in Jaskot et al. (2017)). However, this galaxy also displays one of the highest [Oiii]/[Oii]values in this study ([Oiii]/[Oii] =

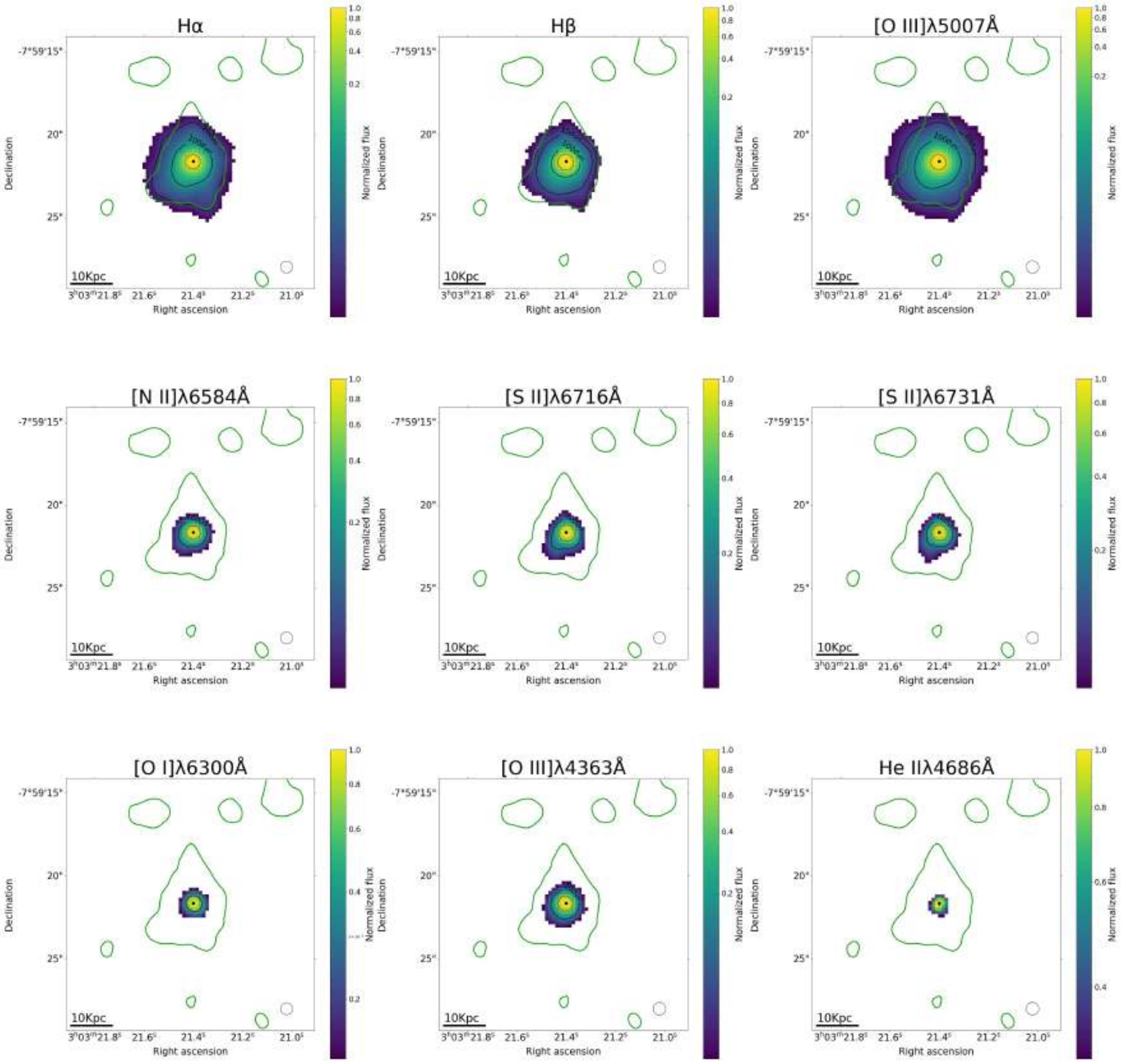

Figure 3.2 Emission line maps for GP06 are presented. The black line at the bottom-left indicates a 10 kpc distance, while the circle at the bottom-right serves as a representation of the seeing. The peak in the H α emission is marked by a black point at the center. Green and black contours signify the 3 σ_{sky} level of the galaxy's corresponding continuum map. All maps in this study include these features, with the exception of the continuum maps, which lack the continuum contour. Black contours delineate regions where the $signal = k \times \sigma_{sky}$, with $k = 10, 100$. All spaxels depicted in all maps surpass the 3 σ_{sky} threshold. The red contour outlines the FWHM of the map, and these contours are consistent across each emission line map and continuum map in this research.

6.56). This hints at the possibility of alternative escape routes for ionizing photons in other directions (Izotov et al. 2022).

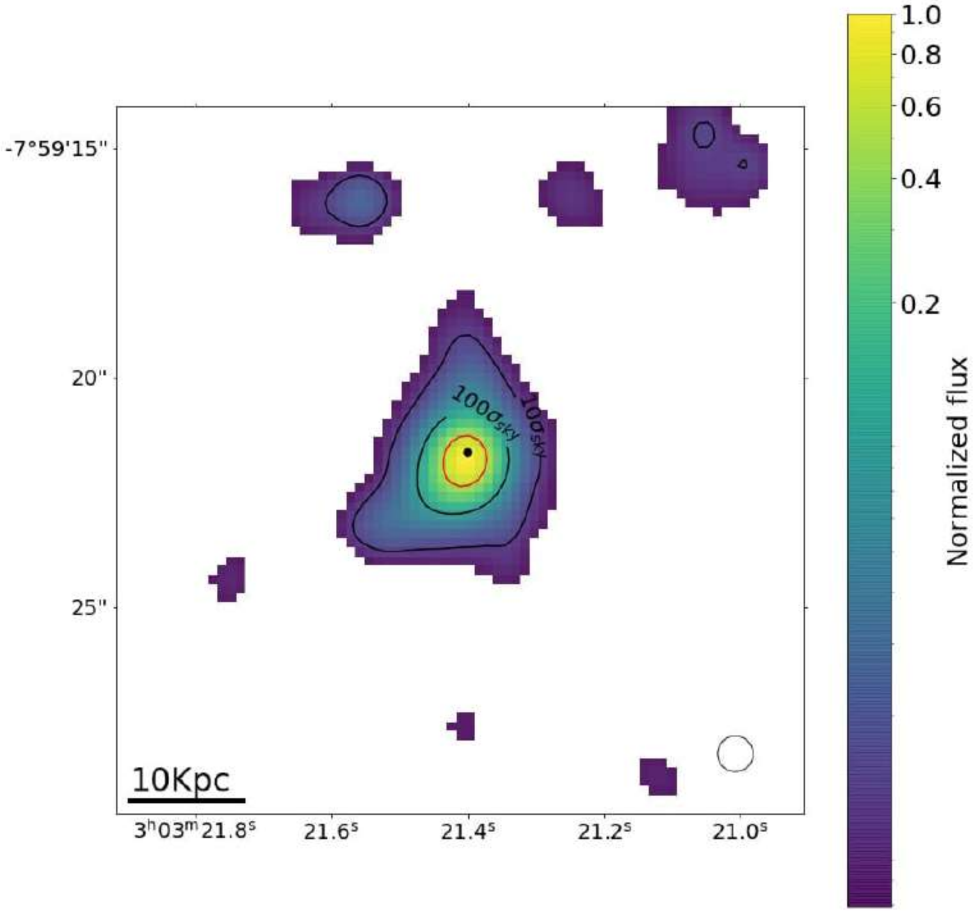

Figure 3.3 Continuum map of GP06. Integration is done between 4154 Å and 7026 Å in rest frame.

3.3.2 Emission line ratio maps

This section introduces maps featuring key line ratios to investigate the ionization structure of the gas in the sample of GPs.

The line ratios have been corrected for reddening, utilizing the corresponding $c(\mathrm{H}\beta)$ for each spaxel. The reddening coefficient, $c(\mathrm{H}\beta)$, was calculated from the observed-to-theoretical ratio Hα/Hβ, based on the (Cardelli et al. 1989) reddening law. Assumptions include case B recombination, an electron temperature of $T_e = 10^4$ K, and an electron density of $n_e = 100$ cm^{-3}, yielding an intrinsic value of Hα/Hβ = 2.86. Figure 3.4 displays the Hα/Hβ map for GP06 uncorrected for reddening. This Hα/Hβ map serves as an indicator of regions with higher dust content. Areas with elevated extinction are likely to contain dust that obstructs the passage of high-energy photons (Weingartner et al. 2006). Consequently, if LyC photons are escaping, they would likely do so in directions with lower extinction. Emission line ratio maps for all GPs can be found in Appendix B.2.

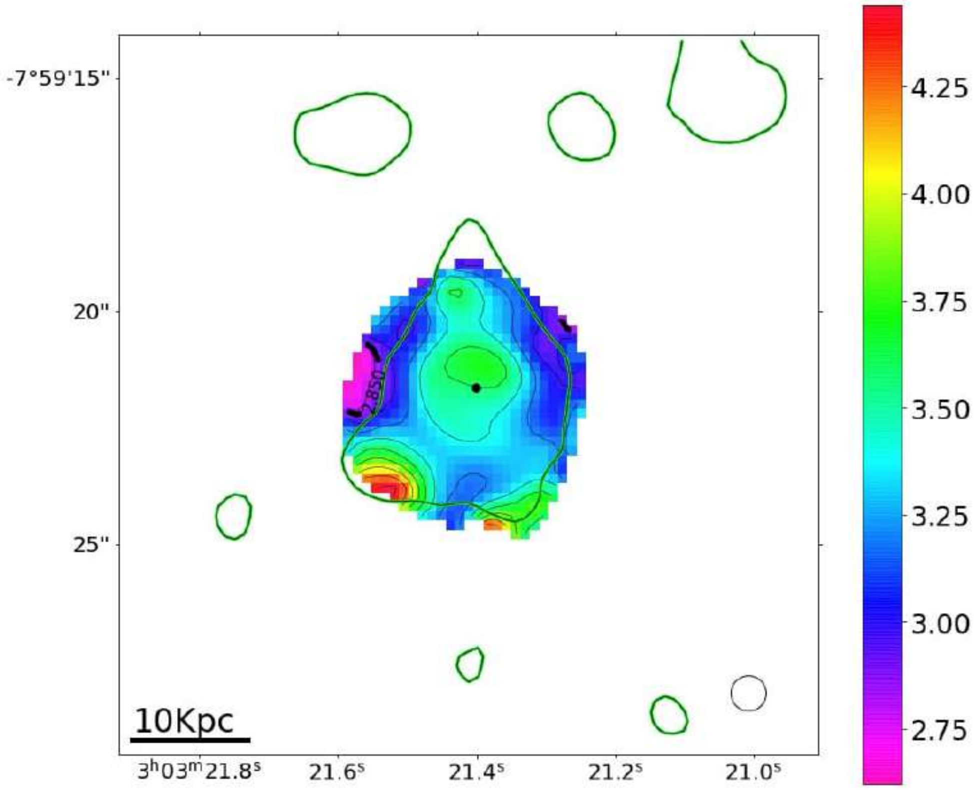

Figure 3.4 Hα/Hβ map of GP06 before reddening correction.

The spectral range covered by MUSE enables the observation of the [OII] lines in 13 of the GPs in this study, owing to their redshifts. As a result, it becomes feasible to examine the map of the [OIII]/[OII] line ratio in these galaxies. This ratio serves as a marker for gas ionization (refer to Appendix B.2 for more details). Figure 3.5 illustrates this ratio map for GP13 ([OII] lines are not observed for GP06), which is the most extended galaxy in the sample. Elevated values of the [OIII]/[OII] ratio indicate areas of the galaxy with high ionization levels. These high-ionization regions are generally concentrated near the galactic center, where the Hα peaks and the primary ionizing sources are situated. The most elevated

[OIII]/[OII] values are observed in the maps of the confirmed LyC leakers of this sample GP22 and GP15 (Izotov et al. 2016b,a) , reaching values up to 6.5 (see Figs. B.45 and B.38).

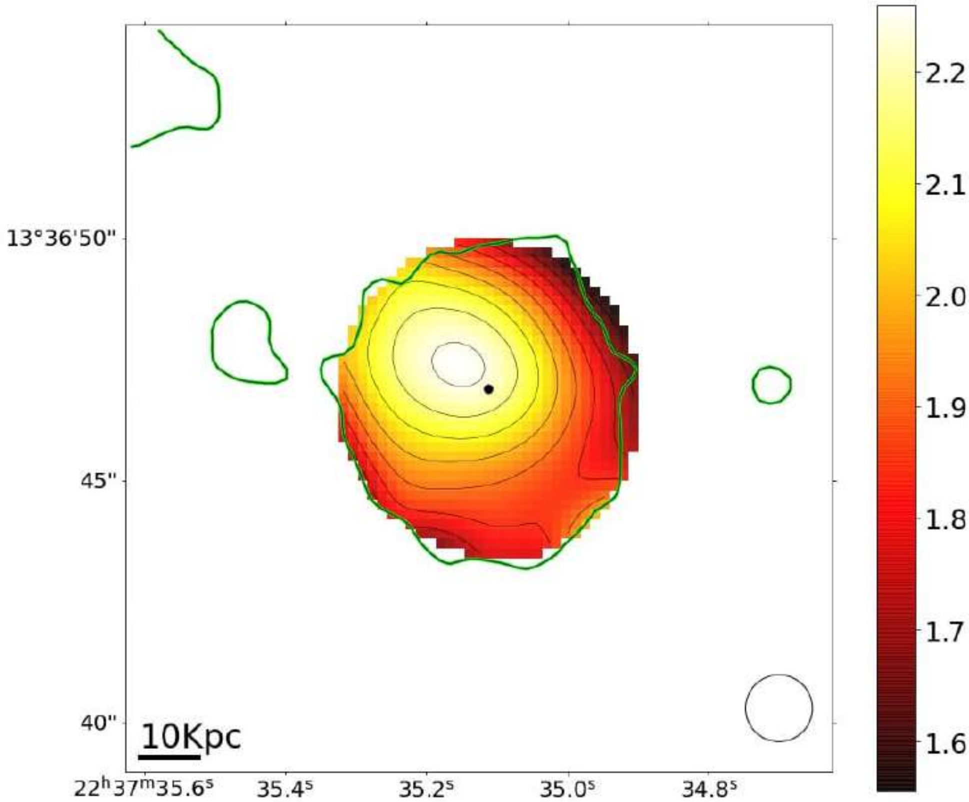

Figure 3.5 [OIII]/[OII] map of GP13.

The ratios used in the BPT diagrams are [OIII]/Hβ, [NII]/Hα, [SII]/Hα and [OI]/Hα. Examples of maps corresponding to these line ratios are displayed in Fig. 3.6. Areas with high [OIII]/Hβ values are indicative of ionized gas with relatively higher excitation levels. The maps of this ratio, [OIII]/Hβ, do not show substantial spatial variations for almost any of the GPs, with a maximum difference of less than 0.1 dex. This suggests low spatial gradients in gas excitation across these galaxies. However, GP06 is an exception; for this galaxy, the spatial variation in [OIII]/Hβ reaches up to 0.4 dex. The maximum [OIII]/Hβ occurs very close to the center where Hα emission peaks (see Fig. 3.6). In the outer regions of this galaxy, where the value of log([OIII]/Hβ) drops to approximately 0.45, high levels of extinction are observed, with a Hα/Hβ ratio of around 4.25 (see the north, south-east, and south-west regions in Figs 3.4 and 3.6). This suggests that photons emanating from the central starburst tend to be absorbed as they move through dusty regions, causing the radiation to soften. Among the galaxies studied, GP20 exhibits the highest value of [OIII]/Hβ, reaching a log value of 0.91 (see Fig. B.43). This galaxy also features the most prominent emission lines, as detailed in B.1.

Low values of [NII]/Hα in the maps are indicative of regions with elevated gas excitation and serve as tracers for zones with low metallicity (Pettini & Pagel 2004). The maps for this emission line ratio, [NII]/Hα, do not show substantial spatial variations, with a maximum difference of 0.14 dex observed for GP08 (see Fig. B.31). The minimum values for [NII]/Hα are observed in GP06, GP15, and GP20 (see Figs. B.29, B.38, and B.43). These three galaxies are also noteworthy for displaying the nebular HeII line, indicative of the presence of hard ionizing sources.

The [SII]/Hα ratio serves as a tracer for the opacity of the column of gas, meaning the gas in the line of sight for each spaxel (Pellegrini et al. 2012). The ratio [OI]/Hα peaks at the ionization front, which is the edge of ionization-bounded regions. Low values for both of these ratios suggest thin columns of gas (density-bounded regions) and, correspondingly, elevated levels of gas excitation where LyC photons are more likely to escape (Iglesias-Páramo & Munoz-Tunón 2002; Paswan et al. 2022). It is observed that most GPs exhibit a blister-type morphology, characterized by an optically thin galactic center. As one moves to the outer regions of the galaxy (around 5-10 kpc), the medium becomes increasingly optically thick (see Appendix B.2). An extremely low value for the ratio [SII]/Hα could serve as an indicator for a region where photons can escape (Wang et al. 2021). The most extreme cases for this ratio are found in the HeII emitters: GP06, GP15, and GP20 (see Figs. B.29, B.38, and B.43).

The final two maps introduced here focus on the emission line ratios [SII]λ6716 Å /[SII]λ6731 Å and [OIII]λ4363 Å /[OIII]. Examples of maps corresponding to these ratios are displayed in Fig. 3.7. These ratios provide valuable information about electron density and electron temperature, respectively (e.g., Pérez-Montero 2017). Higher values of the ratio [SII]λ6716 Å /[SII]λ6731 Å correlate with lower electron densities, while higher values of the ratio [OIII]λ4363 Å /[OIII] correlate with higher electron temperatures.

Maps representing these two line ratios do not show clear radial variations. However, they do exhibit a range of morphologies despite the low spatial extension of these dim emission lines (see Appendix B.2).

In the specific case of GP06, the values for the ratio [SII]λ6716 Å /[SII]λ6731 Å are elevated in regions where the gas shows lower excitation levels (as indicated by the ratios [OIII]/Hβ and [SII]/Hα) and higher extinction (as indicated by the ratio Hα/Hβ). This suggests

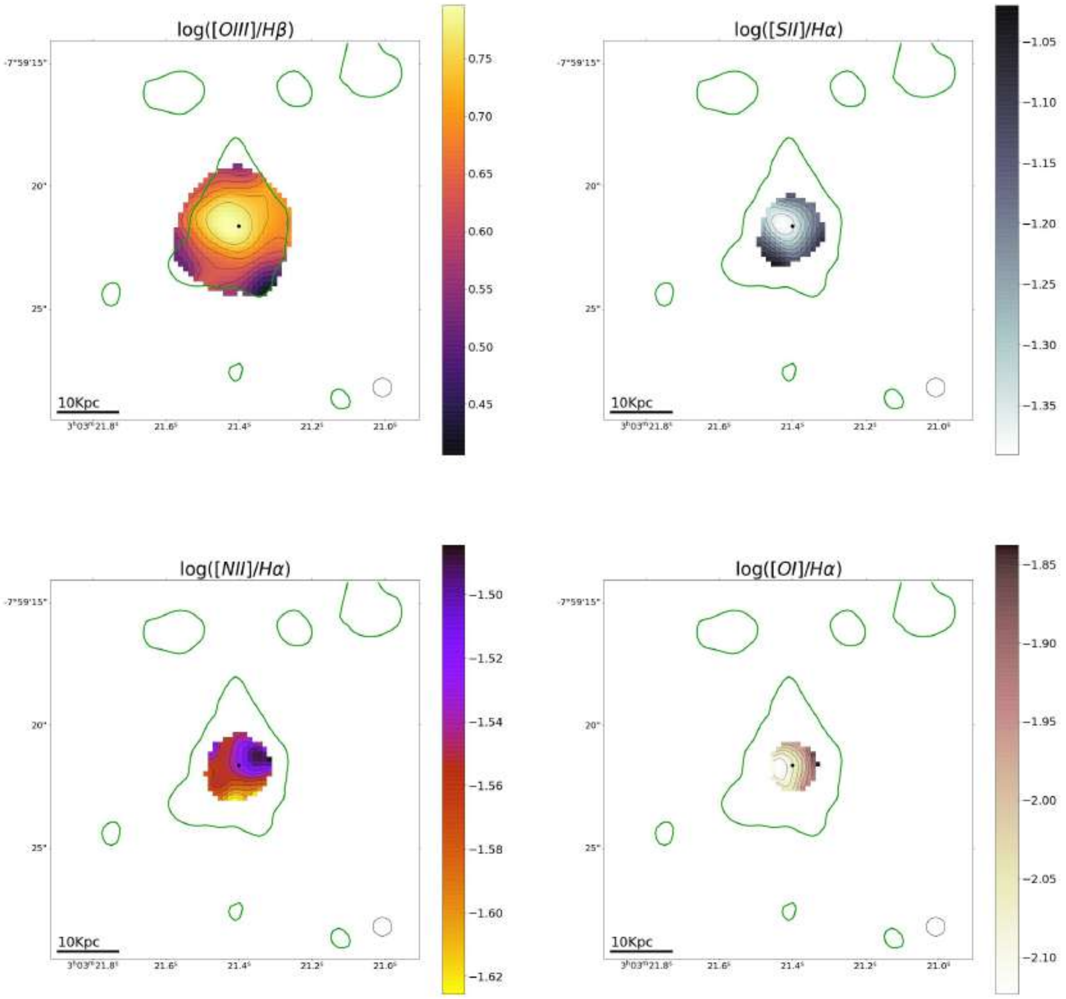

Figure 3.6 BPT maps corresponding to GP06.

that in GP06, regions with higher dust content and lower gas excitation tend to have lower electron densities.

Additionally, the highest values for the ratio [OIII]λ4363 Å /[OIII], which serves as an indicator of electron temperature, occur in galaxies that exhibit HeII line emission. These galaxies are GP06, GP15, and GP20 (see Figs. B.29, B.38, and B.43). This finding further supports the presence of a harder ionizing radiation field in these galaxies (see e.g., Kehrig et al. 2016).

In this study, we introduce radial profiles of the previously discussed emission line ratios. By plotting these ratios against radial distance from the galactic center, we can clearly see how these ratios vary across the galaxy. This form of representation aids in the identification

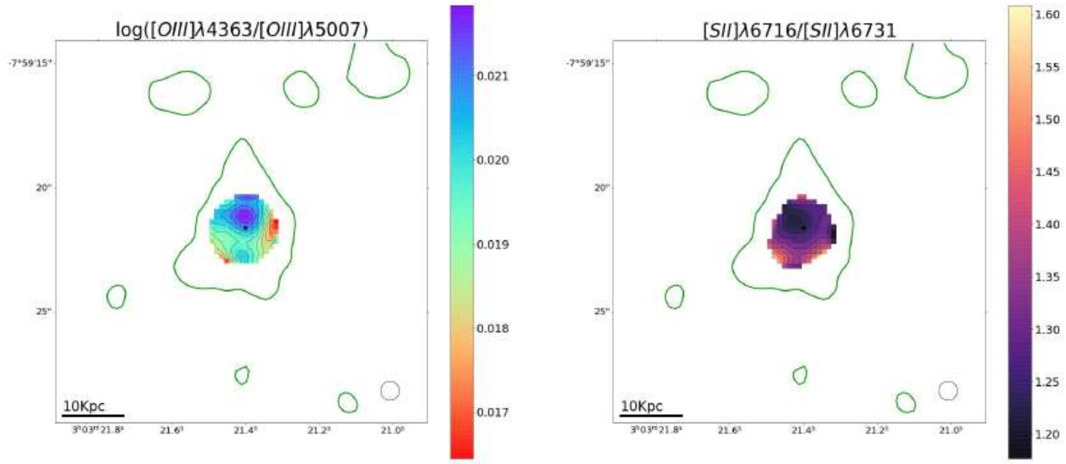

Figure 3.7 Maps corresponding to GP06.

of radial trends and offers a more complete understanding of how these ratios change with distance from the galactic core.

To generate these radial profiles, a method involving the integration of circular crowns centered on the peak of Hα emission was used. The code computes the average value of the emission line ratio within each of these crowns and plots this value against the radial distance from the center of the galaxy. Radial profiles for the ratio Hα/Hβ can be seen in Fig. 3.8. Additional radial profiles for other line ratios are available in Appendix B.4.

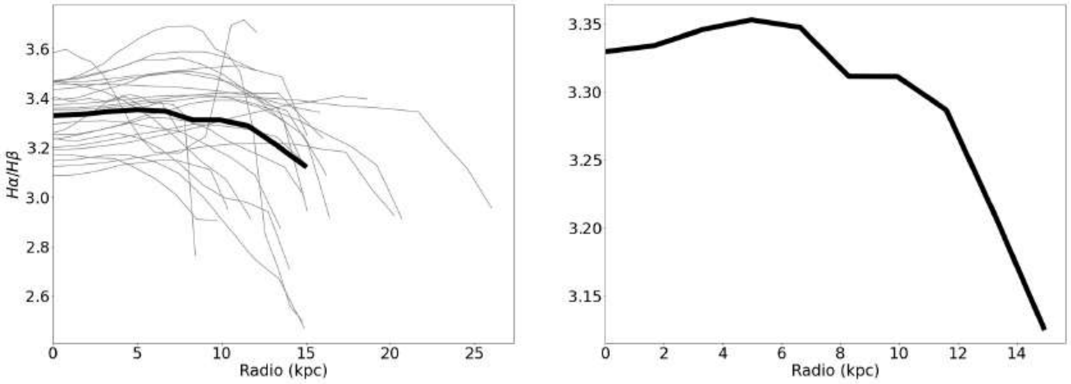

Figure 3.8 Radial profile of Hα/Hβ. The left image displays the profiles of all GPs for which line information is available, shown in gray. The black line represents the mean profile of all these galaxies and extends up to a radius where only 30 % of the galaxies have available data at larger radii. The right image offers a zoomed-in view of this mean profile. This format is consistent across all line ratio profiles presented in the appendix.

One significant observation is that the general radial trends of the emission line ratio profiles are consistent across the entire galaxy set (e.g. increasing [SII]/Hα as we go to larger radii from the center. See B.4). However, there are substantial variations in the absolute values of the ratios between different galaxies, typically around 0.5 dex. In contrast, within each individual galaxy, the radial change in the emission line ratios is relatively small, usually less than 0.1 dex. This minimal radial variation within each galaxy might be attributed to the low spatial resolution of our observations. Despite the minimal radial change within each galaxy, the average radial profiles of all galaxies reveal clear trends for various emission line ratios studied. These profiles offer valuable insights into the ionization state of the galaxies.

A consistent trend is observed as one moves away from the galactic center: the [OIII]/[OII] and [OIII]/Hβ ratios decrease, while the [SII]/Hα, [OI]/Hα, and [NII]/Hα ratios increase. This suggests that regions with the highest ionization levels and density bounded tracers are mainly found in the central areas of the galaxies. However, the average variations in the [OIII]/Hβ and [NII]/Hα ratios are minimal, at 0.03 dex and 0.015 dex respectively. This highlights the near uniformity in the radial changes of these emission line ratios.

Moreover, the radial pattern in the Hα/Hβ ratio manifests a diminishing inclination as one transitions towards the galaxy peripheries. This observation implies an elevated extinction or augmented dust attenuation in the central regions, as a result of a higher Hα/Hβ ratio relative to the outer zones of the galaxy.

Contrastingly, the radial changes in the [SII]λ6716 Å /[SII]λ6731 Å and [OIII]λ4363 Å /[OIII] ratios are minimal, being approximately of the same magnitude as the aforementioned [NII]/Hα ratio, and lack a distinct radial trend. These specific ratios may either be less susceptible to radial fluctuations or might be affected by other variables such as excitation conditions or uncertainties in observations.

In summary, the average radial profiles of the emission line ratios coherently delineate the spatial heterogeneities in the ionization state of the galaxies. The discerned tendencies corroborate the hypothesis that the central areas of the galaxies manifest elevated ionization states and more abundant density bounded tracers, whereas the outer zones are characterized by a lower level of ionization.

3.3.3 BPT diagrams

The BPT diagrams, evaluated on a spaxel by spaxel basis for all the GPs under study, are depicted in Fig. 3.9. Displayed therein are the line ratios [OIII]/Hβ vs [NII]/Hα, [SII]/Hα, and [OI]/Hα. Smaller dots represent measurements obtained from individual spaxels within each galaxy. The larger green dots indicate the line ratios calculated from the composite spectra, as elaborated in Section 3.4; these numerical values are tabulated in Table B.2.

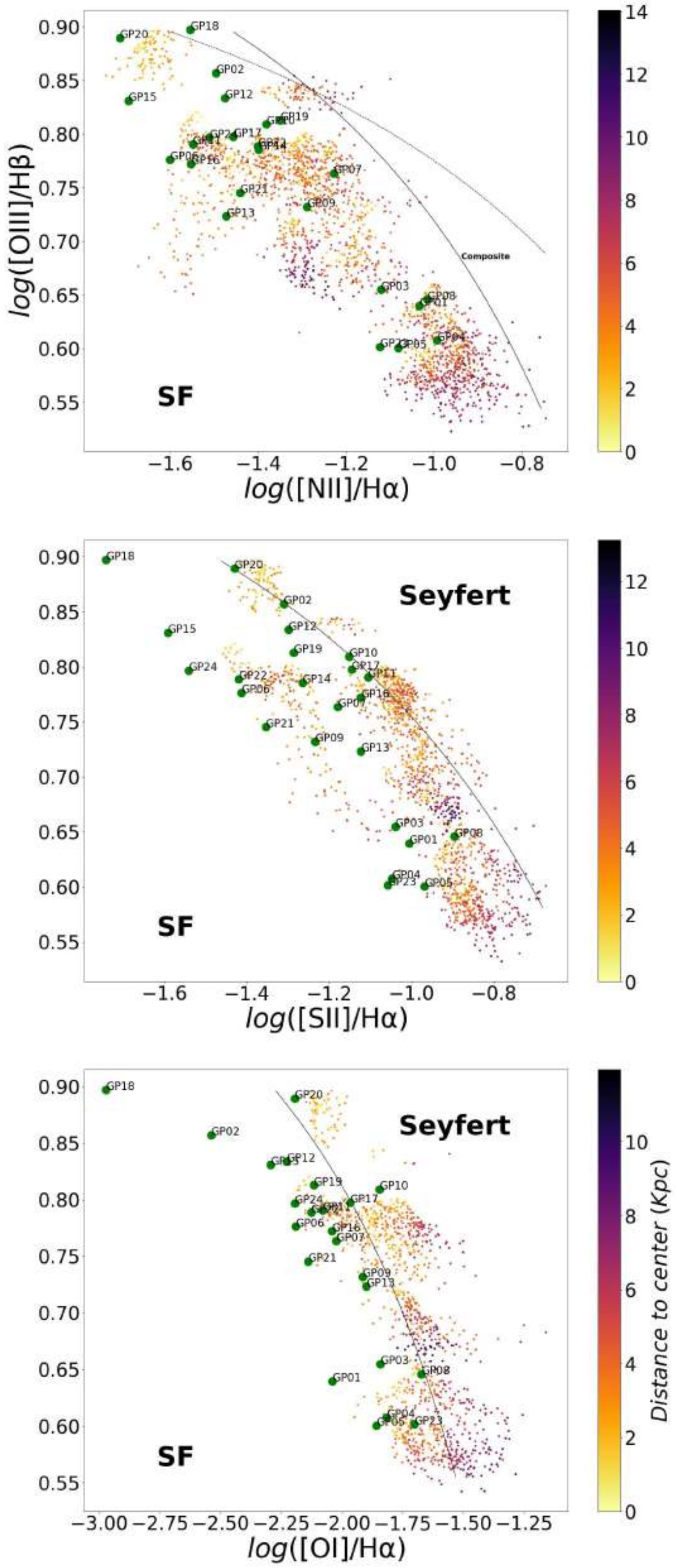

Figure 3.9 BPT diagram. Small dots transition in color from yellow to dark purple to represent individual spaxels within each galaxy. Larger green dots signify the integrated spectra of each galaxy, and adjacent to these green dots, the names of the respective galaxies are indicated. The color gradient of the smaller dots is determined by their proximity to the galaxy center: dots nearer to the center are rendered in yellow, while those farther away adopt a darker hue. The boundary lines demarcating each region are sourced from Kewley et al. (2001) and Kauffmann et al. (2003).

Collectively, the GPs in our study align within the canonical range of star-forming entities, as delineated by the spectral categorization frameworks outlined by Baldwin et al. (1981) and Kewley et al. (2006). This alignment implies that the primary excitation mechanism in these galaxies is photoionization from high-mass stars. More specifically, the GPs are situated in the upper-left quadrant of the diagram, an area predominantly occupied by galaxies displaying extreme characteristics, such as reduced metallicity and elevated excitation states of ionized gas. This proclivity for GPs is substantiated in prior research (e.g., Cardamone et al. 2009; Jaskot & Oey 2013). Additionally, as demonstrated by Pérez-Montero et al. (2021), GPs share the same locus with other EELGs in the [OIII]/Hβ vs [NII]/Hα diagram.

Moreover, we did not detect the Fe[X]λ6374 Å emission line in the spectra of any of our GPs. This specific line serves as an indicator of BH activity. Luminosities of this line within the range of 10^{36} – 10^{39} erg s^{-1} are consistent with the presente of a BH with a mass of approximately 10^5 M$_\odot$ (Molina et al. 2021). However, the considerable distance to the GPs constrains the capacity to detect lines with luminosities considerably less than 10^{40} erg s^{-1}. Such observational constraints lead to the inference that GPs are unlikely to harbor actively accreting BHs with masses significantly exceeding 10^5 M$_\odot$.

Additionally, we employed a methodology for estimating BH masses that utilizes the BH mass - stellar mass relationship, a relationship posited to be nearly invariant with respect to redshift (Shankar et al. 2020). However, the minimum stellar mass covered in our sample of GPs spans from $10^{8.3}$ M$_\odot$ to 10^{10} M$_\odot$, falls well below the predictive purview of this relationship. Therefore, its applicability is restricted to GPs possessing higher masses (approximately 10^{10} M$_\odot$), for which the predicted BH mass does not exceed $10^{6.7}$ M$_\odot$.

Such estimations significantly surpass the 10^5 M$_\odot$ threshold, suggesting that if these galaxies do contain BHs, these BHs are likely to have a mass that is relatively low compared to the stellar mass of the galaxy. It merits mentioning that the Shankar et al. (2020) relation is not particularly effective at predicting BH masses in galaxies with stellar masses less than $10^{9.8}$ M$_\odot$. This limitation makes it challenging to extract meaningful information regarding BHs in GPs with lower stellar masses. Further observational and analytical endeavors are requisite for confirming the existence and accurately determining the masses of any BHs within these galaxies.

In the BPT diagrams, distance from the galactic center also features as a parameter. Across all galaxies, a consistent trend is observable. Closer proximity to the galactic center is correlated with an elevated [OIII]/Hβ ratio, signifying higher excitation levels in the central regions. Conversely, lower [SII]/Hα and [OI]/Hα ratios are noted, implying that the central regions of these galaxies are optically thinner, and neutral oxygen is comparatively more abundant in the outskirts. As for the [NII]/Hα ratio, its value appears to be relatively distance-independent, which may suggest a lack of substantial metallicity gradients. These findings are congruent with those detailed in the preceding section (Section 3.3.2).

3.4 Properties of GPs from integrated spectra

We further exploit our IFS data to generate 1D spectra for specific regions within each galaxy. To achieve this, for each GP, the flux was summed across all spaxels where the Hα flux measurements yielded a signal-to-sigma-sky ratio exceeding 3 ($S/\sigma_{sky} > 3$). For illustrative purposes, the integrated spectrum for galaxy GP06 is displayed in Fig. 3.10. The collective integrated spectra for all GPs are provided in Fig. B.50. Notably, none of the spectra feature characteristics indicative of WR stars.

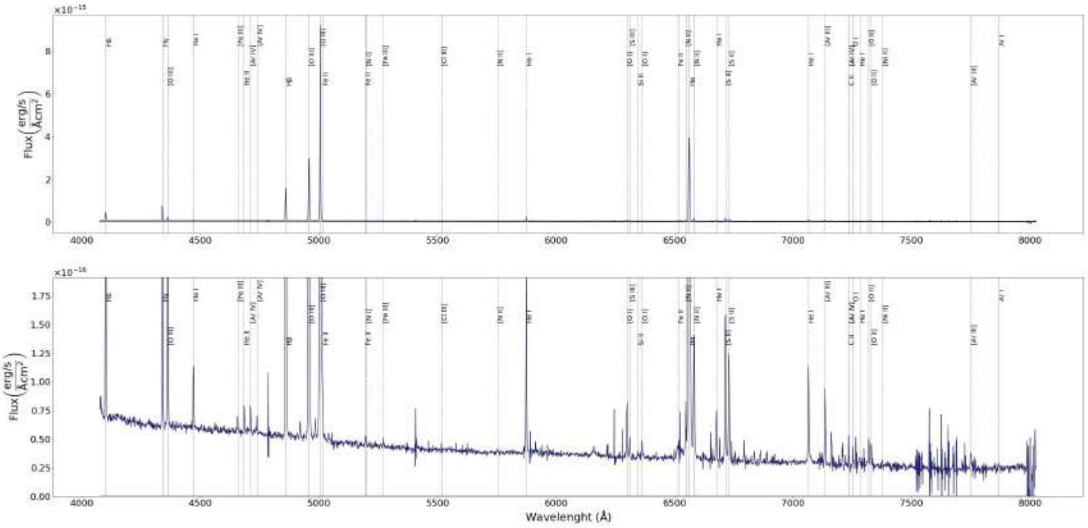

Figure 3.10 Integrated spectrum of GP06. Image in the bottom corresponds to a zoom in the y-scale to the top image.

The integrated spectrum for each GP is utilized to identify and quantify the most significant emission lines. The methodology employed is consistent with that detailed in Section 3.3 for the calculation of emission line fluxes, associated errors, and extinction correction. All pertinent emission line data are cataloged in Table B.6. To validate the accuracy of our flux measurements, a comparative analysis was conducted between the MUSE integrated spectra and the SDSS spectra. The average ratio of fluxes per line was found to be 1.003 ± 0.038. Additionally, the spectral coverage offered by SDSS is broader in terms of shorter wavelengths compared to MUSE. This enables the acquisition of the flux for the [O II] doublet in the 11

GPs where this line is not detectable in MUSE. For all other instances, MUSE fluxes were employed.

3.4.1 SFR

Utilizing the Kennicutt relation (Kennicutt Jr 1998), the SFR is derived from the Hα luminosity, which was obtained using luminosity distances from the UCLA cosmology calculator[2]. The SFR is calculated as follows:

$$\mathrm{SFR}(\mathrm{M}_\odot\ \mathrm{yr}^{-1}) = 1.26 \times 10^{41} L_{\mathrm{H}\alpha}(\mathrm{erg\ s}^{-1})$$

. The majority of the stellar masses ($\mathrm{M}_\star$) were sourced from Izotov et al. (2011). However, not all galaxies in our sample had their masses calculated by Izotov et al. (2011), and in those instances, values from Cardamone et al. (2009) were utilized. The recalculated masses by Izotov et al. (2011) were systematically lower due to the subtraction of the contribution from gaseous continuum emission during the SED fitting. No errors were reported in the original studies. The corresponding specific SFRs (sSFR) were computed as sSFR = $\mathrm{SFR} \times \mathrm{M}_\star^{-1}$.

In Fig. 3.11, the plot of sSFR against stellar mass is presented. In this diagram, GPs reside in a distinct region from that of normal present-day galaxies (those at z<0.05) (Catalán-Torrecilla et al. 2015). Specifically, GPs are characterized by lower masses and substantially higher sSFRs. Indeed, GPs occupy the same region in this diagram as high-redshift galaxies with $z = 1.1 - 4$. The mass-doubling timescale (sSFR^{-1}) for GPs is, on average, 2 dex lower than that of present-day galaxies, dropping to approximately 15 Myr for GP20, GP22, GP18, and GP15.

The depletion timescale, a marker for the duration of the starburst, approximates the mass-doubling timescale under the condition that the mass of hydrogen available for star formation (M_H) is comparable to the stellar mass ($\mathrm{M}_\star$). However, if $\mathrm{M}_\mathrm{H} > \mathrm{M}_\star$, the duration of the starburst surpasses the mass-doubling timescale. If one assumes that $\mathrm{M}_\mathrm{H} \simeq \mathrm{M}_\star$, this implies that GPs are transient phenomena. The systems would struggle to maintain such elevated SFRs over extended periods. The primary factors limiting the SFR include the exhaustion of gas reservoirs and feedback from stellar supernovae (Amorín et al. 2012b).

From an observational standpoint, limited data exists on whether GPs will cease star formation imminently. However, should they persist in forming stars, a rapid accumulation of stellar mass would occur alongside an increase in blue stellar luminosity. Consequently, the EW of the emission line [O III] would decline. Under such circumstances, these galaxies would no longer qualify as GPs based on the criterion of possessing high EW in [O III].

---

[2] see https://astro.ucla.edu/ wright/CosmoCalc.html

Employing this line of reasoning, it can be posited that GPs may represent the early stages of the galaxies responsible for the reionization of the Universe.

In relation to GP15 and GP22, they have been classified as a LyC leakers, both with an escape fraction for LyC, f_{esc}(LyC) = 0.08 , as reported by Izotov et al. (2016b,a) respectively. Regarding GP15, it is also measured a high Lyα escape fraction (f_{esc}(Lyα) = 0.51) as indicated by (Jaskot et al. 2017). This is consistent with the prevailing notion that the most vigorous starburst activities (i.e. higher sSFR) generally produce a greater abundance of ionizing photons. Additionally, both galaxies exhibits some of the most extreme line ratios conducive to the escape of ionizing photons, specifically high [OIII]/[OII] and for GP15 low [SII]/Hα and [NII]/Hα ratios, as outlined in Table B.2.

3.4.2 Electron density, temperature and abundances of the ionized gas

In this section, we focus on determining the chemical abundances within the ionized gas as well as the electron temperatures (T_e) and densities (n_e). The emission line [OIII]λ4363 Å plays a pivotal role for calculating electron temperature, and subsequently, chemical abundances. Out of the 24 GPs investigated in this study, this line is detectable above the 3 sigma threshold in 6 of them. For these particular galaxies, we estimated the T_e values for [OIII] based on the [OIII]λ4363 Å/[OIII] line ratio. We further derived the T_e values associated with [OII] from the empirical relationship between [OII] and [OIII] electron temperatures, as documented by Campbell et al. (1986).

Electron densities were calculated using the [SII]λ6716 Å /[SII]λ6731 Å line ratio. The ionic abundance ratios of oxygen, namely O^+/H^+ and O^{2+}/H^+, were obtained from the [OII] and [OIII] lines, using the respective electron temperatures. We assumed that the total oxygen abundance is the sum of these ionic abundances: $O/H = O^+/H^+ + O^{2+}/H^+$.

For nitrogen, the ionic abundance ratio N^+/H^+ was determined using the [NII] emission line, assuming that T_e[NII] ~ T_e[OII]. The N/O abundance ratio was calculated based on the assumption that $N/O = N^+/O^+$, considering the similarity in ionization potentials between the relevant ions.

These calculations were executed via the Pyneb code (Luridiana et al. 2015). Final errors in the derived quantities were assessed through error propagation methods, incorporating errors in flux measurements. For the remaining subset of GPs where the [OIII]λ4363 Å line is absent, we utilized the HII-CHI-Mistry code (Pérez-Montero 2014) to estimate O/H and N/O abundances along with their corresponding errors. Comprehensive data detailing these gas properties are presented in Table B.2.

In Figure 3.12, the electron density, temperature, and metallicity for the six GPs with the [OIII]λ4363 Å line measurement are illustrated. These parameters are also depicted

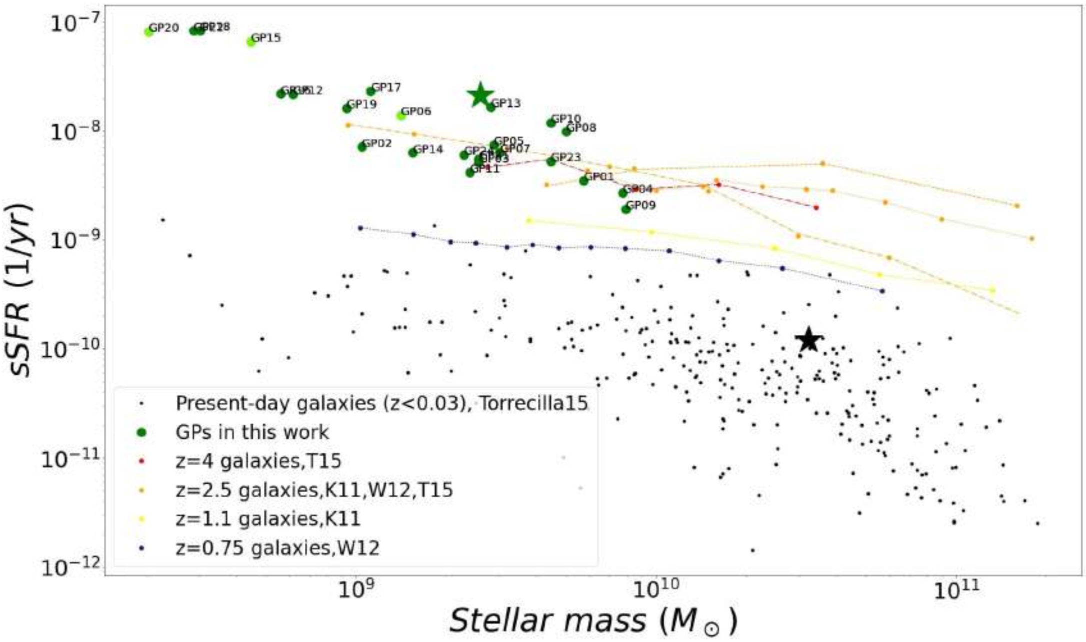

Figure 3.11 Stellar mass vs sSFR. In the graphical representations, green data points indicate the GPs discussed in this study, with lighter green marking GPs exhibiting HeII emissions. The green star symbolizes the median attributes of the GPs, aligning with a stellar mass of 2.6×10^9 $M_\odot$, a sSFR of 12 Gyr^{-1}, and consequently, a mass-doubling timescale of 47 Myr. In contrast, black data points signify a cohort of local galaxies (z<0.03) sourced from the Califa survey (Catalán-Torrecilla et al. 2015) (denoted as Torrecilla15). The black star represents the median of this local galaxy sample, which corresponds to a stellar mass of 3.2×10^{10} $M_\odot$, a sSFR of 0.12 Gyr^{-1}, and thereby a mass-doubling timescale of 8.3 Gyr, approximating the age of the Universe. The graphical presentation also includes sSFR-Mass relations at different redshifts, as documented in Tasca et al. (2015) (dash-dot line, labeled as T15), Karim et al. (2011) (dashed line, labeled as K11), and Whitaker et al. (2012) (dotted line, labeled as W12).

for 35 galaxies sourced from the NASA-Sloan Atlas[3] with EW(λ5007 Å) > 1000 Å, as well as for 37 galaxies from the COS Legacy Archive Spectroscopic SurveY (CLASSY) (Berg et al. 2022). These CLASSY galaxies serve as the most proximate local analogs ($z <$ 0.18) to high-redshift galaxies during the epoch of reionization. The gas properties for these additional galaxies were determined by Peng (2021).

The metallicity observed within our selection of GPs is relatively low, corroborating previous findings; specifically, $12 + \log(\text{O/H}) = 7.6 - 8.4$ (e.g., Amorín et al. 2010). For the subset of GPs that exhibit [OIII]λ4363 Å emission, the electron temperatures vary between

---

[3] http://www.nsatlas.org/

11500 K and 15500 K. Meanwhile, electron densities within these galaxies range from 30 cm^{-3} to 400 cm^{-3}.

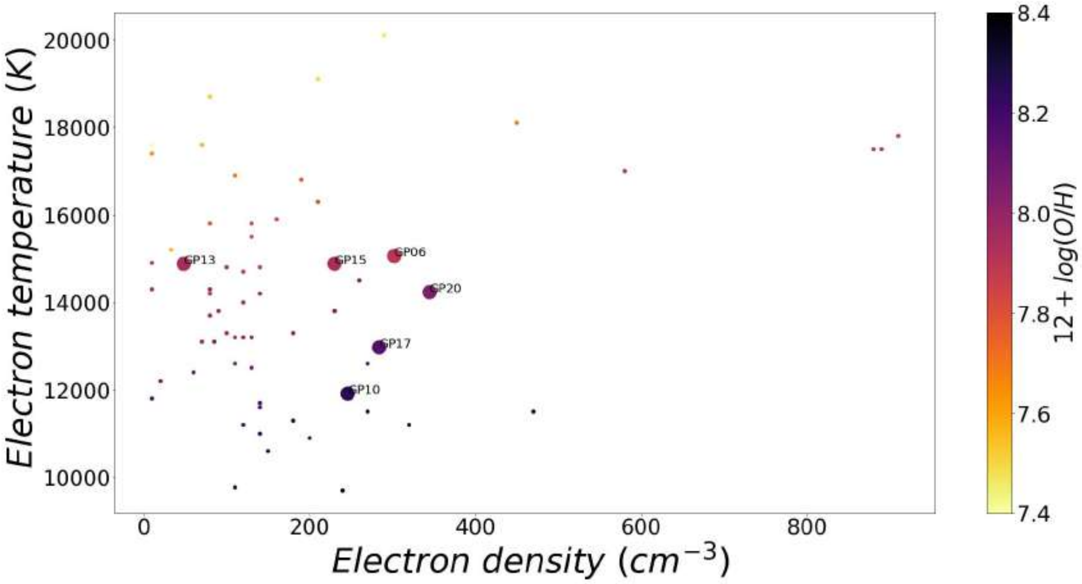

Figure 3.12 Electron density, electron temperature and metallicity representation. Large, labeled markers signify the six GPs where the direct method can be accurately employed. Smaller markers represent all the selected galaxies from the NASA-Sloan Atlas with W(λ5007 Å) > 1000 Å, along with 37 galaxies from the COS Legacy Archive Spectroscopic SurveY.

In Figures 3.13, 3.14, and 3.15, we present the relationships between oxygen abundance and stellar mass, N/O and stellar mass, and N/O vs oxygen abundance, respectively. These figures facilitate a comparative analysis between approximately 200,000 star-forming galaxies (SFGs) from the SDSS (Duarte Puertas et al. 2022) and the GPs under study.

For a given stellar mass, GPs demonstrate lower oxygen abundances compared to the majority of SDSS galaxies, a result in agreement with Amorín et al. (2010). Specifically, GPs adhere to a mass-metallicity relationship that parallels that of SDSS SFGs but is displaced by approximately 0.3 dex towards lower metallicities.

Turning our attention to the N/O as depicted in Fig. 3.14, it becomes apparent that GPs largely follow the trend set by SDSS galaxies, with exceptions at the lower mass end. Notably, GPs such as GP22, GP18, and GP20 exhibit elevated N/O values (visible in Fig. 3.14). The N/O spans a range of log(N/O) = -1.5 to -0.85.

Despite the paucity of metals in GP galaxies, the N/O largely remains stable. This phenomenon could be elucidated by a significant and recent inflow of metal-deficient gas (Pérez-Díaz et al. 2024), essentially neutral hydrogen clouds, sourced from the HI halo of the galaxy reservoir. Such an accretion event would have the effect of diluting the O/H while leaving the N/O largely unmodified (Köppen & Hensler 2005). The fact that the N/O ratios for these galaxies are largely consistent with what would be anticipated based on their stellar masses lends further credence to this interpretation (Amorín et al. 2010).

The hypothesis that a considerable inflow of unenriched gas could simultaneously maintain low metallicity levels and elevate the SFR appears viable. Yet, this brings forth a complex question concerning the existence of such a mechanism at low redshifts. The origins of this pristine gas are still subject to ongoing investigation. However, there is empirical evidence from exceptionally metal-poor galaxies in our close vicinity ($z = 0.03$) that possess significant volumes of neutral hydrogen, which bears resemblance to a halo (e.g., Lequeux & Viallefond 1980; Herenz et al. 2023). These observations provide empirical support for the possibility of similar conditions in GP galaxies, thereby reinforcing the proposed scenario.

Predictions from chemical evolution models (e.g., Mollá et al. 2006; Vincenzo et al. 2016) propose that the shift between primary and secondary nitrogen dominance on the N/O vs O/H plane is influenced by the star formation history of the galaxy, specifically the star formation efficiency. In a galaxy characterized by 'bursty' star formation activity (meaning it has recently undergone a significant starburst event) the N/O ratio would likely increase more rapidly compared to a galaxy with a more stable and prolonged star formation history. Another contributing factor to elevated N/O levels at low metallicity could be the IMF. A higher proportion of massive stars within the IMF could potentially boost primary nitrogen production at low metallicities. Nevertheless, we find that the N/O to stellar mass relationship generally persists. For those galaxies that deviate from this expected correlation (as evidenced by GP22, GP18, and GP20 in Fig. 3.14), fine-tuning the IMF may serve as a plausible explanation.

3.5 Kinematic analysis

In this section, we conduct a kinematical analysis of the ionized gas in our GPs by using the Hα emission line. Our study focuses on creating velocity and velocity dispersion maps and performing a multi-gaussian fit to the line profile in the integrated spectrum of each of our galaxies. These findings will contribute to exploring the luminosity-sigma (L-σ) relation (comparing our results with other galaxy types as discussed in Terlevich et al. (2015)), to enhance our understanding of the evolutionary context of GPs.

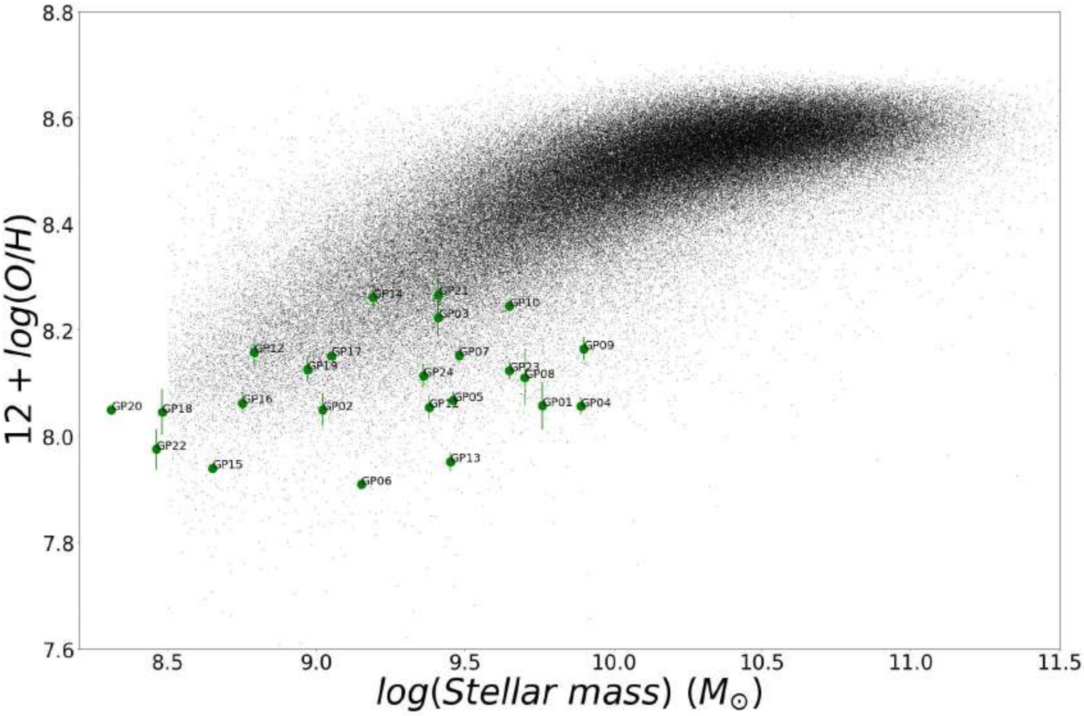

Figure 3.13 Oxygen abundance vs stellar mass. GPs are the green points. Black points correspond to ~ 200000 galaxies from Duarte Puertas et al. (2022)

3.5.1 Kinematical maps and multi-gaussian fit.

For analyzing the kinematics of the GPs, we focus on the profiles of the Hα line.By using this line profile we will extract both velocity and velocity dispersion maps of the ionized gas. For each spaxel that meets our signal-to-noise criterion ($S/N > 3$), a single Gaussian fit is applied. We then measure the central wavelength and the standard deviation of the Gaussian that best fits the emission line profiles at each spaxel. The central wavelength of each emission line is crucial for determining the velocity field by using the longitudinal relativistic Doppler effect. This effect can be quantified by the equation:

$$v = c\left(\frac{(\lambda/\lambda_0)^2 - 1}{(\lambda/\lambda_0)^2 + 1}\right) \tag{3.1}$$

where v represents the velocity, c is the speed of light, λ denotes the observed wavelength, and λ_0 is the rest wavelength. This formula for the Doppler effect was consistently applied to all velocity calculations throughout our analysis. The standard deviation, derived from the Gaussian fits to the line profiles, provides us with the basis for calculating the velocity dispersion field.

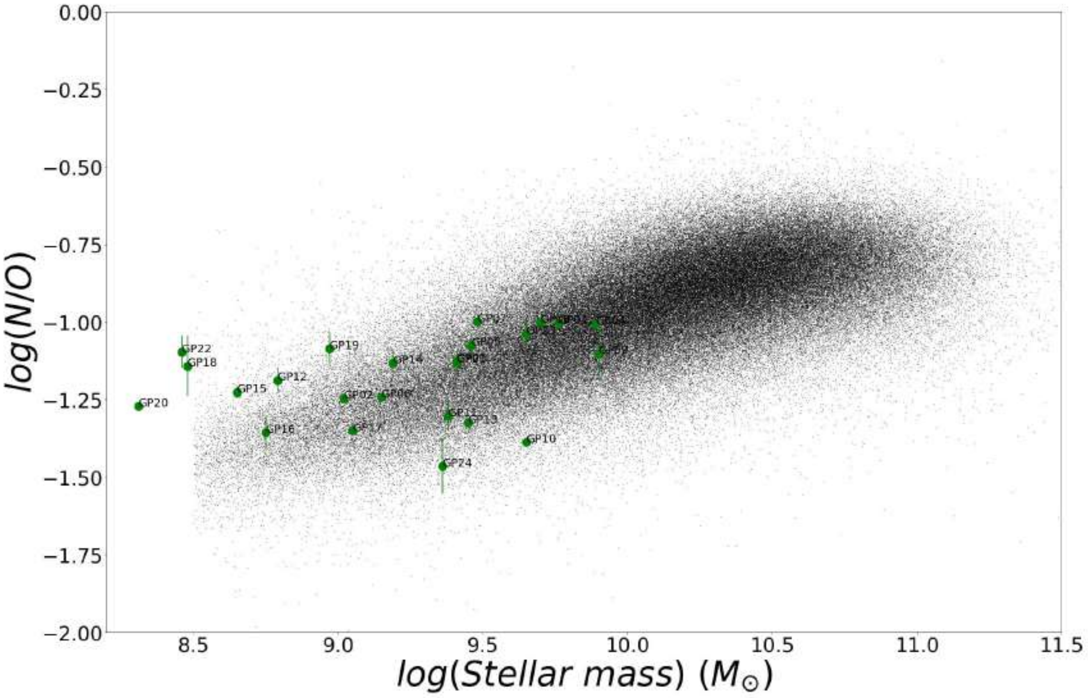

Figure 3.14 N/O vs stellar mass. GPs are the green points. Black points correspond to ~ 200000 galaxies from Duarte Puertas et al. (2022)

In order to obtain the corrected velocity dispersion (σ), we took into account the instrumental and thermal widths (σ_{inst}, σ_{thermal}). The correction was performed as follows:

$$\sigma^2 = \sigma^2_{\text{obs}} - (\sigma^2_{\text{inst}} + \sigma_{\text{thermal}}) \tag{3.2}$$

The instrumental width was calculated from the width of the the lamp line profiles, resulting in a standard deviation of $\Delta\lambda = 0.9$ Å. Meanwhile, σ_{thermal} was calculated by using the Maxwell-Boltzmann distribution:

$$\sigma^2_{\text{thermal}} = \frac{KT_e}{m} \tag{3.3}$$

where K is the Boltzmann constant, T_e the electronic temperature and m is the hydrogen mass.

In addition to instrumental and thermal widths, we could consider the effects of fine structure and natural broadening (σ_{fs} and σ_{natural}). Fine structure, leads to a subdivision of emission lines that can be interpreted as a broadening. The σ_{fs} is only well characterised for atoms with one electron and is usually around 2-3 km s^{-1} (e.g., García-Díaz et al. 2008) so

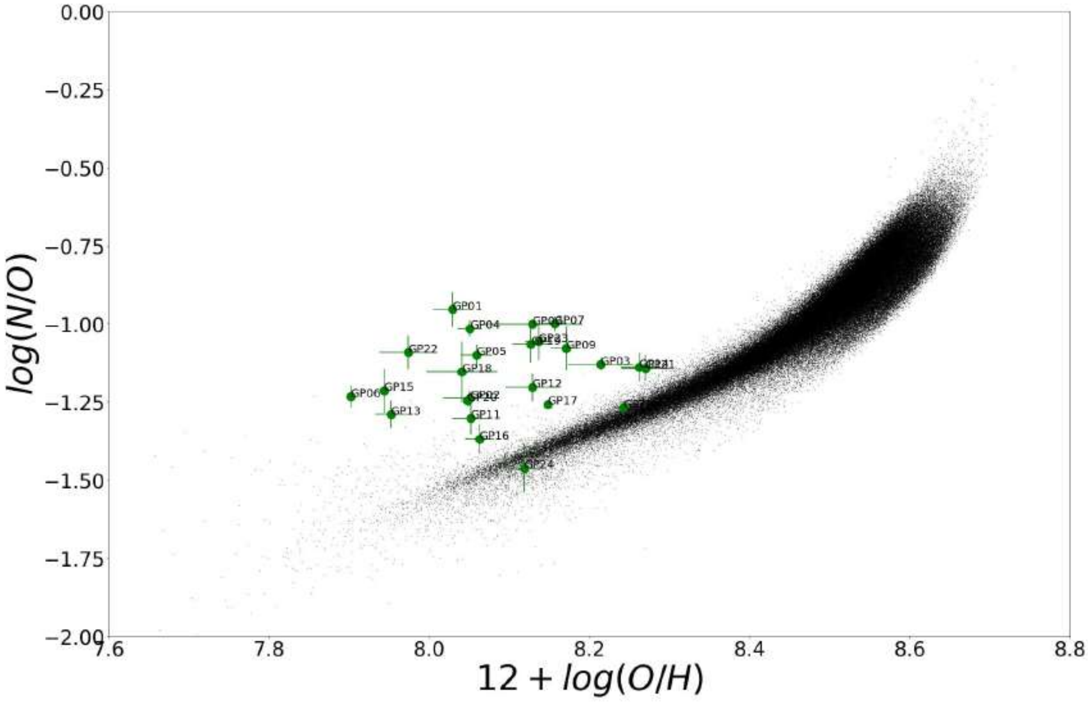

Figure 3.15 N/O vs oxygen abundance. GPs are the green points. Black points correspond to ~ 200000 galaxies from Duarte Puertas et al. (2022)

for our spectral resolution we can ignore this effect. Natural broadening, governed by the Heisenberg uncertainty principle ($\Delta E \cdot \Delta t \geq h/4\pi$) in our case is minimal. Lifetimes of excited states of the H atom are about 10 nanoseconds, leading to a natural linewidth broadening of only a few m s^{-1}, which is significantly smaller than other broadening mechanisms encountered in most astrophysical observations.

Additionally, our analysis extends to the integrated spectra of each GP. Despite the absence of spatial information in this approach, the integrated spectra offer a significantly improved signal-to-noise ratio compared to single spaxel spectra. This enhancement is pivotal for our study, as it allows us to detect potentially dim and broad components in the emission lines, which are often obscured or not discernible in individual spaxel spectra.

Employing a multi-Gaussian fit to these spectral lines enables us to dissect and understand the complex velocity structures within the galaxies. This method is not just about identifying various components of the emission lines; it is about revealing the underlying kinematic features that are otherwise lost in the noise. Crucially, we utilize the Akaike information criterion (AIC) to determine the optimal number of Gaussian components for each line profile.

The multi-Gaussian fitting process is instrumental in separating the overlapping velocity components and isolating the subtle features that contribute to the overall line profile.

All this analysis is summarized in a series of figures for each galaxy, displaying luminosity, velocity, and velocity dispersion maps. These visuals provide an immediate understanding of the kinematic behavior within each galaxy. Additionally, each figure includes a multi-Gaussian fit of the integrated spectrum for the emission line, offering insights into the velocity structures. As an example we can see this representation for GP06 in Fig. 3.16, the rest of Figs. are in Appendix B.7.

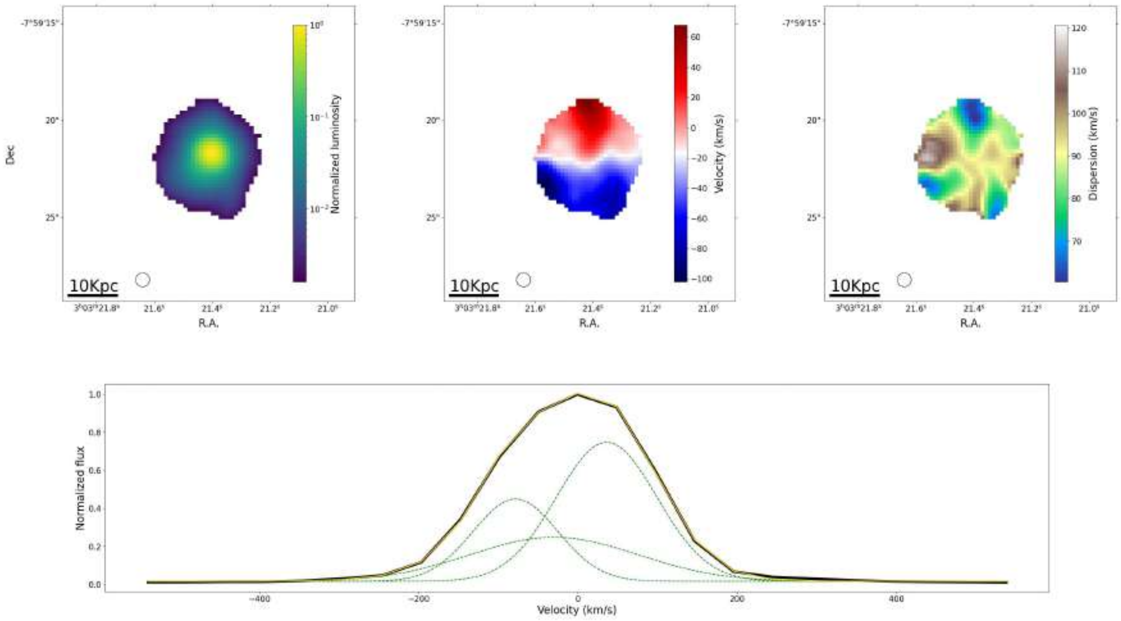

Figure 3.16 Kinematic analysis of GP06. Top row: Left, middle and right panels display the maps for the Hα luminosity, velocity and velocity dispersion, respectively. Bottom row: Integrated spectrum of the galaxy showing a zoom around the Hα line. The black line represents the line profile, the yellow line is the fit and each gaussian component is represented in green.

Regarding the kinematic features of GP06 (see Fig. 3.16), the velocity field suggests a disturbed rotational pattern (i.e. a region of the galaxy with positive velocities and the opposite region with negative velocities), hinting at a rotation overimposed onto a more chaotic kinematic behavior. Notably, the velocity field displays three local maximum/minimum points, which correspond to minima in the velocity dispersion field ($\sigma < 70$ km s^{-1}). These zones can be distinctly identified by the blue regions in the velocity dispersion map (Fig. 3.16). Additionally, these regions exhibit the highest levels of extinction (Hα/H$\beta > 3.6$), as inferred from the Hα/Hβ map (see Fig. 3.4), and the lowest ionization levels (log([OIII]/Hβ) < 0.55 dex), as indicated by the [OIII]/Hβ map (see Fig. 3.6).

Furthermore, other regions of the galaxy, characterized by higher velocity dispersion values ($\sigma > 100$ km s^{-1}), align with areas of less pronounced velocity gradients. These areas are identifiable as yellowish-brown regions in the velocity dispersion map (Fig. 3.16). Of particular interest is the eastern part of the galaxy, which exhibits the maximum velocity dispersion. This region has been previously discussed as a potential pathway for the escape of LyC photons (see Section 3.3.2). The observed high velocity dispersion values, reaching up to 120 km s^{-1} in the eastern region of GP06, might be indicative of a disruption in the gas due to stellar feedback, creating escape paths (Amorín et al. 2024). In comparison, the typical velocity dispersion expected from the virial motion of gas in our set of GPs, with Hβ luminosities ranging from 10^{41} to 10^{42} erg/s (Terlevich et al. 2015), is about 40-60 km s^{-1}. Velocity dispersion values exceeding this range suggest the injection of additional kinematic energy into the gas, beyond gravitational attraction. Therefore, the elevated velocity dispersion in the eastern region could be tracing outflows potentially carving openings in the ISM for LyC photons to escape.

The rotational pattern indicate the presence of a defined plane of rotation in the galaxy. This could be due to the presence of a rotating disk within the galaxy, or it might reflect the interaction between two disconnected parts (i.e. knots) of the galaxy. HST images of GPs presents these disconnected parts or knots in most cases (e.g., Amorín et al. 2012b; Yang et al. 2017a). The dual but wavelength-shifted components observed in the line profile lean towards the latter interpretation. However, the current spatial resolution of the MUSE data cube is insufficient to conclusively distinguish between these scenarios. High spatial resolution observations are essential to clearly differentiate rotationally supported galaxies from interacting systems or pressure-supported systems, as highlighted in Mason et al. (2017).

Notably, a wide component in the Hα line profile fit is observed in almost all GPs in our sample (see Appendix B.7). This characteristic is often interpreted as an indicator of outflows, potentially driven by stellar feedback mechanisms such as supernovae (Amorín et al. 2012b). A previous study (Hogarth et al. 2020), has pointed to the elevated metallicity in these outflows, with the widest component exhibiting a metallicity that is notably 0.3 dex higher than its narrow counterparts. Moreover, the work by Amorín et al. (2024) brings an additional layer of understanding by demonstrating that LyC leakers showcase a wide component in their emission line profiles, with a velocity dispersion exceeding 100 km s^{-1}. Furthermore, these galaxies exhibit a direct correlation between the escape fraction of LyC photons and the magnitude of the velocity dispersion and blueshift in this wide component. This relationship underscores the significance of high-velocity outflows in the context of galaxy evolution and star formation, suggesting that the most intense LyC leakers are also the ones experiencing the most vigorous kinematic activity.

3.5.2 L-σ relation

In an extension of our kinematic analysis, we visit the L-σ relation presented in Terlevich et al. (2015) (see Fig. 3.17), incorporating our GP galaxy dataset. The L-σ relation describes a connection between the luminosity and the velocity dispersion in a galaxy. In simpler terms, brighter galaxies tend to have more mass and thus gas/stars are moving around their center at faster speeds. In this case, this integration is particularly insightful as it includes each component derived from the multi-gaussian fits for each GP. What emerges from this plot is a nuanced view of the kinematic behavior within these galaxies. Notably, the more intense, narrower components of the emission lines tend to align with the L-sigma relation observed in Terlevich et al. (2015), suggesting that these components predominantly represent areas within the galaxies where the motion of the gas is governed by gravitation.

Conversely, the dimmer, broader components deviate significantly below the established relation. This deviation indicates that the corresponding regions in the galaxies possess kinematic energies greatly exceeding those expected from gravitational interactions alone. Such findings point to more turbulent processes at play, potentially driven by phenomena like stellar feedback or BH activity (Amorín et al. 2012b), reinforcing the complexity of the internal dynamics of GPs.

3.5.3 Rotation vs dispersion dominated systems

In our study of the GPs, an examination of the velocity fields (see Appendix B.7) reveals that a significant majority, approximately 20 out of 24 galaxies, display characteristics indicative of rotational patterns (i.e. there is one axis in the galaxy where radial velocities gradually change from positive to negative). This observation suggests that these galaxies are predominantly rotation-dominated, potentially hinting at the presence of disk-like structures or at least a clearly defined angular momentum in the galaxies. To explore this interpretation further, we employ the criteria outlined in Hogarth et al. (2020), who provides a framework to distinguish between rotation and dispersion-dominated galaxies. In Fig. 3.18, a detailed plot illustrates the relationship between the median velocity dispersion (σ_{median}) and the maximum velocity difference (V_{max}) for each GP. Employing the criterion $V_{max}/\sigma_{median} \lesseqgtr 1$ as proposed in Hogarth et al. (2020), allows us to categorize galaxies as either rotation or dispersion-dominated. Intriguingly, the plot reveals that only two galaxies, GP06 and GP02,

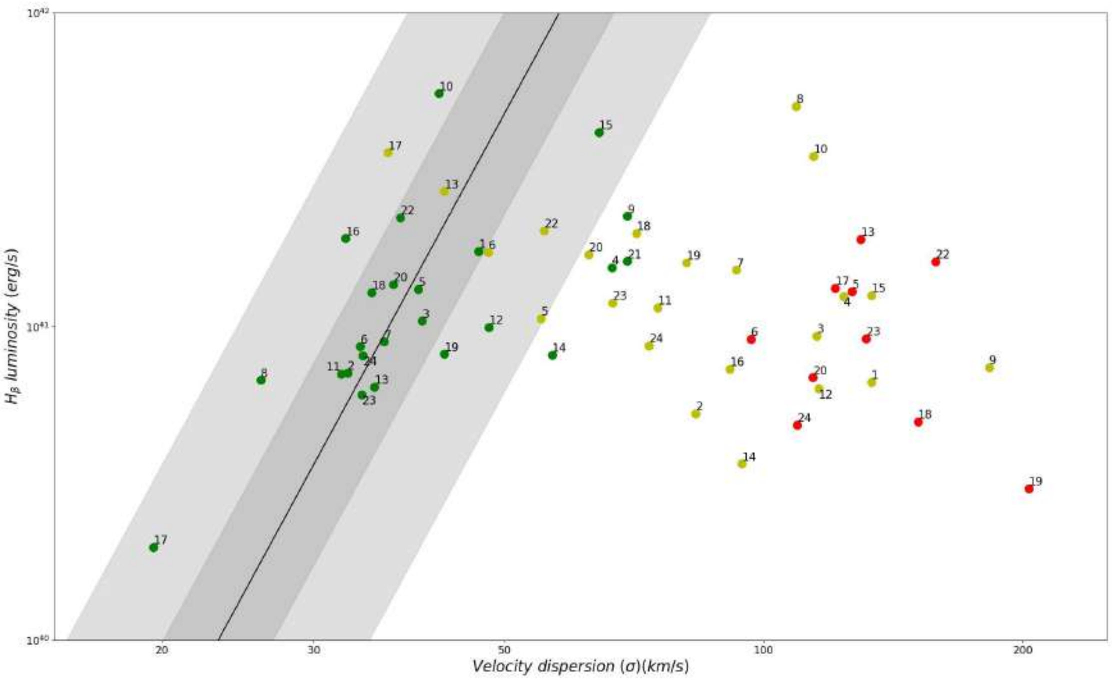

Figure 3.17 L-σ relation. Green points represent the gaussian component with the smallest velocity dispersion for each GP. Yellow points represent the gaussian component with the second smallest velocity dispersion in GPs with two or more gaussian components. Red points represent the gaussian component with the highest velocity dispersion in GPs with three gaussian components. Black line represents the lineal interpolation of the points in Terlevich et al. (2015). Dark (light) gray area represents the region where these points spread up to 1 σ (3 σ)

are rotation-dominated, with GP06 being particularly notable for its exceptionally high V_{max} value, exceeding 160 km s^{-1}.

This finding is significant as it indicates that, generally, GPs are more characterized by dispersion and chaotic movements rather than by coherent, rotationally dominated velocity fields. Such a pattern suggests that while rotational elements are present, they are often overshadowed by more turbulent kinematic processes (possible arising from stellar feedback). This observation is crucial in understanding the dynamical state of GPs, pointing to a prevalence of complex internal motions over simple rotational dynamics.

3.6 Summary and conclusions

We have undertaken a comprehensive analysis of the physical and chemical attributes of 24 GPs through the MUSE/VLT data cubes. Given that these galaxies serve as some of the

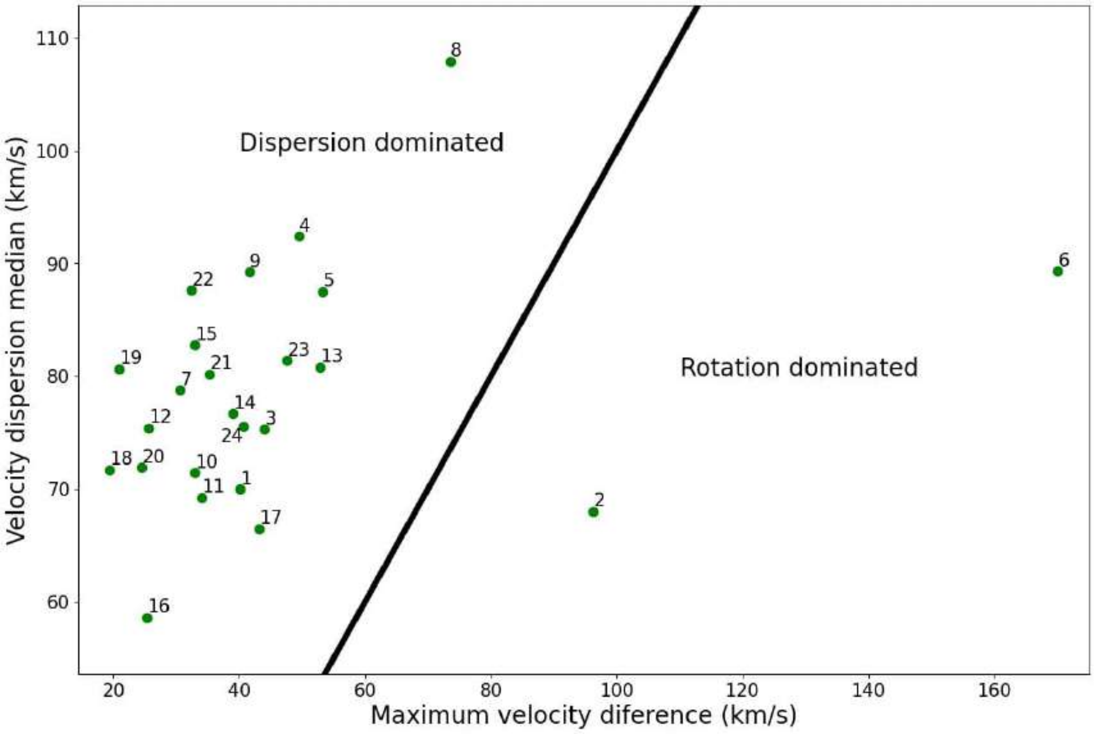

Figure 3.18 V_{max} vs σ_{median} criterion for rotation/dispersion dominated systems. Green points correspond to GPs, the black line indicates the one-to-one relationship that differentiates the two defined states.

closest local counterparts to high-redshift galaxies, their examination is crucial for gaining insights into the initial stages of galaxy formation and assembly, particularly in the context of reionization.

In this investigation, one of our key objectives was to ascertain the spatial extent of the GPs under study. To this end, we conducted an analysis concerning the spatial extension of all sources located within the FoV of the MUSE data cube. Utilizing a set of criteria, we compared the FWHM, FW$\frac{1}{10}$M and FW$\frac{1}{100}$M of our GPs and of star-like objects in the same FoV. As a result, we identified seven GPs that are spatially extended in both the core and low surface brightness regions, five that are extended in the core, and four that are extended in the low surface brightness regions. These findings are summarized in Table 3.2.

Furthermore, we performed a comparative analysis between emission line maps and continuum maps. Among the set, only four emission line maps, corresponding to GP06, GP07, GP13, and marginally GP01, lack circular symmetry. In contrast, continuum maps reveal a far more intricate structure across all GPs, acting as a proxy for the underlying stellar population. The [OIII] maps exhibit the greatest spatial extent, serving as tracers for low surface brightness regions of ionized gas.

In relation to the ionization structure of the GPs, maps of the Hα/Hβ ratio reveal areas with varying dust concentrations as well as regions where photons are less likely to be absorbed due to low extinction. The morphology displayed by these maps is distinct for each GP. The ionization parameter, represented by the [OIII]/[OII] ratio, generally peaks at the centers of these galaxies. This suggests that the zones of highest ionization are closely aligned with star-forming regions. Notably, GP20, GP06, GP15, and GP22 exhibit the most pronounced ionization, as indicated in Table B.2 and Figures B.38 and B.45.

Further insight into the ionization state is offered by the study of [OIII]/Hβ, [NII]/Hα, [SII]/Hα, and [OI]/Hα ratios through maps and BPT diagrams. These analyses reveal a predilection for higher gas excitation at the galactic centers, evidenced by increased ratios of [OIII]/Hβ and decreased ratios of [SII]/Hα and [OI]/Hα proximal to the peak of Hα emission.

Nevertheless, the ratios [OIII]/Hβ and [NII]/Hα display limited spatial variation across most GPs, with a maximum difference of 0.14 dex. The exception is GP06, which shows a variation exceeding 0.4 dex. This implies a general uniformity in both gas excitation and metallicity within these galaxies.

Finally, the ratios [SII]/Hα and [OI]/Hα serve as indicators for the outer limits of the ionized gas. These ratios exhibit their lowest values near the centers of the galaxies, which points to a blister-type morphology, especially evident in galaxies such as GP06, GP08, GP10, GP13, and GP23.

BPT diagrams affirm that hot, massive stars are the primary sources of ionizing photons in GPs. Specifically, our GPs are situated in the top-left quadrant of the BPT diagram, where galaxies with the most extreme characteristics (lowest metallicity and highest gas excitation) reside. The lack of the [FeX]λ6374 Å line in all observed spectra negates the possibility of BHs with masses exceeding $10^5 M_\odot$ contributing to gas ionization.

By integrating the flux over regions defined by the Hα map, we generated integrated spectra for each GP. SFRs inferred from the Hα line luminosity, indicate star formation bursts with mass-doubling timescales that are 2 dex shorter than those observed in typical star-forming galaxies. Examination of ionized gas properties through emission lines reveals low gas metallicity ($12+\log(\mathrm{O/H}) = 7.6-8.4$), high electron temperatures ranging from 11500 K to 15500 K, and electron densities spanning from 30 cm^{-3} to 530 cm^{-3}. In terms of chemical abundances, the N/O ratio vs stellar mass in GPs generally aligns with the trend seen in SDSS galaxies, as shown in Figure 3.14. The ratio ranges between $\log(\mathrm{N/O}) = -1.5$ and -0.85. However, our GPs diverge from the SDSS sequence in the $\log(\mathrm{N/O})$ vs $12+\log(\mathrm{O/H})$

diagram (see Figure 3.15), suggesting the possible accretion of pristine, metal-poor gas into these galaxies.

The nebular HeII line was detected in the galaxies GP06, GP15 (this specific galaxy being a confirmed LyC leaker (Izotov et al. 2016b)) and GP20. This detection signifies the presence of extremely hard ionizing photons (E > 4 Ry). Notably, none of these GPs exhibit WR features in their spectra, countering the hypothesis of WR stars as the primary agents for HeII excitation (e.g., Senchyna et al. 2017; Kehrig et al. 2015, 2018). Additionally, two of these GPs display some of the highest sSFR, exceeding 8×10^8 yr^{-1}. This implies that, apart from low metallicity, high sSFR could be a significant determinant for the HeII-emitting nature of a galaxy (Kehrig et al. 2020; Pérez-Montero et al. 2020).

Regarding the kinematic analysis, we have made a velocity, velocity dispersion maps and multi-Gaussian fit of the integrated spectra derived from the Hα emission line (see Fig. 3.16). It all underscores the complexity of gas movements within these compact starbursts. By dissecting the integrated spectra through multi-Gaussian fits, we reveal that the internal kinematics of GPs are not solely governed by gravitational forces but are significantly influenced by stellar feedback mechanisms, as evidenced by the presence of high-velocity outflows. These outflows, characterized by broad spectral line components, highlight the dynamical interplay between star formation processes and the dispersal of ionized gas, possibly facilitating the escape of LyC photons (Amorín et al. 2024).

Moreover, our exploration of the L-σ relation (see Fig. 3.17) and the distinction between rotation vs dispersion-dominated systems (see Fig. 3.18) underscore the predominance of dispersion over rotational movements in the majority of our GPs. This suggests a turbulent internal environment, potentially driven by intense star formation activity and the ensuing stellar feedback. Still, a rotational pattern is seen in most of the galaxies (see Appendix B.7), indicating the presence of a plane of rotation.

Through this comprehensive analysis, our study offers a window into the formative processes of galaxies in the local Universe that mirror the conditions of the early cosmic epochs. The intricate dance of gas dynamics, star formation, and chemical enrichment in GPs thus stands as a testament to the complexity of galaxy evolution, paving the way for further explorations into the origins of galaxy assembly and the role of feedback mechanisms in shaping the cosmos.

Chapter 4

Unraveling the Kinematics of IZw18: A Detailed Study of Ionized Gas with MEGARA/GTC

This chapter is based on the publication:

"Unraveling the Kinematics of IZw18: A Detailed Study of Ionized Gas with MEGARA/GTC"
Antonio Arroyo-Polonio et al.
Published in A&A (2024).

https://doi.org/10.1051/0004-6361/202449606

4.1 Introduction

The study of galaxy kinematics provides an invaluable tool for understanding the processes that shape the evolution of galaxies. Specifically, analyzing the motion of ionized gas within these celestial structures uncovers patterns indicative of both their current dynamical state and historical phenomena, such as possible rotations and feedback processes.

This chapter is focused on IZw18, which is identified as a BCD (e.g., Petrosian et al. 1996; Tikhonov 2007; Ramos et al. 2011) located approximately 18 Mpc away (Lebouteiller et al. 2017). IZw18 has attracted attention due to its extremely low metallicity in its ionized gas (12+log(O/H) = 7.11 aprox 3% solar; e.g., Kehrig et al. (2016)), which places IZw18 among the most metal-poor star-forming systems in the local Universe. Such low metallicity suggests the presence of chemically unevolved stellar populations and makes IZw18 one of the prime candidates for investigating galaxy formation and evolution processes happening in the primordial Universe.

IZw18 has a highly irregular morphology, a characteristic common among BCDs, which further enhances its scientific interest. While its morphology could be the result of recent starburst activity or interactions with other galaxies, the underlying mechanisms resposible for this remain a subject of active investigation (e.g., Legrand et al. 1997; Legrand 1999; Kehrig et al. 2015).

In terms of the kinematics of IZw18, the field has been a subject of diverse investigations that have enriched our understanding yet left many questions open. Early works (Petrosian et al. 1995, 1996) noted velocity dispersion values (~20 km s^{-1}) higher that expected from a self-gravitational model (Terlevich et al. 2015). Furthermore, it was found potential rotational motion in the neutral hydrogen component, leading to speculative theories about the existence of a dark matter Halo around the galaxy (van Zee et al. 1998). However, these are far from being the only intriguing features observed in IZw18.

A study employing long-slit echelle spectroscopy, specifically exploring the spatial changes in the Hα profile, scrutinized the ionized gas within IZw18 in great detail (Martin 1996). This investigation unveiled evidence for a supergiant shell, manifesting as a bipolar outflow in the south-west and north-east extensions of the galaxy, and expanding at speeds between 30 km s^{-1} and 60 km s^{-1}. However, a subsequent study by Petrosian et al. (1996) presents a contrasting view. It suggests that the perceived bipolar outflow might not be a singular, coherent structure but rather a conglomerate of clumpy HII regions. These regions, presumably powered by star formation, challenge the earlier interpretation of a supergiant shell, proposing a more fragmented and fractal star-forming environment within the galaxy.

In IZw18, disparities in gas kinematics are evident between Hα and HeII spectral lines. Notably, HeII lines show a redshift of about 30 km s^{-1} compared to Hα in regions with peak HeII emission (Vaught et al. 2021). This discrepancy, potentially linked to supernova remnants or young stellar clusters, suggests a complex and diverse kinematic structure within the galaxy.

IZw18 has been studied as part of a collective analysis of BCDs, as it exemplifies this class of galaxies, characterized by low metallicity (12+log(O/H) between 7.1 and 8.3), irregular and clumpy morphology, high star formation, compact structure, and significant gas richness (e.g., Thuan & Martin 1981; Pilyugin 1992; Izotov & Thuan 1999). These features, indicative of a young stellar population and ongoing star formation processes, offer insights into the early stages of galactic evolution in low mass environments. In addition, these galaxies often exhibit chaotic kinematics in HI, overlaying a disk rotation (Lelli et al. 2012). However, IZw18 stands out with its exceptionally low metallicity and high SFR, which ranges from 10^{-2} to 10^{-1} $M_\odot$ yr^{-1} kpc^{-2} as noted by Aloisi et al. (1999). This is significantly higher compared to the SFRs of irregular galaxies in the Local Group, which are typically in the range of 10^{-4} to 10^{-2} $M_\odot$ yr^{-1} kpc^{-2} (Aloisi et al. 1999). In a broader examination of XMPs (i.e. $Z < Z_\odot/10$), such as IZw18, recent studies like (e.g., Olmo-García et al. 2017; Isobe et al. 2023; Xu et al. 2023) have observed typical features like rotation in ionized gas, shell outflows, chemical inhomogeneity (although this has not been seen by Kehrig et al. (2016) in IZw18) and a high loading factor (over 10), indicative of substantial matter ejection relative to SFR. These findings underscore that XMPs are systems influenced by both inflow and outflow mechanisms. The extremely low metallicity in such galaxies could be attributed to the accretion of pristine gas, indeed driven by these inflows. Outflows are likely a result of intense stellar feedback, amplified by the low gravitational pull in these low mass galaxies (e.g., Amorín et al. 2012b; Bosch et al. 2019; Hogarth et al. 2020). This is evidenced by the broad components in the emission line profiles (Olmo-García et al. 2017).

The observational data presented here offer a unique opportunity to deepen our understanding of the ionized gas kinematics of IZw18. The data were obtained using MEGARA (Gil de Paz et al. 2016), an advanced integral field spectrograph capable of capturing detailed spectral data across a two-dimensional FoV with high spectral resolution.

By analysing the spectral data of the main body (MB) and two regions in the Halo of IZw18, this study seeks to generate a comprehensive kinematic portrait of this intriguing galaxy. This investigation constitutes a step forward in our understanding of the complex kinematics in dwarf galaxies, paving the way for future detailed studies on similar low mass starburst systems in the Universe.

The upcoming sections detail the observational strategy, the data reduction process, and the specific methodologies applied to obtain our results. Following these, there are dedicated sections where we present and discuss the results, culminating in a final section that outlines the conclusions drawn from our study.

4.2 Observations

The observational data for this study were acquired using MEGARA, situated at the Cassegrain focus of the 10.4 m GTC telescope at La Palma Observatory (Gil de Paz et al. 2016). The IFU of MEGARA, also known as the Large Compact Bundle (LCB), offers a FoV of 12.5 x 11.3 arcseconds, consisting of 567 hexagonal spaxels, each measuring 0.62 arcseconds. What sets MEGARA apart as a uniquely suitable instrument for this research is its capability to provide two-dimensional spectroscopic data with high spectral resolution. This enables unprecedented detailed two-dimensional kinematic studies of the ionized gas in IZw18, a level of analysis that has not been conducted before. Consequently, the configuration and capabilities of MEGARA make it an invaluable tool for in-depth examinations of individual regions within nearby galaxies.

Our observations focused on three distinct regions within the galaxy IZw18: the MB and two external regions corresponding to the north-east and south-west zones of the Halo (hereafter Halo NE and Halo SW) in the galaxy. Fig. 4.1 shows the MEGARA footprint overimposed on these three regions.

The data reduction process was performed using the MEGARA data reduction package (Pascual et al. 2019). This software pipeline allowed for sky and bias subtraction, flat-field correction, spectra tracing and extraction, correction of fiber and pixel transmission, and wavelength calibration. As the primary objective was a kinematic analysis, no flux calibration was applied. Thus, through this chapter, all luminosity values are in arbitrary units.

As for the specific settings of the MEGARA instrument during the observations, the LR-R Volume-Phased Holographic (VPH) was employed. This covered a spectral range of 6300 Å - 7363 Å with a spectral resolution of R $\sim$ 6000. For the Hα line at a wavelength of 6563 Å, this corresponds to a spectral resolution of approximately 1.09 Å. In terms of velocity, this spectral resolution is equivalent to approximately 50 km s^{-1}. In Table 4.1, we present the log of observations.

4.3 Main kinematical analysis

In this section we are presenting the main results of this study, which are the maps of luminosity, velocity and velocity dispersion based on the gaussian fit of the Hα profile. The methodology followed to construct these maps is also presented here.

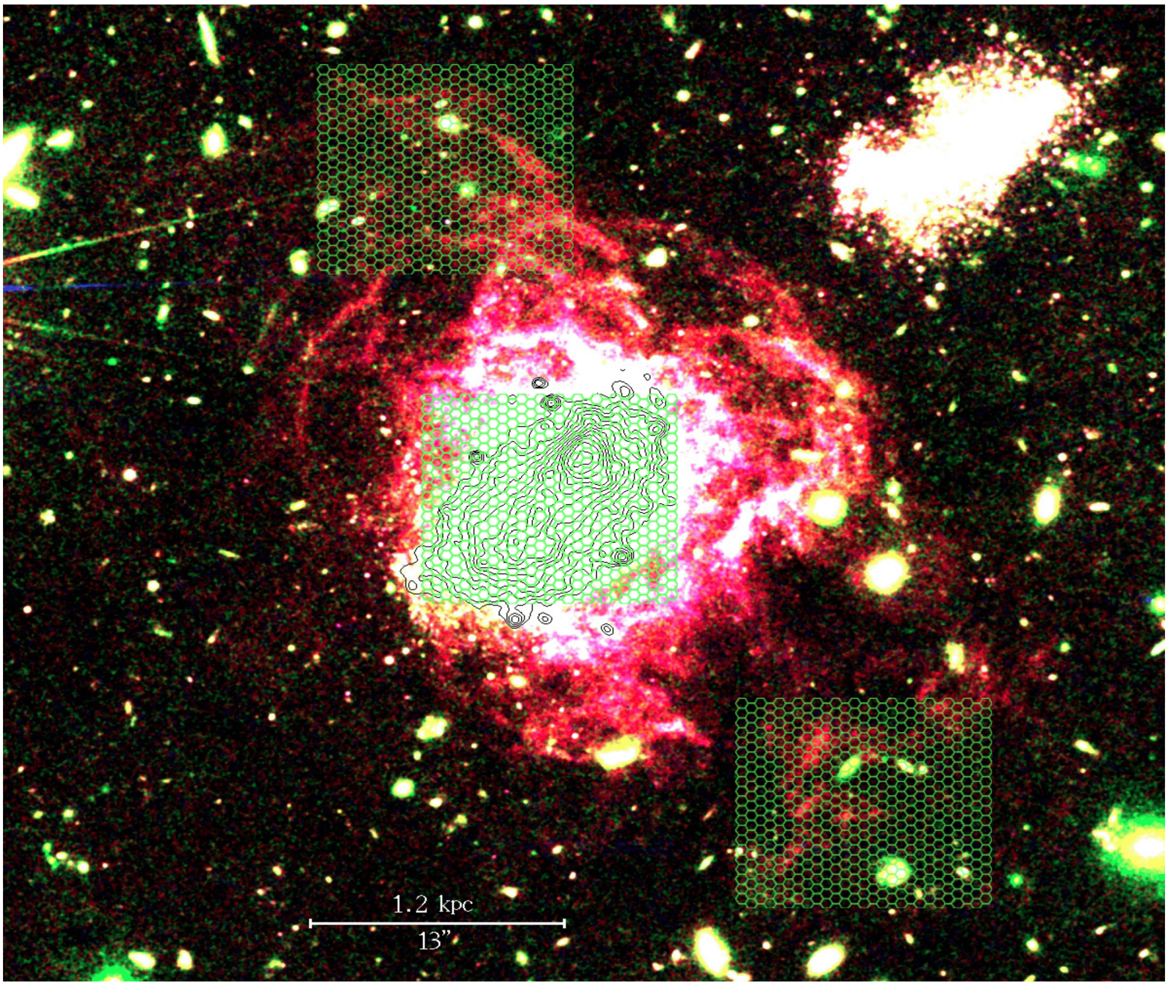

Figure 4.1 High contrast composite image of IZw18 using HST ACS R, I, and V bands shown in the red, green, and blue channels, respectively; isocontours delineate the central knots (adapted from Papaderos & Östlin (2012)). The three LCB pointings are shown. north is up, East is left here and in all subsequent figures.

4.3.1 Methodology

The data analysis for this study was executed on a total of six data cubes. These were categorized into two sets: the first set comprised three data cubes (one per pointing) with sky subtraction, while the second set corresponds to the same data cubes but for which no sky subtraction was performed.

In the initial phase of our analysis we observed that the center of the [OI] (note that as in the previous chapter we are referring to [OI]λ6300 Å) sky line presented spaxel to spaxel variations (up to 0.7 Å). This lead us to hypothesize that the wavelength calibration might not be entirely accurate, at least not to the precision we require for our kinematical analysis. Consequently, we decided to use the [OI] sky line as a reference point for calibrating the

Table 4.1 Log of the observations.

Pointing (1)	Exptime (s) (2)	R.A. (J2000.0) (3)	Dec (J2000.0) (4)	Date (5)
IZw18 MB	3 × 750	09:34:02.06	55:14:26.5	2022-02-06
IZw18 SW	3 × 1800	09:34:00.37	55:14:08.3	2022-02-08
IZw18 NE	3 × 1500	09:34:02.87	55:14:44.4	2022-02-07

Column (1): Name of each pointing in the observations of the galaxy. Column (2): Exposure time. First it is shown the number of pointings times the exposition time of each one. Columns (3) and (4): Position of the center of each pointing. Column (5): Date of observation.

velocity of the Hα line. For now, to determine the observed central wavelength of each line, we are employing a simple Gaussian fit to each spaxel. The central wavelength of the [OI] sky line and the Hα line as a function of space is represented in Figs 4.2 and 4.3.

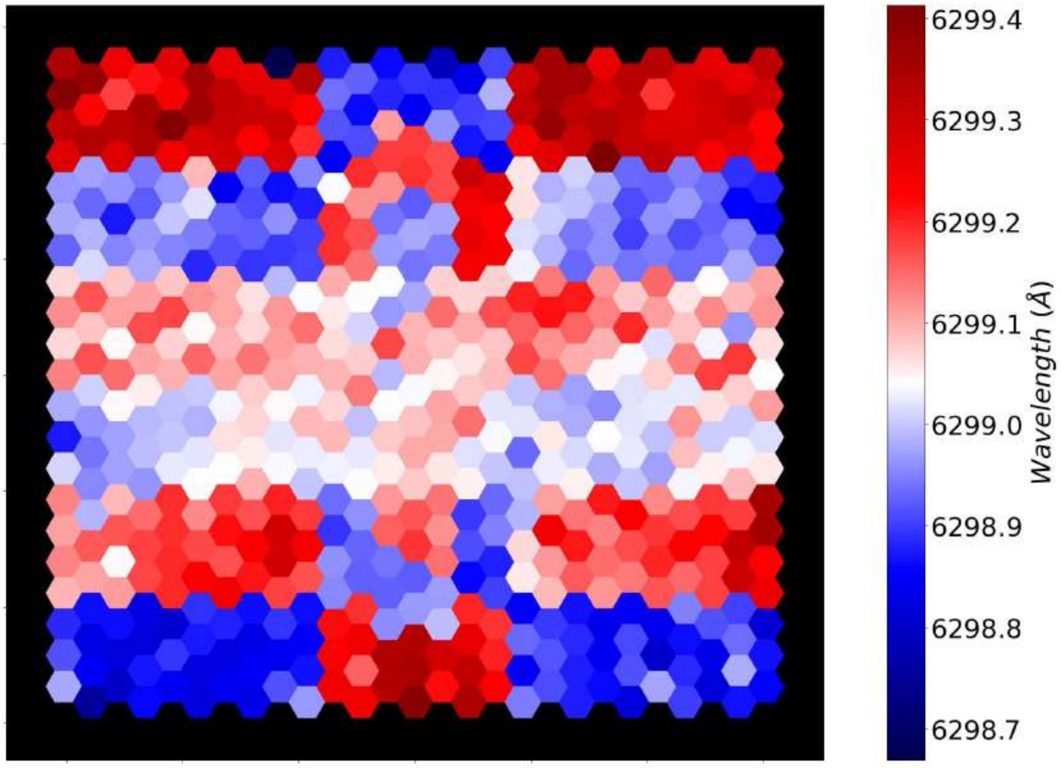

Figure 4.2 Observed wavelength field of the [OI] sky line in the MB after the standard wavelength calibration.

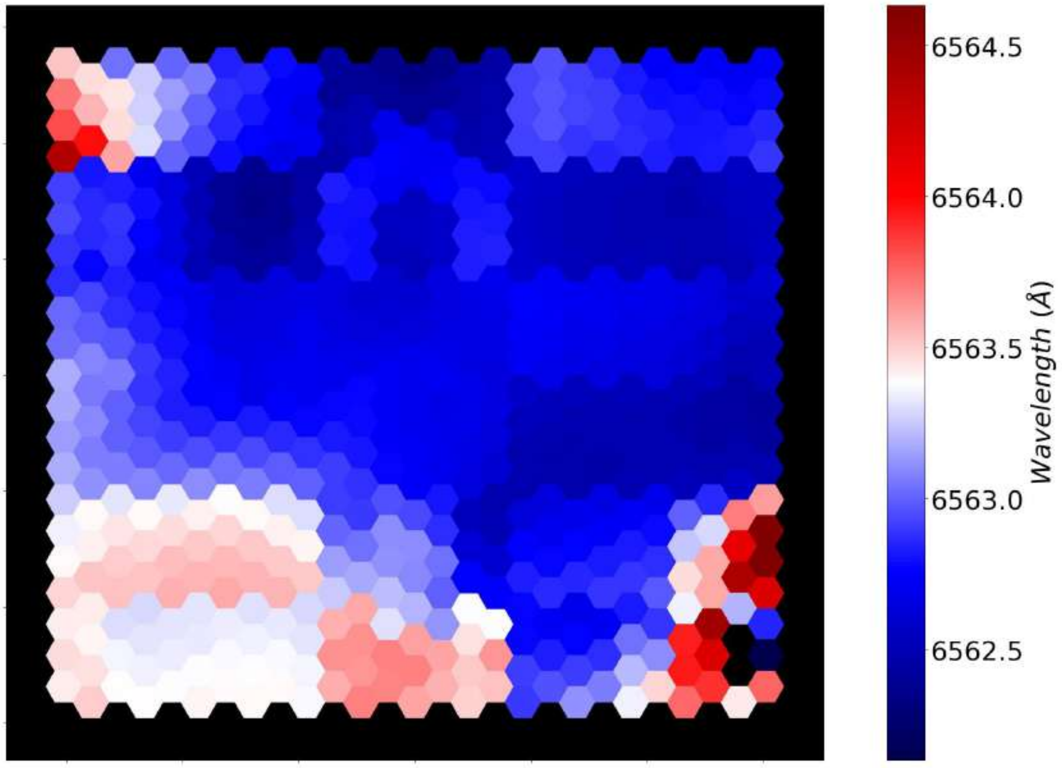

Figure 4.3 Observed wavelength field of the Hα line in the MB after the standard wavelength calibration.

Thus, we took the center of the [OI] sky line as our reference wavelength field. Then we derived the velocity field of the Hα line referenced to the [OI] sky line, which is shown in Fig. 4.4. Importantly, using this methodology, we ensured that any potential inaccuracies in the wavelength calibration were minimized. By referring the position of the Hα line to the sky line of [OI], we generated a more accurate wavelength field in Hα. This effectively neutralized any potential systemic shifts introduced by wavelength calibration uncertainties.

At this point, attention was shifted to the cubes with sky subtraction. The Hα line profiles were examined, and Gaussian fits were applied. Initially, we started with a single Gaussian fit to the Hα line profile in each spaxel. However, the observation of broader and more complex profiles in some spaxels led us to explore dual-component fitting. The Hα profile of one of these spaxels exhibits a distinctively broadened base with a wavelength shift (see Fig. 4.5), indicative of complex underlying kinematic processes. This spaxel is represented in Fig. 4.4 to verify its spatial position.

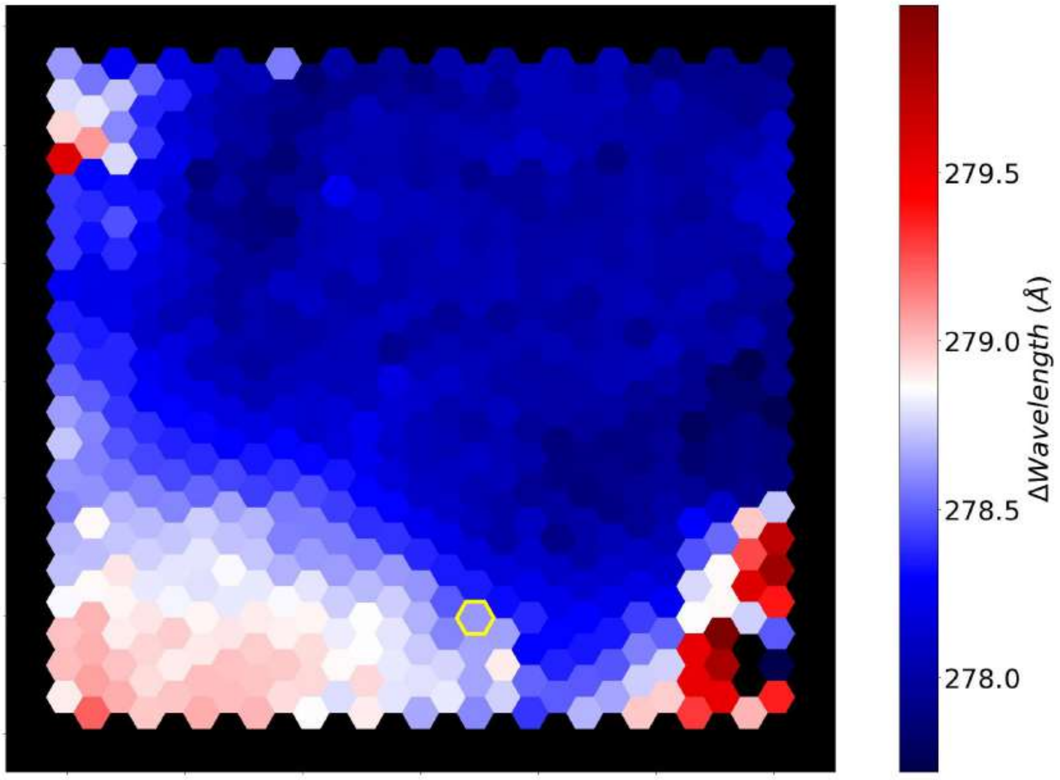

Figure 4.4 Wavelength field of the Hα line minus the wavelength field of the [OI] sky line in the MB. This corresponds to what we called the corrected wavelength field of the Hα line. The spectrum of the highlighted yellow spaxel is represented in Fig. 4.5.

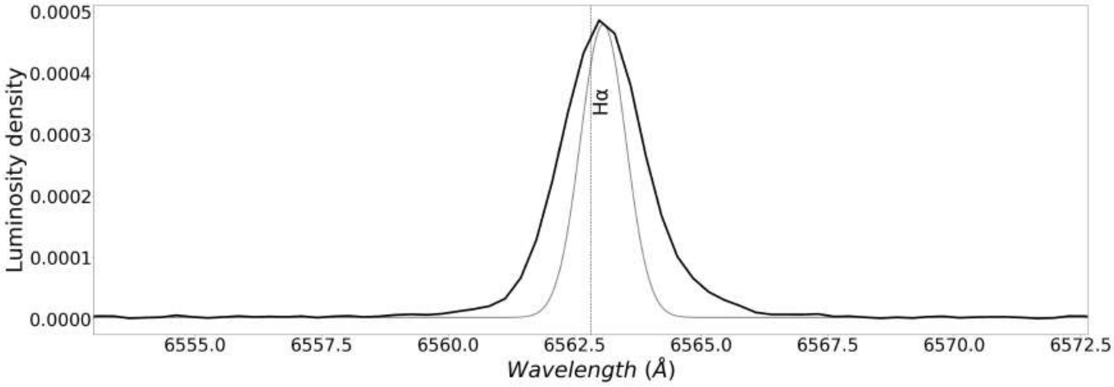

Figure 4.5 Hα profile of the spaxel highlihgted in Fig.4.4. Black line represents the Hα profile of a single spaxel. The gray line is a Gaussian with the instrumental FWHM. The vertical line highlights the Hα wavelength.

In this way, for each spaxel, both one- and two-component fits were performed, yielding line luminosity, velocity, and velocity dispersion from each Gaussian. Luminosity was calculated from the Gaussian area. To convert the wavelength field to a velocity field the longitudinal relativistic Doppler effect was used:

$$v = c\left(\frac{(\lambda/\lambda_0)^2 - 1}{(\lambda/\lambda_0)^2 + 1}\right) \tag{4.1}$$

where v is the velocity, c is the speed of light, λ is the observed wavelength, and λ_0 is the rest wavelength. This Doppler effect conversion was consistently applied in all subsequent velocity calculations.

In order to obtain the corrected velocity dispersion (σ), we took into account the instrumental and thermal widths ($\sigma_{\rm inst}$, $\sigma_{\rm thermal}$). The correction was performed as follows:

$$\sigma^2 = \sigma^2_{\rm obs} - (\sigma^2_{\rm inst} + \sigma_{\rm thermal}) \tag{4.2}$$

The instrumental width was calculated from the width of the [OI] sky line ($\sigma_{\rm inst}$=0.45 Å). Meanwhile, $\sigma_{\rm thermal}$ was calculated by using the Maxwell-Boltzmann distribution:

$$\sigma^2_{\rm thermal} = \frac{KT_e}{m} \tag{4.3}$$

where K is the Boltzmann constant, T_e the electronic temperature retrieved from Kehrig et al. (2016) (with a value of 20,600 K) and m is the hydrogen mass.

In addition to instrumental and thermal widths, we could consider the effects of fine structure and natural broadening ($\sigma_{\rm fs}$ and $\sigma_{\rm natural}$). Fine structure, leads to a subdivision of emission lines that can be interpreted as a broadening. The $\sigma_{\rm fs}$ is only well characterised for atoms with one electron and is usually around 2-3 km s^{-1} (e.g., García-Díaz et al. 2008) so for our spectral resolution we can ignore this effect. Natural broadening, governed by the Heisenberg uncertainty principle ($\Delta E \cdot \Delta t \geq h/4\pi$) in our case is minimal. Lifetimes of excited states of the H atom are about 10 nanoseconds, leading to a natural linewidth broadening of only a few m s^{-1}, which is significantly smaller than other broadening mechanisms encountered in most astrophysical observations.

In our one-component fit analysis, certain spaxels are excluded to maintain data integrity. This exclusion is based on three criteria: spaxels where the FWHM of the Hα line is narrower than the instrumental FWHM, discrepancies between the Hα and Hβ line profiles, and a Signal/Noise ratio below 3, where Signal represents the peak flux of the Hα line and Noise denotes the standard deviation of the continuum beneath the line. Those spaxels were tacked away from the representation of the luminosity, velocity and the velocity dispersion maps. In the two-component fitting process, we applied two extra conditions. One crucial condition was using the AIC. If any Hα profile (at a particular spaxel) was better fitted by the single-component fit as indicated by a lower AIC value, it was excluded from the dual-component analysis. Additionally, any Gaussian with an amplitude less than 2.5 times the standard deviation of the continuum was disregarded in the two-component fit.

Due to the high precision required for the two-component fits, all the data cubes were spatially smoothed prior to the fitting process using a Gaussian kernel with a FWHM of 1.4”. This specific choice of FWHM was arrived after exploring several kernel sizes, aiming to optimize the trade-off between enhancing coherence among adjacent spaxels and minimizing the loss of spatial resolution. The smoothing process, therefore, not only improved the coherence between adjacent spaxels but did so while carefully considering the inevitable compromise in spatial resolution. In Ebeling et al. (2006) it is shown the high utility of using gaussian kernels for smoothing astronomical images.

Finally, it was necessary to distinguish between the primary and secondary components of each dual-component fit. This distinction was made using two criteria: the residual area after subtracting the two Gaussians of the dual fit from the single-component Gaussian, and the absolute velocity difference between each of the dual component velocities and the single component velocity.

For the velocity difference criterion, we defined the velocity of the single-component fit as v_{single}, and the velocities of the two components of the dual fit as $v_{1,\mathrm{dual}}$ and $v_{2,\mathrm{dual}}$. Then, we computed the absolute velocity differences, $|v_{\mathrm{single}} - v_{1,\mathrm{dual}}|$ and $|v_{\mathrm{single}} - v_{2,\mathrm{dual}}|$. The component from the dual fit with the smallest absolute velocity difference was identified as the primary component, thus ensuring that the primary component velocity was as similar as possible to the single component velocity.

For the residual area criterion, we compared the residual areas, where $G_{\mathrm{single}}(\lambda)$ represents the Gaussian fit for the single-component model, and $G_{1,\mathrm{dual}}(\lambda)$ and $G_{2,\mathrm{dual}}(\lambda)$ are the Gaussian fits for the first and second components of the dual fit, respectively. These residual areas are defined as $A_{\mathrm{residual}_1} = \int |G_{\mathrm{single}}(\lambda) - G_{1,\mathrm{dual}}(\lambda)| d\lambda$ and $A_{\mathrm{residual}_2} = \int |G_{\mathrm{single}}(\lambda) - G_{2,\mathrm{dual}}(\lambda)| d\lambda$. The component with the lower residual area, more closely aligning with the single-component fit, was designated as the primary component.

As a final remark, every calculation of the velocity is relative to the velocity of the center of mass of the ionized gas emitting Hα. Since the mass of gas is proportional to the luminosity, we can set the velocity of the center of mass as the zero velocity.

4.3.2 Luminosity, velocity and velocity dispersion maps

The result of this methodical process was a comprehensive suite of nine maps including each of the three pointings: MB, Halo SW and Halo NE. Each one displaying luminosity, velocity, or velocity dispersion of the Hα line for the three different components (the two components of the dual-fit and the one in the single-fit).

The maps are designed to offer a holistic yet detailed view of the different regions of the galaxy. Each map features a background layer sourced from deep HST observations, which cover a wide field of view to capture the galaxy in its entirety. This panoramic backdrop serves to contextualize the more targeted data overlays from the MEGARA/GTC observations. Specifically, three distinct overlays are superimposed on the HST background in each map, each corresponding to one of the observed regions of the galaxy: the MB, the Halo SW, and the Halo NE.

Single-componnent

We begin our exploration with the maps derived from a single-component Gaussian fit. Initially, attention is drawn to the luminosity map, depicted in Fig. 4.6, which delineates the distribution of Hα luminosity across the different regions of the galaxy IZw18. The Hα luminosity distribution serves as a bedrock for comprehending the structure of the ionized gas within the galaxy. The luminosity map of the IZw18 MB distinguishes three main features which are pretty well known: two star-forming knots, one situated in the south and the other in the north, and an arc-like structure ('plume') which has one end rooted in the vicinity of the north knot (e.g., Davidson et al. 1989; Dufour & Hester 1990; Dufour et al. 1996; Vílchez & Iglesias-Páramo 1998; Papaderos & Östlin 2012; Kehrig et al. 2016). These features underscore the known morphology of IZw18, presenting a lucid portrayal of the distribution and nature of ionized gas, which is particularly insightful for the kinematic study being undertaken. When focusing on the two Halos, it is apparent from the luminosity map that their luminosity is significantly diminished compared to that of the MB (around 2 orders of magnitude). Moreover, these maps also trace the outer shells of IZw18, as we can see comparing with the background HST image, thereby providing a nuanced understanding of the ionized gas distribution and its overarching structure.

Following the examination of the luminosity map, the focus transitions to the velocity map illustrated in Fig. 4.7. This map emerges as an indispensable tool for unraveling the kinematic behavior of the ionized gas within IZw18, offering insights into the internal motion within both the MB and the Halos, and unearthing patterns and flows that are pivotal to understand the dynamical state of the galaxy.

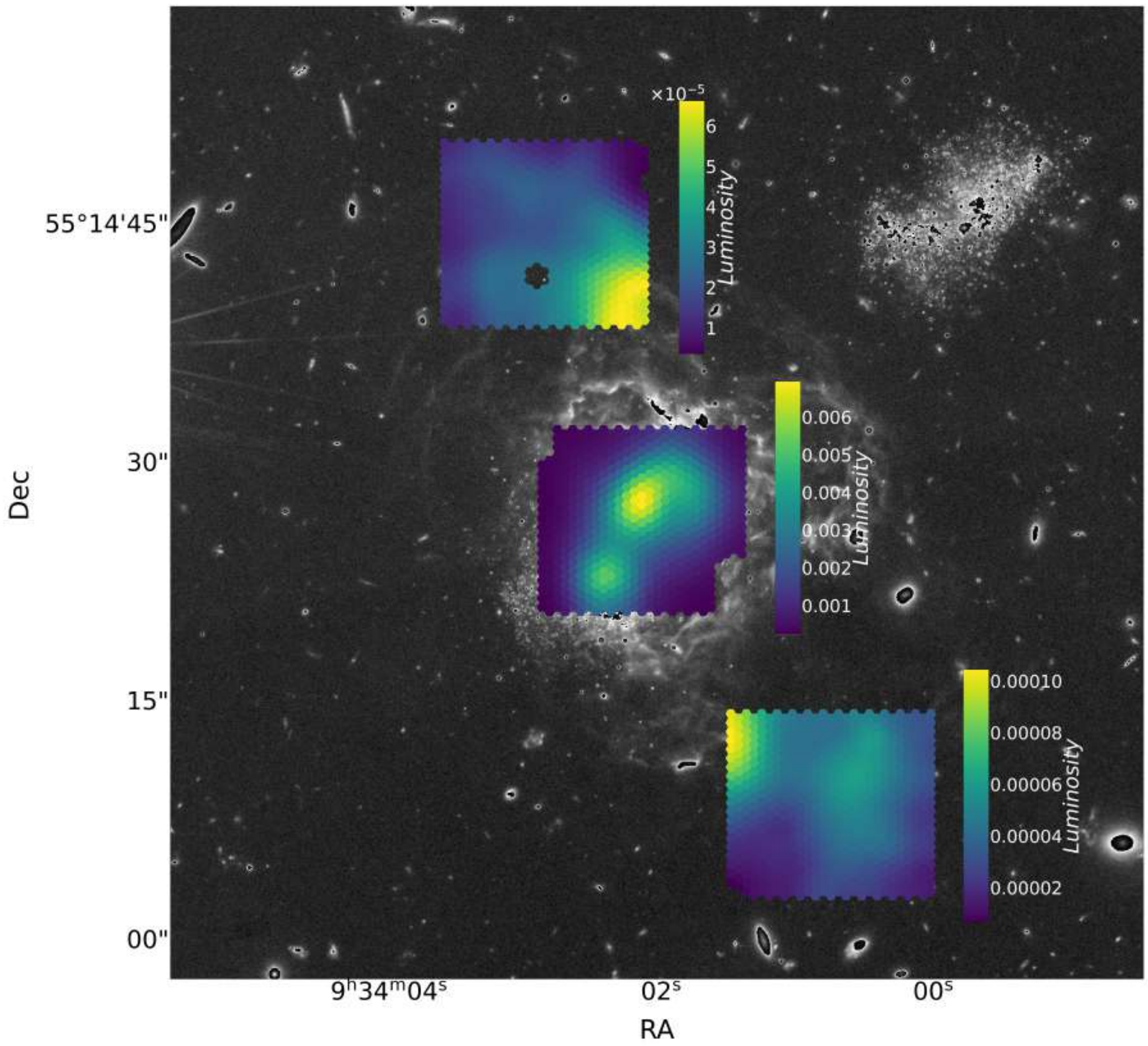

Figure 4.6 Hα luminosity maps for the MB and Halos obtained from the single-component fit. The background layer, presented in a cyclical gray scale, represents the wide-field deep image from the HST using the f814w and f606w filters of the WFC2 instrument. This background is used in all the images of IZw18 where the MB and both Halos are represented.

Within the MB, the velocity map distinctly unveils a rotation pattern between the two central knots, harmonizing with findings from several studies that have explored such kinematics in Hα and HI using the 21 cm line (Petrosian et al. 1996; van Zee et al. 1998; Lelli et al. 2012; Vaught et al. 2021; Isobe et al. 2023; Xu et al. 2023). Notably, this rotational feature seems to dissipate towards the north-east and south-west peaks of the MB map, where a shift towards redder velocities (i.e., positive velocities or gas moving away from us) is observed, indicative of outward or recessionary motion.

Transitioning to the Halos, the velocity maps presented herein are pioneering, unveiling for the first time the kinematics of ionized gas in these outer realms of IZw18 and tracing the movement of the shells enveloping the galaxy. Previous studies (e.g., Vaught et al. 2021) studied the kinematics of the Hα line up to ~ 0.75 kpc from the center of the galaxy. In our study we observe these two regions of the Halo up to 3 kpc away from the center. Particularly in the Halo NE, a relatively uniform map is observed, with velocities leaning towards the blue albeit with some velocity gradients present. Conversely, the Halo SW exhibits a more complex kinematic structure, with gas manifesting a large scale turbulent motion, possibly hinting at underlying dynamical processes or interactions occurring within this region.

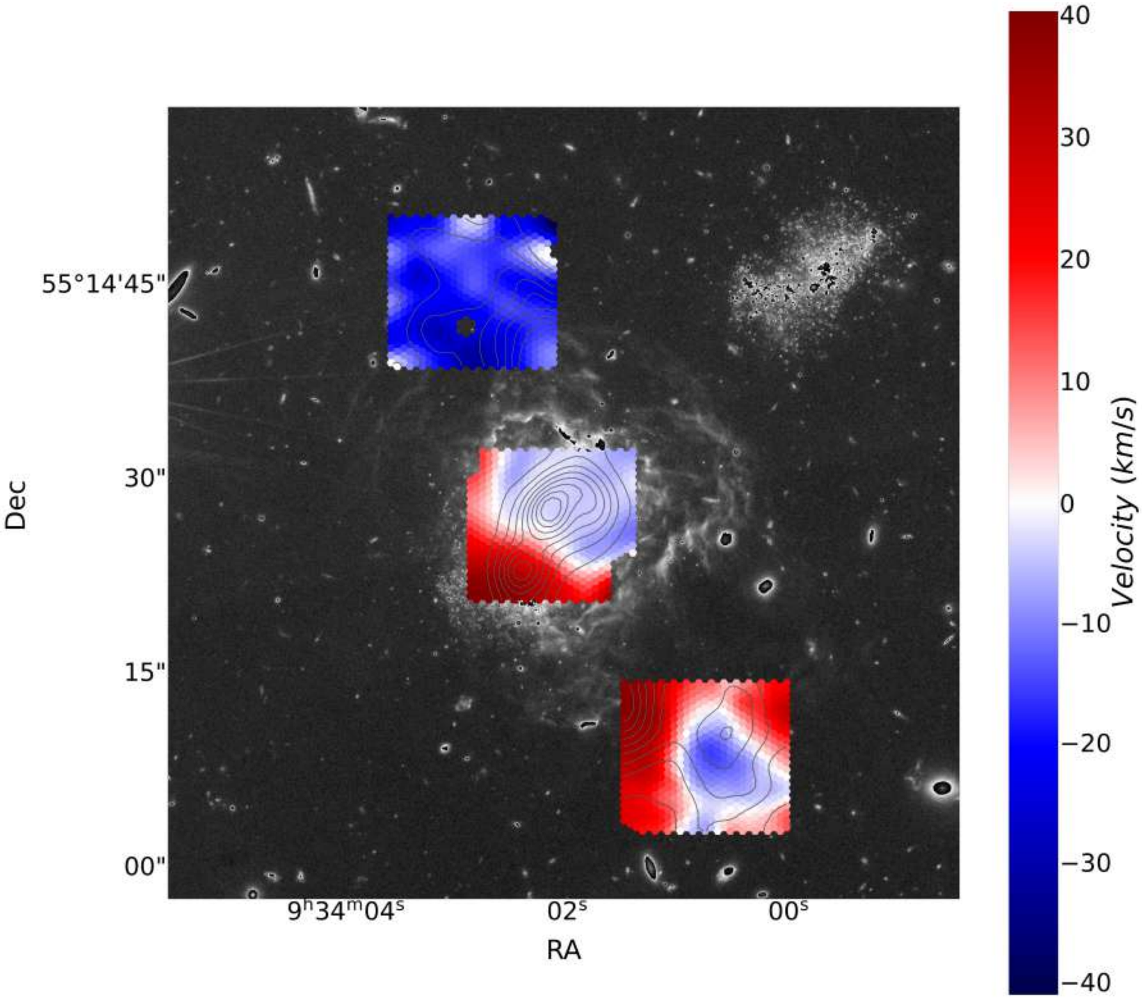

Figure 4.7 Hα velocity maps for the MB and Halos obtained from the single-component fit. The contours correspond to the Hα luminosity in log scale obtained from the same fit component. The same contours are represented in all Hα velocity and velocity dispersion maps.

Wrapping up our exploration of single-component maps, the velocity dispersion maps depicted in Fig. 4.8 merits a close examination. This map elucidates the spectrum of velocities inherent within each region, serving as a discerning gauge of areas of dynamic stability or potential turbulence.

A foundational aspect to consider is the theoretical velocity dispersion IZw18 would exhibit if the gas in the galaxy adheres to the virial theorem, as delineated in Terlevich et al. (2015). We retrieved the Hβ integrated luminosity from the Hβ flux (1.59×10^{-13} erg s^{-1} cm^{-2}) in Kehrig et al. (2016) and the distance (18.2 Mpc) in Aloisi et al. (2007). From this Hβ luminosity (6.3×10^{39} erg s^{-1}) we conclude according to Terlevich et al. (2015) that if the observed velocity dispersion surpasses the threshold of $\sim$ 20 km s^{-1}, it signifies the presence of another process (beyond the natural random motion induced by gravitational interaction) that escalates the kinetic energy of the gas, thereby augmenting the velocity dispersion.

In scrutinizing the map, it is notable that a majority of the regions encompassing the MB and the Halo NE exhibit velocity dispersions $<$ 25 km s^{-1}. This suggests that, broadly, these velocity dispersions could predominantly be attributed to the virial motion of the gas. However, within the MB, particularly in the top-left and bottom-right corners (see again Fig. 4.8), velocity dispersions surge to up to 40 km s^{-1}. This escalation hints at broadening or added complexity in the Hα profile in these regions. Regarding the Halos, the Halo NE presents a pretty mild velocity dispersion which do not go above 35 km s^{-1} indicating that there is not much turbulent motion in this region. The Halo SW nevertheless presents the higher value going up to 55 km s^{-1} in most regions where the velocity is zero (see regions with white velocity according to the colorbar in Fig. 4.7 and zones with brown to white velocity dispersion in Fig. 4.8).

The corresponding one-component fit of the spectrum shown in Fig. 4.5 is represented in Fig. 4.9. As we can see, this simple fit does not capture all the complexities inherent in the observed line profile, which exhibits broadening in the base. Regions where the single-component fit shows high velocity dispersions are often indicative of a more complex or broad Hα line profile.

Double-componnent

In contrast, a double-component Gaussian fit, applied to the same spectrum, provides a more nuanced and accurate representation (see Fig. 4.10). The small, broad Gaussian component successfully fits the broadening in the base of the profile, thereby resolving the complexity in the profile. This dual-component approach proves particularly valuable in regions where the velocity dispersion is high, as it disentangles the overlapping velocity structures and offers a clearer understanding of the internal dynamics of the galaxy.

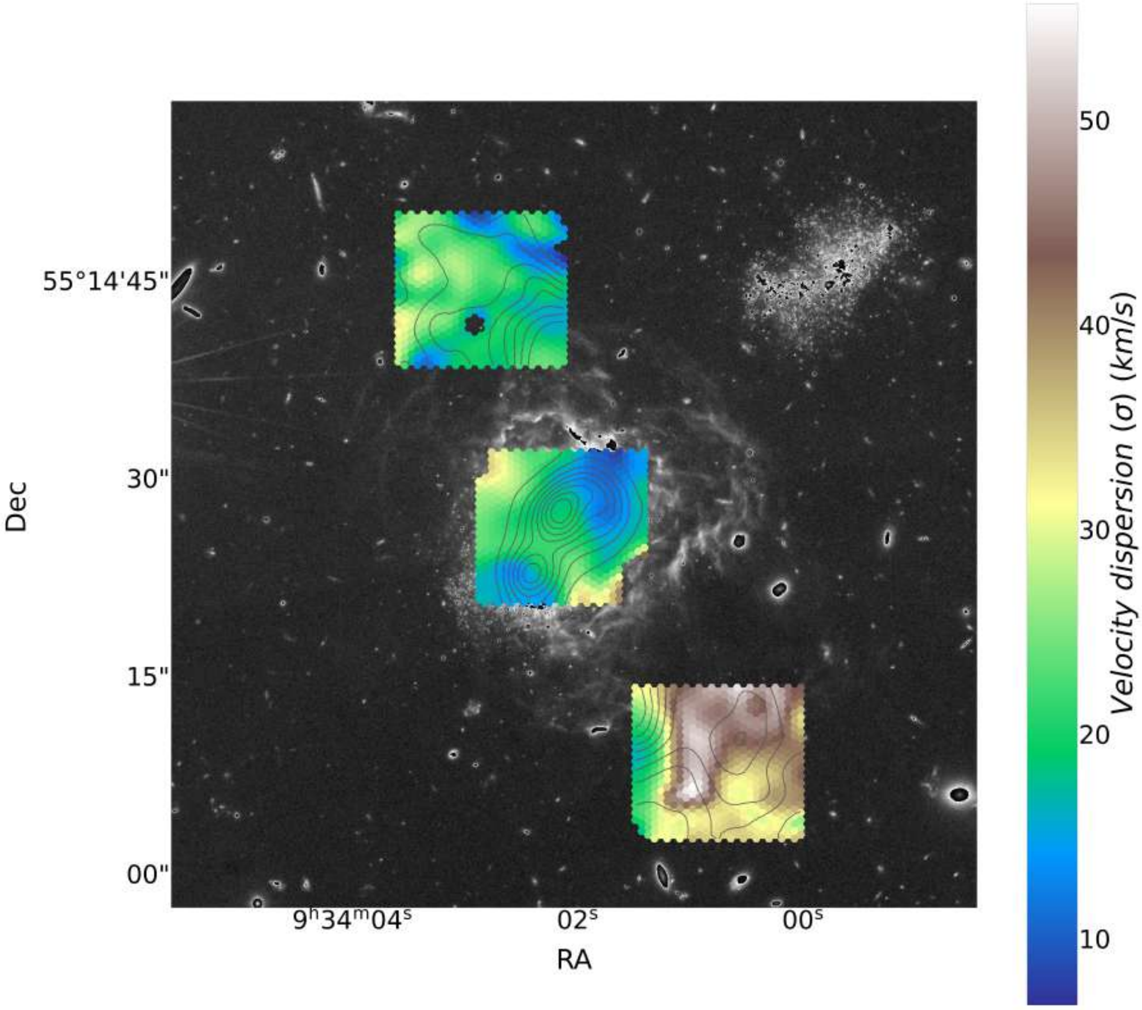

Figure 4.8 Hα velocity dispersion maps for the MB and Halos obtained from the single-component fit.

Expanding our discussion to encompass the double-component Gaussian fits, we simultaneously examine both the principal and secondary components. In doing so, we aim to provide a more comprehensive understanding of the intricate dynamics at play within the different regions of the galaxy.

We initiate our discussion with the Hα luminosity maps, depicted in Figs. 4.11 and 4.12 for the principal and secondary components, respectively. It is noteworthy that the sum of the luminosities from the principal and secondary components in each spaxel closely approximates the luminosity captured by the single-component fits. This indicates a high degree of correspondence between the two approaches, yet with the double-component fit offering a more nuanced view. The principal component is typically more luminous compared to the secondary component (typically 4 times more in the MB, 2 times more in the Halo

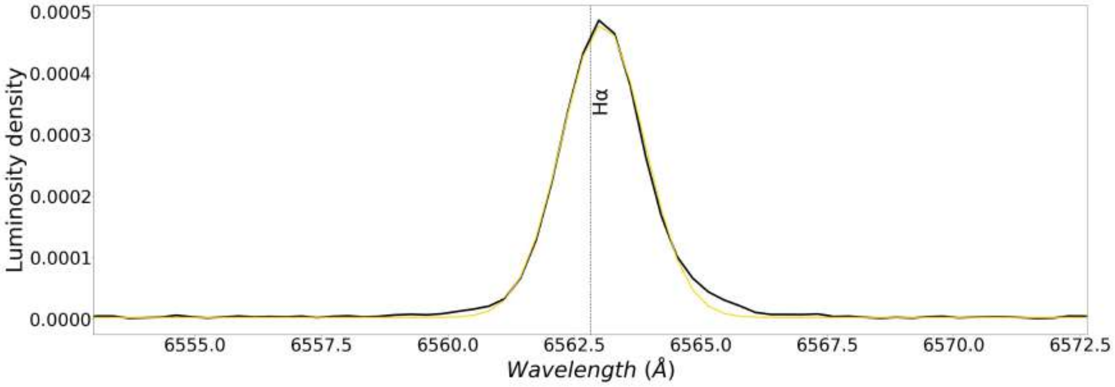

Figure 4.9 One-component fit of a Hα profile of a single spaxel in the south-west of the MB (same spaxel as in Fig. 4.5) of the galaxy. The profile is depicted in black, meanwhile the one-component fit is represented in yellow.

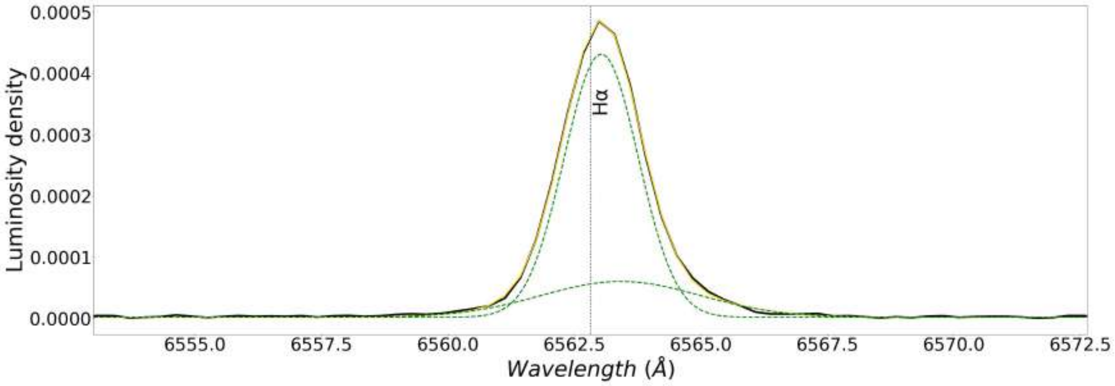

Figure 4.10 Double-component fit of a Hα profile of a single spaxel in the south-west of the MB (same spaxel as in Fig. 4.5) of the galaxy. The profile is depicted in black, meanwhile the double-component fit is represented in yellow. The green lines represent each of the gaussian corresponding to the double-component fit.

NE and similar in the Halo SW), fitting well with the two knots in the MB of the galaxy. Meanwhile, the secondary component appears to trace the plume of the galaxy.

Transitioning to the Hα velocity, the maps presented in Figs. 4.13 and 4.14 elucidate the internal kinematics of the ionized gas in IZw18. Remarkably, the velocity map of the principal component bears a close resemblance to that of the single-component fit, both exhibiting patterns indicative of rotation. This similarity is especially pronounced in regions where the single-component velocity dispersion is low (<25 km s^{-1}), suggesting that the Hα profile is less complex and that the single-component fit is sufficiently accurate in those areas. However, this is not the case for the Halo SW, where the velocity of the principal component

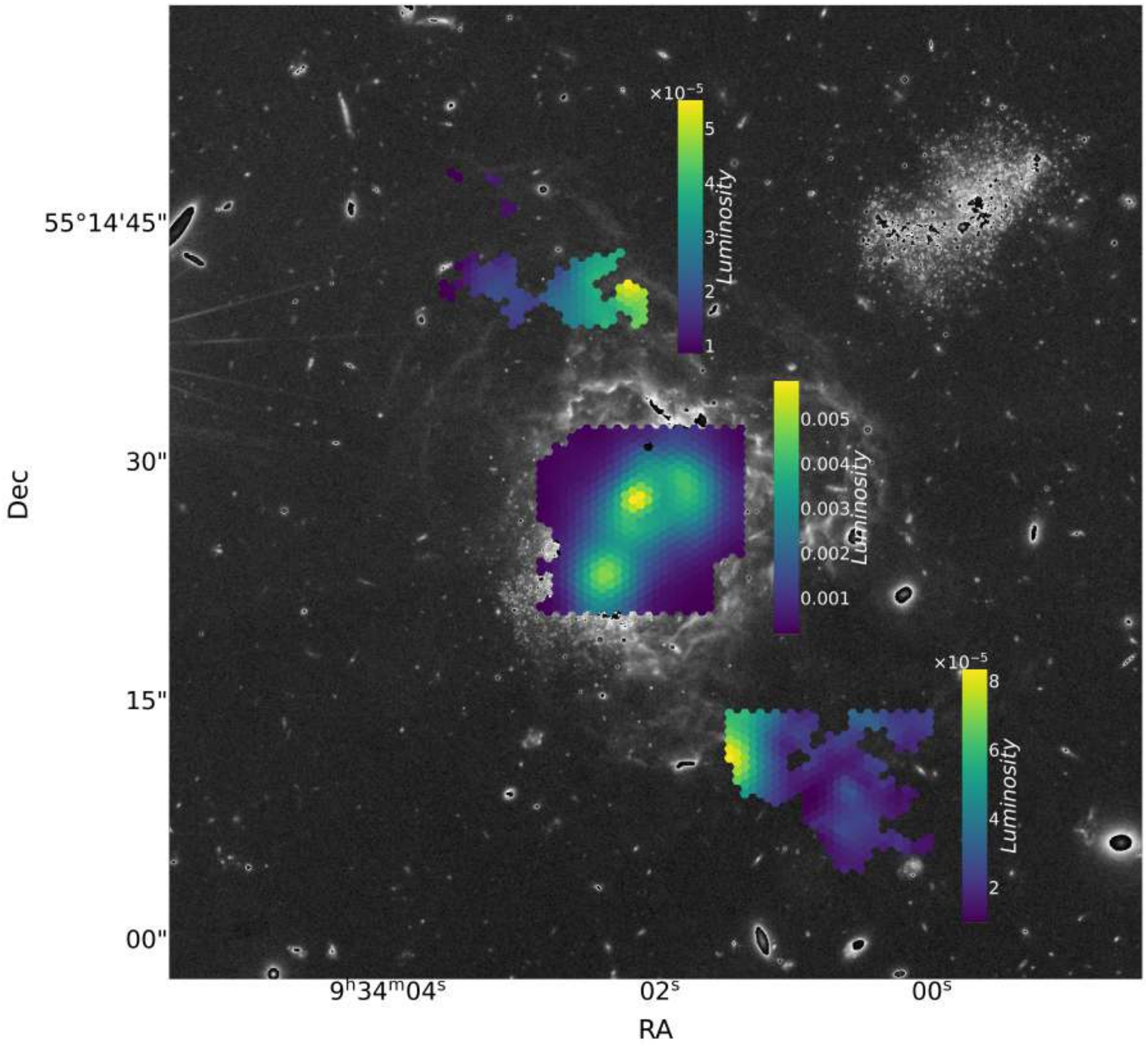

Figure 4.11 Hα luminosity maps for the MB and Halos corresponding to the principal double-component fit.

divides this region into two distinct zones, north and south, with markedly different velocities. The transition between these zones is abrupt, indicating a significant variation in the kinematic properties of the Halo SW.

The secondary component presents a significantly different picture. Its velocity range is more extensive than that of the principal component (principal component goes from -40 km s^{-1} to 55 km s^{-1}, secondary instead goes from -55 km s^{-1} to 80 km s^{-1}), possibly pointing to higher velocities in more subtle areas of the galaxy. The shape and distribution of velocities in this secondary component are also more challenging to interpret. While the principal component largely aligns with previously studied HI gas rotations (e.g., Lelli et al. 2012), the

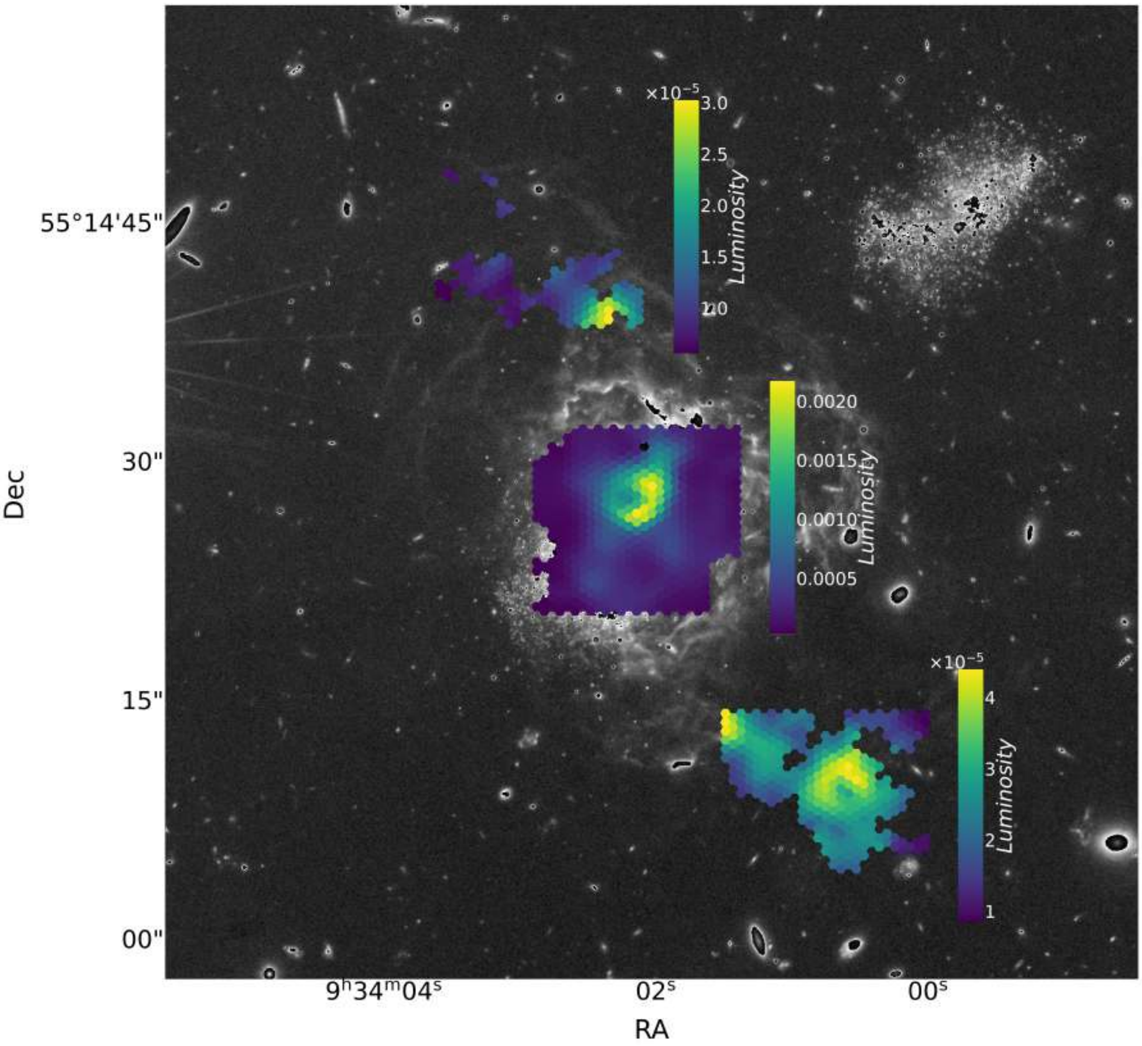

Figure 4.12 Hα luminosity maps for the MB and Halos corresponding to the secondary double-component fit.

secondary component could either be tracing different gases in different regions or potentially be indicative of large-scale turbulent motions within the galaxy.

Lastly, we explore the Hα velocity dispersion maps for both components, as shown in Figs. 4.15 and 4.16. The velocity dispersion in the principal component closely resembles that of the single-component fit, particularly in regions where both are low (<25 km s^{-1}). Notably, in areas where the single-component dispersion is high (>25 km s^{-1}), the principal component often shows a lower dispersion value, hinting at the limitations of the single-component approach in capturing the full dynamical complexity.

The secondary component, on the other hand, presents a markedly different scenario. Its velocity dispersion values are up to more than five times greater than those retrieved

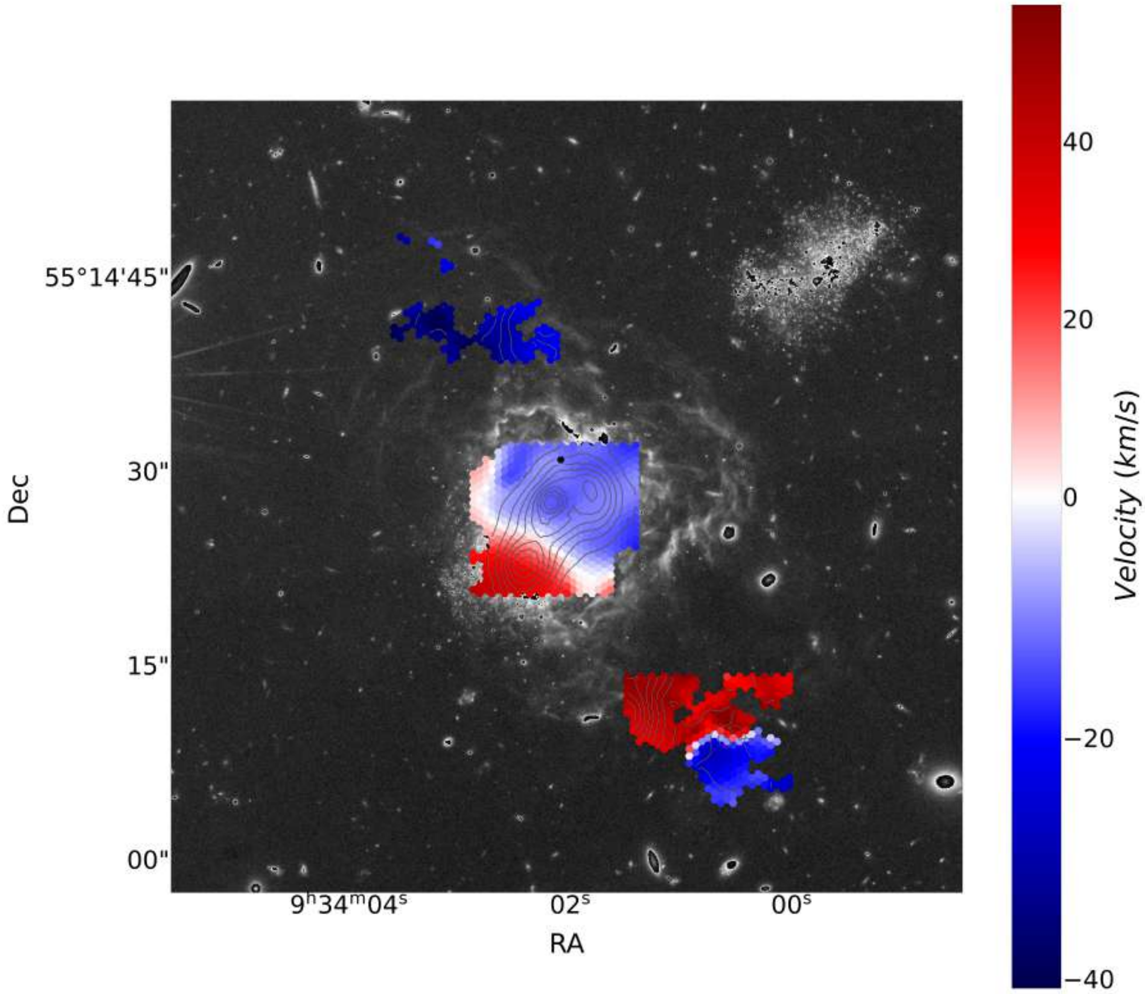

Figure 4.13 Hα velocity maps for the MB and Halos corresponding to the principal double-component fit.

from either the single or principal components, underscoring the presence of high turbulence and or kinematical complexity in more nuanced regions of the galaxy. Most strikingly, the eastern (and with less relevance also the western) part of the MB exhibits velocity dispersions reaching up to 225 km s^{-1}, potentially tracing underlying outflows in this particular zone of IZw18. A 3D representation of all this kinematical features of the observed regions of IZw18 can be seen in Appendix C.1.

4.3.3 Luminosity weighted velocity

In this section, we delve into the analysis of the kinematics of IZw18 through luminosity-weighted histograms for velocity and velocity dispersion, based on the maps discussed in

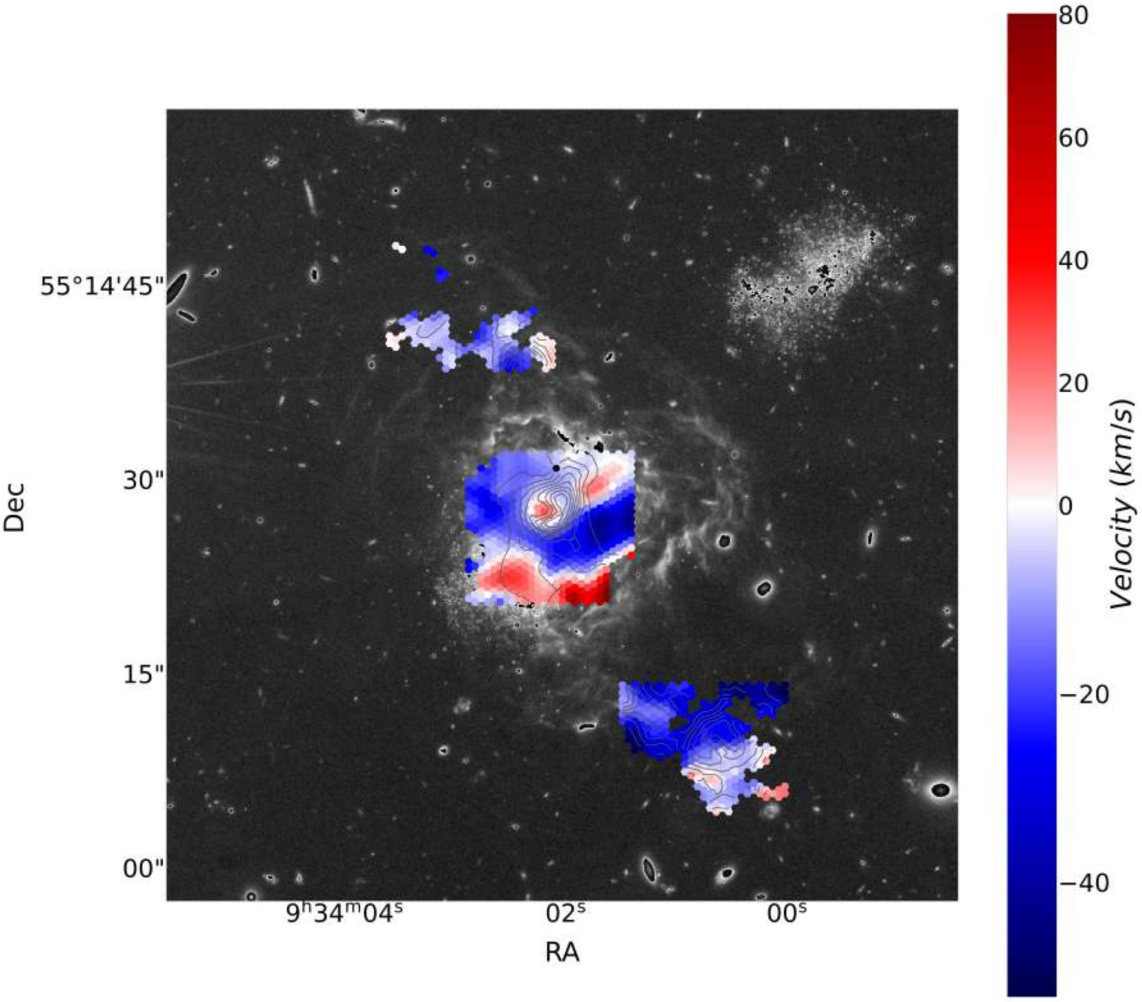

Figure 4.14 Hα velocity maps for the MB and Halos corresponding to the secondary double-component fit.

section 4.3.2. The core of this approach lies in weighting the velocity and velocity dispersion values by the luminosity associated with each spaxel, which is derived from the Hα emission line. This luminosity is directly proportional to the number of ionized hydrogen atoms, and thus to the mass of ionized gas, providing a mass-weighted perspective of the kinematic properties. By employing this method, we aim to emphasize the contributions from regions with higher mass concentrations, offering a more nuanced understanding of the dynamic behavior of the galaxy.

To construct the velocity histograms, we start by establishing the range of velocities, defined by the maximum and minimum values observed in the velocity map. This range is then divided into uniformly sized bins. For each bin, we aggregate the luminosities of all spaxels whose velocities fall within the range of the bin, effectively creating a sum of

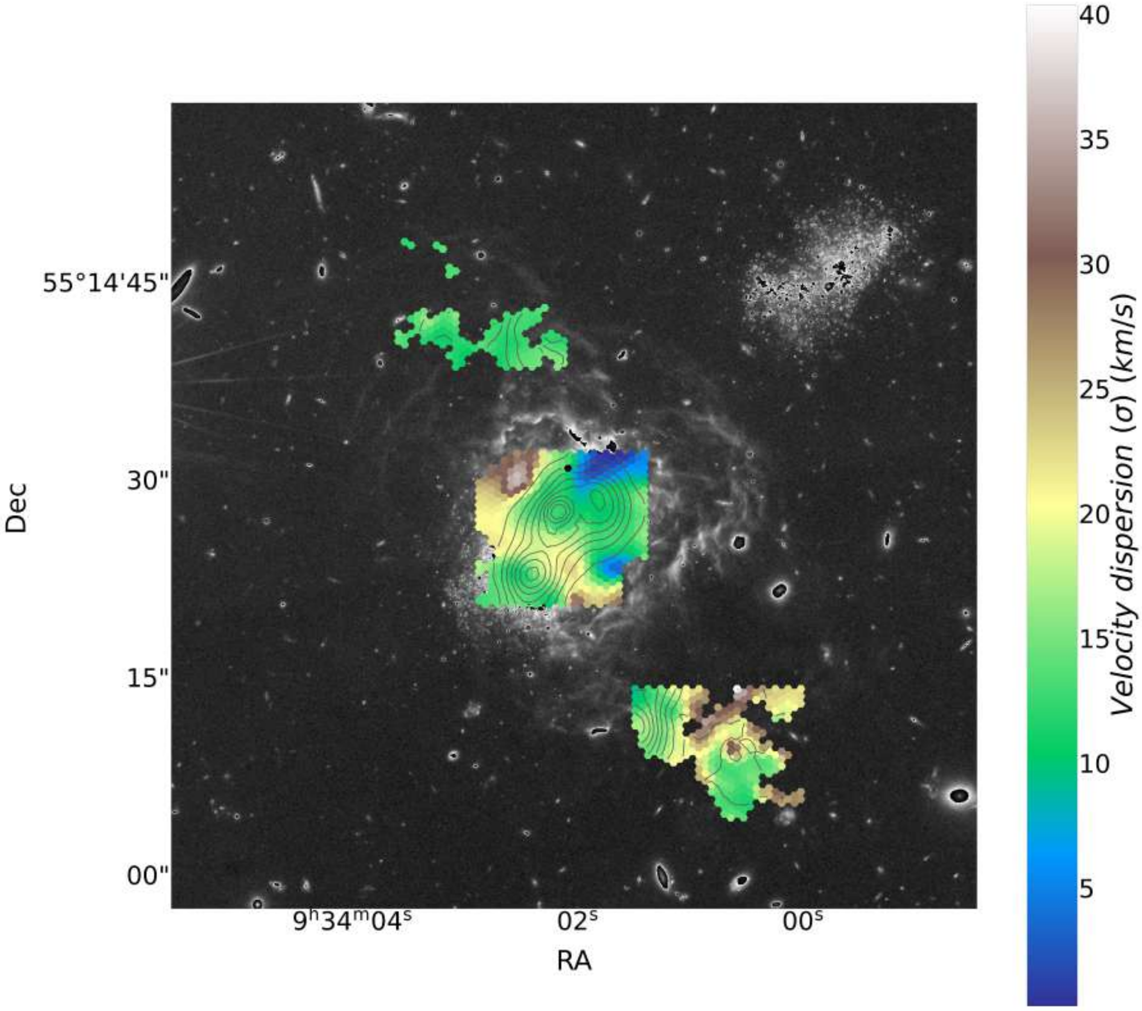

Figure 4.15 Hα velocity dispersion maps for the MB and Halos corresponding to the principal double-component fit.

luminosities that represent the mass of ionized gas moving at those velocities. Normalizing these sums by the total luminosity of all spaxels yields the luminosity-weighted velocity histogram. A peak in this histogram indicates a predominant velocity at which a significant mass of ionized gas is moving, providing insight into the dominant kinematic flows of the galaxy.

Similarly, the velocity dispersion histograms are constructed using the same luminosity-weighting approach, allowing us to assess the spread of velocities around the mean motion in a mass-weighted manner. This method enriches our understanding of the internal motions within the ionized gas, revealing the complexities of its dynamics and the forces at play.

Starting with the MB of IZw18 in Fig. 4.17, we present the constructed histograms, elucidating the distributions of velocity and velocity dispersion, each weighted by luminosity.

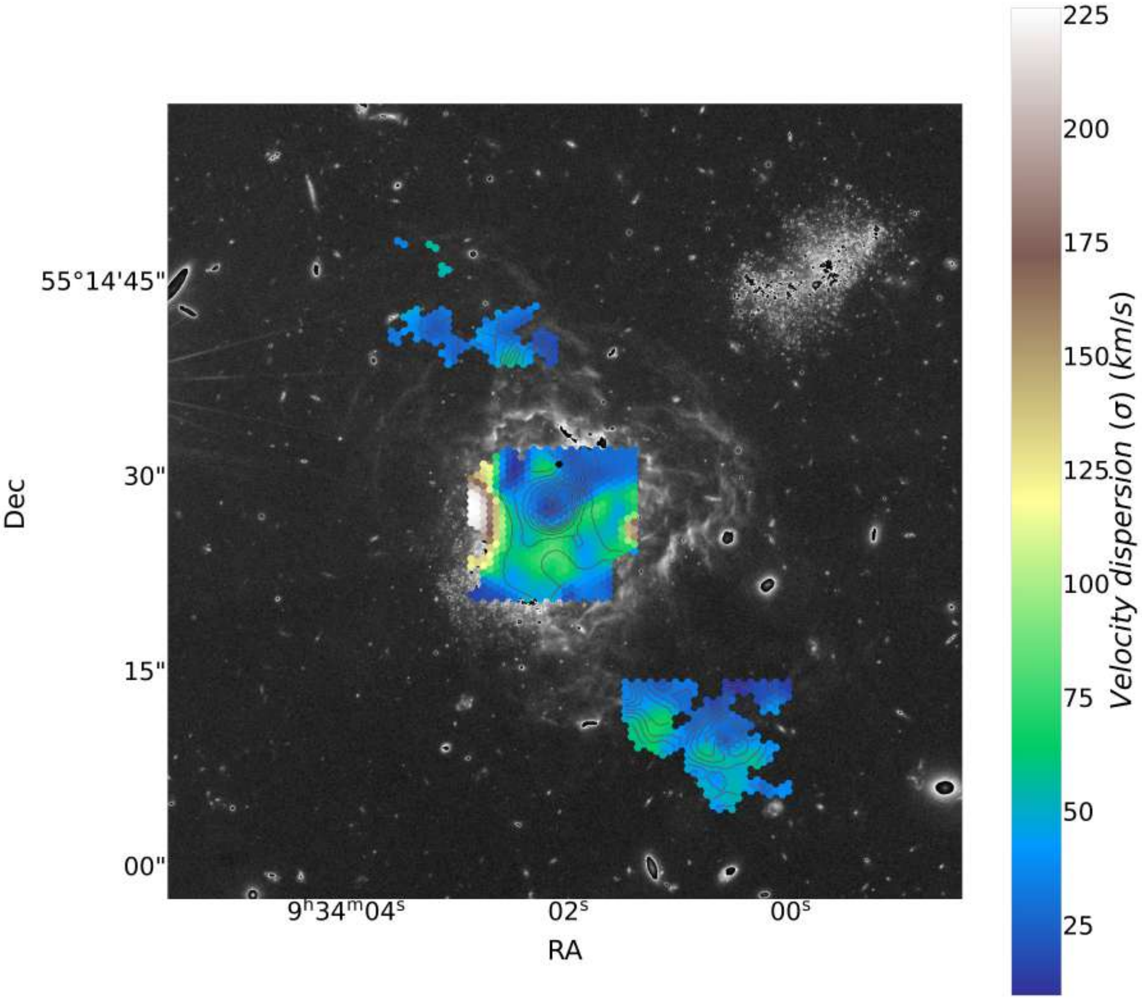

Figure 4.16 Hα velocity dispersion maps for the MB and Halos corresponding to the secondary double-component fit.

The top-left histogram in Fig. 4.17 delineates the luminosity-weighted velocity histogram, highlighting the predominant velocities within the ionized gas. A noteworthy observation from this histogram is the resemblance in shape between the single-component fit and the principal double-component fit, with both showcasing peaks at around -5 km s^{-1}, a velocity that aligns with the brightest part of the MB of IZw18, the north knot. These components also present a secondary peak at around 30 km s^{-1} which correspond with the south knot. However, the secondary double-component fit displays a more dispersed pattern in velocity, extending the breadth of the observed velocities.

Conversely, the top-right histogram in Fig. 4.17 illustrates the luminosity-weighted velocity dispersion histogram, shedding light on the prevailing velocity dispersions within the galaxy. Similar to the velocity histogram, the single-component fit in the velocity dispersion histogram bears a resemblance to the principal double-component fit in shape. Nevertheless, there are stark differences in the values they reach. The principal double-component fit achieves lower velocity dispersions, with its median situated around 15 km s^{-1}, whereas the median of the single-component fit is approximately 20 km s^{-1}. The secondary double-component fit, on the other hand, reveals markedly higher velocity dispersion, with a median of 50 km s^{-1} and being much more spread that the other components.

The middle panels in Fig. 4.17 show the histograms of the Halo NE of IZw18, offering insights into the luminosity-weighted distributions of velocity and velocity dispersion. The middle-left histogram in Fig. 4.17 distinctly outlines the luminosity-weighted velocity histogram, emphasizing the prevailing velocities within the ionized gas of this region. On the other hand, the middle-right histogram in Fig. 4.17 portrays the luminosity-weighted velocity dispersion histogram, revealing the dominant velocity dispersions within the Halo NE of the galaxy.

Upon close examination of these histograms, we observe stark kinematic distinctions between the principal and secondary components of the double-component fit. The principal component is distinctly shifted to bluer, or lower, velocities, exhibiting a median at around -30 km s^{-1} and presenting a relatively low velocity dispersion with a median around 13 km s^{-1}. In contrast, the secondary component is skewed towards redder velocities, with a median at around 3 km s^{-1}, and manifests a higher velocity dispersion, characterized by a median around 32 km s^{-1}.

This pronounced separation in the kinematics of the different components is corroborated by the velocity and velocity dispersion maps of the Halo NE (see Figs. 4.13, 4.14, 4.15 and 4.16), which vividly depict the disparate kinematic patterns. Interestingly, the single-component fit occupies a middle ground between these two configurations, serving as a poignant illustration of the limitations inherent in single-component fits in capturing the full spectrum of kinematic information. Indeed, even in the regions of the galaxy that are relatively kinematically quiescent (i.e. those presenting lower velocity differences and reduced velocity dispersion) significant kinematic diversity is observable, underscoring the necessity of employing nuanced analytical approaches to unravel the multifaceted kinematic landscape of the galaxy.

Similarly, for the Halo SW of IZw18, our focus shifts to the bottom histograms in Fig. 4.17. These panels unveil the developed histograms, demonstrating the distributions of velocity and velocity dispersion, each weighted by luminosity, within this segment of the galaxy. Bottom-left histogram in Fig. 4.17 offers an in-depth perspective on the luminosity-weighted velocity histogram, highlighting the prominent velocities within the ionized gas of the Halo SW. Conversely, bottom-right histogram in Fig. 4.17 reveals insights into the

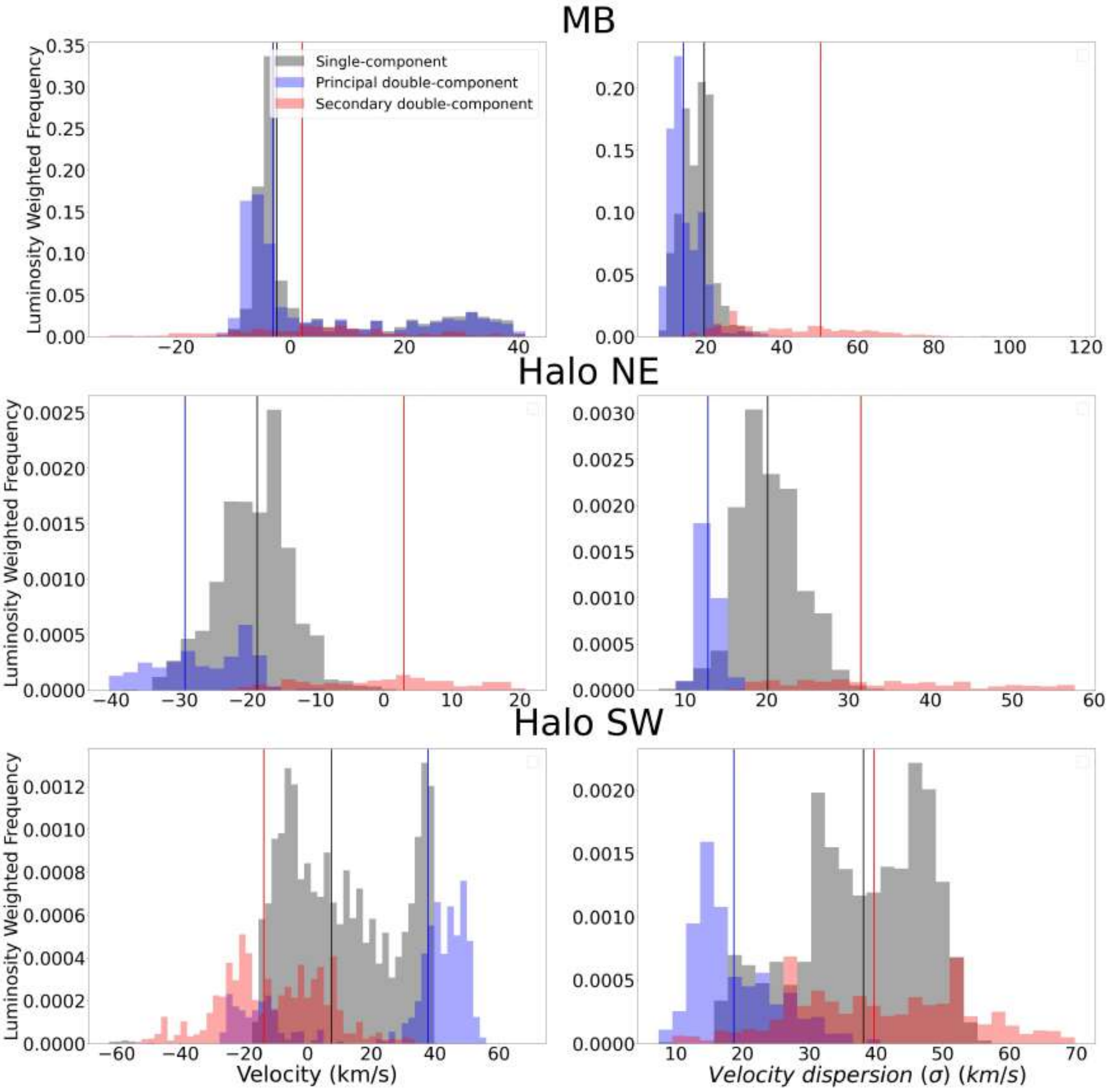

Figure 4.17 Histograms of the luminosity-weighted velocity and velocity dispersion. Top row corresponds to the MB, middle row to the Halo NE and bottom row to the Halo SW. In the left column we represent the luminosity-weighted velocity and in the right column it is represented the luminosity-weighted velocity dispersion. The black color represent calculations made with the single-component fit, meanwhile blue and red colors represent the principal and secondary double-component fit, respectively. Vertical solid thick lines represents the median of each distribution. The width of each cell in the x axis is selected to be 2 km s^{-1}

luminosity-weighted velocity dispersion histogram, illustrating the predominant velocity dispersions in this region.

A salient observation here is the comparable luminosities between the principal and secondary components of the double-component fit, rendering the distinction between a principal and a secondary component somewhat ambiguous in this instance. In terms of velocity, the principal component is bifurcated into two regions, around -15 km s^{-1} and 45 km s^{-1}, with the latter leaning towards the redder, or higher velocities. The secondary component has its median also around -15 km s^{-1} but extends to bluer, or lower velocities, distinguishing it as the bluer component this time. The single-component fit situates itself between these two components, without reaching the extreme velocities exhibited by them.

In relation to velocity dispersion, the observations here parallel those in other regions of the galaxy, with the principal component exhibiting lower and the secondary component displaying higher and more varied velocity dispersion. However, it is noteworthy that the shape of the single component in this region aligns more with the secondary component than with the principal one.

An additional noteworthy point is the heightened kinematic excitement in the Halo SW compared to the Halo NE. This added layer of kinetic complexity likely intensifies the intricacy of the system, making the interpretations more challenging. This nuance underscores the importance of meticulous analysis in decoding the diverse and intricate kinematic patterns inherent in different regions of the galaxy.

This comprehensive approach, encompassing different regions of the galaxy, furnishes a holistic understanding of the disparate kinematic behaviors and patterns pervading throughout the various segments of IZw18.

4.4 Integrated spectra

We also took advantage of our IFS data to produce the 1D spectra of selected galaxy regions. These integrated spectra allow us to study each galactic region (MB knots, Halo NE and Halo SW) as a whole, while at the same time improving the signal to noise ratio.

While the integrated spectra (for each region) could be constructed using all available spaxels, a more discerning approach is employed to optimize the quality of the spectra obtained. Rather than indiscriminately incorporating every spaxel, we strategically add one spaxel at a time, starting with the most luminous ones, to strike a balance between enhancing signal strength and minimizing noise interference. This method allows us to identify a point where the S/N is optimized. We halt the addition of spaxels at this point to avoid diluting the quality of the spectra with excessive noise from less luminous spaxels. In essence, this meticulous approach ensures that the resultant integrated spectra are both robust and representative of the true characteristics of the selected galactic regions. As a way to demonstrate this approach, Fig 4.18 is represents the S/N vs the number of spaxels in the MB of IZw18. The signal (S) is the Hα luminosity, meanwhile the noise (N) is the standard deviation of the whole continuum times the Full Width at Zero Intensity (FWZI). This allows us to compare the area of the line profile with an area defined by the noise, which makes S/N to be dimensionless. We can see that the maximum S/N is reached using the 85 brightest spaxels in this case. Furthermore, in Fig. 4.19 we represent the optimal spectrum of the IZw18 MB along with the integrated spectra retrieved from taking into account all spaxels. We can clearly see that the optimized spectrum shows a lower lever of noise than the other one.

In the integrated spectra of the MB of IZw18, we observe a rich variety of spectral lines beyond the Hα emission. Notably, the spectrum reveals the presence of the [NII] doublet and the [SII] doublet, as well as [OI], [SIII]λ6312 Å, recombination lines from HeI, and [ArIII]λ7135 Å. These additional spectral features are evident in Fig. 4.19. In contrast, the spectral analysis of both Halos of IZw18 presents a markedly different scenario. Here, we observe only the Hα line, with no discernible presence of other spectral lines. This is attributed to the faintness of the emission in these regions.

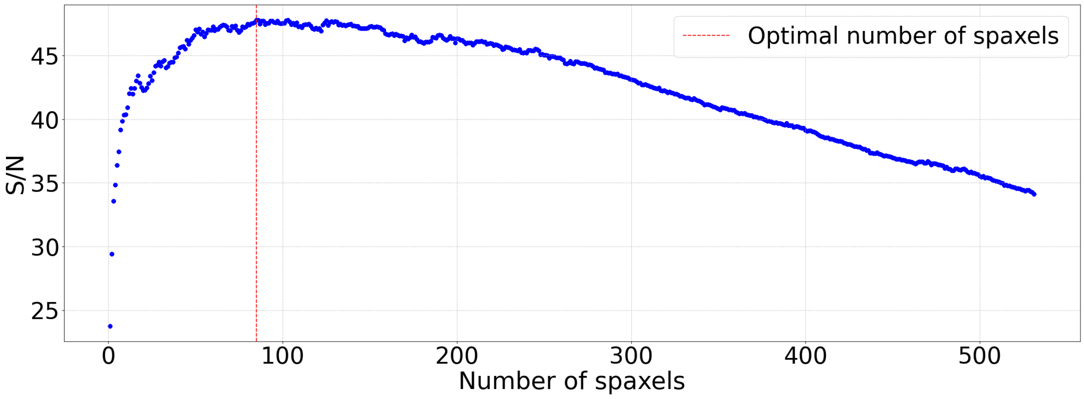

Figure 4.18 S/N vs number of spaxels in the MB of IZw18

To provide a visual representation of our selective approach in constructing integrated spectra, in Fig. 4.20 we present the Hα maps of the observed galactic regions showing only the spaxels that were used to create the integrated spectra. Each subfigure within this composite figure represents only the spaxels that were utilized to make the optimal integrated spectra. As we can see in this image, the MB is divided in two disconnected regions, the north knot and the south knot. In this way, we have done one integrated spectrum for each knot in order to distinguish their kinematical behaviour. We can compare this image with

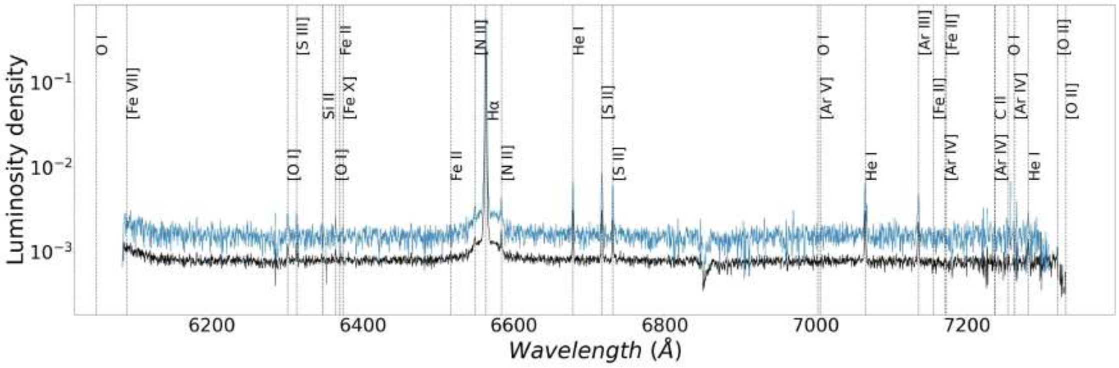

Figure 4.19 Integrated spectrum of the MB. In black it is represented the spectrum which optimizes S/N, in blue it is represented the integrated spectrum where all spaxels were used.

the one that shows all spaxels (see Fig. 4.6). Noticeable, only a small area comprising the brightest spaxels of each region is used in order to construct the best quality integrated spectra.

To delve deeper into the kinematical properties of each galactic region, we present a detailed view of the Hα line profile of the integrated spectra in Figs. 4.21, 4.22, 4.23 and 4.24. In each region, a multi-Gaussian fit is performed on the Hα line to extract the kinematical properties that represent these regions as a whole, utilizing the optimal S/N provided by our data. The AIC is employed to determine the optimal number of Gaussians for the fit, ensuring a balance between the goodness of fit and the complexity of the model. This approach allows us to accurately model the Hα profile of each region and gain insights into the underlying kinematical structures with enhanced reliability. To quantify the uncertainties associated with the Gaussians in the fit, we employed the bootstrapping method (Efron & Tibshirani 1985). In table 4.2 it is shown the luminosity percentage, velocity, velocity dispersion and FWZI (along with their corresponding errors) of the components that fit each region.

In examining the Hα profile of the north (south) knot of the MB (see Figs. 4.21 and 4.22), the AIC suggests a fit with four (three) Gaussian components for the Hα line, alongside two additional Gaussians for the [NII] lines. The four (three) Gaussians comprise two (one) principal components, which account for $\sim$ 90% (in both cases) of the total luminosity and exhibit low velocity dispersion (from 6 km s^{-1} to 21 km s^{-1}), two broad components, contributing around 7% and 4% to the luminosity (in both cases), characterized by velocity dispersions of 65 km s^{-1} (56 km s^{-1}) and an exceedingly broad velocity dispersion of 730 km s^{-1} (840 km s^{-1}), respectively (see Table 4.2). Furthermore, the FWZI for the north and south knots is measured to be 3000 km s^{-1} and 2600 km s^{-1}, respectively, underscoring the extensive breadth of the Hα profile, particularly in the context of the very broad components.

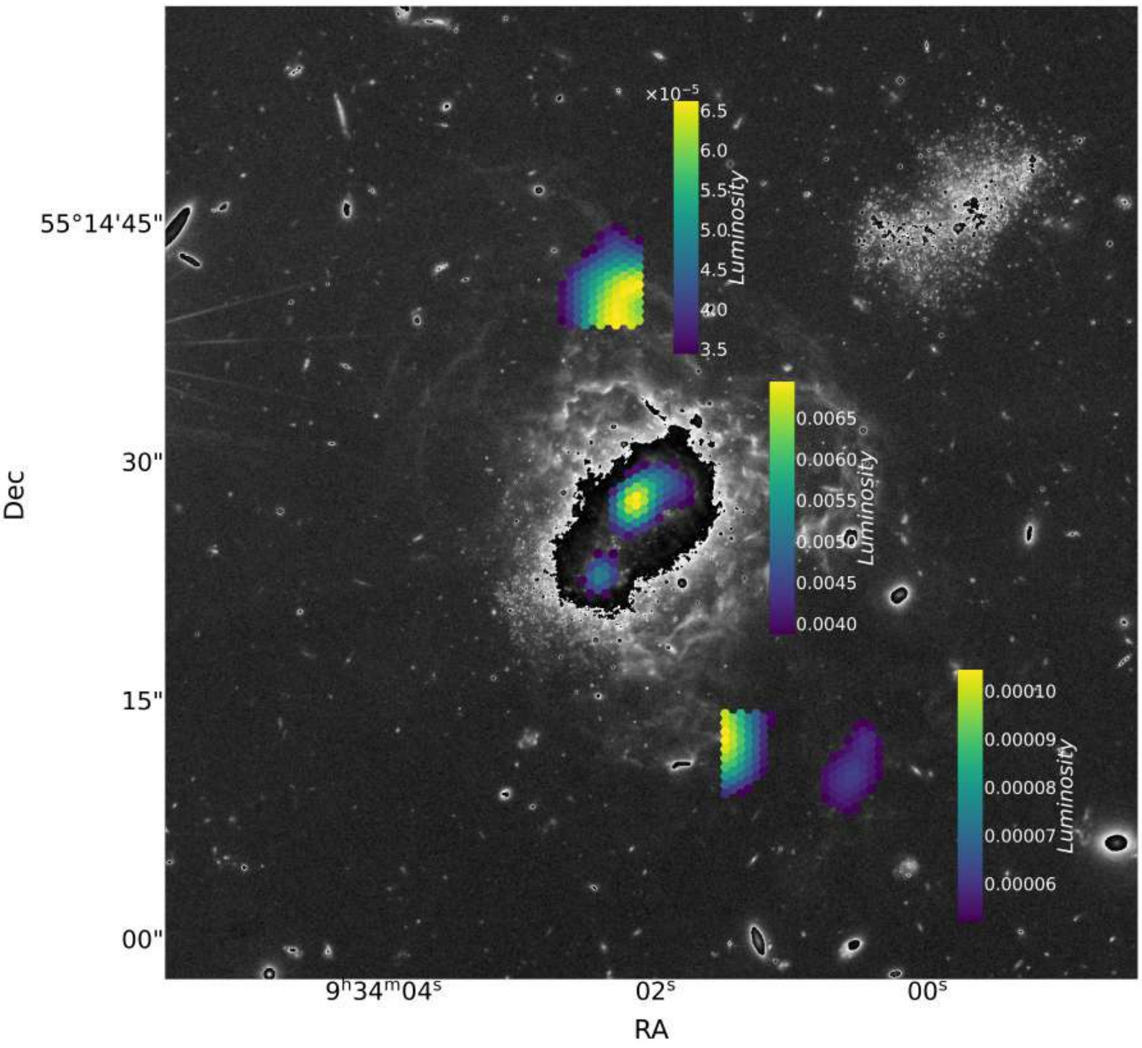

Figure 4.20 Hα luminosity map of the single-component fit. The spaxels represented here are the ones used for making the integrated spectra in each region.

The emergence of these broad and very broad components introduces a complex layer to our understanding of the kinematical structure of the galaxy. Notably, the very broad components not only are found shifted to the red in comparison to the narrow components by at least ~ 40 km s^{-1}, but they also exhibit a velocity spatial gradient that is almost three times that of the narrow components. Specifically, the velocity difference between the south and north knot for the very broad components is approximately 110 km s^{-1}, which, after adjusting for the 40 km s^{-1} attributed to the rotation of the galaxy, results in a net difference of 70 km s^{-1}. This finding indicates that the very broad components are not only redshifted relative to the narrow ones but also suggest that the dynamics of the very broad components are significantly distinct, highlighting that a fraction of the ionized gas in the MB of IZw18

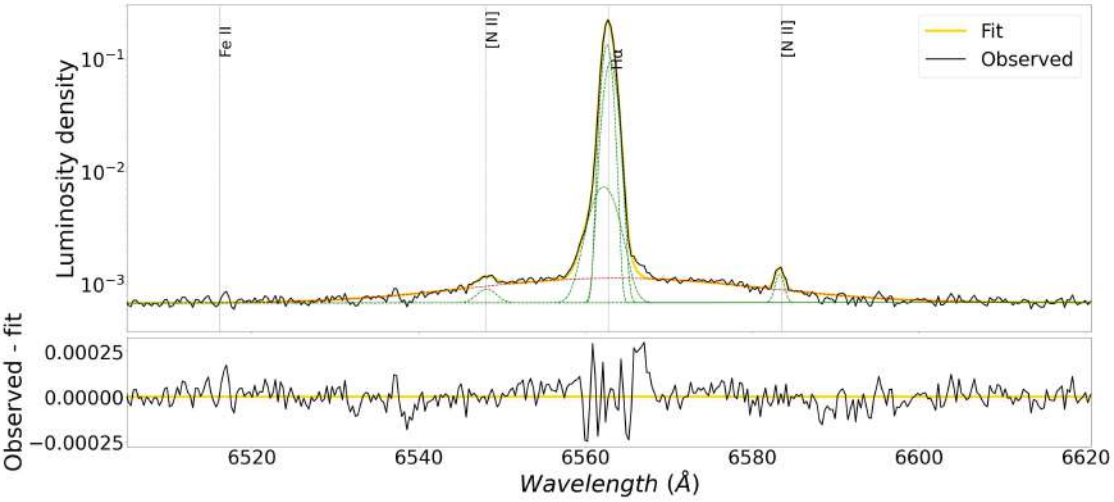

Figure 4.21 Zoom in to the Hα line in the integrated spectrum of the north knot of the MB. In black it is represented the observed spectrum and in yellow the multi-gaussian fit. In green we can see the continuum plus the individual gaussians. In red it is represented the gaussian with high standard deviation (σ>10 Å). This same approach is used in the following representation of the integrated spectra.

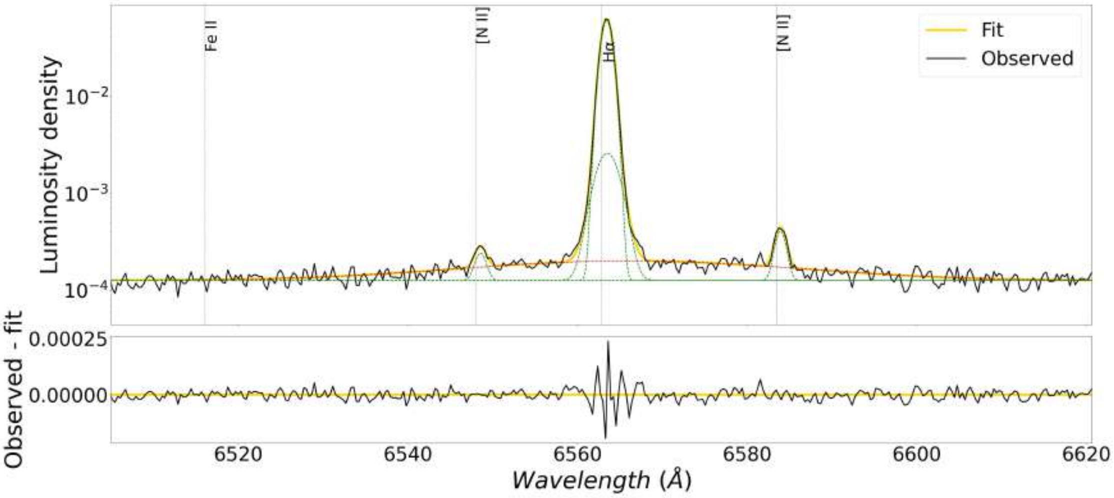

Figure 4.22 Zoom in to the Hα line in the integrated spectrum of the south knot of the MB.

possesses remarkably high kinetic energy, potentially due to dynamic processes within the galaxy.

The likely physical mechanisms that could impart such a significant input of kinetic energy into the gas include supernovae explosions and/or BH accretion. Supernovae, with their colossal energy output, can create shock waves that propagate through the ISM, thereby inducing turbulent motion in the gas. Similarly, if there is a BH present in IZw18, its accretion activity and associated energetic outputs (such as jets or outflows) could also serve as a potent source of kinetic energy, stirring the surrounding gas into a frenzied, disordered state. Even broader components (FWHM>10^4 km s^{-1}) are seen in a similar (very metal-poor dwarf) galaxy called SBS 0335-052E in Hatano et al. (2023), where they argued about the possibility of an AGN being the source behind this broad emission. The discernment of this very broad component not only challenges our previous kinematical analyses but also beckons a deeper exploration into the internal dynamics and potential energy sources within IZw18, offering a rich avenue for further study and discussion.

The absence of discernible indicators of these broad components in earlier stages, and the fact that so many components are found in the integrated spectra of the MB of IZw18, indicate that the dual-component fit in the previous 2D-kinematical analysis could be conflating these (up to four) components, especially in the secondary one. This revelation necessitates a reevaluation of the kinematical structure and the potential interplay between these components. Currently, our 2D-kinematical study extends up to the dual-component fit, emphasizing the two predominant (brightest) components discerned in the fit of the integrated spectra. The newfound complexity and multiplicity of components in the integrated spectral data invite further, more granular exploration into the kinematical properties of IZw18.

In the context of the Halo NE of IZw18, the integrated spectrum discernibly aligns with a two-component fit (see Fig. 4.23). Our comprehensive 2D-kinematical examination of this region corroborates this dual-component structure, revealing distinct kinematics in the different maps (see Figs. 4.13, 4.14, 4.15 and 4.16). The two components manifest as a brighter, blue-shifted element with lower velocity dispersion and a dimmer, red-shifted counterpart exhibiting higher velocity dispersion. This dual-structure is consistently evident in the integrated spectrum fit (see Fig. 4.23), where both components are distinctly recognizable. The Halo NE stands out as a region of relative kinematic simplicity, featuring two discernible components that can be readily attributed to distinct ionized gases exhibiting differing kinematics. This scenario exemplifies a case where our mathematical approach of Gaussian fitting converges with direct physical interpretations, offering insights into the movements of the ionized gas within this region.

Observations of the Halo SW of IZw18 reveal a consistent two-component fit within the integrated spectra for this region (see Fig. 4.24), mirroring the dual-structure found in the Halo NE. However, the components here exhibit an inverse configuration compared to those in the Halo NE. Specifically, the brighter component is redshifted and exhibits a wider spread, contrasting with the narrower, blue-shifted dimmer component. The components

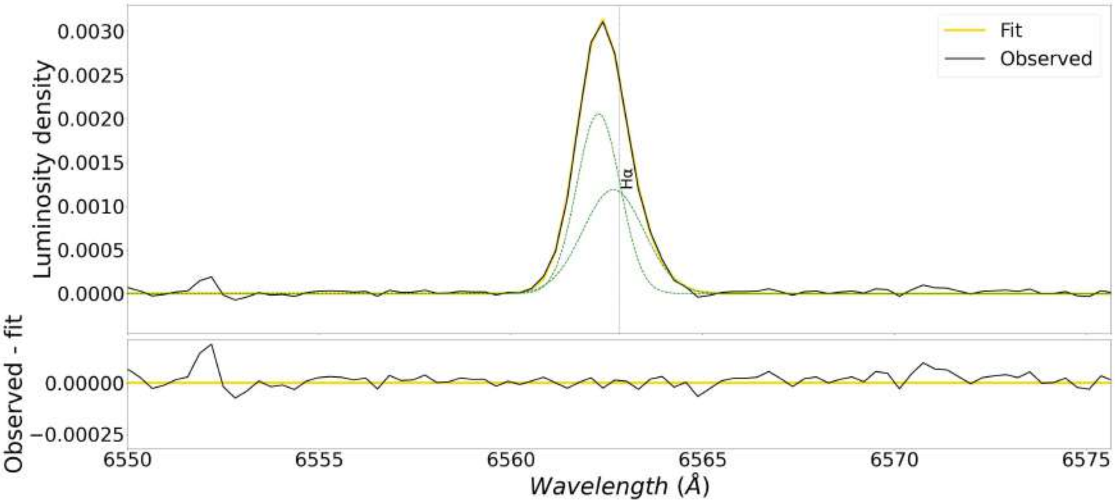

Figure 4.23 Zoom in to the Hα line in the integrated spectrum of the Halo NE.

in this region tend to have higher velocity dispersion, indicative of a broader kinetic range, reflecting the inherent kinematic complexity of the Halo SW already seen in 4.3.2.

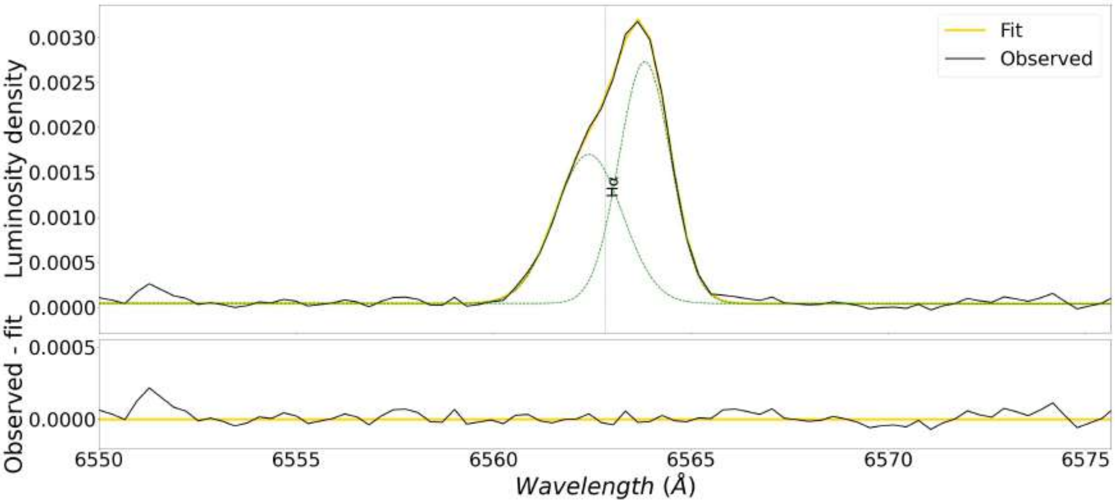

Figure 4.24 Zoom in to the Hα line in the integrated spectrum of the Halo SW.

4.5 Very broad component

Based on the previous discovery of the very broad component (present in the knots of the MB) and the striking different velocities of this very broad component which respect the narrow

Table 4.2 Hα fit kinematical values.

Galactic region (1)	Component (2)	Luminosity % (3)	Velocity (km s^{-1}) (4)	Velocity dispersion (σ) (km s^{-1}) (5)	FWZI (km s^{-1}) (6)
MB north knot	Principal	0.5±0.2	-11.0±0.8	6±2	3000±200
	Secondary	0.4±0.2	10±8	21±3	
	Broad	0.064±0.004	-29±3	65±2	
	Very broad	0.046±0.002	40±40	730±30	
MB south knot	Principal	0.896±0.006	28.94±0.02	17.0±0.08	2600±300
	Broad	0.074±0.004	32.0±0.7	56±2	
	Very broad	0.031±0.003	150±80	840±90	
Halo NE	Principal	0.7±0.3	-23±3	12±4	210±40
	Secondary	0.3±0.3	0±30	20±20	
Halo SW	Principal	0.6±0.2	46±4	18±5	270±30
	Secondary	0.4±0.2	-20±20	30±8	

Column (1): Name of the galactic region. Column (2): Name given to each gaussian component. Column (3): Normalized luminosity corresponding to each component. Column (4): Velocity corresponding to each component. Column(5): Velocity dispersion corresponding to each component. Column(6): FWZI of the line profile.

ones, we have made a similar approach than the one used in Section 4.3.2. This approach enabled us to generate luminosity, velocity, and velocity dispersion maps specifically for this very broad component.

Nevertheless, as we have noted before in Fig. 4.5 the very broad component can not be seen in individual spaxels. One way to solve this is to make a harder Gaussian spatial smoothing to the spaxels, in this way at the cost of further loosing of spatial resolution we are able to reach a point in which we have enough signal to distinguish this dim component from the continuum. This time, the Gaussian kernel used has a FWHM of 2.5 ” which enlarges the area of the FWHM of the Gaussian kernel 3 times the previous one used.

Furthermore, in order to properly fit the very broad component we have to get rid of the more luminous narrow Hα emission and the [NII] lines. For this we take away the points in the spectra that distance less than 5 Å (2.5 Å) from the center of the Hα line ([NII] lines).

Now we make a one-component Gaussian fit to the profiles that appear after all this procedure. The fit corresponding to the same spaxel as Fig. 4.5 is represented in Fig. 4.25. Here we can see that thanks to the enhanced smoothing of the new kernel the very broad component is clearly visible and can be well fitted.

The same criteria for excluding spaxels as the one applied in Section 4.3 is done here. Particularly, in this case the S/N ratio below 3 criterion is the one that takes away most of the spaxels.

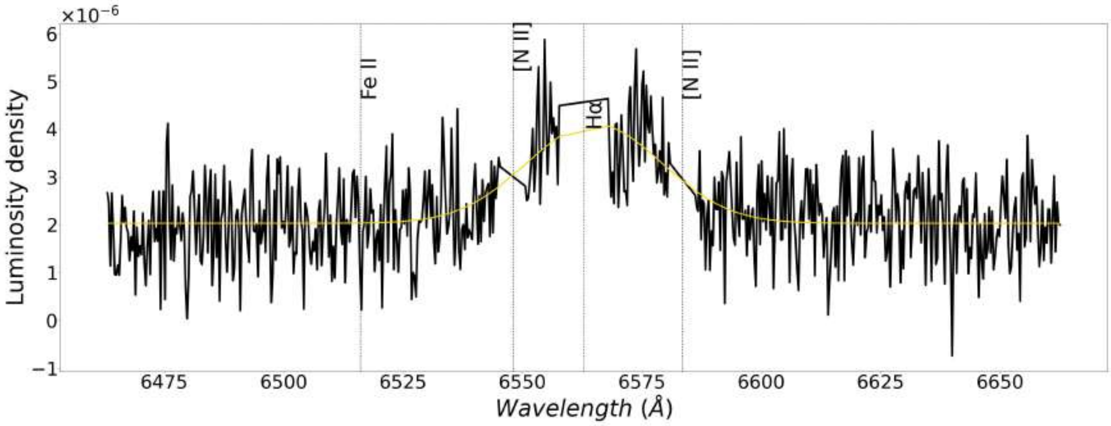

Figure 4.25 One-component fit of the defined broad Hα component. The profile comes from the same spaxel as used in Fig. 4.5. The profile is depicted in black, meanwhile the one-component fit is represented in yellow.

To effectively compare these new results with the previously done one-component fit in Section 4.3, we have reapplied the one-component fitting procedure to the entire Hα line, employing the new Gaussian kernel. This approach reaffirms the previously presented results, but with enhanced smoothing.

The maps of the very broad component are represented in Fig. 4.26 and luminosity ratio (Very broad component luminosity / Full Hα luminosity) and velocity difference (Very broad component velocity - Full Hα velocity) maps are in Fig. 4.27.

The maximum of emission of the very broad component is slightly to the south of the maximum of the total Hα emission (see top panel in Fig. 4.26). Nevertheless, the maximum luminosity ratio is in the eastern and western part of the MB (see top panel in Fig. 4.27), where we reach up to 35 % of the emission in the form of this very broad component. These regions are actually the same that presents a velocity dispersion of around 200 km s^{-1} in the secondary component of the dual-fitting (see Fig. 4.16). In this way, as we mentioned before, this secondary component is fitting several components of the Hα line profile seen in the integrated spectra of the knots (see Figs. 4.21 and 4.22), making it difficult to interpret. In the south knot we do not see any secondary maximum in luminosity regarding the very broad component, as it is seen in the luminosity map (see top panel in Fig. 4.26). This is reflected in the luminosity ratio map where in this region its value reaches a minimum of 3%. The south part of the north knot along with the previously mentioned eastern and western regions of the MB present the maximum luminosity ratio, indicating possible zones dominated by outflows. The wide extended spatial region that shows very broad component emission indicates that the reason behind this high kinematic input in the gas should not be local, as we could expect from localized supernovae or AGN in the north knot.

Furthermore, looking at the velocity and velocity dispersion maps (see middle and bottom panels in Fig. 4.26) we recall the tremendous kinematic excitement of this gas. The velocity has a range of more than 160 km s^{-1}, which is more than 3 times the velocity range presented in the one-component fit of the MB. The velocity dispersion does not present much spatial variation ranging from 600 km s^{-1} to more than 800 km s^{-1} in the south knot. The velocity difference between the very broad component and the whole Hα line (see bottom panel in Fig. 4.27) shows that the very broad component is mostly redshifted with respect the narrow component. Only to the west of the north knot this difference in velocity goes to zero and even reaches negative values. This high velocity difference between the narrow and the very broad component indicates that these gases maybe occupy a different region along the line of sight (being the very broad component gas likely behind the narrow component gas). A possible explanation of this behaviour is the presence of high density gas near the origin of kinematic input. This high density gas could act like a wall, that to some extent reflects back the momentum of the gas itself, producing the observed change in the velocity of the low density gas in an opposite direction. In this way, in the red velocities of the bottom panel in Fig. 4.27 this theoretical wall would be in the front part of the galaxy which respect the line of sight (closer to us). On the other hand, the blue velocities in this same map indicates that this high density gas is in the back of the galaxy with respect to the line of sight (far away from us). This kinematic interaction of different gases within the ISM is reminiscent of the turbulent mixing layer mechanism, where emission-line broadening occurs at the interface of cold disc gas and warmer outflow gas, as discussed by Hogarth et al. (2020). The observed shifts in velocities between broad and narrow components have been seen in other galaxies like GP J 0820 (Bosch et al. 2019). This might be explained by this reflection of momentum along the line of sight. In fact, this could be a result of the high-density gas acting as a barrier (gas density gradients along the line of sight), influencing the dynamics of the gas flow and leading to the velocity shifts seen in the spectral lines.

4.6 Conclusions

This study presents a comprehensive analysis of the kinematical behaviour of the ionized gas in IZw18, a galaxy known for its extremely low metallicity and proximity. Our research delves into the kinematic complexities of IZw18, exploring its structure and dynamics through an in-depth examination of the Hα line profiles across different regions. By applying both single and double Gaussian component fits to the spectrum of each spaxel, we successfully generated luminosity, velocity, and velocity dispersion maps for each Gaussian component in the MB of the galaxy and two distinct regions of the Halo (Halo NE and Halo SW). Additionally, our methodology included creating integrated spectra for select regions of the galaxy, focusing on maximizing the S/N ratio. Finally, we extended our analysis by constructing luminosity, velocity, and velocity dispersion maps of the very broad component (discovered in the integrated spectra), employing a larger Gaussian kernel to enhance the signal, thereby allowing for a more detailed observation of this elusive component.

In the MB, our analysis reveals a notable rotational pattern connecting the north and south knots. However, the secondary double-component fit uncovers a different and more complex kinematic pattern. This complexity is further highlighted in the integrated spectra of both knots, where up to four Gaussian components were required to adequately fit the Hα profile. Notably, one of these components exhibited a FWHM of almost 2000 km s^{-1}, accounting for 4% of the total flux, suggesting the presence of a high-energy outflow. Particularly, this very broad component exhibits a significant spatial extent that not only challenges the notion of localized high-energy events, such as supernovae or AGN activity, but also questions the likelihood of bipolar outflows. Such outflows are generally expected in scenarios involving localized sources of kinetic energy. The widespread nature of this component instead suggests more global, galaxy-scale processes at work, indicating a complex interplay of dynamics that extends beyond traditional models of localized energetic events.

The Halo regions of the galaxy reflect the behavior of the shells in IZw18. The Halo NE exhibits a relatively tranquil kinematic state, with two Gaussian components in the integrated spectra showing low velocity dispersion ($\leq$ 20 km s^{-1}). These components align with the two components of the double-Gaussian fit, presenting bluer velocities than the MB. In contrast, the Halo SW is characterized by a more complex kinematical behaviour than the Halo NE. This is reflected in the presence of higher velocities and velocity dispersions and more complex kinematical patterns in the maps.

This research aligns with and expands upon the existing body of work on the kinematics of dwarf galaxies, particularly those with characteristics similar to IZw18, a BCD. Consistent with observations in other galaxies of its class, our study confirms that IZw18 exhibits chaotic kinematics alongside a discernible rotation pattern. This finding suggests that while a primary rotational pattern encompassing the knots of the MB is evident, a secondary and more intricate mechanisms are also at play. These mechanisms, possibly stemming from stellar feedback, introduce additional kinetic energy into the ISM, resulting in a more chaotic and unpredictable motion of the ionized gas of the galaxy.

Furthermore, a critical aspect of our findings revolves around the significant velocity differences observed between the narrow and the very broad components of the Hα line. This disparity hints at a distinct spatial segregation of these gases within the line of sight, with the very broad component likely residing behind the narrow component. Intriguingly, this spatial arrangement might be influenced by the presence of high-density gas near the origin of the kinematic input. This dense gas could function to some extent as a wall, reflecting back the momentum of the surrounding gas. Such a reflection would manifest as a change in the velocity of the center of mass of the low density gas, directed opposite to this wall of dense gas. In this way, the redshifted velocities on the bottom panel in Fig. 4.27 suggest that this dense gas is located towards the front of the galaxy, relative to the line of sight (closer to us). Conversely, the blueshifted velocities imply that the high-density gas lies towards the back of the galaxy (farther from our perspective). These observations provide a novel interpretation of the internal gas dynamics in IZw18, pointing to complex, multi-layered kinematic interactions within the galaxy, and challenging conventional understandings of gas motion and distribution in such environments.

The study of IZw18, with its notably low metallicity, offers a crucial window into understanding the early galaxy formation and evolution in the Universe. This metal-poor environment in IZw18 closely resembles the conditions prevalent in the first galaxies, providing a unique opportunity to observe and infer behaviors and processes that were likely common in the high-redshift Universe. Our proximity to IZw18, coupled with the high spatial resolution of our observations, has allowed us to discern its kinematic complexity in unprecedented detail. This complexity, likely a characteristic of many galaxies, becomes vividly apparent in IZw18 due to our advantageous observational position. However, the intricate nature of these kinematic patterns presents significant challenges in interpretation, underscoring the sophisticated dynamical processes at play in such early-stage galactic environments. Through IZw18, we gain insights into the nascent stages of galaxy evolution, observing firsthand the intricate dance of forces shaping galaxies at the dawn of the cosmos.

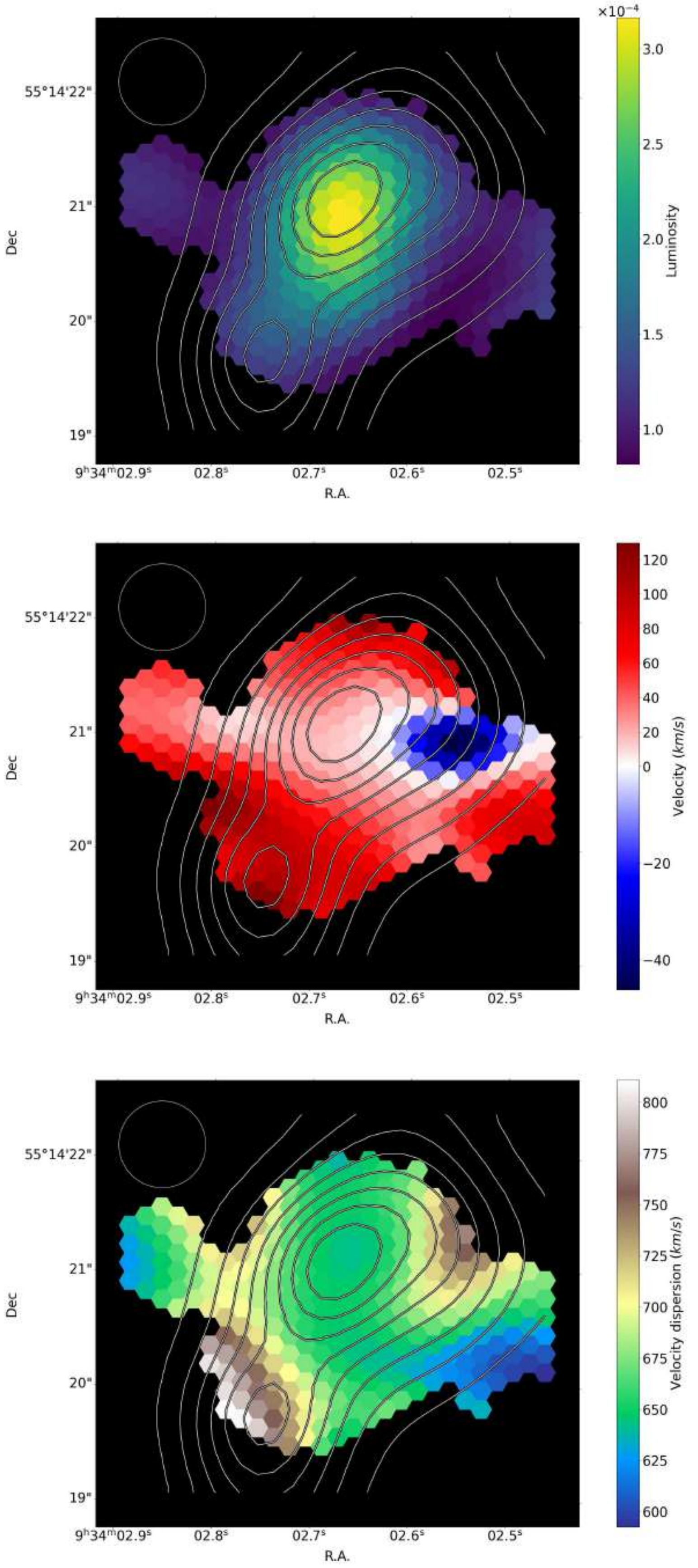

Figure 4.26 Luminosity (top panel), velocity (middle panel) and velocity dispersion (bottom panel) of the very broad component. In all maps we can see overplotted the contours of the total Hα luminosity and a circle representing the FWHM of the seeing.

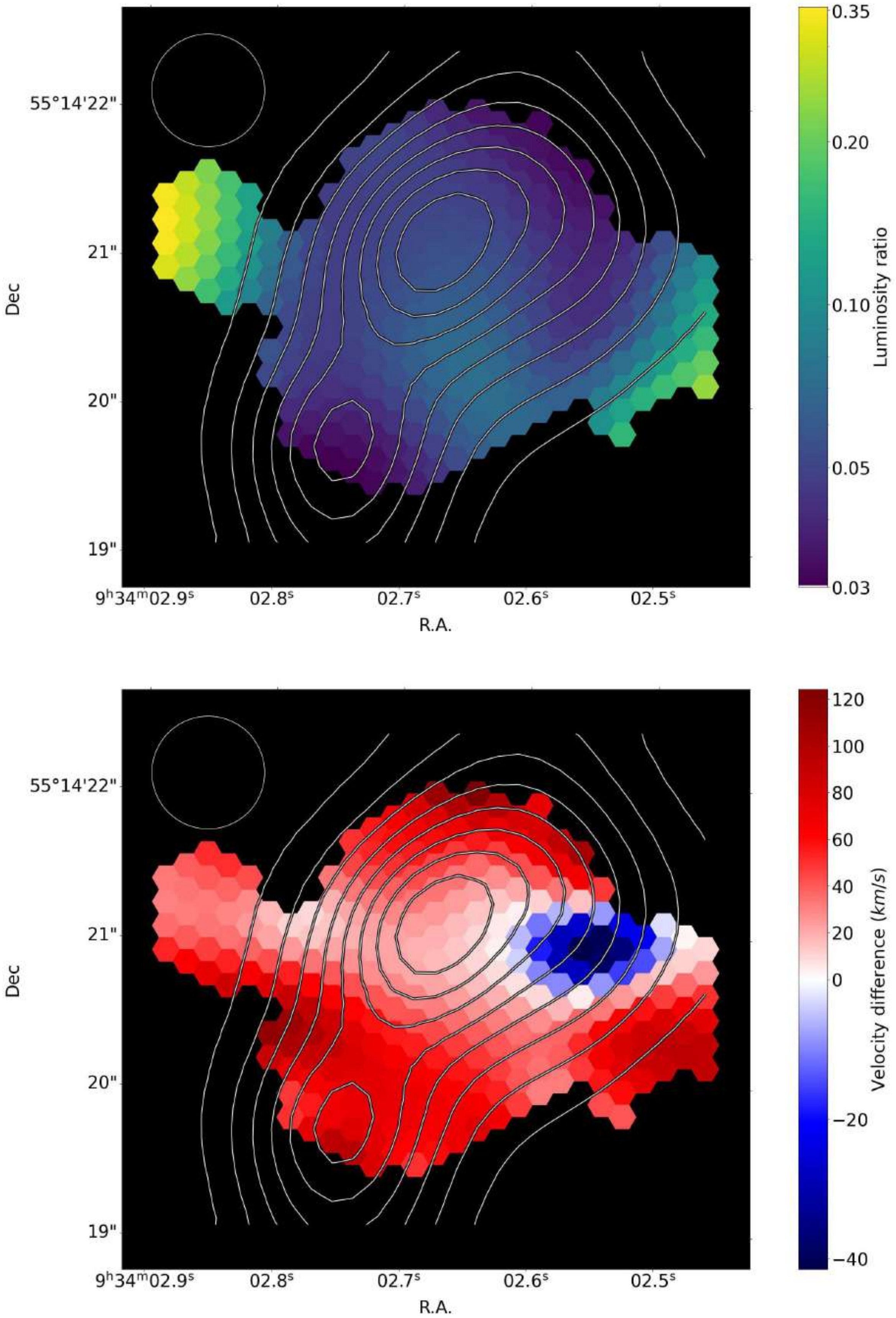

Figure 4.27 Top map correspond to the luminosity ratio: Very broad component luminosity / Full Hα luminosity. Bottom map represents the velocity difference: Very broad component velocity - Full Hα velocity. In all maps we can see overplotted the contours of the total Hα luminosity and a circle representing the FWHM of the seeing.

Chapter 5

Conclusions

5.1 Overview

This thesis represents a comprehensive journey into the heart of the physical phenomena occuring in primeval galaxies by closely examining their local analogues, focusing on extreme star formation events or starbursts. Starting with the broad analysis within J-PAS to identify EELGs as markers of starburst phenomena, we meticulously narrowed our focus to a set of 24 GPs (seen with MUSE/VLT) on the limit of spatial resolution. Finally, the culmination of this work consists in a detailed kinematic study of IZw18 (seen with MEGARA/GTC), a galaxy that epitomizes the extreme conditions akin to the early Universe. This progression from a wide-field survey to intense scrutiny of individual galaxies illuminates local extreme star-forming conditions, offering a window into the universal mechanisms of star formation and galactic evolution.

5.2 Summary

The discovery and analysis of 19 EELGs candidates within the miniJPAS and J-NEP data (covering 1.25 square degrees) exemplify the efficiency of our methodology in detecting galaxies undergoing extreme starbursts. Using this preliminary data from the J-PAS survey, we searched for EELGs by applying a method based on the contrast between the emission lines seen in J-PAS narrow-band filters and the continuum of the adjacent filters. EELGs were defined as galaxies exhibiting $\mathrm{EW}_0 \geq 300$ Å in at least one of the emission lines [OII], [OIII], or Hα. The derived redshifts showed excellent agreement with spectroscopic redshifts, with $\Delta z/(1+z_{spec}) \leq 0.01$.

Most star-forming EELGs were identified through [OIII] emission, with some detected in Hα, while QSOs were mainly detected in Lyα. The confirmed 19 EELGs cover the redshift range $0 \leq z \leq 0.748$, with a concentration of sources detected in [OIII] between $0.2 \leq z \leq 0.3$ (the redshift range where most GPs are detected). If J-PAS has similar depth as miniJPAS and J-NEP, it will be suitable to investigate high-luminosity EELGs detected in Hα and [OIII] at redshifts greater than 0.25 and 0.5, respectively.

Comparing our sample to others is challenging due to different selection criteria, but our EELG counts are reasonably consistent with other studies, though slightly lower than Amorín et al. (2015) using zCOSMOS data. Despite the small sample size, this study demonstrates the effectiveness of our methodology in detecting EELGs.

Our spatially resolved study of 24 GPs through MUSE/VLT data cubes has provided significant insights into their physical and chemical attributes, underscoring the similarities between these local analogues and high-redshift galaxies. By analyzing the spatial extension of the sources, we identified seven GPs that are extended in both core and low surface brightness regions, five in the core, and four in the low surface brightness regions. Comparative analysis of emission line maps and continuum maps revealed that [OIII] maps had the greatest spatial extent, serving as tracers for ionized gas regions.

Our investigation into ionization structures showed that Hα/Hβ ratio maps highlighted varying dust/gas concentrations, with extinction peaking close to galaxy centers. Furthermore our GPs present high [OIII]/[OII] ratios (specially in the confirmed LyC leakers) indicating high ionization gas. BPT diagrams confirmed that hot, massive stars are the dominant ionizing sources, placing our GPs in the top-left quadrant, characterized by low metallicity and high gas excitation.

Integrated spectra from these galaxies indicated high SFRs with mass-doubling timescales much shorter than typical star-forming galaxies. Emission line analysis revealed low gas metallicity ($12 + \log(\mathrm{O/H}) = 7.6 - 8.4$), high electron temperatures (11,500 K to 15,500 K), and varied electron densities (30 cm^{-3} to 530 cm^{-3}). Chemical abundances showed that in our GPs the N/O ratio aligns with SDSS galaxies trends, but regarding the $12 + \log(\mathrm{O/H})$ vs stellar mass diagram, GPs are below the main sequence, suggesting possible accretion of metal-poor gas.

We detected the nebular HeII line in three GPs, indicating the presence of extremely hard ionizing photons. Together with the lack of broad WR features in their spectra, this suggests other sources responsible for the HeII excitation. The high sSFR in these GPs imply that, in addition to low metallicity, high sSFRs could drive HeII emission.

Our kinematic analysis, using velocity and velocity dispersion maps derived from the Hα line, revealed the complexity of gas movements influenced by stellar feedback mechanisms.

High-velocity outflows seen as broad spectral line components indicated the presence of dynamic interactions between star formation processes and ionized gas dispersal, potentially facilitating LyC photon escape. The L-σ relation and the distinction between rotation and dispersion-dominated systems highlighted a predominance of turbulent internal environments driven by intense star formation and feedback, although a rotational pattern was also observed in most GPs.

Through this comprehensive analysis, our study offers a window into the formative processes of galaxies in the local Universe that mirrors early cosmic conditions. The interplay of gas dynamics, star formation, and ionization structure in GPs stands as a testament to the complexity of galaxy evolution.

The detailed examination of the kinematics of IZw18 using MEGARA/GTC data offers a compelling narrative of the complexities inherent in a galaxy known for its extremely low metallicity. This study presents a comprehensive analysis of the ionized gas kinematics in IZw18, exploring its structure and dynamics through in-depth examination of the Hα line profiles across different regions. By applying both single and double Gaussian component fits, we generated luminosity, velocity, and velocity dispersion maps for each Gaussian component in the MB of the galaxy and two distinct halo regions (Halo NE and Halo SW). Our analysis revealed a notable rotational pattern in the MB, with complex kinematic behavior uncovered by the secondary double-component fit, including a very broad component with a FWHM of nearly 2000 km s^{-1}, suggesting high-energy outflows.

The Halo regions displayed differing kinematic states, with the Halo NE exhibiting relatively tranquil behavior and the Halo SW showing higher velocities and more complex patterns. Our findings align with and expand upon existing work on dwarf galaxy kinematics, confirming that IZw18 exhibits chaotic kinematics alongside a discernible rotation pattern. This suggests that while a primary rotational pattern is evident, secondary mechanisms, likely driven by stellar feedback, introduce additional kinetic energy into the ISM, resulting in more chaotic motion of the ionized gas.

A critical aspect of our findings revolves around the significant velocity differences between the narrow and very broad components of the Hα line, possibly indicating distinct line of sight spatial segregation of these gases. This spatial arrangement might be influenced by high-density gas near the origin of the kinematic input, acting as a wall that reflects the momentum of surrounding gas. Redshifted velocities in the broad component suggest that this dense gas is located towards the front of the galaxy, while blueshifted velocities imply it is towards the back. These observations challenge conventional understandings of gas motion and distribution in metal-poor environments, highlighting the multi-layered kinematic interactions within IZw18.

The study of IZw18 offers crucial insights into early galaxy formation and evolution, closely resembling conditions in the first galaxies. Our proximity to IZw18 and the high spatial and spectral resolution of our observations have allowed us to discern its kinematic complexity in unprecedented detail, providing a unique opportunity to observe and infer behaviors common in the high-redshift Universe. This study underscores the sophisticated dynamical processes at play in early-stage galactic environments, revealing the intricate dance of forces shaping galaxies at the dawn of the cosmos.

5.3 Future work

In conclusion, this thesis not only enhances our understanding of the physical processes driving star formation and galactic evolution in the early Universe but also establishes a methodological framework for future explorations into the role of starbursts in galaxy evolution.

With the ongoing J-PAS survey covering a much larger area (~8500 square degrees), it is expected that a significant number of EELGs will be detected, unveiling the nature and evolution of EELGs on a larger scale. This project will also enable the search for Lyman-break galaxies by identifying no flux detections in blue filters, allowing us to study not only local analogues but also galaxies closer to the primeval Universe.

A spectroscopic follow-up of the sample is necessary to determine the percentage of false detections (if any) and verify the precision of emission line fluxes estimated using miniJPAS and J-NEP data. Additionally, more precise studies similar to those conducted on GPs and IZw18 could be applied to newly discovered starburst galaxies.

We will focus on the companions of GPs using the large FoV of MUSE. Preliminary analysis has shown that 7 out of the 24 GPs have companions. The kinematical properties of these companions in relation to the GPs are being studied. We will examine the alignment between the rotational planes of GPs and the positions of their companions to detect any signs of past interactions. By considering the distance between GPs and their companions and estimating the timing of the starburst in GPs, we can determine whether these companions played a role in triggering star formation in GPs.

For IZw18, we plan to complete the kinematical study by analyzing the rest of the optical spectral lines in both the MB and the Halo. This will illuminate possible correlations between the ionization structure and the kinematics in this galaxy. Such a comprehensive analysis will deepen our understanding of the complex dynamics and ionization processes in metal-poor environments, contributing to the broader knowledge of early galaxy evolution.

Furthermore, we will examine the asymmetry in the line profiles when stellar feedback is embedded in a gas density gradient along the line of sight. This will be achieved by creating an elastic collision model between particles with initial conditions that mimic the physical scenario.

These future endeavors will build on the foundations laid by this thesis, pushing the boundaries of our understanding of galaxy formation and evolution, and refining the methodologies used to explore these fascinating cosmic phenomena.

Bibliography

Ahumada, R., Prieto, C. A., Almeida, A., et al. 2020, The Astrophysical Journal Supplement Series, 249, 3

Ahumada, R., Prieto, C. A., Almeida, A., et al. 2020, The Astrophysical Journal Supplement Series, 249, 3

Aloisi, A., Clementini, G., Tosi, M., et al. 2007, The Astrophysical Journal, 667, L151

Aloisi, A., Tosi, M., & Greggio, L. 1999, The Astronomical Journal, 118, 302

Amorín, R., Pérez-Montero, E., Contini, T., et al. 2015, Astronomy & Astrophysics, 578, A105

Amorín, R., Pérez-Montero, E., Vílchez, J., & Papaderos, P. 2012a, The Astrophysical Journal, 749, 185

Amorín, R., Rodríguez-Henríquez, M., Fernández, V., et al. 2024, arXiv preprint arXiv:2401.04278

Amorín, R., Vílchez, J. M., Hägele, G. F., et al. 2012b, The Astrophysical Journal Letters, 754, L22

Amorín, R. O., Pérez-Montero, E., & Vílchez, J. 2010, The Astrophysical Journal Letters, 715, L128

Bacon, R., Accardo, M., Adjali, L., et al. 2010, in Ground-based and Airborne Instrumentation for Astronomy III, Vol. 7735, SPIE, 131–139

Bae, H.-J., Woo, J.-H., Karouzos, M., et al. 2017, The Astrophysical Journal, 837, 91

Baldwin, J. A., Phillips, M. M., & Terlevich, R. 1981, Publications of the Astronomical Society of the Pacific, 93, 5

Barkana, R. & Loeb, A. 2001, Physics reports, 349, 125

Bekki, K. 2015, Monthly Notices of the Royal Astronomical Society: Letters, 454, L41

Benitez, N., Dupke, R., Moles, M., et al. 2014, arXiv preprint arXiv:1403.5237

Benítez, N., Moles, M., Aguerri, J., et al. 2009, The Astrophysical Journal, 692, L5

Berg, D. A., James, B. L., King, T., et al. 2022, The Astrophysical Journal Supplement Series, 261, 31

Bernard, J.-P., Paradis, D., Marshall, D., et al. 2010, Astronomy & Astrophysics, 518, L88

Bertin, E. & Arnouts, S. 1996, Astronomy and astrophysics supplement series, 117, 393

Bonoli, S., Marín-Franch, A., Varela, J., et al. 2021, Astronomy & Astrophysics, 653, A31

Bosch, G., Hägele, G. F., Amorín, R., et al. 2019, Monthly Notices of the Royal Astronomical Society, 489, 1787

Boyett, K. N., Stark, D. P., Bunker, A. J., Tang, M., & Maseda, M. V. 2022, Monthly Notices of the Royal Astronomical Society, 513, 4451

Brasken, M. & Kyrola, E. 1998, Astronomy and Astrophysics, v. 332, p. 732-738 (1998), 332, 732

Breda, I., Vilchez, J. M., Papaderos, P., et al. 2022, Astronomy & Astrophysics, 663, A29

Briscese, F., Elizalde, E., Nojiri, S., & Odintsov, S. D. 2007, Physics Letters B, 646, 105

Bromm, V. & Larson, R. B. 2004, Annu. Rev. Astron. Astrophys., 42, 79

Bromm, V. & Yoshida, N. 2011, Annual Review of Astronomy and Astrophysics, 49, 373

Brunker, S. W., Salzer, J. J., Janowiecki, S., Finn, R. A., & Helou, G. 2020, The Astrophysical Journal, 898, 68

Bundy, K., Fukugita, M., Ellis, R. S., Kodama, T., & Conselice, C. J. 2004, The Astrophysical Journal, 601, L123

Cairós, L., Caon, N., Zurita, C., et al. 2009, Astronomy & Astrophysics, 507, 1291

Cairós, L. M., Vílchez, J. M., Pérez, J. N. G., Iglesias-Páramo, J., & Caon, N. 2001, The Astrophysical Journal Supplement Series, 133, 321

Campbell, A., Terlevich, R., & Melnick, J. 1986, Monthly Notices of the Royal Astronomical Society, 223, 811

Cardamone, C., Schawinski, K., Sarzi, M., et al. 2009, Monthly Notices of the Royal Astronomical Society, 399, 1191

Cardelli, J. A., Clayton, G. C., & Mathis, J. S. 1989, The Astrophysical Journal, 345, 245

Cassata, P., Le Fèvre, O., Charlot, S., et al. 2013, Astronomy & Astrophysics, 556, A68

Castellano, M., Pentericci, L., Fontana, A., et al. 2017, The Astrophysical Journal, 839, 73

Catalán-Torrecilla, C., De Paz, A. G., Castillo-Morales, A., et al. 2015, Astronomy & Astrophysics, 584, A87

Cava, A., Pérez-González, P. G., Eliche-Moral, M. C., et al. 2015, The Astrophysical Journal, 812, 155

Cedrés, B., Bongiovanni, Á., Cerviño, M., et al. 2021, Astronomy & Astrophysics, 649, A73

Cen, R. & Kimm, T. 2015, The Astrophysical Journal Letters, 801, L25

Cenarro, A. J., Moles, M., Cristóbal-Hornillos, D., et al. 2019, Astronomy & Astrophysics, 622, A176

Chen, Z., Stark, D. P., Endsley, R., et al. 2023, Monthly Notices of the Royal Astronomical Society

Choi, J.-H. & Nagamine, K. 2009, Monthly Notices of the Royal Astronomical Society, 393, 1595

Comparat, J., Zhu, G., Gonzalez-Perez, V., et al. 2016, Monthly Notices of the Royal Astronomical Society, 461, 1076

Conselice, C. J., Yang, C., & Bluck, A. F. 2009, Monthly Notices of the Royal Astronomical Society, 394, 1956

Conti, P. S. 1991, Astrophysical Journal, Part 1 (ISSN 0004-637X), vol. 377, Aug. 10, 1991, p. 115-125., 377, 115

Cowie, L. L. & Hu, E. M. 1998, The Astronomical Journal, 115, 1319

Croswell, K. 1996, The alchemy of the heavens.

Curtis-Lake, E., Carniani, S., Cameron, A., et al. 2022, arXiv preprint arXiv:2212.04568

Curtis-Lake, E., Carniani, S., Cameron, A., et al. 2023, Nature Astronomy, 7, 622

Darvish, B., Mobasher, B., Sobral, D., et al. 2015, The Astrophysical Journal, 814, 84

Davidson, K., Kinman, T., & Friedman, S. 1989, Astronomical Journal (ISSN 0004-6256), vol. 97, June 1989, p. 1591-1599., 97, 1591

De Barros, S., Oesch, P., Labbé, I., et al. 2019, Monthly Notices of the Royal Astronomical Society, 489, 2355

Delgado, R. G., Díaz-García, L., de Amorim, A., et al. 2021, Astronomy & Astrophysics, 649, A79

Djorgovski, S., Castro, S., Stern, D., & Mahabal, A. 2001, The Astrophysical Journal, 560, L5

Dodelson, S. & Schmidt, F. 2020, Modern cosmology (Academic press)

Dressler, A., Henry, A., Martin, C. L., et al. 2015, The Astrophysical Journal, 806, 19

Duarte Puertas, S., Vilchez, J. M., Iglesias-Páramo, J., et al. 2022, Astronomy & Astrophysics, arXiv:2205.01203

Dufour, R. J., Esteban, C., & Castañeda, H. O. 1996, The Astrophysical Journal, 471, L87

Dufour, R. J. & Hester, J. J. 1990, Astrophysical Journal, Part 1 (ISSN 0004-637X), vol. 350, Feb. 10, 1990, p. 149-154., 350, 149

Ebeling, H., White, D., & Rangarajan, F. 2006, Monthly Notices of the Royal Astronomical Society, 368, 65

Efron, B. & Tibshirani, R. 1985, Behaviormetrika, 12, 1

Endsley, R., Stark, D. P., Chevallard, J., & Charlot, S. 2021, Monthly Notices of the Royal Astronomical Society, 500, 5229

Erb, D. K., Pettini, M., Steidel, C. C., et al. 2016, The Astrophysical Journal, 830, 52

Feltre, A., Maseda, M. V., Bacon, R., et al. 2020, https://www.aanda.org/articles/aa/abs/2020/09/aa38133-20/aa38133-20.htmlAstronomy & Astrophysics, 641, A118

Frebel, A. & Bromm, V. 2012, The Astrophysical Journal, 759, 115

García-Díaz, M. T., Henney, W., López, J., et al. 2008, arXiv preprint arXiv:0802.0518

Giavalisco, M. 2002, Annual Review of Astronomy and Astrophysics, 40, 579

Gil de Paz, A. G., Carrasco, E., Gallego, J., et al. 2016, in Ground-based and Airborne Instrumentation for Astronomy VI, Vol. 9908, SPIE, 420–439

Götberg, Y., de Mink, S., Groh, J., Leitherer, C., & Norman, C. 2019, Astronomy & Astrophysics, 629, A134

Greif, T. H., Johnson, J. L., Klessen, R. S., & Bromm, V. 2008, Monthly Notices of the Royal Astronomical Society, 387, 1021

Haemmerlé, L., Mayer, L., Klessen, R. S., et al. 2020, Space Science Reviews, 216, 48

Hatano, S., Ouchi, M., Nakajima, K., et al. 2023, arXiv preprint arXiv:2304.03726

Hayes, M. J., Runnholm, A., Scarlata, C., Gronke, M., & Rivera-Thorsen, T. E. 2023, Monthly Notices of the Royal Astronomical Society, 520, 5903

Henry, A., Berg, D. A., Scarlata, C., Verhamme, A., & Erb, D. 2018, The Astrophysical Journal, 855, 96

Herenz, E. C., Hayes, M., Papaderos, P., et al. 2017, Astronomy & Astrophysics, 606, L11

Herenz, E. C., Inoue, J., Salas, H., et al. 2023, Astronomy & Astrophysics, 670, A121

Hogarth, L., Amorín, R., Vílchez, J., et al. 2020, Monthly Notices of the Royal Astronomical Society, 494, 3541

Hubble, E. 1929, Proceedings of the national academy of sciences, 15, 168

Hubble, E. P. 1926, Astrophysical Journal, 63, 236-274 (1926), 63

Huggins, W. 1864, Philosophical Transactions of the Royal Society of London, 437

Iglesias-Páramo, J., Arroyo, A., Kehrig, C., et al. 2022, Astronomy & Astrophysics, 665, A95

Iglesias-Páramo, J. & Munoz-Tunón, C. 2002, Monthly Notices of the Royal Astronomical Society, 336, 33

Isobe, Y., Ouchi, M., Nakajima, K., et al. 2023, The Astrophysical Journal, 951, 102

Izotov, Y., Chisholm, J., Worseck, G., et al. 2022, Monthly Notices of the Royal Astronomical Society, 515, 2864

Izotov, Y., Orlitová, I., Schaerer, D., et al. 2016a, Nature, 529, 178

Izotov, Y., Schaerer, D., Thuan, T., et al. 2016b, Monthly Notices of the Royal Astronomical Society, 461, 3683

Izotov, Y. I., Guseva, N. G., & Thuan, T. X. 2011, The Astrophysical Journal, 728, 161

Izotov, Y. I. & Thuan, T. X. 1999, The Astrophysical Journal, 511, 639

James, B., Tsamis, Y., & Barlow, M. 2010, Monthly Notices of the Royal Astronomical Society, 401, 759

Jaskot, A. & Oey, M. 2013, The Astrophysical Journal, 766, 91

Jaskot, A. & Oey, M. 2014, The Astrophysical Journal Letters, 791, L19

Jaskot, A. E., Oey, M., Scarlata, C., & Dowd, T. 2017, The Astrophysical Journal Letters, 851, L9

Johnson, J. L. 2010, Monthly Notices of the Royal Astronomical Society, 404, 1425

Karim, A., Schinnerer, E., Martínez-Sansigre, A., et al. 2011, The Astrophysical Journal, 730, 61

Kauffmann, G., Heckman, T. M., Tremonti, C., et al. 2003, Monthly Notices of the Royal Astronomical Society, 346, 1055

Kauffmann, G., Heckman, T. M., Tremonti, C., et al. 2003, Monthly Notices of the Royal Astronomical Society, 346, 1055

Kehrig, C., Iglesias-Páramo, J., Vílchez, J., et al. 2020, Monthly Notices of the Royal Astronomical Society, 498, 1638

Kehrig, C., Vílchez, J., Guerrero, M. A., et al. 2018, Monthly Notices of the Royal Astronomical Society, 480, 1081

Kehrig, C., Vílchez, J., Pérez-Montero, E., et al. 2015, The Astrophysical Journal Letters, 801, L28

Kehrig, C., Vílchez, J., Pérez-Montero, E., et al. 2016, Monthly Notices of the Royal Astronomical Society, 459, 2992

Kehrig, C., Vílchez, J., Sánchez, S., et al. 2008, Astronomy & Astrophysics, 477, 813

Kennicutt Jr, R. C. 1998, The astrophysical journal, 498, 541

Kerutt, J., Wisotzki, L., Verhamme, A., et al. 2022, Astronomy & Astrophysics, 659, A183

Kewley, L. J., Dopita, M. A., Sutherland, R. S., Heisler, C. A., & Trevena, J. 2001, The Astrophysical Journal, 556, 121

Kewley, L. J., Groves, B., Kauffmann, G., & Heckman, T. 2006, Monthly Notices of the Royal Astronomical Society, 372, 961

Khostovan, A. A., Sobral, D., Mobasher, B., et al. 2016, Monthly Notices of the Royal Astronomical Society, 463, 2363

Khusanova, Y., Le Fèvre, O., Cassata, P., et al. 2020, Astronomy & Astrophysics, 634, A97

Kim, K., Malhotra, S., Rhoads, J. E., Butler, N. R., & Yang, H. 2020, The Astrophysical Journal, 893, 134

King, A. 2005, The Astrophysical Journal, 635, L121

Kolb, E. W. & Turner, M. S. 2018, The early universe (CRC press)

Köppen, J. & Hensler, G. 2005, Astronomy & Astrophysics, 434, 531

Kroupa, P. 2004, arXiv preprint astro-ph/0412069

Kunth, D., Leitherer, C., Mas-Hesse, J. M., Östlin, G., & Petrosian, A. 2003, The Astrophysical Journal, 597, 263

Kunth, D. & Sargent, W. 1986, The Astrophysical Journal, 300, 496

Labbé, I., Oesch, P. A., Bouwens, R. J., et al. 2013, The Astrophysical Journal Letters, 777, L19

Laufman, L., Scarlata, C., Hayes, M., & Skillman, E. 2022, The Astrophysical Journal, 940, 31

Lebouteiller, V., Péquignot, D., Cormier, D., et al. 2017, Astronomy & Astrophysics, 602, A45

Legrand, F. 1999, arXiv preprint astro-ph/9912115

Legrand, F., Kunth, D., Roy, J.-R., Mas-Hesse, J., & Walsh, J. 1997, arXiv preprint astro-ph/9707279

Lelli, F., Verheijen, M., Fraternali, F., & Sancisi, R. 2012, (**?**)Astronomy & Astrophysics, 537, A72

Lemaître, G. 1927, Annales de la Société Scientifique de Bruxelles, A47, p. 49-59, 47, 49

Lequeux, J. & Viallefond, F. 1980, Astronomy & Astrophysics, 91, 269

Lintott, C. J., Schawinski, K., Slosar, A., et al. 2008, Monthly Notices of the Royal Astronomical Society, 389, 1179

Lofthouse, E. K., Houghton, R. C., & Kaviraj, S. 2017, Monthly Notices of the Royal Astronomical Society, 471, 2311

Lumbreras-Calle, A., López-Sanjuan, C., Sobral, D., et al. 2021, arXiv preprint arXiv:2112.06938

Lumbreras-Calle, A., López-Sanjuan, C., Sobral, D., et al. 2022, Astronomy & Astrophysics, 668, A60

Luridiana, V., Morisset, C., & Shaw, R. A. 2015, Astronomy & Astrophysics, 573, A42

Ma, X., Hayward, C. C., Casey, C. M., et al. 2019, Monthly Notices of the Royal Astronomical Society, 487, 1844

Maio, U., Ciardi, B., Dolag, K., Tornatore, L., & Khochfar, S. 2010, Monthly Notices of the Royal Astronomical Society, 407, 1003

Malhotra, S. & Rhoads, J. E. 2002, The Astrophysical Journal, 565, L71

Martin, C. L. 1996, arXiv preprint astro-ph/9601107

Martínez-Solaeche, G., Delgado, R. G., García-Benito, R., et al. 2021, Astronomy & Astrophysics, 647, A158

Martínez-Solaeche, G., Delgado, R. G., García-Benito, R., et al. 2022, Astronomy & Astrophysics, 661, A99

Maseda, M. V., van der Wel, A., Rix, H.-W., et al. 2018, The Astrophysical Journal, 854, 29

Mason, C. A., Treu, T., Fontana, A., et al. 2017, The Astrophysical Journal, 838, 14

Mathis, J. S. 1990, Annual Review of Astronomy and Astrophysics, 28, 37

Matthee, J., Naidu, R. P., Pezzulli, G., et al. 2022, Monthly Notices of the Royal Astronomical Society, 512, 5960

McKinney, J. H., Jaskot, A. E., Oey, M., et al. 2019, The Astrophysical Journal, 874, 52

Melia, F. & Yennapureddy, M. K. 2018, Monthly Notices of the Royal Astronomical Society, 480, 2144

Molina, M., Reines, A. E., Latimer, C. J., Baldassare, V., & Salehirad, S. 2021, The Astrophysical Journal, 922, 155

Mollá, M., Vílchez, J., Gavilán, M., & Díaz, A. I. 2006, Monthly Notices of the Royal Astronomical Society, 372, 1069

Monreal-Ibero, A., Relaño, M., Kehrig, C., et al. 2011, Monthly Notices of the Royal Astronomical Society, 413, 2242

Moustakas, J. & Kennicutt Jr, R. C. 2006, The Astrophysical Journal Supplement Series, 164, 81

Nadler, E. O., Benson, A., Driskell, T., Du, X., & Gluscevic, V. 2023, Monthly Notices of the Royal Astronomical Society, 521, 3201

Naidu, R. P., Matthee, J., Oesch, P. A., et al. 2022a, Monthly Notices of the Royal Astronomical Society, 510, 4582

Naidu, R. P., Oesch, P. A., van Dokkum, P., et al. 2022b, The Astrophysical Journal Letters, 940, L14

Nakajima, K., Fletcher, T., Ellis, R. S., Robertson, B. E., & Iwata, I. 2018, Monthly Notices of the Royal Astronomical Society, 477, 2098

Nakamura, F. & Umemura, M. 2001, The Astrophysical Journal, 548, 19

Nozawa, T., Kozasa, T., & Habe, A. 2006, The Astrophysical Journal, 648, 435

Olive, K. A., Steigman, G., & Walker, T. P. 2000, Physics Reports, 333, 389

Olmo-García, A., Almeida, J. S., Muñoz-Tuñón, C., et al. 2017, The Astrophysical Journal, 834, 181

Ono, Y., Ouchi, M., Shimasaku, K., et al. 2010, The Astrophysical Journal, 724, 1524

Osterbrock, D. E. & Ferland, G. J. 2006, Astrophysics of gaseous nebulae and active galactic nuclei, 2nd

Papaderos, P., Gomes, J., Vílchez, J., et al. 2013, Astronomy & Astrophysics, 555, L1

Papaderos, P. & Östlin, G. 2012, Astronomy & Astrophysics, 537, A126

Pascual, S., Cardiel, N., Gil de Paz, A., et al. 2019, Highlights on Spanish Astrophysics X, 227

Paswan, A., Saha, K., Leitherer, C., & Schaerer, D. 2022, The Astrophysical Journal, 924, 47

Peebles, P. J. & Yu, J. 1970, Astrophysical Journal, vol. 162, p. 815, 162, 815

Peebles, P. J. E. 1993, Principles of physical cosmology, Vol. 27 (Princeton university press)

Pellegrini, E. W., Oey, M. S., Winkler, P. F., et al. 2012, The Astrophysical Journal, 755, 40

Peng, Z. 2021, PhD thesis, University of California. Santa Barbara

Pérez-Díaz, B., Pérez-Montero, E., Fernández-Ontiveros, J. A., et al. 2024, Astronomy & Astrophysics, 685, A168

Pérez-Montero, E. 2014, Monthly Notices of the Royal Astronomical Society, 441, 2663

Pérez-Montero, E. 2017, Publications of the Astronomical Society of the Pacific, 129, 043001

Pérez-Montero, E., Amorín, R., Sánchez Almeida, J., et al. 2021, Monthly Notices of the Royal Astronomical Society, 504, 1237

Pérez-Montero, E., Kehrig, C., Vílchez, J., et al. 2020, Astronomy & Astrophysics, 643, A80

Pérez-Montero, E., Vílchez, J., Cedrés, B., et al. 2011, Astronomy & Astrophysics, 532, A141

Petrosian, A., Boulesteix, J., Comte, G., Kunth, D., & Coarer, E. L. 1996, arXiv

Petrosian, A., Comte, G., Boulesteix, J., et al. 1995, Astrophysics, 38, 335

Pettini, M. & Pagel, B. E. 2004, Monthly Notices of the Royal Astronomical Society, 348, L59

Pilyugin, L. 1992, Astronomy and Astrophysics (ISSN 0004-6361), vol. 260, no. 1-2, p. 58-66., 260, 58

Pontoppidan, K. M., Barrientes, J., Blome, C., et al. 2022, The Astrophysical Journal Letters, 936, L14

Prada, F., Vitvitska, M., Klypin, A., et al. 2003, The Astrophysical Journal, 598, 260

Ramos, R. C., Annibali, F., Fiorentino, G., et al. 2011, The Astrophysical Journal, 739, 74

Rhoads, J. E., Wold, I. G. B., Harish, S., et al. 2022, The Astrophysical Journal, arXiv:2207.13020

Robertson, B., Tacchella, S., Johnson, B., et al. 2022, arXiv preprint arXiv:2212.04480

Ryden, B. 2017, Introduction to cosmology (Cambridge University Press)

Salvaterra, R., Ferrara, A., & Dayal, P. 2011, Monthly Notices of the Royal Astronomical Society, 414, 847

Schaerer, D., Marques-Chaves, R., Barrufet, L., et al. 2022, Astronomy & Astrophysics, 665, L4

Schechter, P. 1976, The Astrophysical Journal, 203, 297

Senchyna, P., Stark, D. P., Vidal-García, A., et al. 2017, Monthly Notices of the Royal Astronomical Society, 472, 2608

Shankar, F., Weinberg, D. H., Marsden, C., et al. 2020, Monthly Notices of the Royal Astronomical Society, 493, 1500

Shirazi, M. & Brinchmann, J. 2012, Monthly Notices of the Royal Astronomical Society, 421, 1043

Siana, B., Teplitz, H. I., Colbert, J., et al. 2007, The Astrophysical Journal, 668, 62

Singh, S., Nambissan T, J., Subrahmanyan, R., et al. 2022, Nature Astronomy, 6, 607

Smit, R., Bouwens, R. J., Franx, M., et al. 2015, The Astrophysical Journal, 801, 122

Smith, B. M., Windhorst, R. A., Cohen, S. H., et al. 2020, The Astrophysical Journal, 897, 41

Sobral, D., Best, P. N., Smail, I., et al. 2014, Monthly Notices of the Royal Astronomical Society, 437, 3516

Sobral, D. & Matthee, J. 2019, Astronomy & Astrophysics, 623, A157

Sobral, D., Matthee, J., Darvish, B., et al. 2018a, Monthly Notices of the Royal Astronomical Society, 477, 2817

Sobral, D., Santos, S., Matthee, J., et al. 2018b, Monthly Notices of the Royal Astronomical Society, 476, 4725

Sobral, D., Smail, I., Best, P. N., et al. 2013, Monthly Notices of the Royal Astronomical Society, 428, 1128

Spinoso, D., Orsi, A., López-Sanjuan, C., et al. 2020, Astronomy & Astrophysics, 643, A149

Springel, V., White, S. D., Jenkins, A., et al. 2005, nature, 435, 629

Tasca, L., Le Fèvre, O., Hathi, N., et al. 2015, Astronomy & Astrophysics, 581, A54

Terlevich, R. & Melnick, J. 1981, Monthly Notices of the Royal Astronomical Society, 195, 839

Terlevich, R., Melnick, J., Masegosa, J., Moles, M., & Copetti, M. 1991, Astronomy and Astrophysics Supplement Series (ISSN 0365-0138), vol. 91, no. 2, Dec. 1991, p. 285-324., 91, 285

Terlevich, R., Terlevich, E., Melnick, J., et al. 2015, Monthly Notices of the Royal Astronomical Society, 451, 3001

Thomas, D., Steele, O., Maraston, C., et al. 2013, Monthly Notices of the Royal Astronomical Society, 431, 1383

Thuan, T. X. & Martin, G. E. 1981, Astrophysical Journal, Part 1, vol. 247, Aug. 1, 1981, p. 823-848. Research supported by the Research Corp.;, 247, 823

Tikhonov, N. 2007, Astronomy Letters, 33, 137

van der Wel, A., Straughn, A., Rix, H.-W., et al. 2011, The Astrophysical Journal, 742, 111

van Zee, L., Westpfahl, D., & Haynes, M. P. 1998, The Astronomical Journal, 115, 1000

Vaught, R. J. R., Sandstrom, K. M., & Hunt, L. K. 2021, The Astrophysical Journal Letters, 911, L17

Verhamme, A., Orlitová, I., Schaerer, D., et al. 2017, Astronomy & Astrophysics, 597, A13

Vílchez, J. M. & Iglesias-Páramo, J. 1998, The Astrophysical Journal, 508, 248

Vincenzo, F., Belfiore, F., Maiolino, R., Matteucci, F., & Ventura, P. 2016, Monthly Notices of the Royal Astronomical Society, 458, 3466

Vogelsberger, M., McKinnon, R., O'Neil, S., et al. 2019, Monthly Notices of the Royal Astronomical Society, 487, 4870

Wagoner, R. V. 1973, The Astrophysical Journal, 179, 343

Wang, B., Heckman, T. M., Amorín, R., et al. 2021, The Astrophysical Journal, 916, 3

Weilbacher, P. M., Palsa, R., Streicher, O., et al. 2020, Astronomy & Astrophysics, 641, A28

Weinberg, S. 2008, Cosmology (OUP Oxford)

Weingartner, J. C., Draine, B. T., & Barr, D. K. 2006, The Astrophysical Journal, 645, 1188

Whitaker, K. E., Van Dokkum, P. G., Brammer, G., & Franx, M. 2012, The Astrophysical Journal Letters, 754, L29

Xu, Y., Ouchi, M., Isobe, Y., et al. 2023, (?)arXiv preprint arXiv:2303.12467

Yang, H., Malhotra, S., Gronke, M., et al. 2016, The Astrophysical Journal, 820, 130

Yang, H., Malhotra, S., Gronke, M., et al. 2017a, The Astrophysical Journal, 844, 171

Yang, H., Malhotra, S., Rhoads, J. E., et al. 2017b, The Astrophysical Journal, 838, 4

Yang, H., Malhotra, S., Rhoads, J. E., & Wang, J. 2017c, The Astrophysical Journal, 847, 38

Yurov, A. V., Astashenok, A. V., & Gonzalez-Diaz, P. F. 2008, Gravitation and Cosmology, 14, 205

Zaroubi, S. 2012, The first galaxies: theoretical predictions and observational clues, 45

Zucconi, A., Walmsley, C., & Galli, D. 2001, Astronomy & Astrophysics, 376, 650

Appendix A

J-PAS

A.1 J-spectra and images of the selected EELG candidates

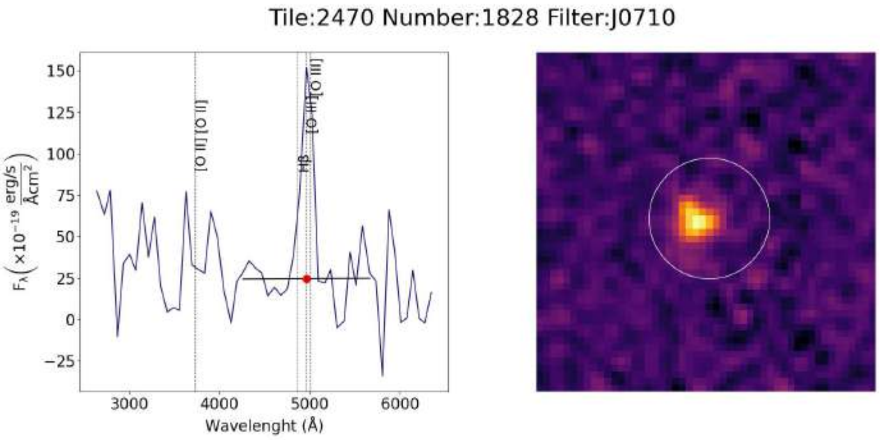

Figure A.1 Data products from J-PAS for the EELG candidates. Left: J-spectrum using the AUTO fluxes. Blue line corresponds to the AUTO fluxes. Red point indicates the central wavelength of the selection filter and the value of the continuum. Black line shows the fit to the continuum The emission lines present in the spectrum are indicated. Right: Cutouts of the image corresponding to the selection filter. The length of the white circle corresponds to 3”.

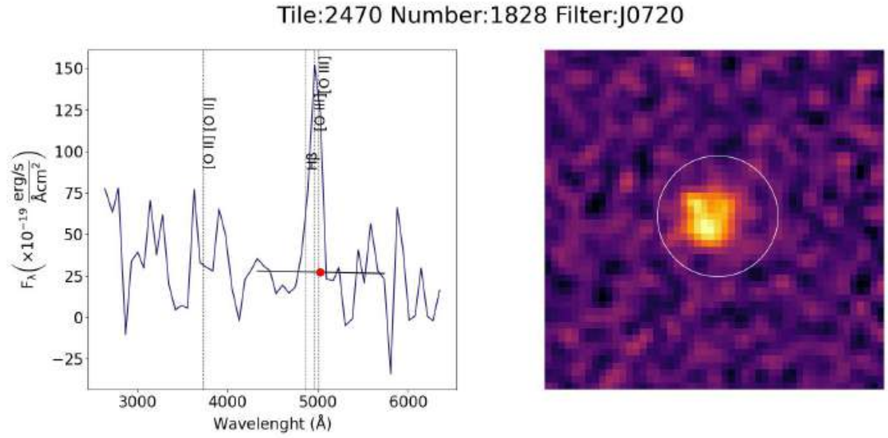
Tile:2470 Number:1828 Filter:J0720

Figure A.1 Continued.

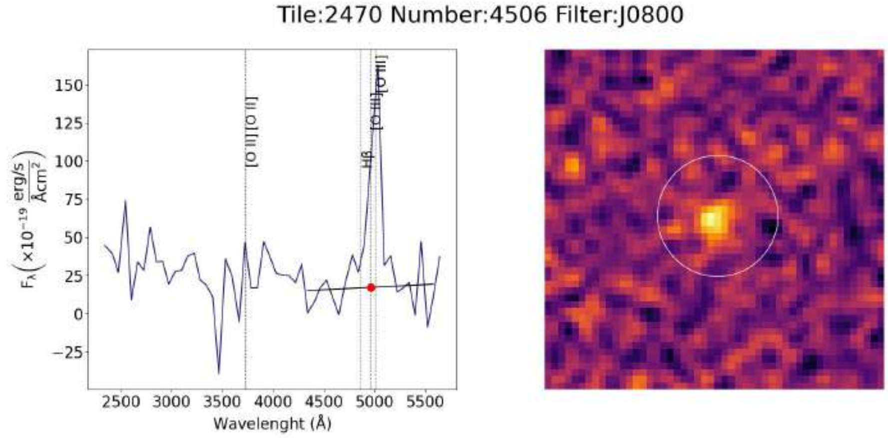
Tile:2470 Number:4506 Filter:J0800

Figure A.1 Continued.

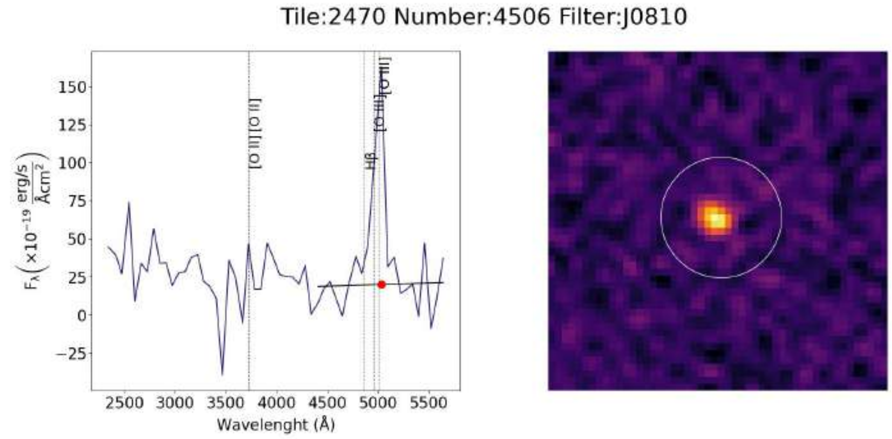

Figure A.1 Continued.

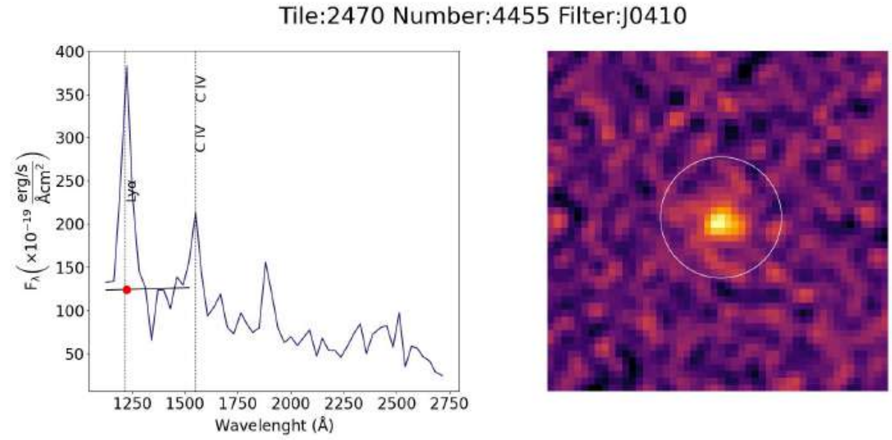

Figure A.1 Continued.

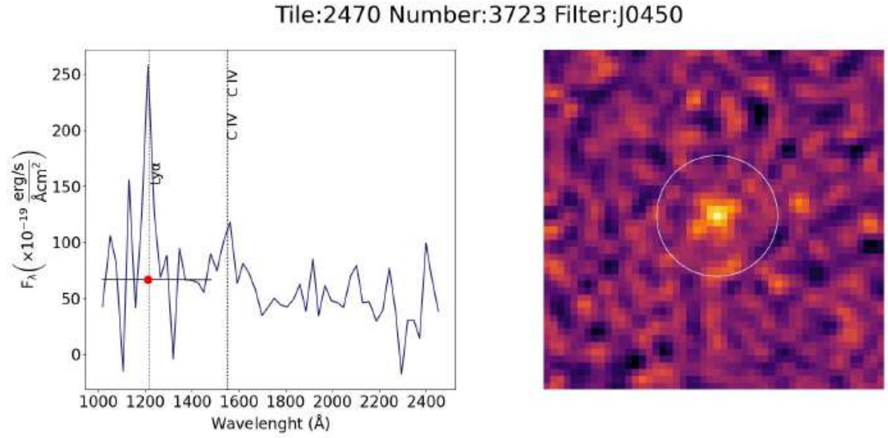

Figure A.1 Continued.

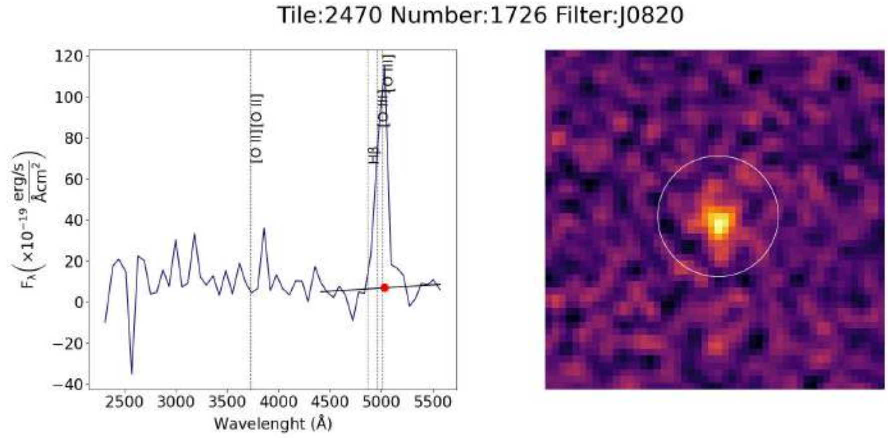

Figure A.1 Continued.

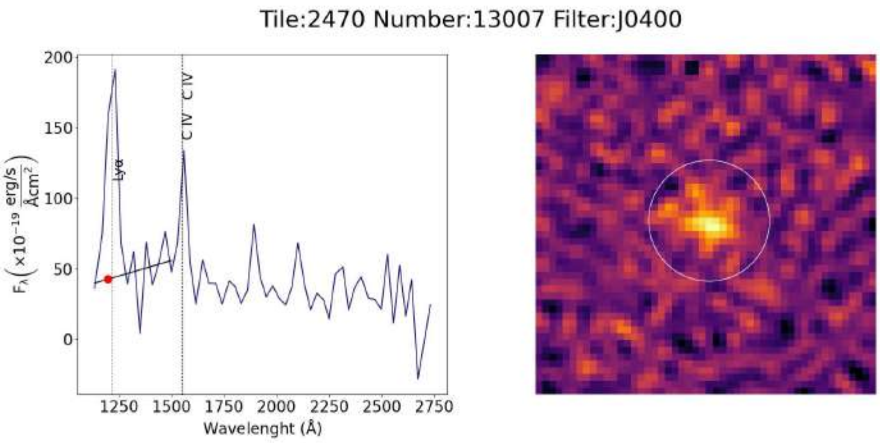

Figure A.1 Continued.

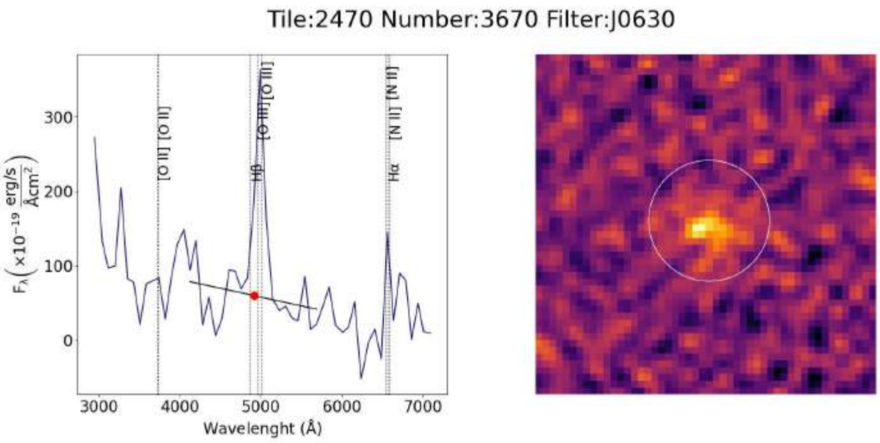

Figure A.1 Continued.

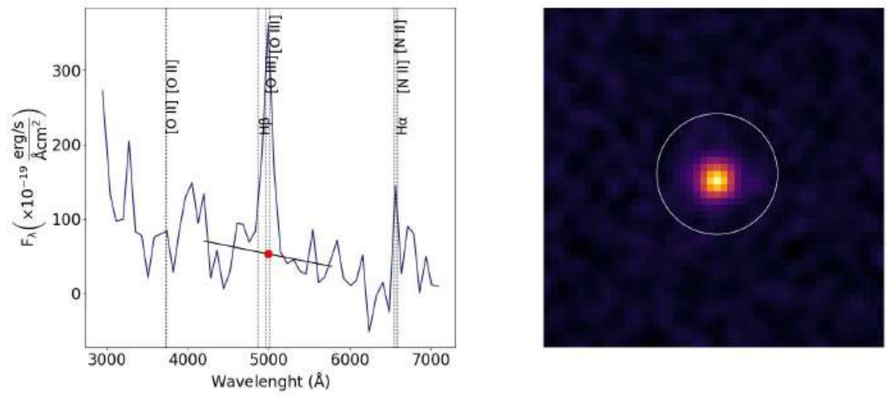

Tile:2470 Number:3670 Filter:J0640

Figure A.1 Continued.

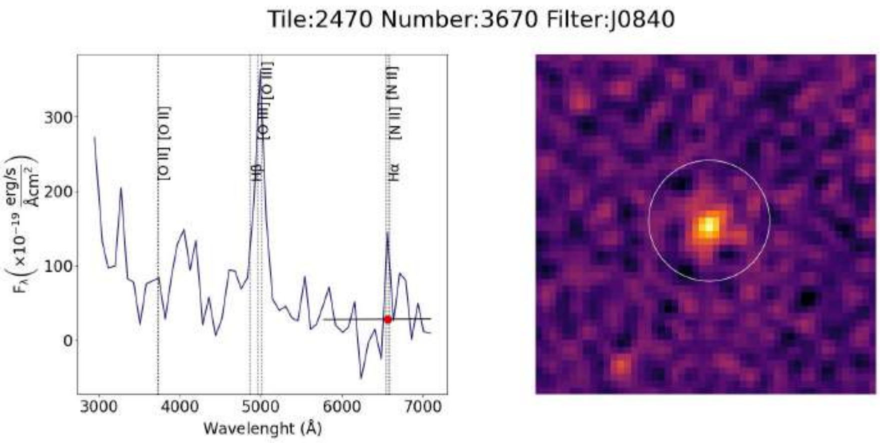
Tile:2470 Number:3670 Filter:J0840

Figure A.1 Continued.

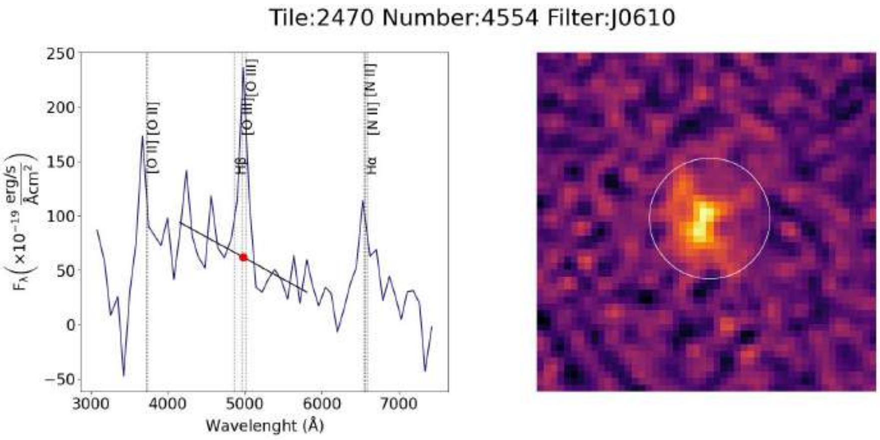
Tile:2470 Number:4554 Filter:J0610

Figure A.1 Continued.

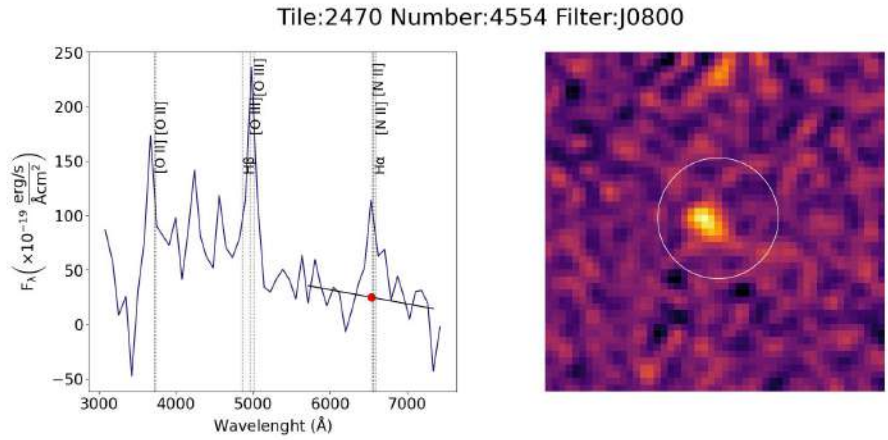

Figure A.1 Continued.

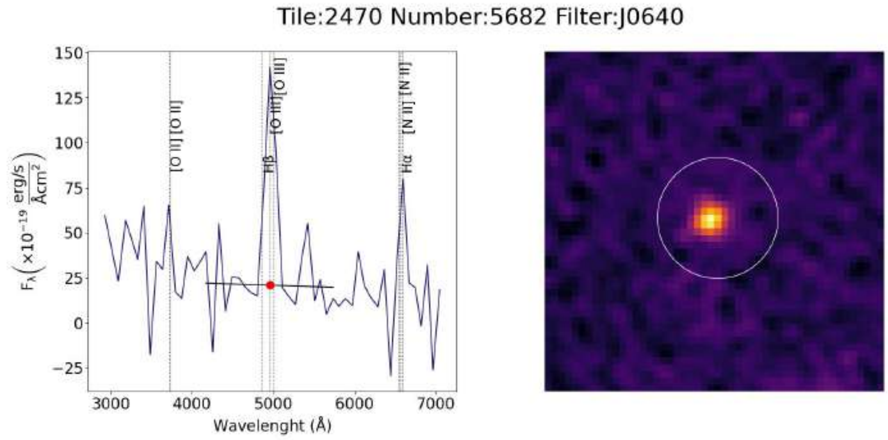

Figure A.1 Continued.

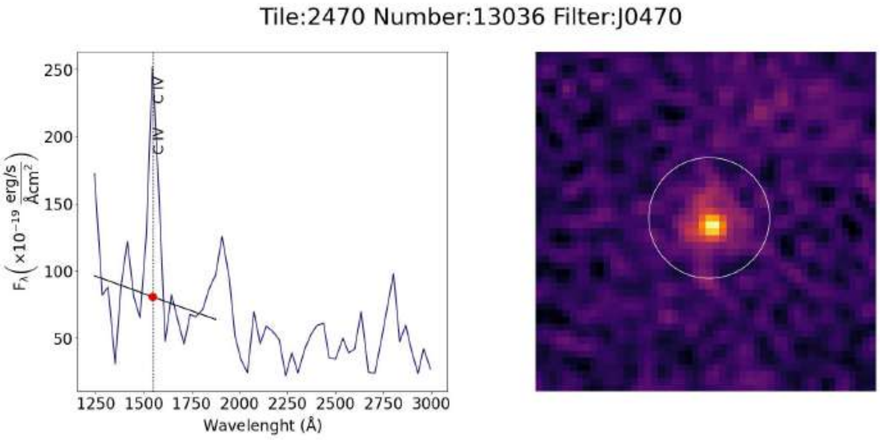

Figure A.1 Continued.

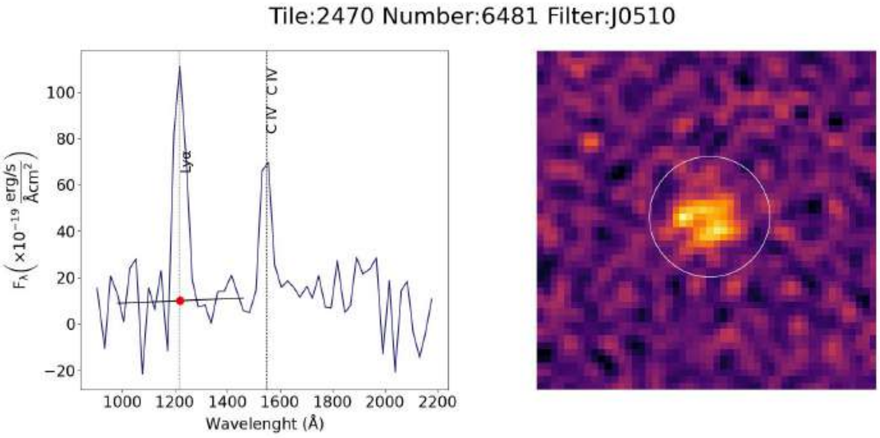

Figure A.1 Continued.

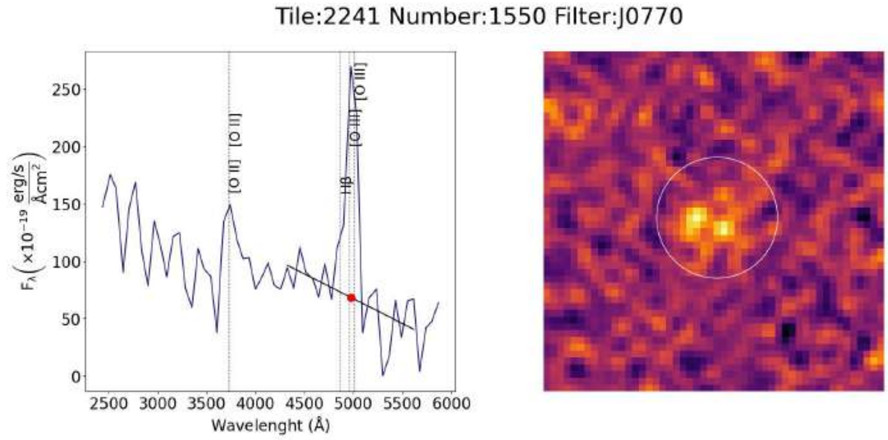

Figure A.1 Continued.

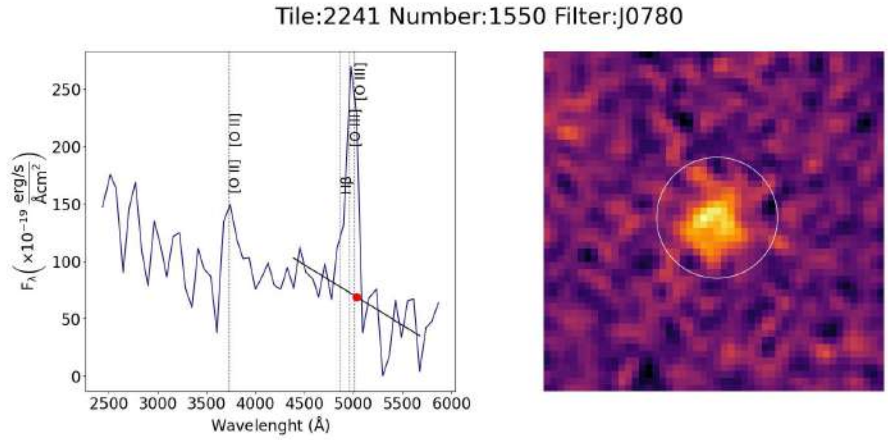

Figure A.1 Continued.

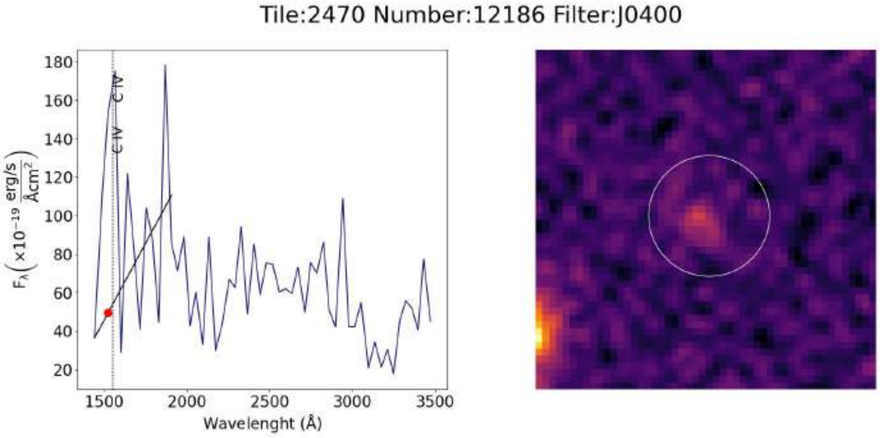

Figure A.1 Continued.

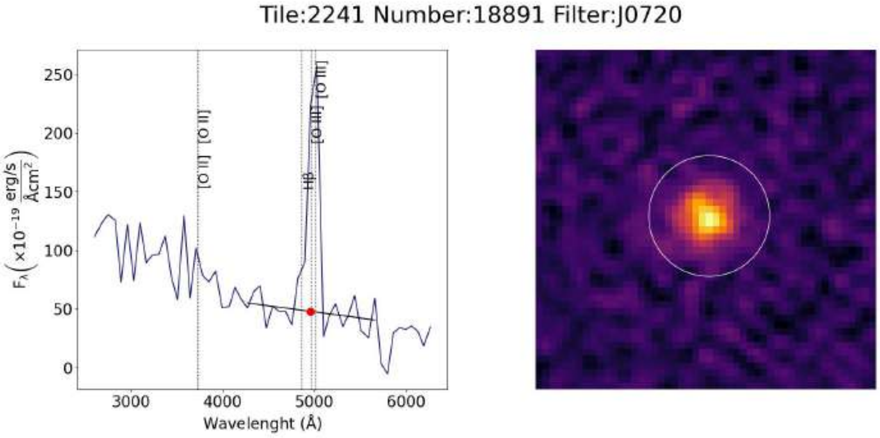

Figure A.1 Continued.

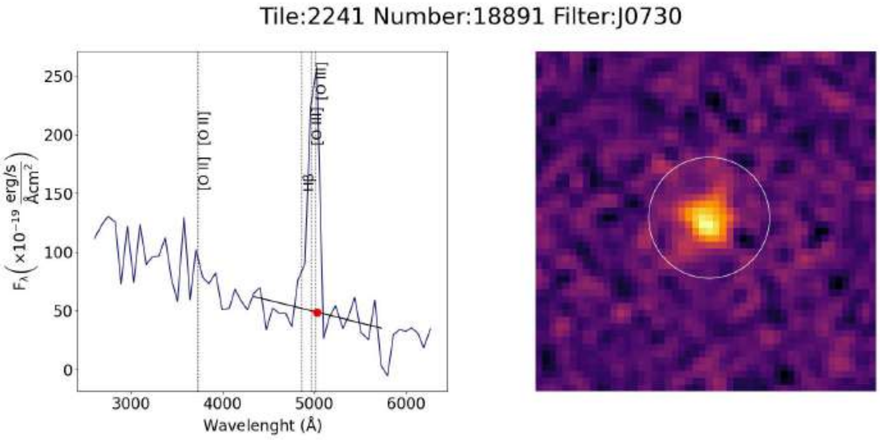

Figure A.1 Continued.

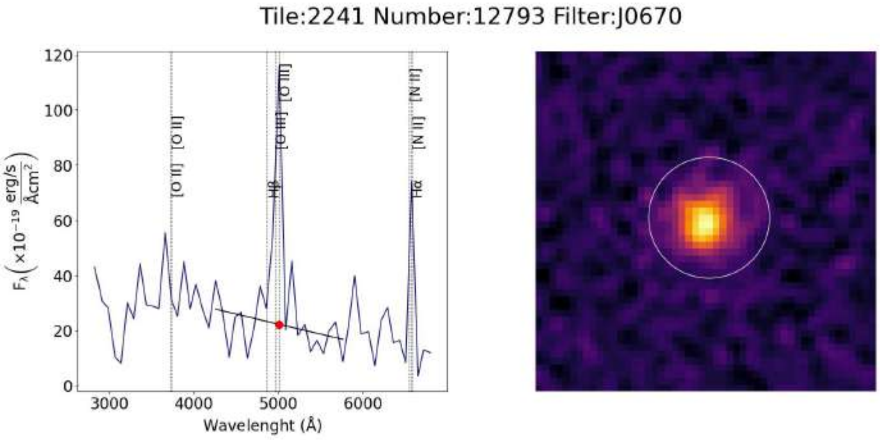

Figure A.1 Continued.

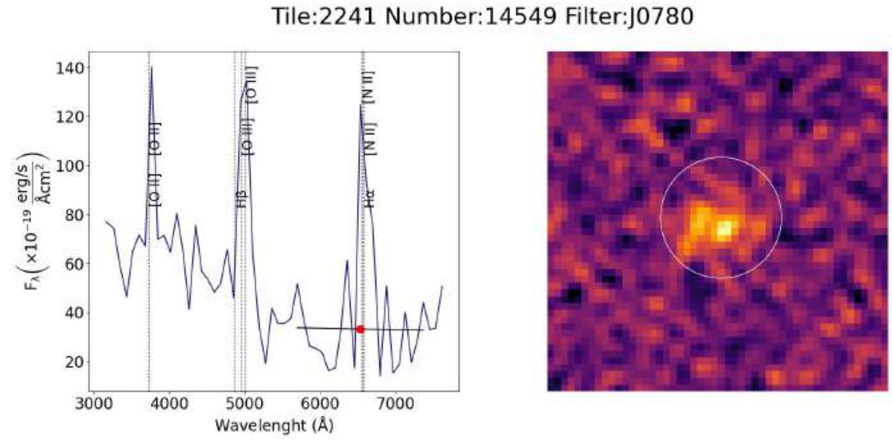

Tile:2241 Number:14549 Filter:J0780

Figure A.1 Continued.

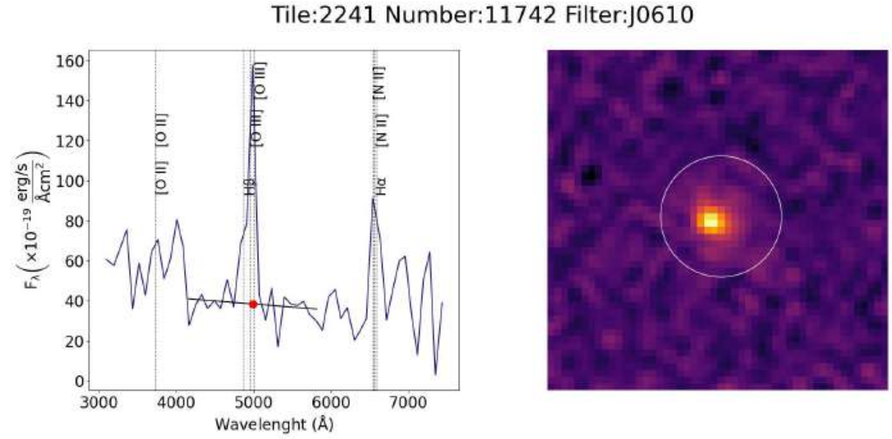

Tile:2241 Number:11742 Filter:J0610

Figure A.1 Continued.

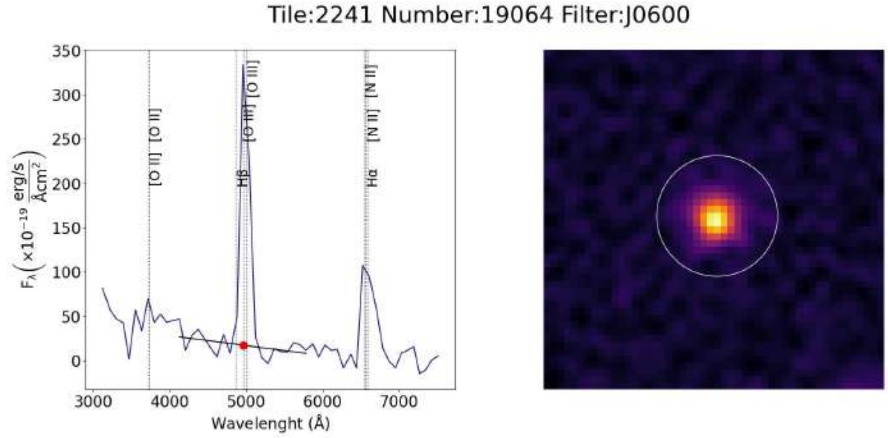

Figure A.1 Continued.

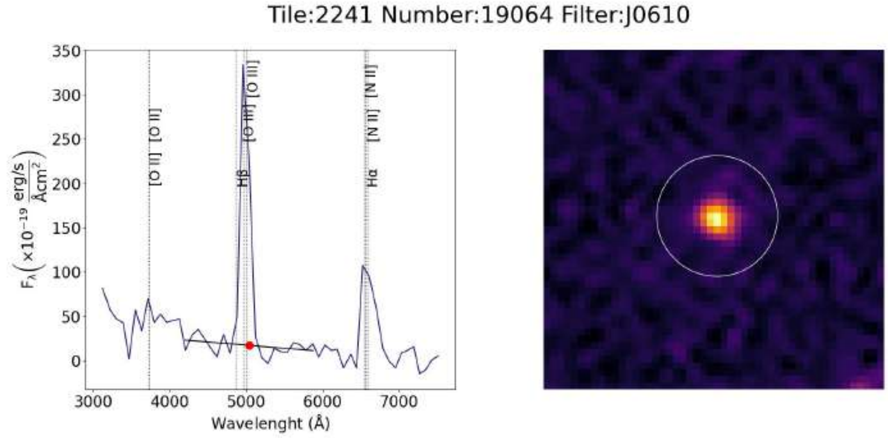

Figure A.1 Continued.

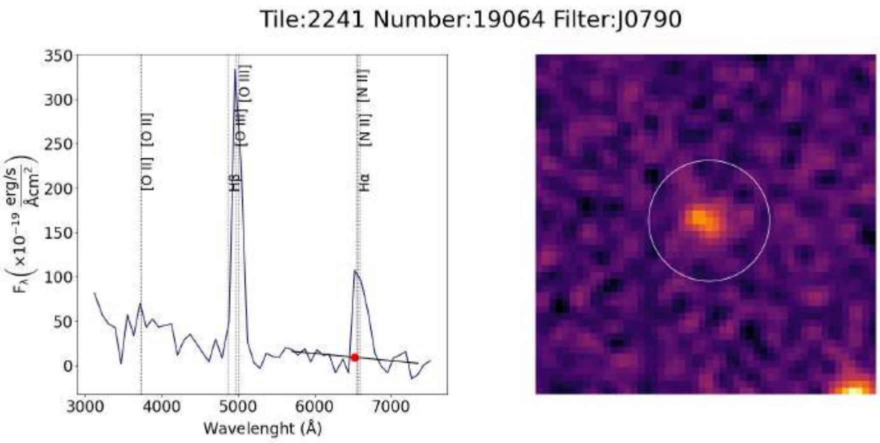

Figure A.1 Continued.

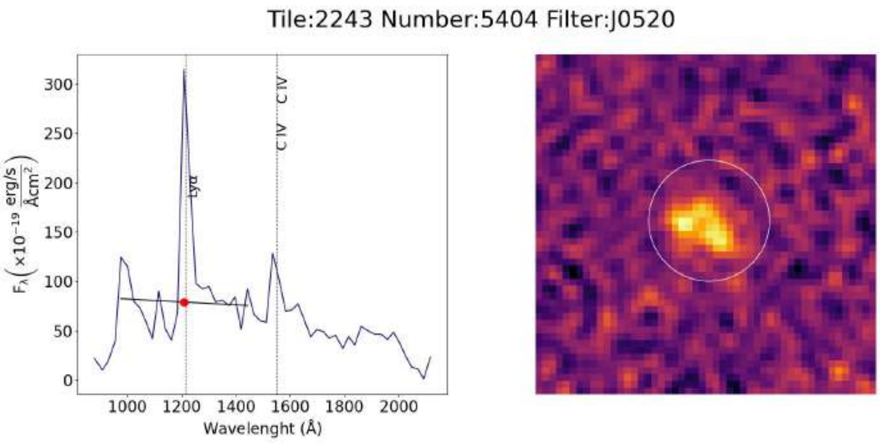

Figure A.1 Continued.

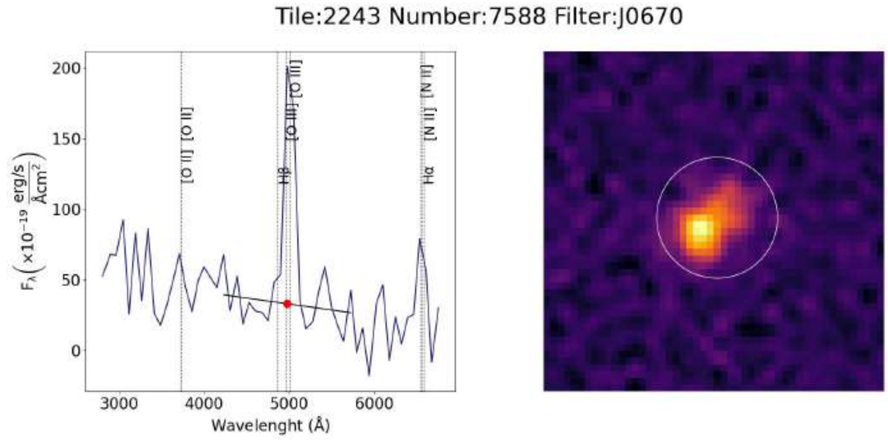

Tile:2243 Number:7588 Filter:J0670

Figure A.1 Continued.

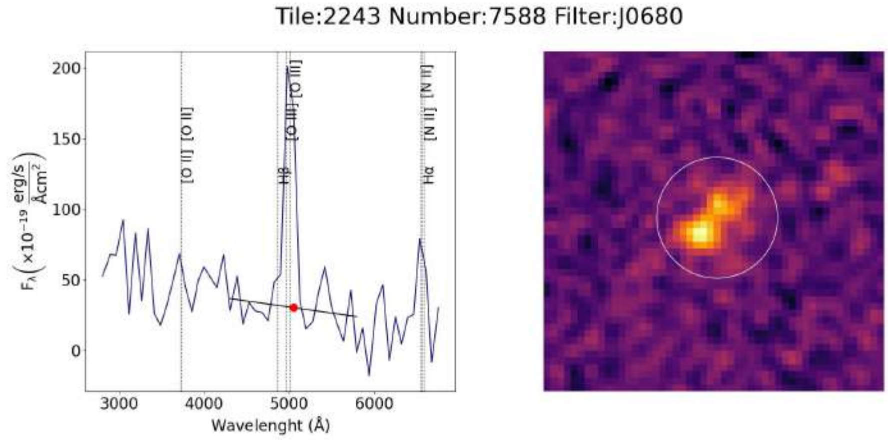

Tile:2243 Number:7588 Filter:J0680

Figure A.1 Continued.

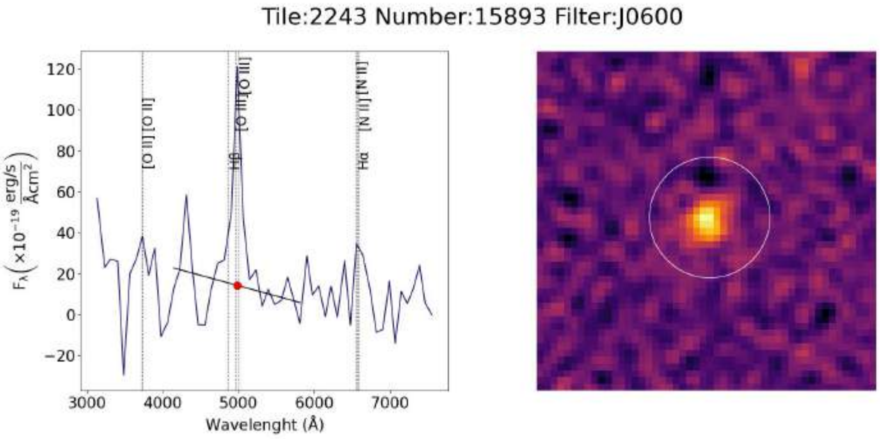

Figure A.1 Continued.

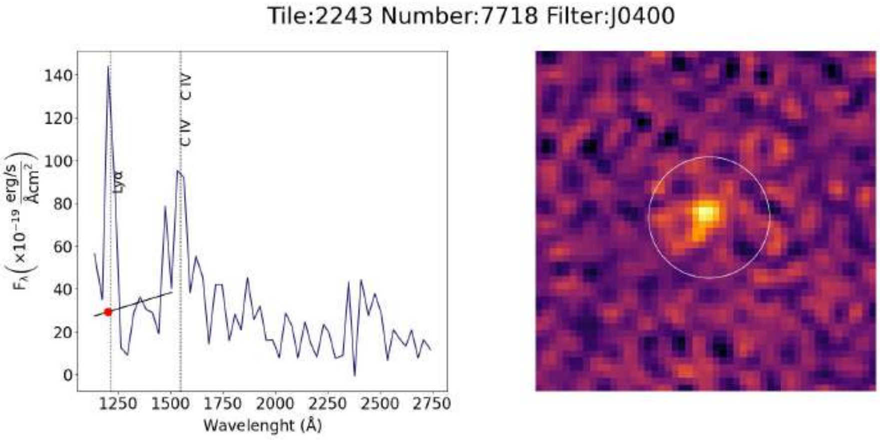

Figure A.1 Continued.

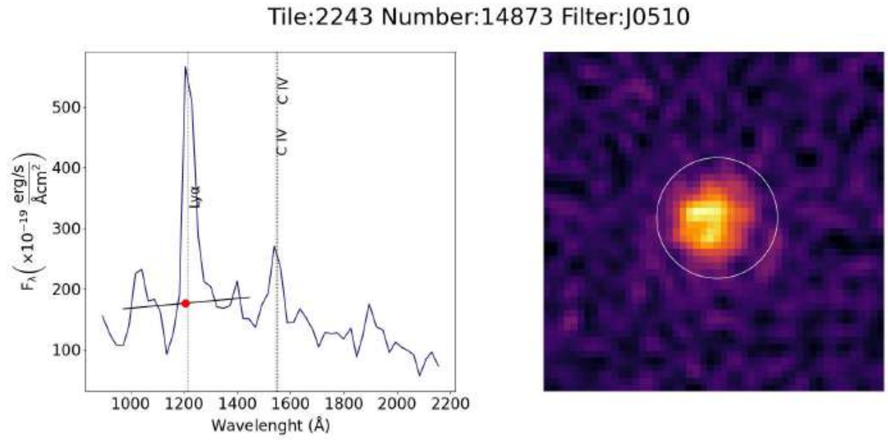

Figure A.1 Continued.

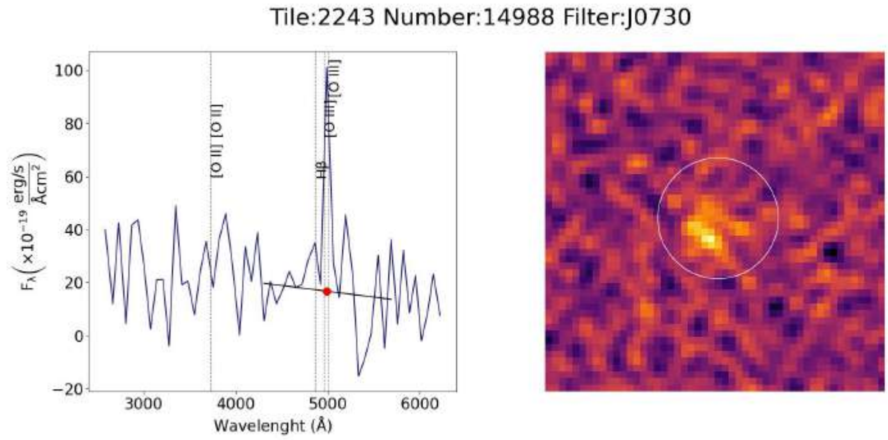

Figure A.1 Continued.

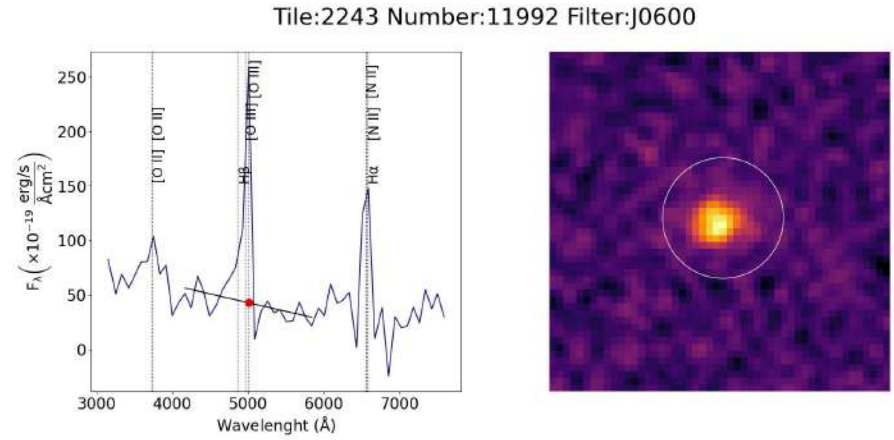

Figure A.1 Continued.

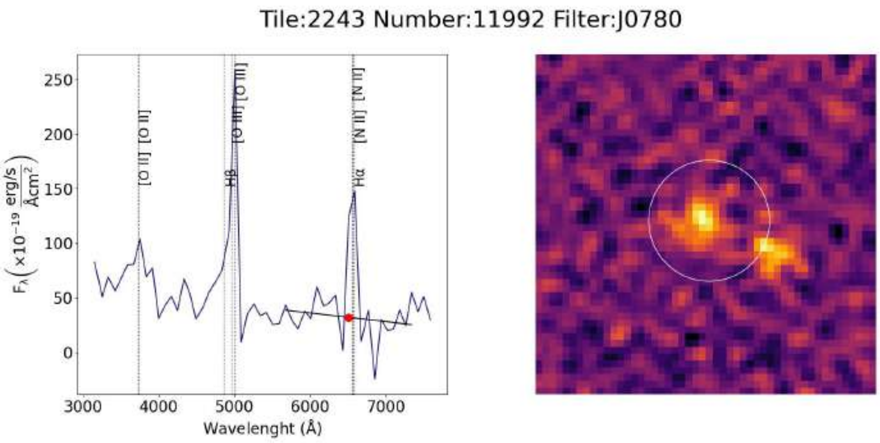

Tile:2243 Number:11992 Filter:J0780

Figure A.1 Continued.

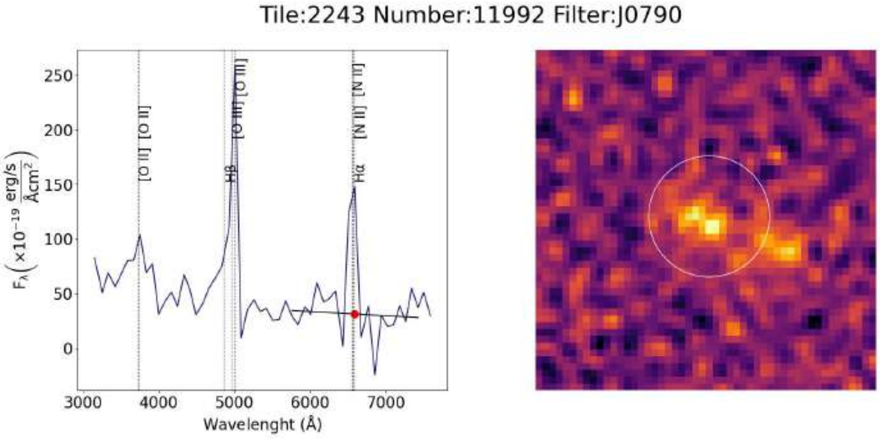

Tile:2243 Number:11992 Filter:J0790

Figure A.1 Continued.

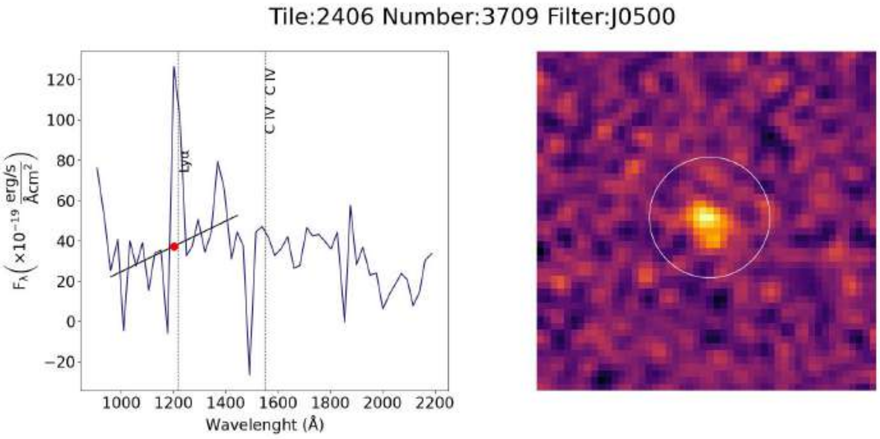

Figure A.1 Continued.

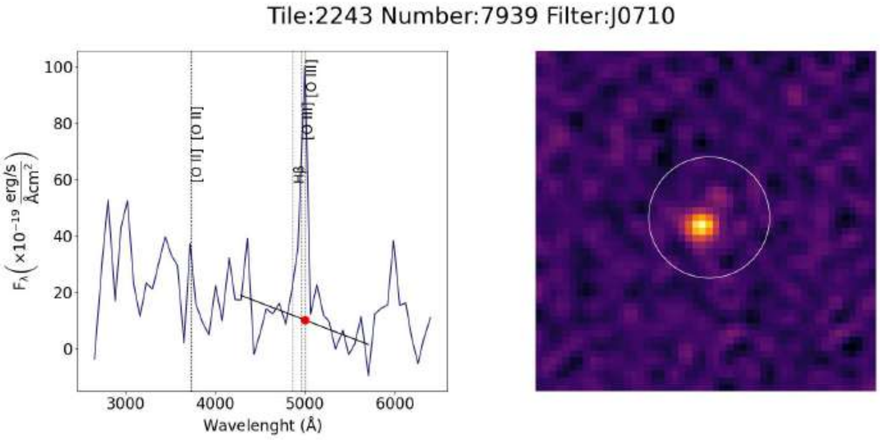

Figure A.1 Continued.

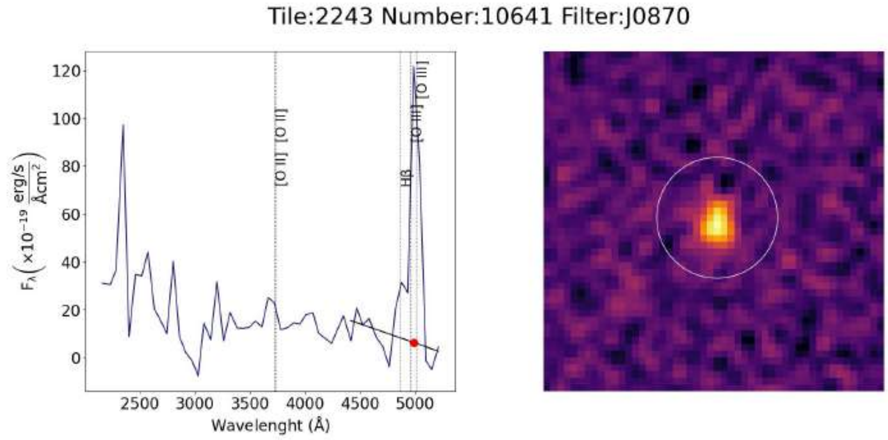

Tile:2243 Number:10641 Filter:J0870

Figure A.1 Continued.

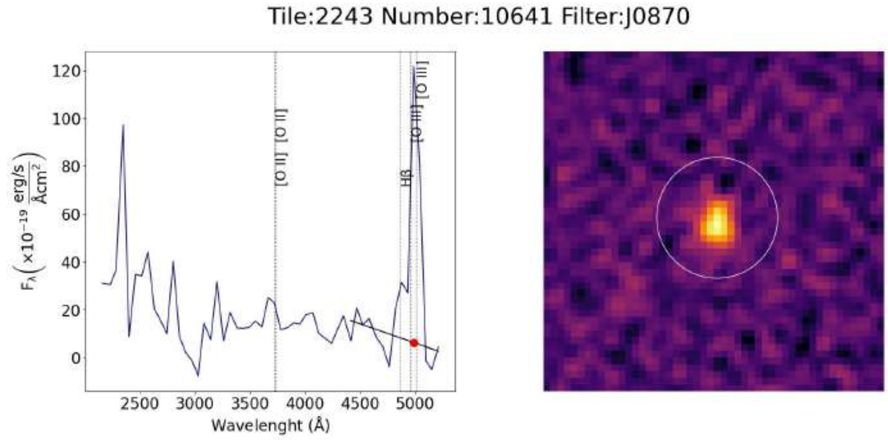

Tile:2243 Number:10641 Filter:J0870

Figure A.1 Continued.

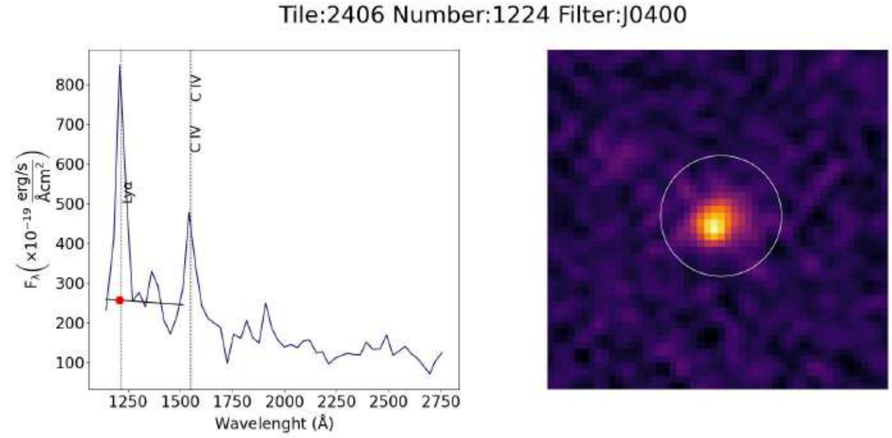

Figure A.1 Continued.

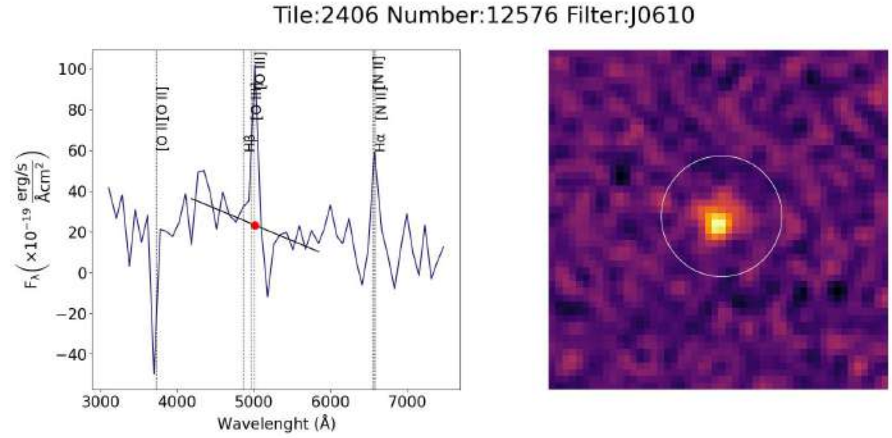

Figure A.1 Continued.

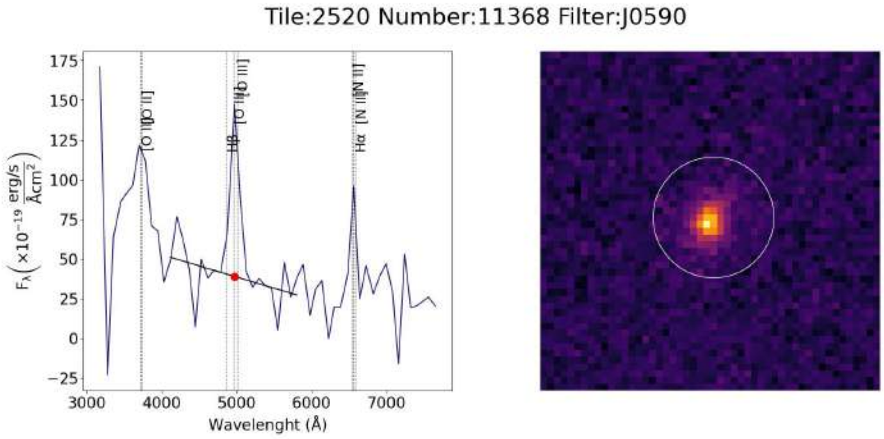

Figure A.1 Continued.

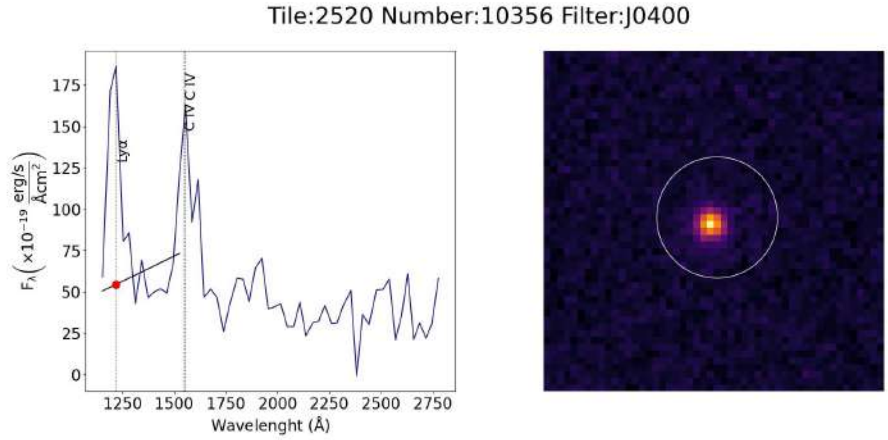

Figure A.1 Continued.

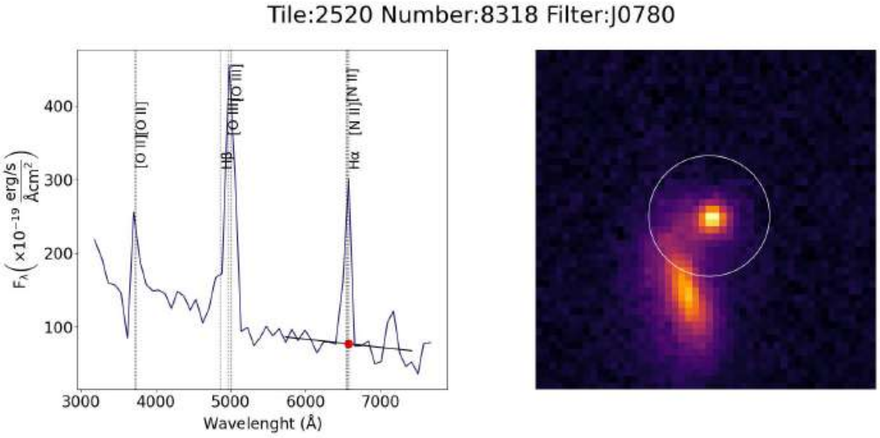

Figure A.1 Continued.

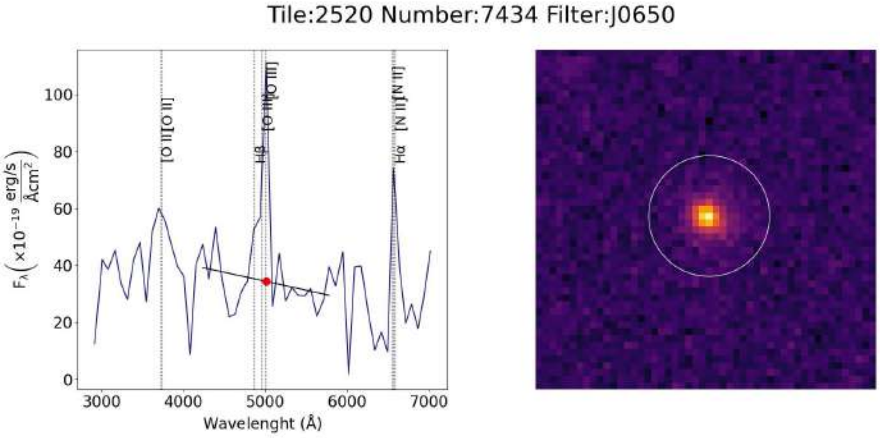

Figure A.1 Continued.

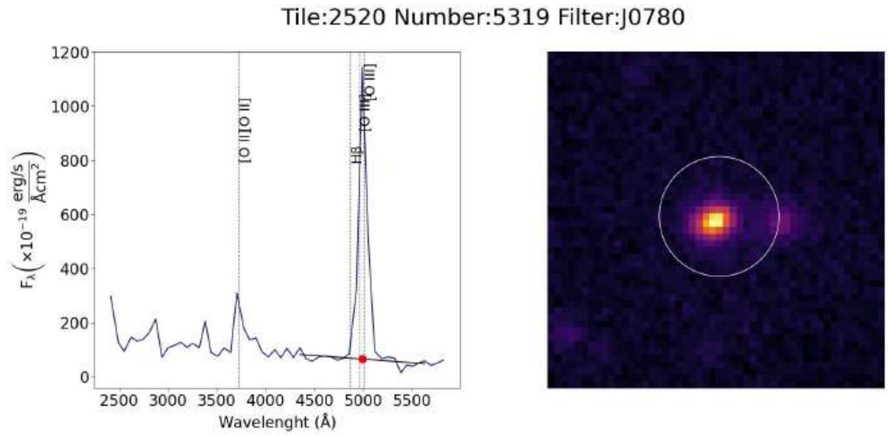

Figure A.1 Continued.

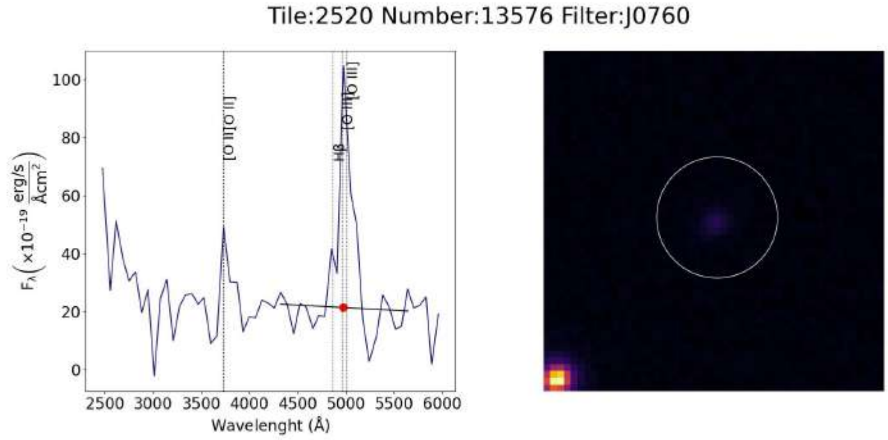

Figure A.1 Continued.

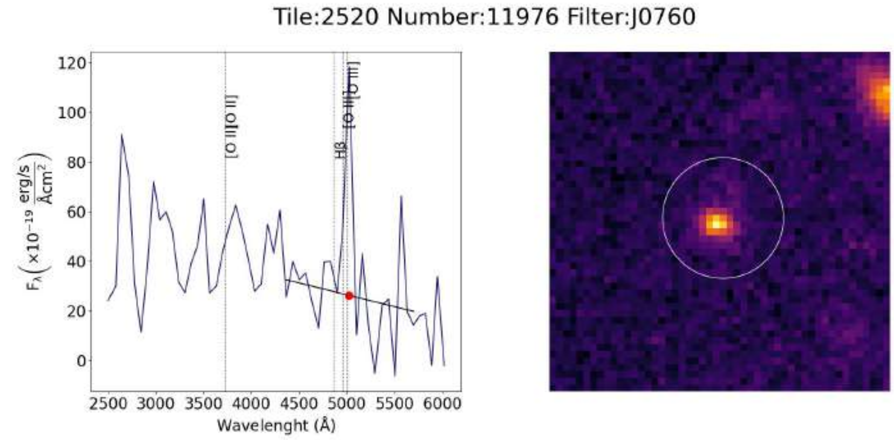

Figure A.1 Continued.

A.2 Basic properties of the EELG candidates

Table A.1 Basic properties of the EELG candidates. Uncertainties of derived quantities appear below the values in parenthesis. Objects highlighted in bold correspond to the confirmed EELGs.

Column (1): J-PAS identifier. Column (2): Right ascension (J2000.0). Column (3): Declination (J2000.0). Column (4): Stellarity index. Column (5): r_{SDSS} magnitude. Column (6): Filter where the object was detected. Column (7): Contrast. Column (8): Redshift estimated in this work. Column (9): Redshift from SDSS. Column (10): Redshift from DEEP2 or DEEP3. Column (11): Emission feature at the detection filter. Column (12): EW$_0$ of the emission feature. Column (13): Flux of the emission feature. Column (14): Luminosity of the emission feature.

Id. (1)	R.A. (deg) (2)	Dec. (deg) (3)	Class (4)	Stell. index (5)	r_{SDSS} (mag) (6)	Filter (7)	z (this work) (8)	z (SDSS) (9)	z (DEEP2/3) (10)	Line (11)	EW$_0^{a,b}$ (Å) (12)	$F^{a,b}$ (×10^{-15}) (erg s^{-1} cm^{-2}) (13)	log$L^{a,b}$ (erg s^{-1}) (14)
2470-1828	213.43786	52.07686	SFG	0.801	22.73	J0710	0.434	—	—	[OIII]	423	1.49	42.02
					(0.12)						(78)	(0.13)	(0.04)
						J0720				[OIII]	373	1.46	42.01
											(60)	(0.11)	(0.03)
2470-4506	213.44792	52.20433	SFG	0.073	22.44	J0800	0.614	0.613	—	[OIII]	696	1.95	42.50
					(0.08)						(218)	(0.39)	(0.08)
						J0810				[OIII]	613	1.97	42.50
											(121)	(0.20)	(0.04)
2470-4455	213.44946	52.20138	QSO	1.000	21.32	J0410	2.354	2.351	—	Lyα	92	3.86	44.24
					(0.03)						(22)	(0.62)	(0.06)
2470-3723	213.61742	52.06311	QSO	1.000	21.70	J0450	2.714	2.689	—	Lyα	114	2.82	44.25
					(0.06)						(30)	(0.60)	(0.09)
2470-1726	213.62304	51.95802	SFG	0.124	23.60	J0820	0.635	—	—	[OIII]	1365	1.52	42.43
					(0.15)						(553)	(0.14)	(0.04)
2470-13007	213.74719	52.40694	QSO	1.000	22.05	J0400	2.334	—	—	Lyα	114	1.66	43.86
					(0.06)						(77)	(0.35)	(0.09)
2470-3670	213.76386	51.97030	SFG	0.000	20.82	J0630	0.284	—	—	—	—	—	—
					(0.06)						—	—	—
						J0640				[OIII]	513	3.45	41.95
											(99)	(0.24)	(0.03)
						J0840				Hα	482	1.72	41.65
											(319)	(0.71)	(0.16)
2470-4554	213.88271	51.94262	SFG	0.000	21.53	J0610	0.226	—	—	[OIII]	267	1.99	41.49
					(0.06)						(39)	(0.21)	(0.04)
						J0800				Hα	422	1.27	41.29
											(159)	(0.35)	(0.11)
2470-5682	213.90483	51.98243	SFG	0.989	22.26	J0640	0.292	—	—	[OIII]	501	1.35	41.57
					(0.09)						(117)	(0.12)	(0.03)
2470-13036	213.92495	52.32272	QSO	1.000	21.46	J0470	2.044	2.036	—	CIV	102	2.52	43.90
					(0.05)						(17)	(0.25)	(0.04)
2470-6481	213.92791	52.15755	QSO	0.974	22.53	J0510	3.180	—	—	Lyα	368	1.52	44.15
					(0.08)						(168)	(0.14)	(0.04)
2241-1550	214.09392	52.30670	SFG	0.000	20.98	J0770	0.552	—	0.546	[OIII]	206	2.15	42.43
					(0.03)						(25)	(0.21)	(0.04)
						J0780				[OIII]	203	2.22	42.44

Id.	R.A. (deg)	Dec. (deg)	Class	Stell. index	r_{SDSS} (mag)	Filter	z (this work)	z (SDSS)	z (DEEP2/3)	Line	$\mathrm{EW}_0^{a,b}$ (Å)	$F^{a,b}$ ($\times10^{-15}$) (erg s^{-1} cm^{-2})	$\log L^{a,b}$ (erg s^{-1})
											(29)	(0.25)	(0.04)
2470-12186	214.13713	52.20877	QSO	1.000	21.58	J0400	1.624	1.600	—	C IV	98	1.38	43.39
					(0.06)						(86)	(0.47)	(0.14)
2241-18891	214.32208	52.53820	SFG	0.000	21.58	J0720	0.454	0.452	0.451	[O III]	320	2.20	42.23
					(0.04)						(29)	(0.10)	(0.02)
						J0730				[O III]	439	3.14	42.39
											(49)	(0.26)	(0.03)
2241-12793	214.34146	52.75227	SFG	0.963	22.01	J0670	0.340	—	—	[O III]	363	1.09	41.63
					(0.04)						(51)	(0.04)	(0.02)
2241-14549	214.34443	52.67455	SFG	0.961	21.70	J0780	0.196	0.193	0.193	Hα	332	1.32	41.17
					(0.04)						(58)	(0.16)	(0.05)
2241-11742	214.38197	52.76887	SFG	0.000	21.60	J0610	0.224	—	—	[O III]	286	1.35	41.31
					(0.04)						(39)	(0.12)	(0.04)
2241-19064	214.43097	52.46827	SFG	1.000	21.92	J0600	0.212	0.208	0.208	[O III]	1758	3.58	41.68
					(0.04)						(259)	(0.08)	(0.01)
						J0610				[O III]	1526	3.20	41.63
											(238)	(0.14)	(0.02)
						J0790				Hα	1287	1.40	41.27
											(416)	(0.16)	(0.04)
2243-5404	214.55589	52.87777	QSO	1.000	21.36	J0520	3.302	3.288	—	Lyα	107	3.63	44.57
					(0.04)						(13)	(0.40)	(0.04)
2243-7588	214.68784	52.94963	SFG	0.000	21.66	J0670	0.348	—	—	[O III]	422	1.87	41.89
					(0.06)						(60)	(0.08)	(0.02)
						J0680				[O III]	502	2.08	41.94
											(84)	(0.16)	(0.03)
2243-15893	214.69939	53.03229	SFG	0.472	22.73	J0600	0.206	—	—	[O III]	718	1.21	41.18
					(0.12)						(181)	(0.14)	(0.05)
2243-7718	214.87076	52.83314	QSO	0.414	22.60	J0400	2.322	—	—	Lyα	176	1.74	43.87
					(0.12)						(109)	(0.35)	(0.08)
2243-14873	214.89826	52.95298	QSO	1.000	20.42	J0510	3.226	3.218	—	Lyα	77	5.77	44.74
					(0.02)						(4)	(0.24)	(0.02)
2243-14988	214.91904	52.94645	SFG	0.846	22.63	J0730	0.464	—	0.461	[O III]	383	0.94	41.88
					(0.13)						(119)	(0.18)	(0.08)
2243-11992	214.92816	53.07305	SFG	0.000	21.69	J0600	0.200	—	0.198	[O III]	477	2.45	41.46
					(0.05)						(53)	(0.16)	(0.03)
						J0780				Hα	419	1.59	41.27
											(95)	(0.29)	(0.07)
						J0790				Hα	444	1.67	41.29
											(83)	(0.22)	(0.05)
2406-3709	214.98989	53.20826	QSO	0.001	21.96	J0500	3.162	—	—	Lyα	85	1.35	44.09
					(0.08)						(26)	(0.30)	(0.09)
2243-7939	215.00404	52.74137	SFG	0.002	22.96	J0710	0.424	—	—	[O III]	686	0.99	41.81
					(0.12)						(182)	(0.09)	(0.03)
2243-10641	215.24110	52.94494	SFG	0.263	23.25	J0870	0.748	—	0.747	[O III]	1236	1.29	42.53
					(0.15)						(902)	(0.11)	(0.03)
2406-1585	215.31301	52.92023	SFG	0.000	22.14	J0540	0.086	—	—	[O III]	245	0.93	40.24
					(0.07)						(55)	(0.14)	(0.06)
2406-1224	215.32499	52.89611	QSO	1.000	20.53	J0400	2.304	2.305	—	Lyα	101	8.57	44.56
					(0.02)						(9)	(0.39)	(0.02)
2406-12576	215.77825	53.18870	SFG	0.972	22.73	J0610	0.218	—	—	[O III]	392	1.11	41.20
					(0.10)						(74)	(0.14)	(0.05)

Id.	R.A. (deg)	Dec. (deg)	Class	Stell. index	r_{SDSS} (mag)	Filter	z (this work)	z (SDSS)	z (DEEP2/3)	Line	$\mathrm{EW}_0^{a,b}$ (Å)	$F^{a,b}$ ($\times10^{-15}$) (erg s^{-1} cm^{-2})	$\log L^{a,b}$ (erg s^{-1})
2520-11368	260.14017	65.77044	SFG	0.217	21.39	J0590	0.190	—	—	[OIII]	261	1.21	41.12
					(0.08)						(23)	(0.11)	(0.04)
2520-10356	260.24775	65.74940	AGN	0.977	21.32	J0400	2.278	—	—	Lyα	109	1.95	43.91
					(0.06)						(83)	(0.36)	(0.08)
2520-8318	260.27529	65.71089	SFG	0.032	20.61	J0590	0.188	—	—	[OIII]	288	3.85	41.61
					(0.10)						(58)	(0.07)	(0.03)
						J0780				Hα	326	2.97	41.50
											(74)	(0.06)	(0.02)
2520-7434	260.59217	65.69187	SFG	0.271	21.59	J0650	0.298	—	—	[OIII]	205	0.911	41.43
					(0.11)						(33)	(0.27)	(0.011)
2520-5319	261.00963	65.63878	SFG	0.071	20.57	J0780	0.566	—	—	[OIII]	1127	11.71	43.20
					(0.09)						(35)	(0.08)	(0.02)
2520-13576	261.08708	65.81467	SFG	0.766	21.94	J0760	0.528	—	—	[OIII]	273	0.89	42.01
					(0.13)						(71)	(0.10)	(0.07)
2520-11976	261.09289	65.78306	SFG	0.405	22.26	J0760	0.513	—	—	[OIII]	285	1.13	42.09
					(0.08)						(55)	(0.13)	(0.04)

Appendix B

GPs

B.1 Emission line maps

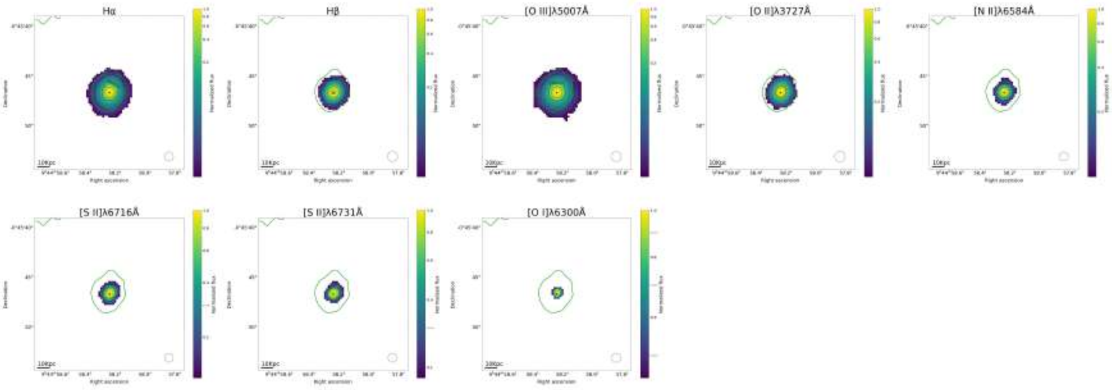

Figure B.1 Emission line maps of GP01.

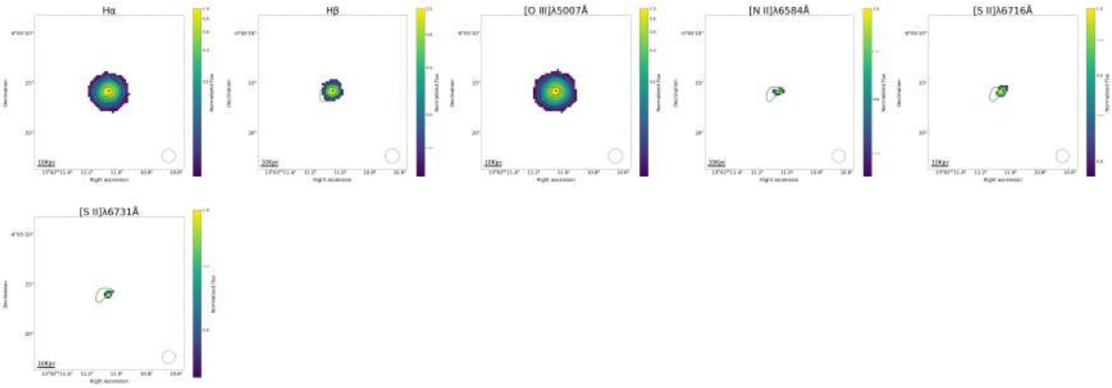

Figure B.2 Emission line maps of GP02

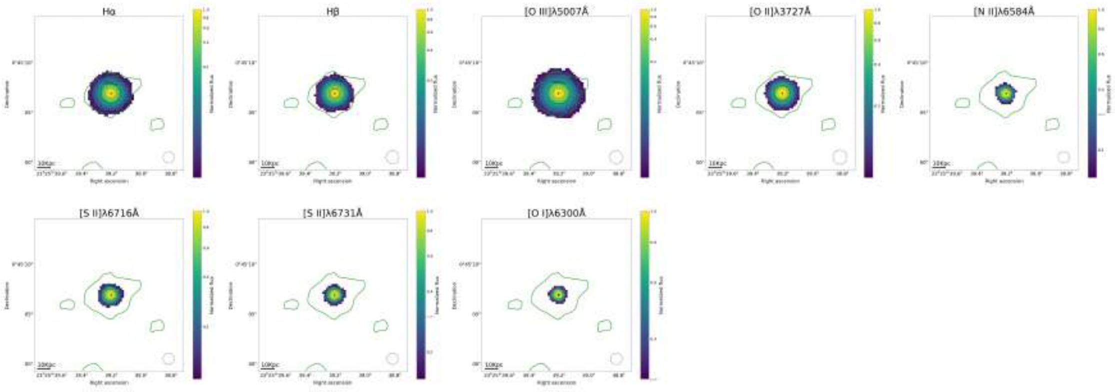

Figure B.3 Emission line maps of GP03

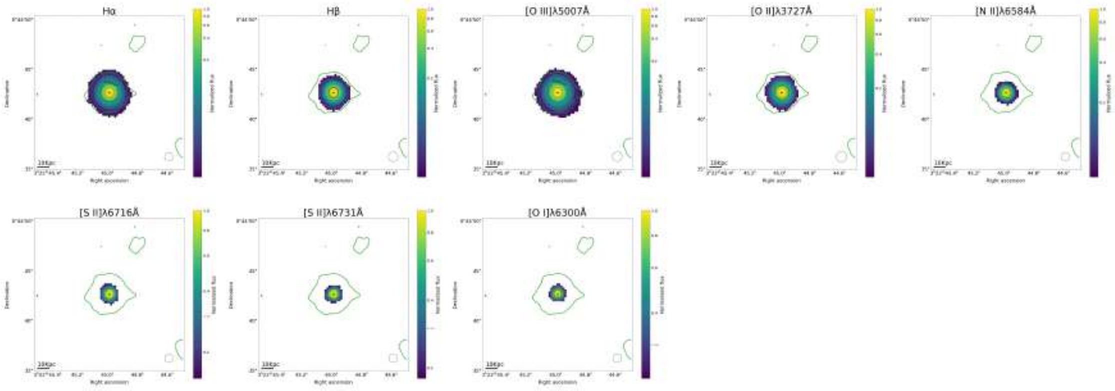

Figure B.4 Emission line maps of GP04

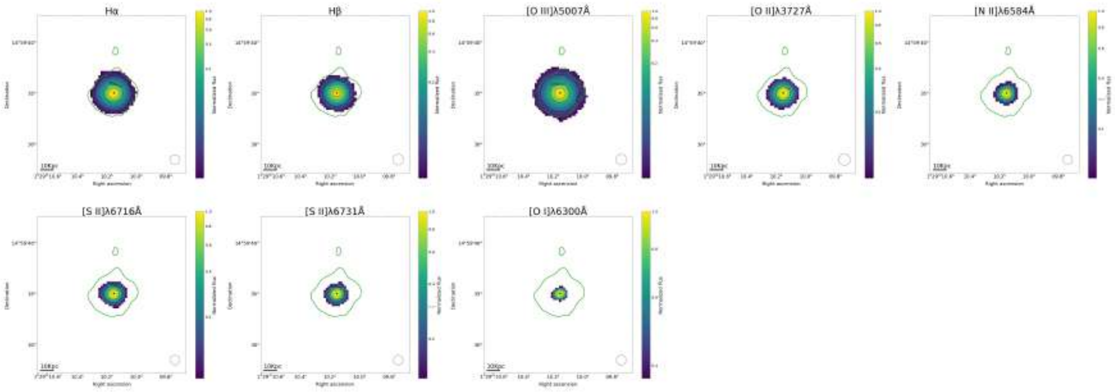

Figure B.5 Emission line maps of GP05

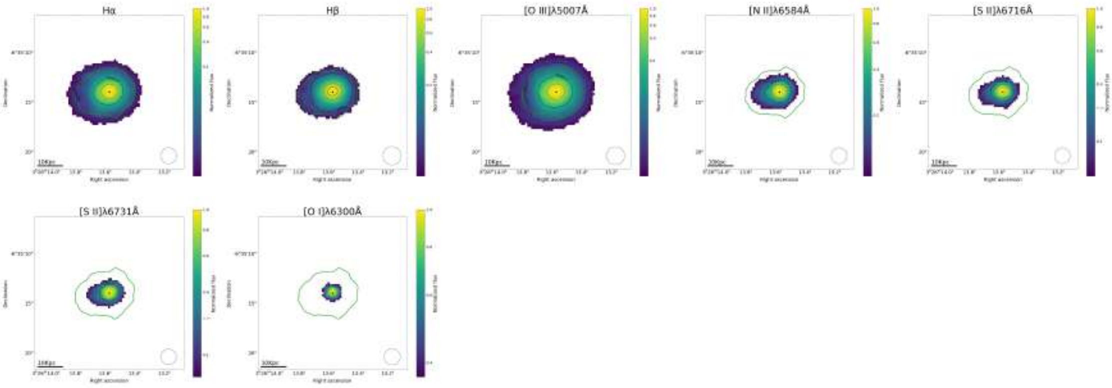

Figure B.6 Emission line maps of GP07

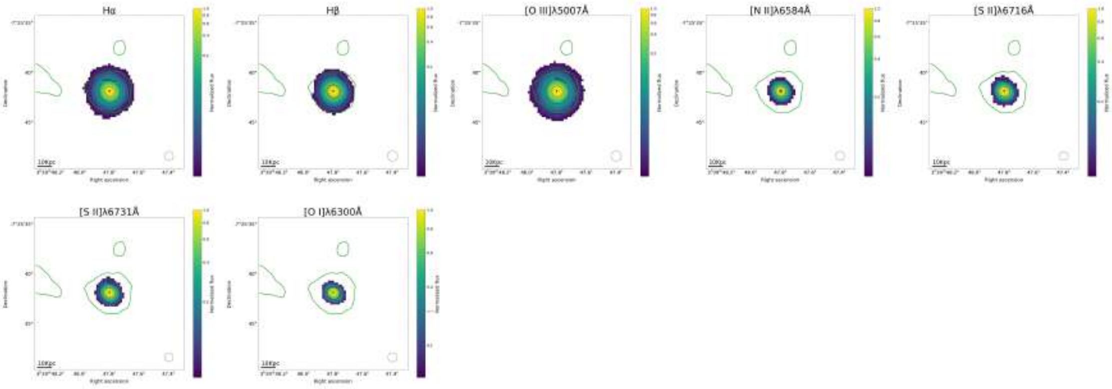

Figure B.7 Emission line maps of GP08

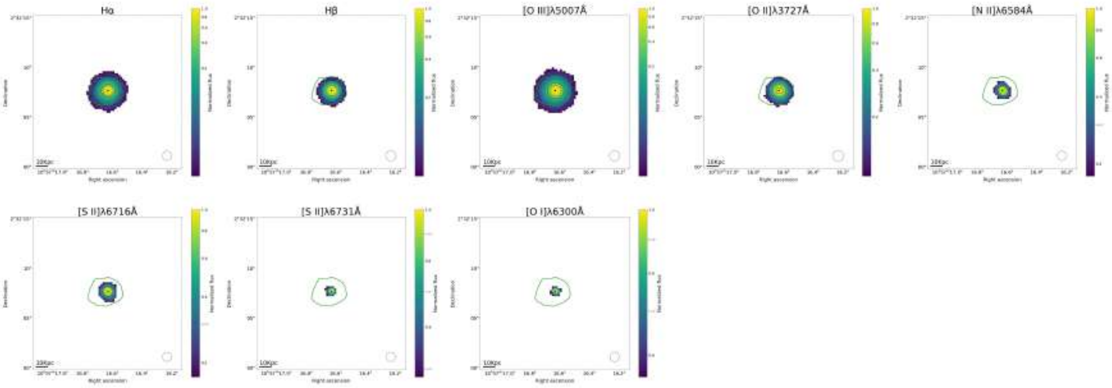

Figure B.8 Emission line maps of GP09

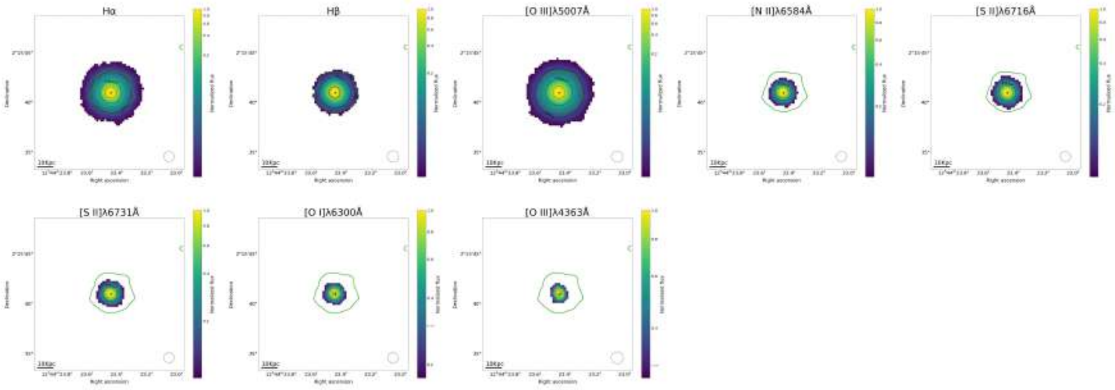

Figure B.9 Emission line maps of GP10

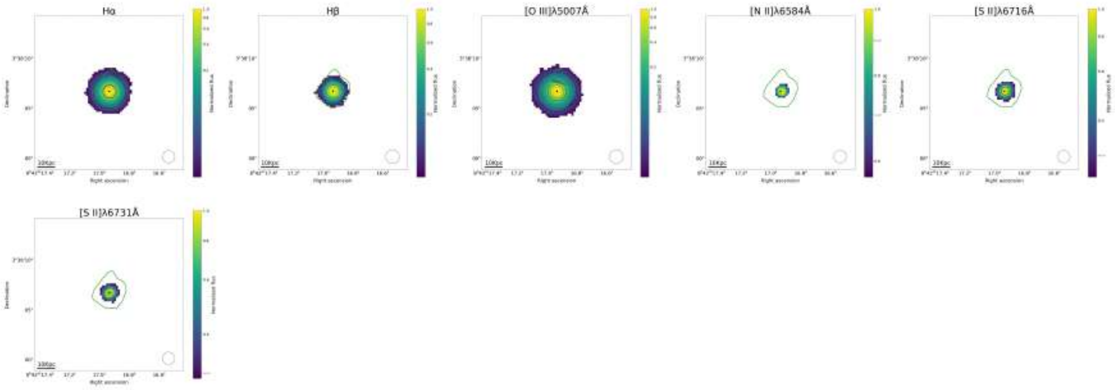

Figure B.10 Emission line maps of GP11

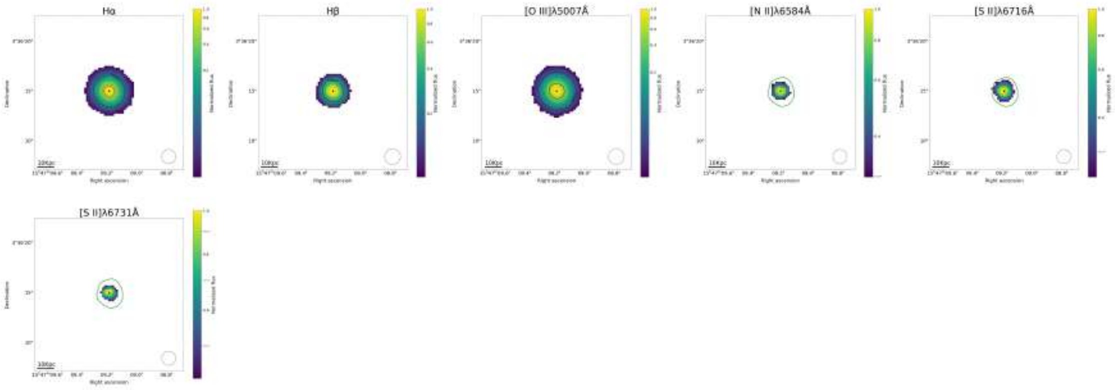

Figure B.11 Emission line maps of GP12

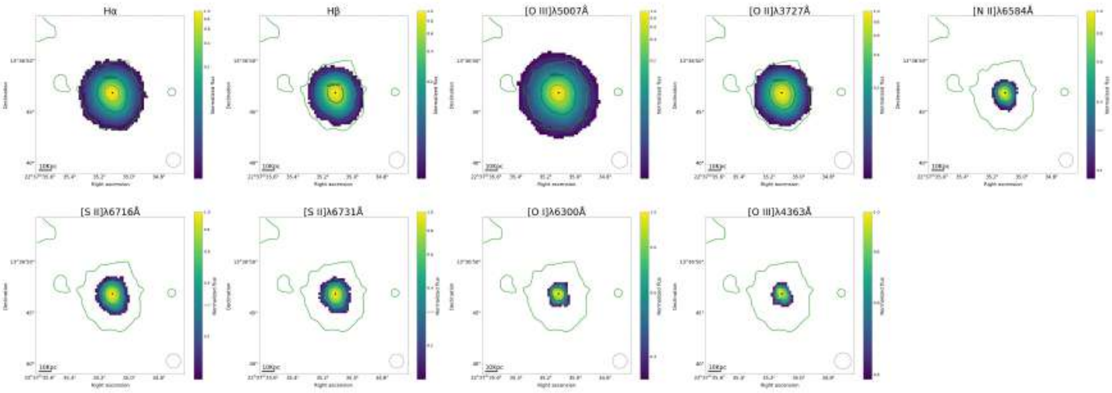

Figure B.12 Emission line maps of GP13

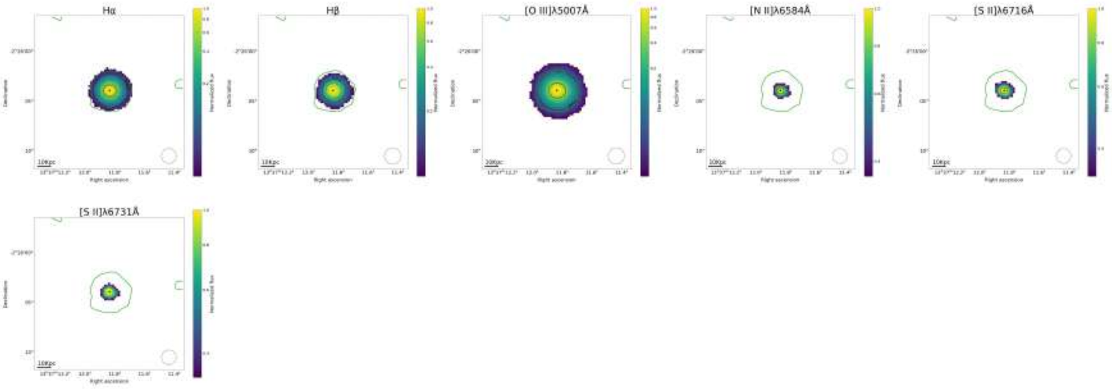

Figure B.13 Emission line maps of GP14

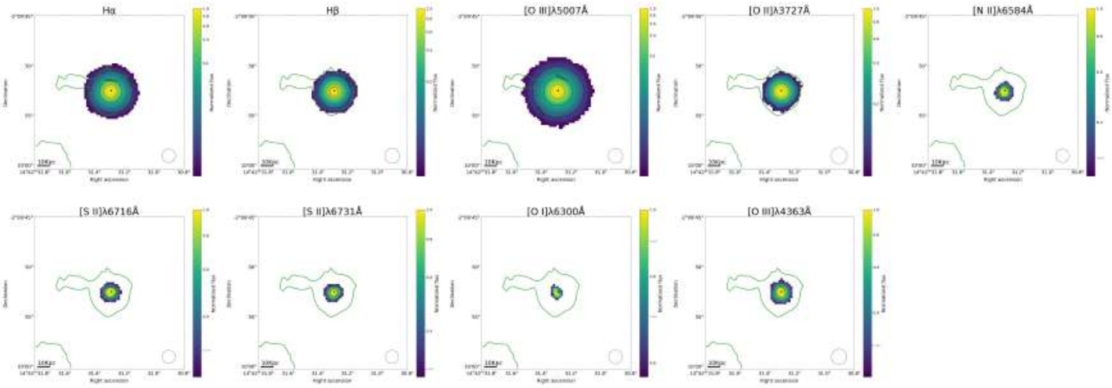

Figure B.14 Emission line maps of GP15

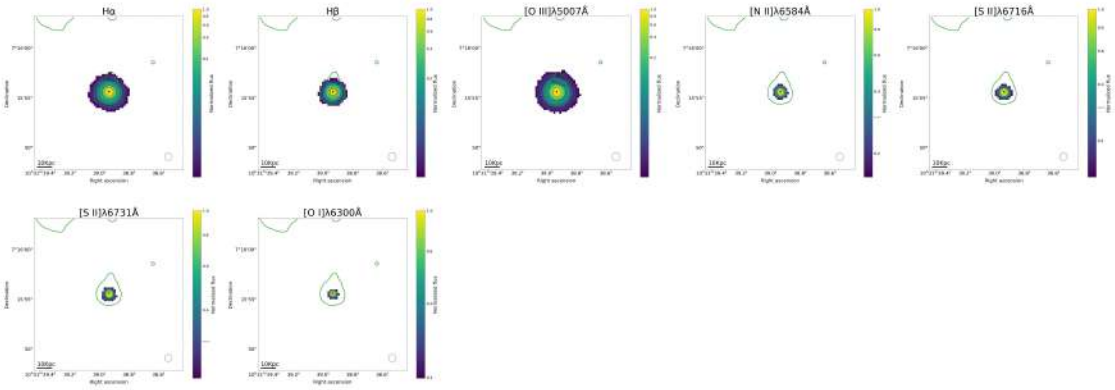

Figure B.15 Emission line maps of GP16

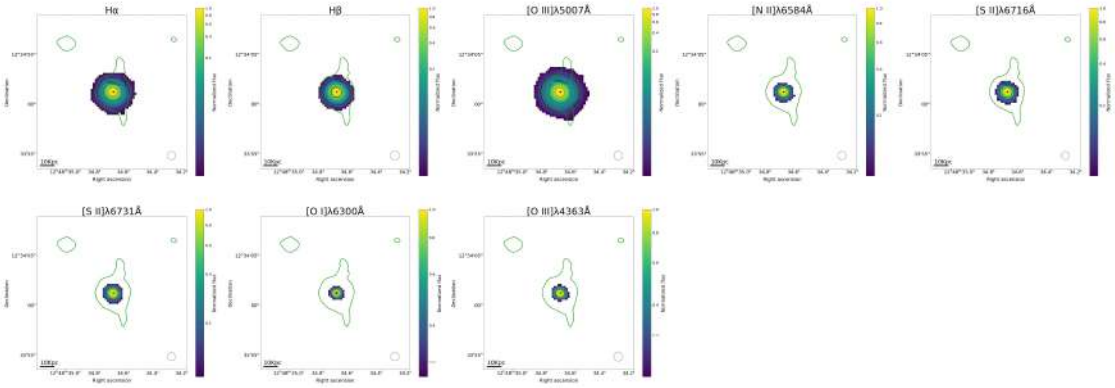

Figure B.16 Emission line maps of GP17

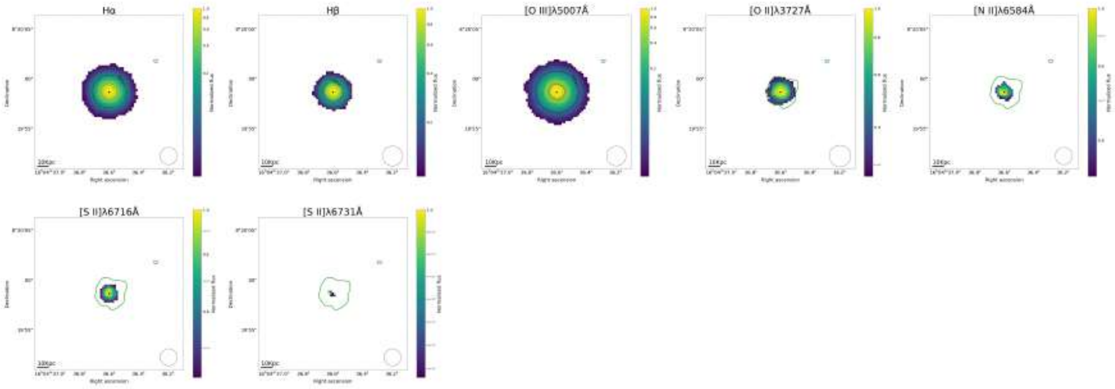

Figure B.17 Emission line maps of GP18

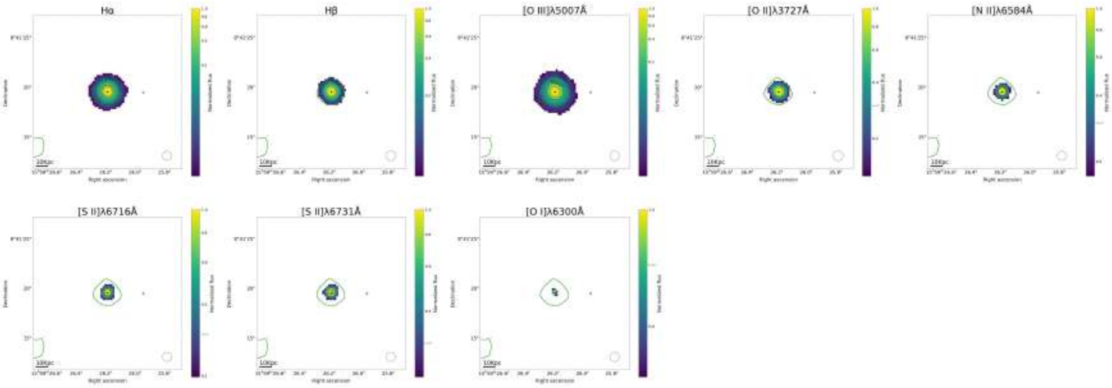

Figure B.18 Emission line maps of GP19

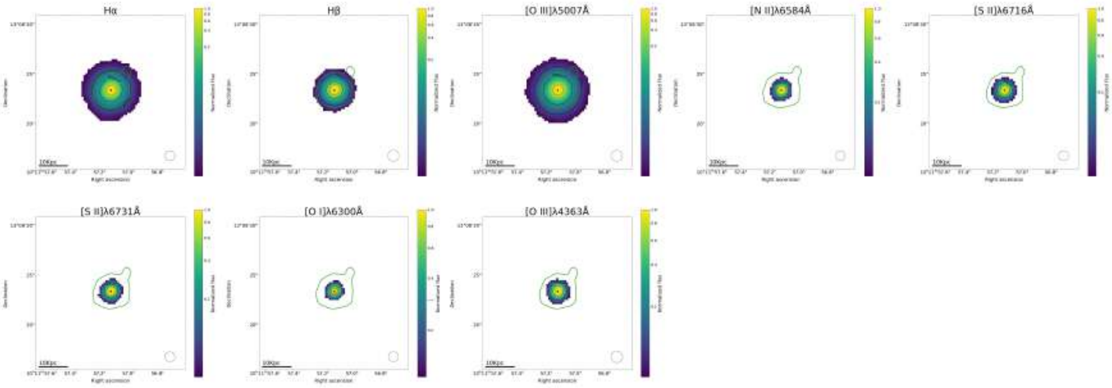

Figure B.19 Emission line maps of GP20

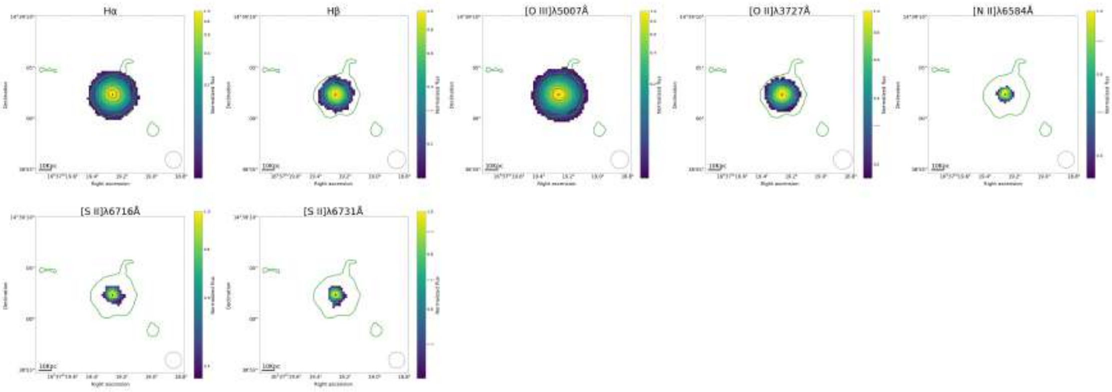

Figure B.20 Emission line maps of GP21

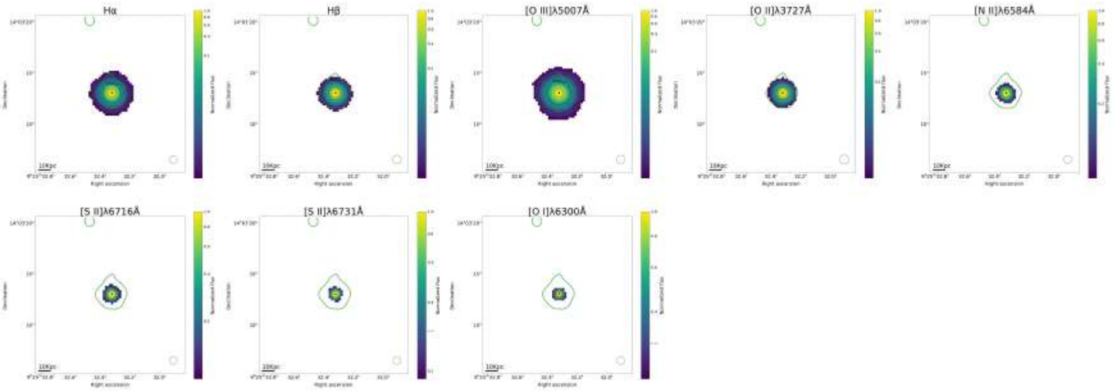

Figure B.21 Emission line maps of GP22

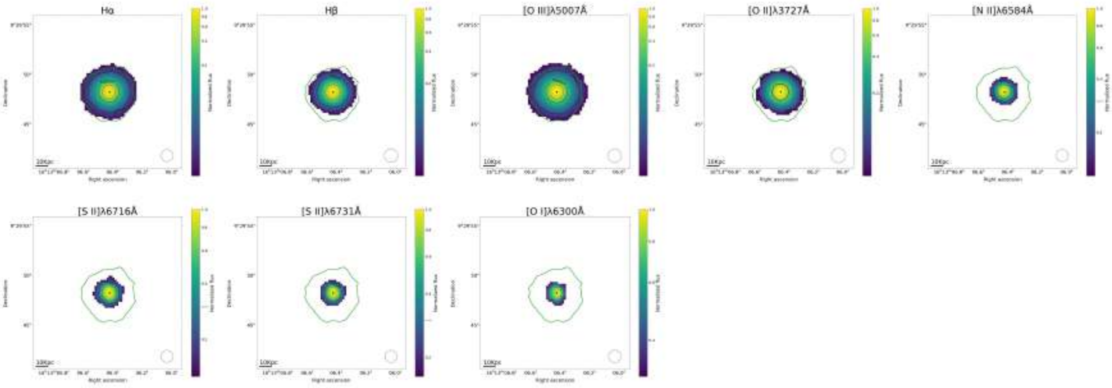

Figure B.22 Emission line maps of GP23

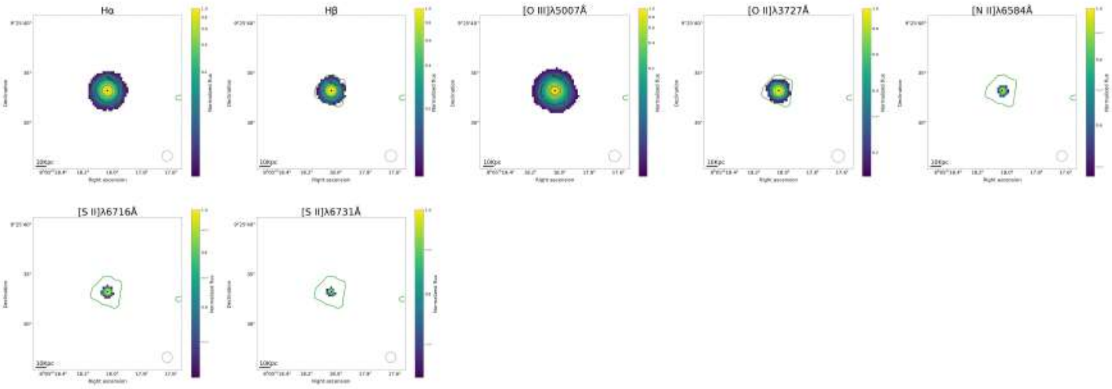

Figure B.23 Emission line maps of GP24

B.2 Line ratio maps

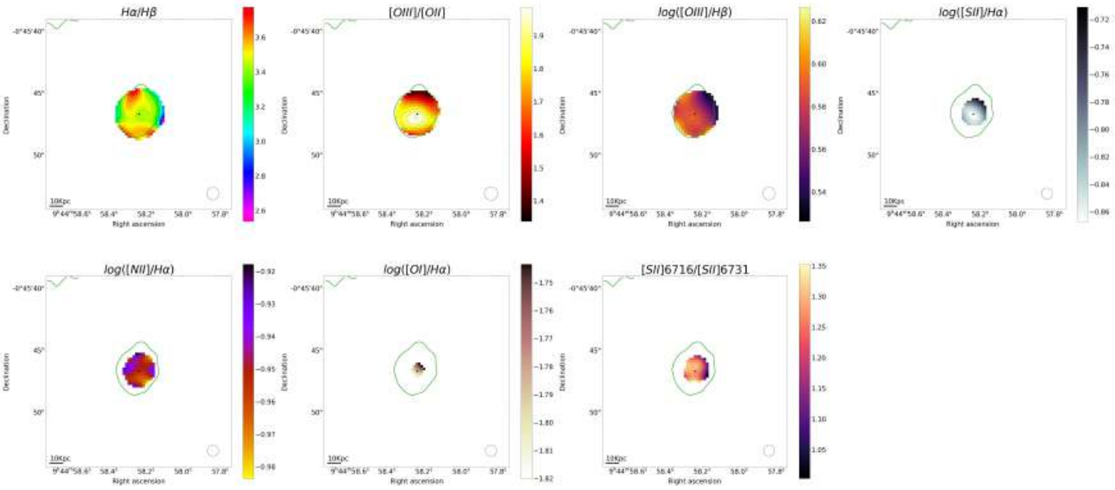

Figure B.24 Line ratio maps for GP01.

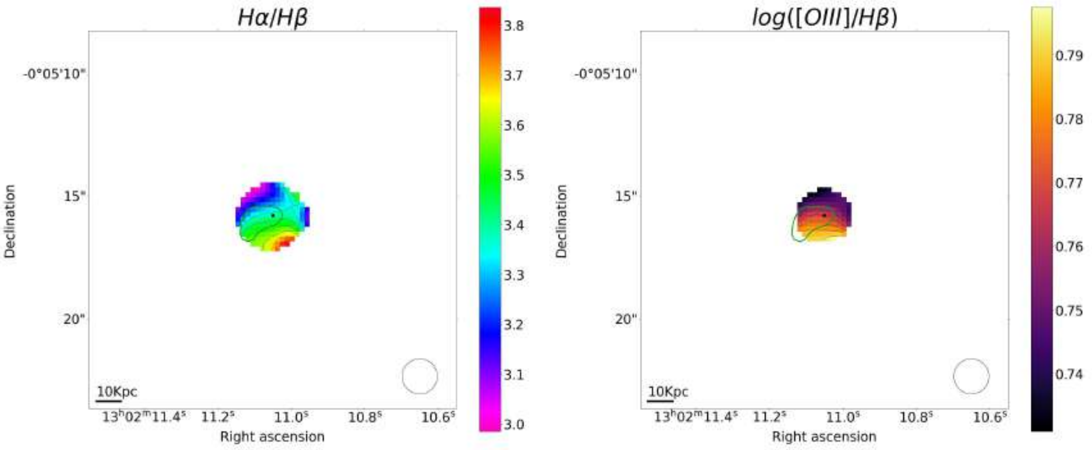

Figure B.25 Line ratio maps for GP02.

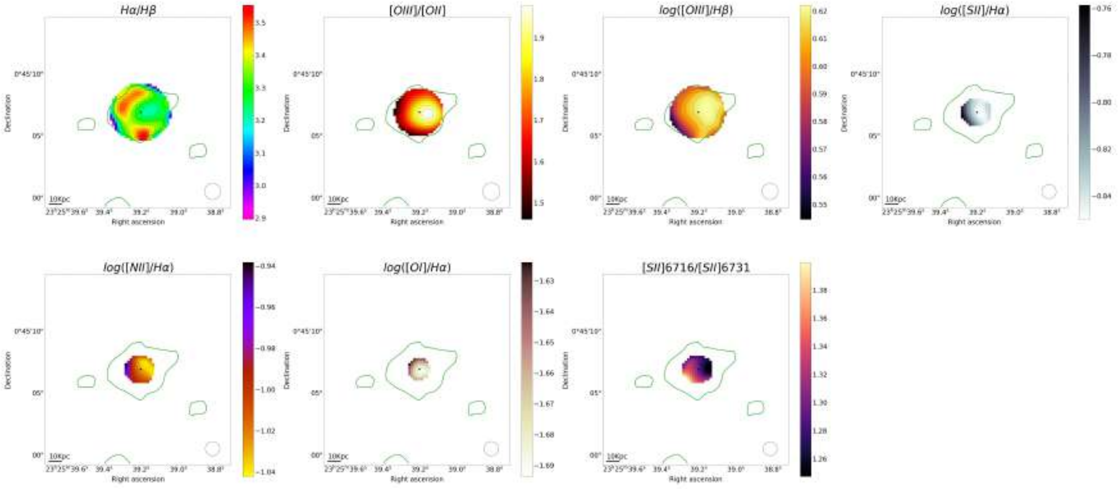

Figure B.26 Line ratio maps for GP03.

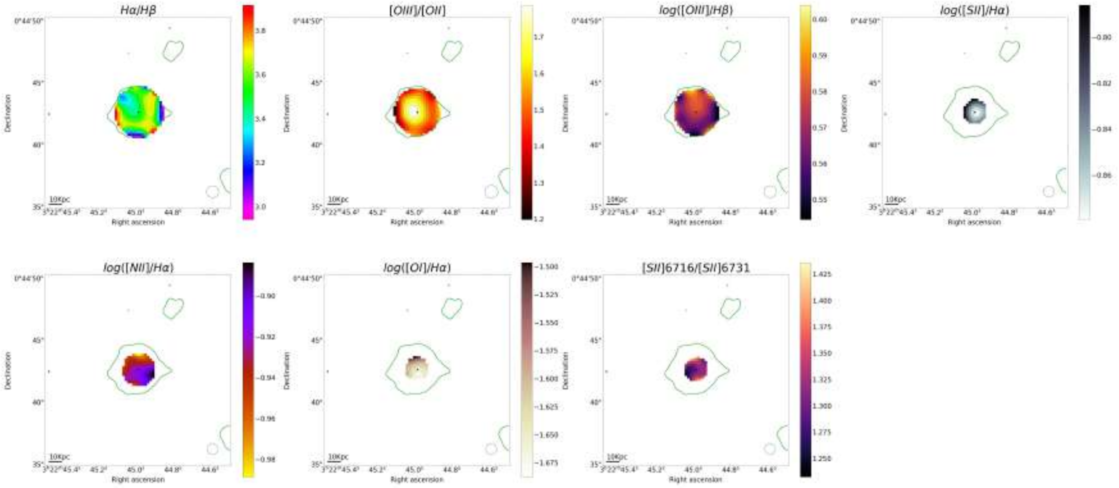

Figure B.27 Line ratio maps for GP04.

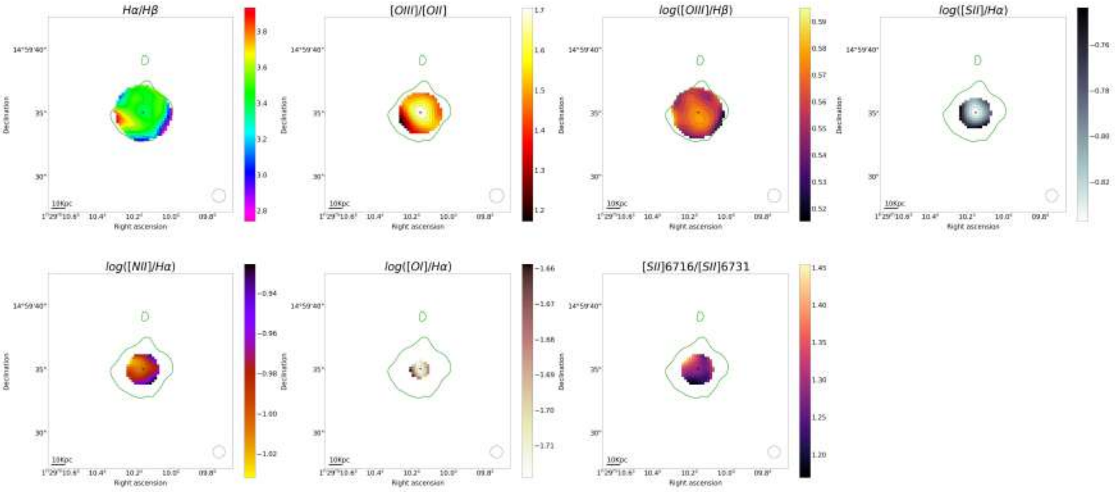

Figure B.28 Line ratio maps for GP05.

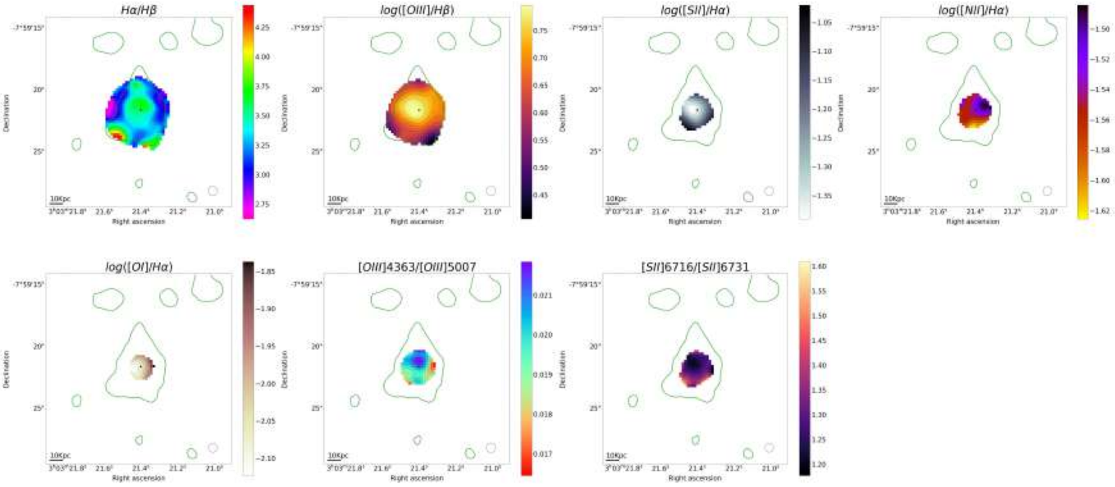

Figure B.29 Line ratio maps for GP06.

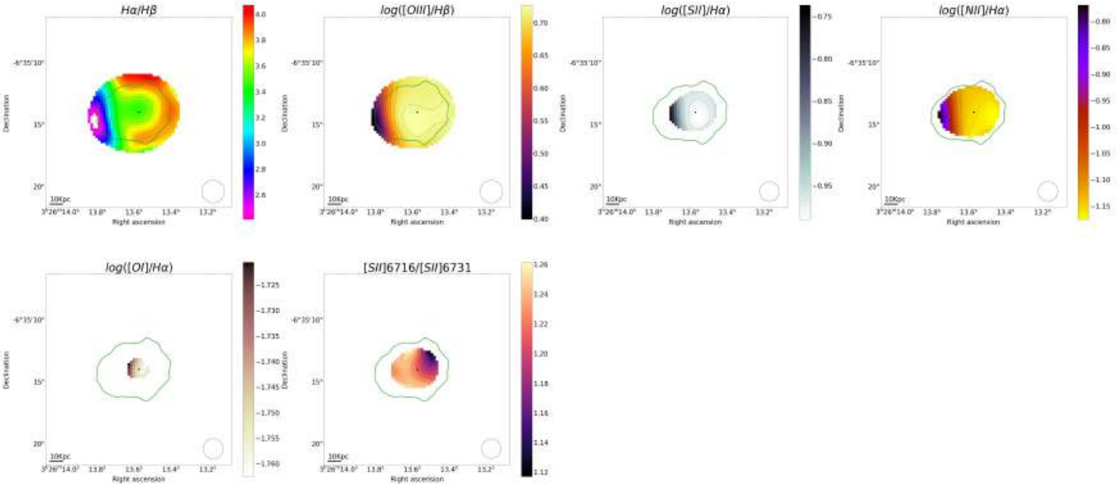

Figure B.30 Line ratio maps for GP07. Spaxels > 20 kpc to the west from the Hα peak are not reliable due to sky contamination.

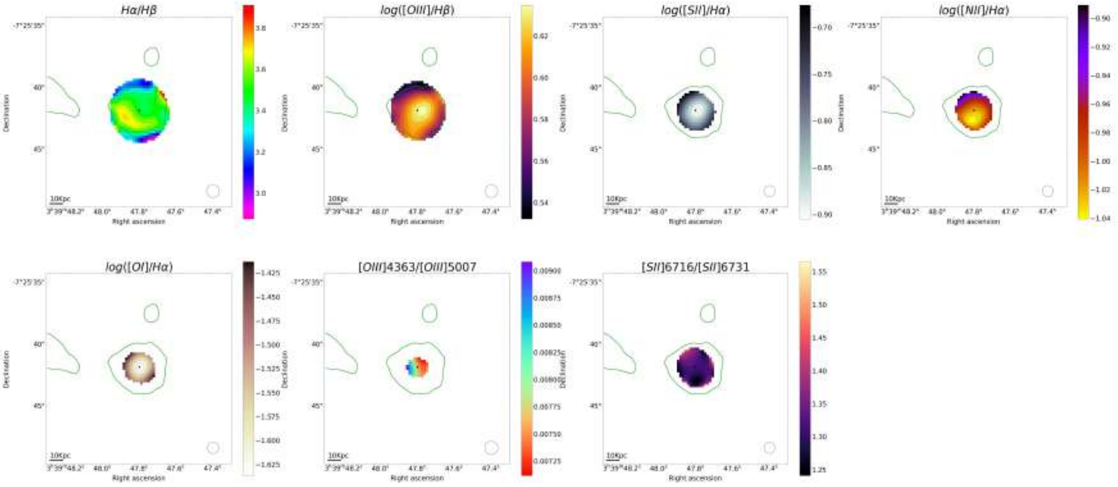

Figure B.31 Line ratio maps for GP08.

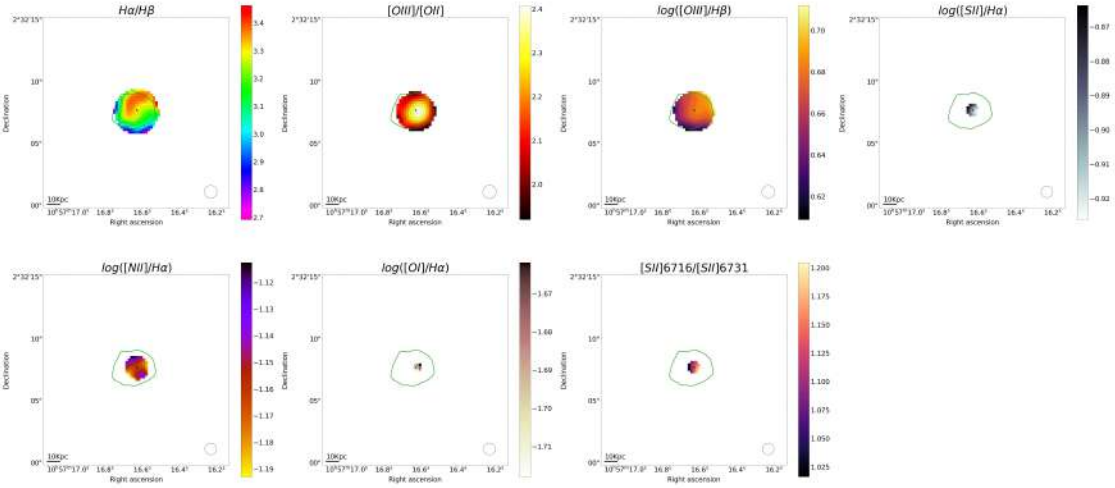

Figure B.32 Line ratio maps for GP09.

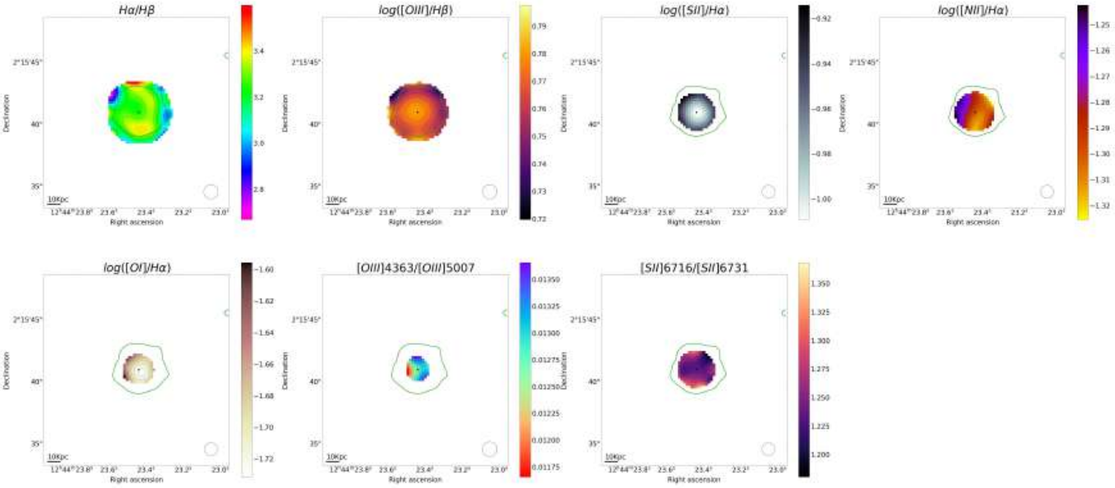

Figure B.33 Line ratio maps for GP10.

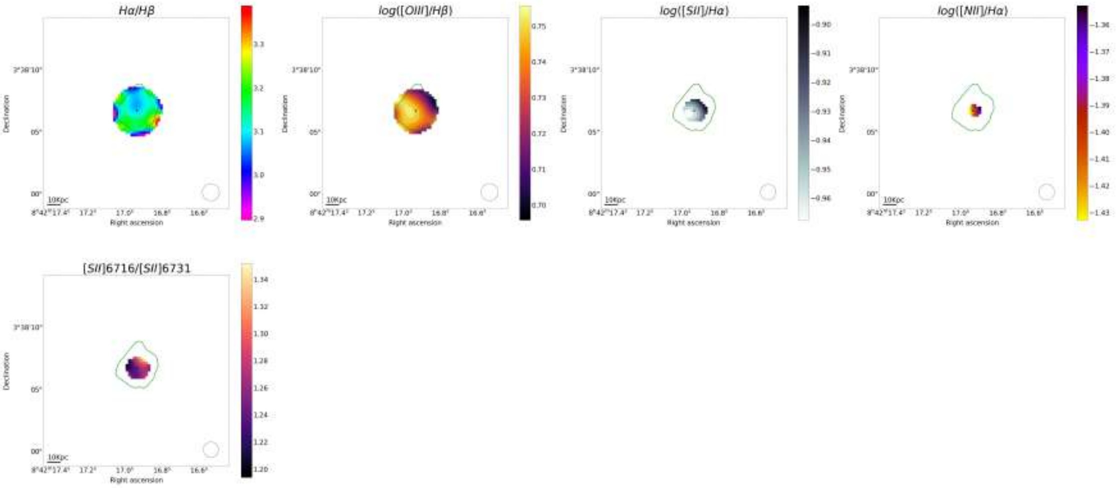

Figure B.34 Line ratio maps for GP11.

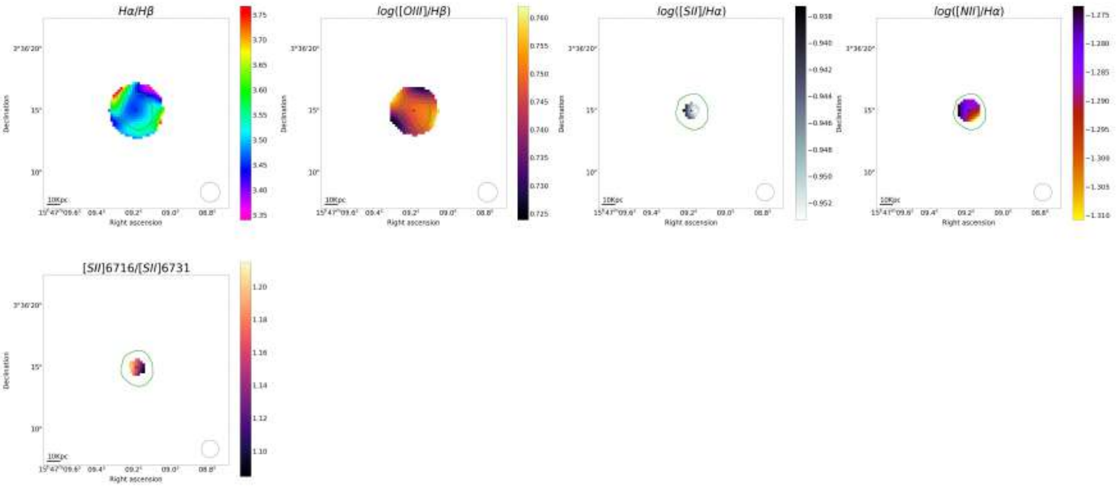

Figure B.35 Line ratio maps for GP12.

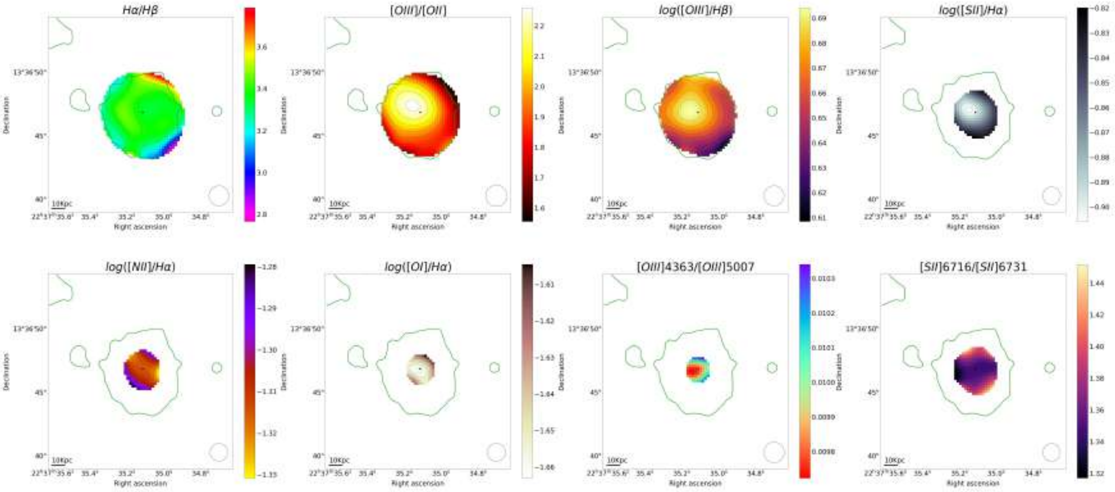

Figure B.36 Line ratio maps for GP13.

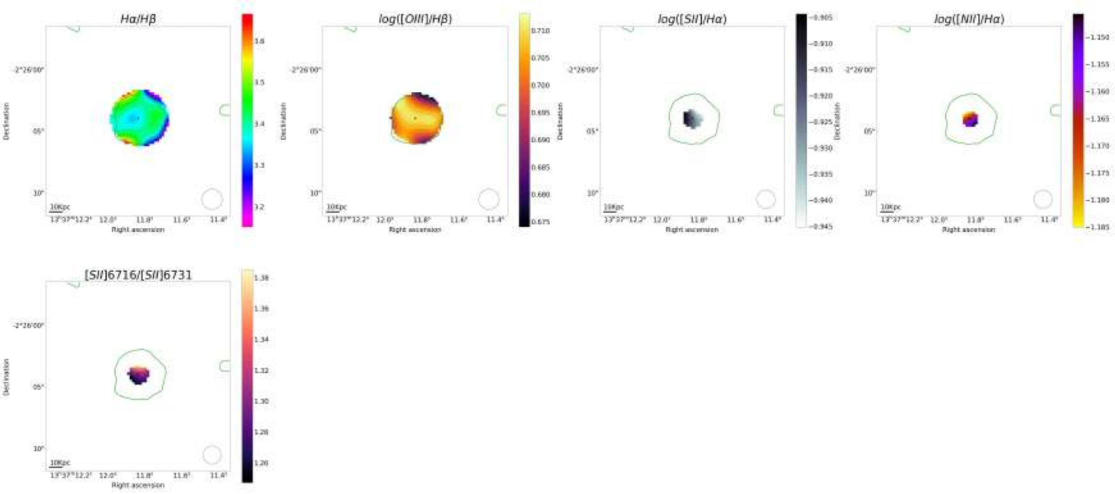

Figure B.37 Line ratio maps for GP14.

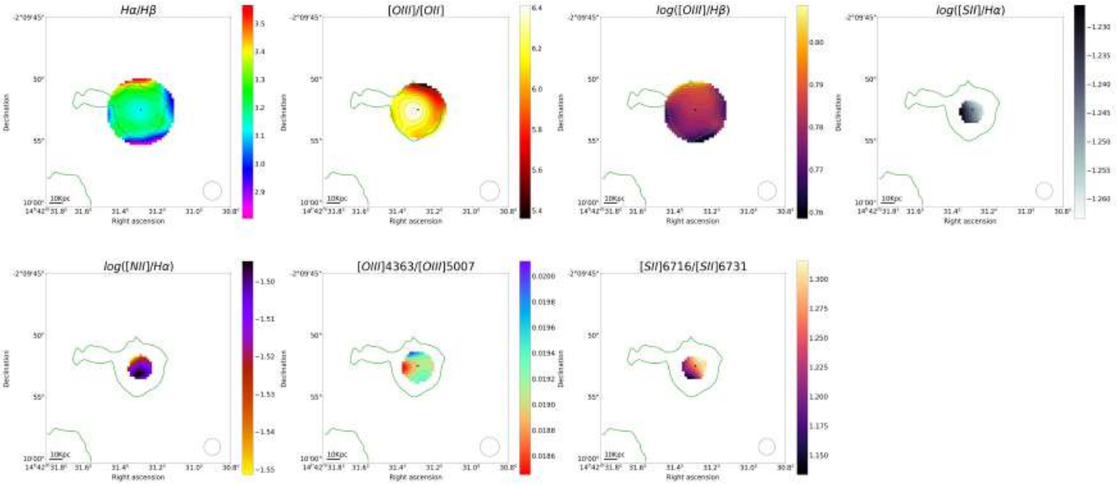

Figure B.38 Line ratio maps for GP15.

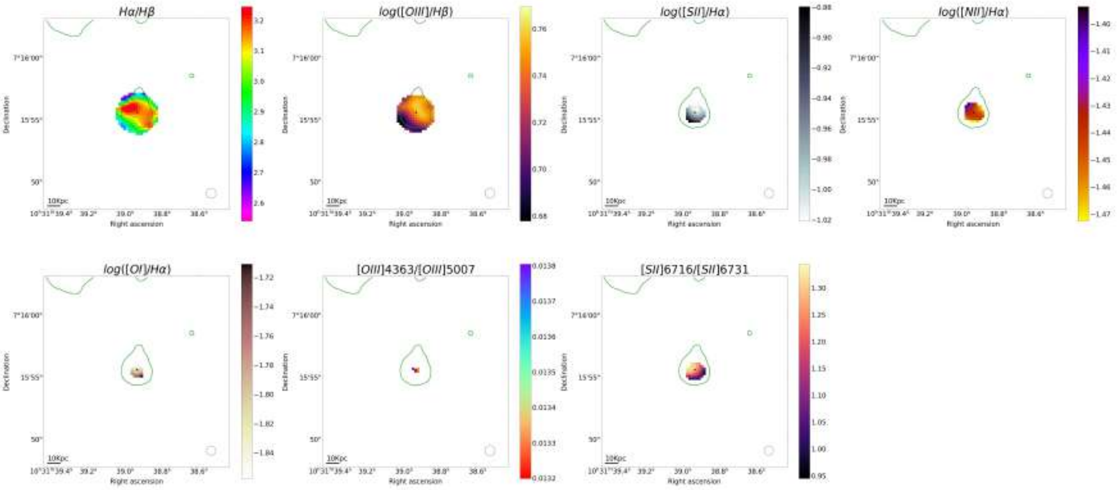

Figure B.39 Line ratio maps for GP16.

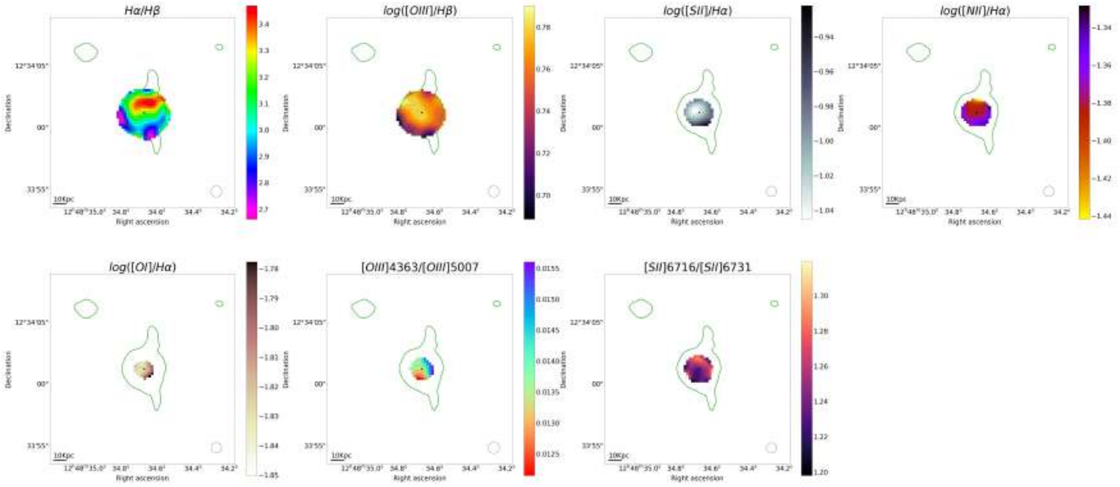

Figure B.40 Line ratio maps for GP17.

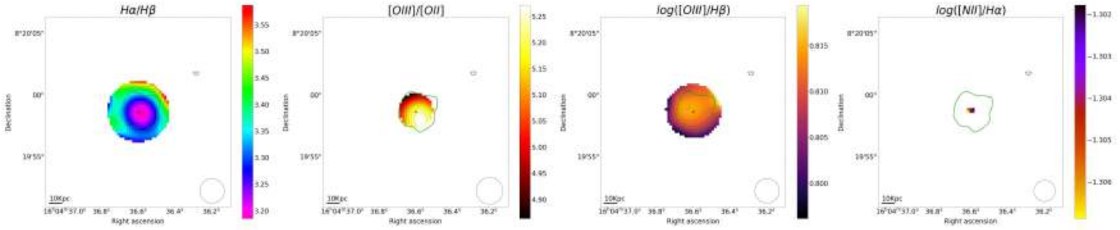

Figure B.41 Line ratio maps for GP18.

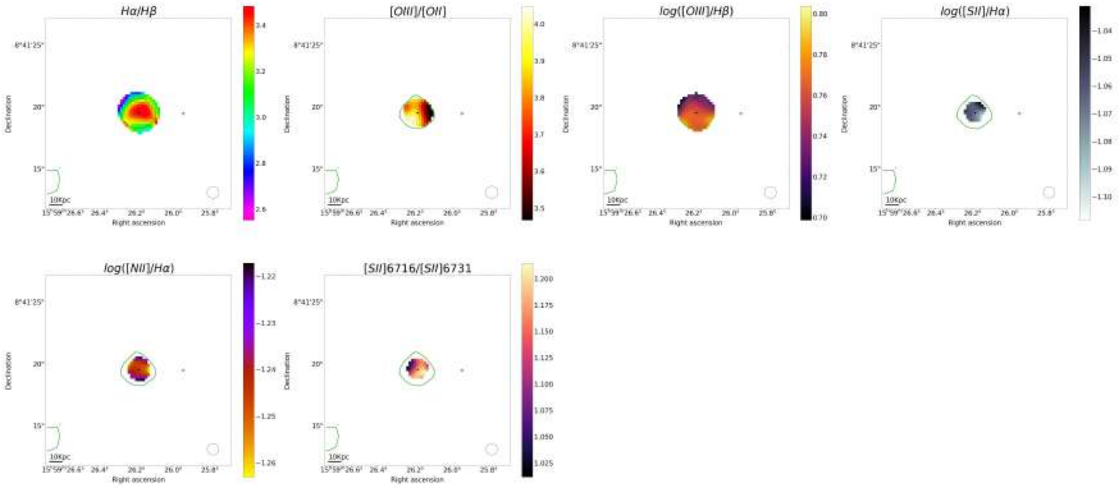

Figure B.42 Line ratio maps for GP19.

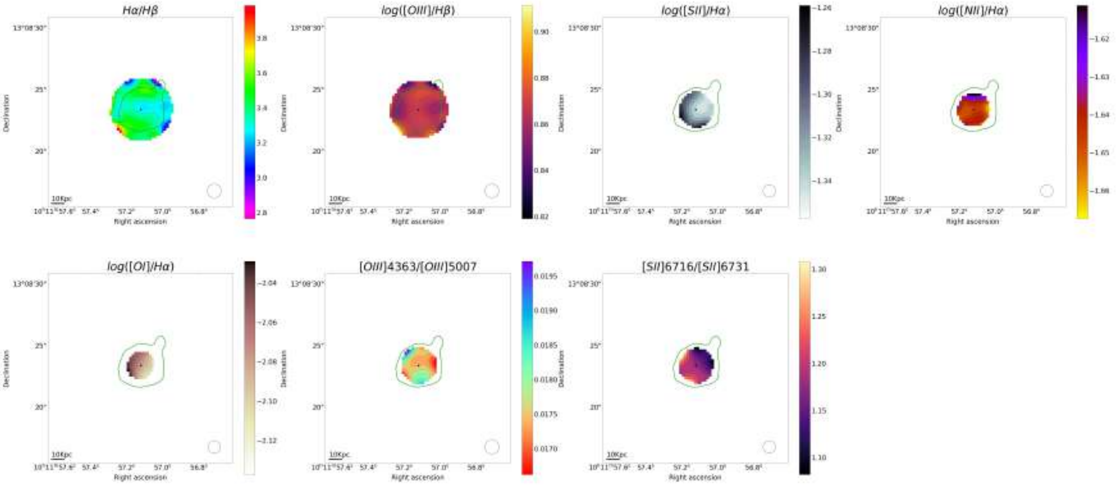

Figure B.43 Line ratio maps for GP20.

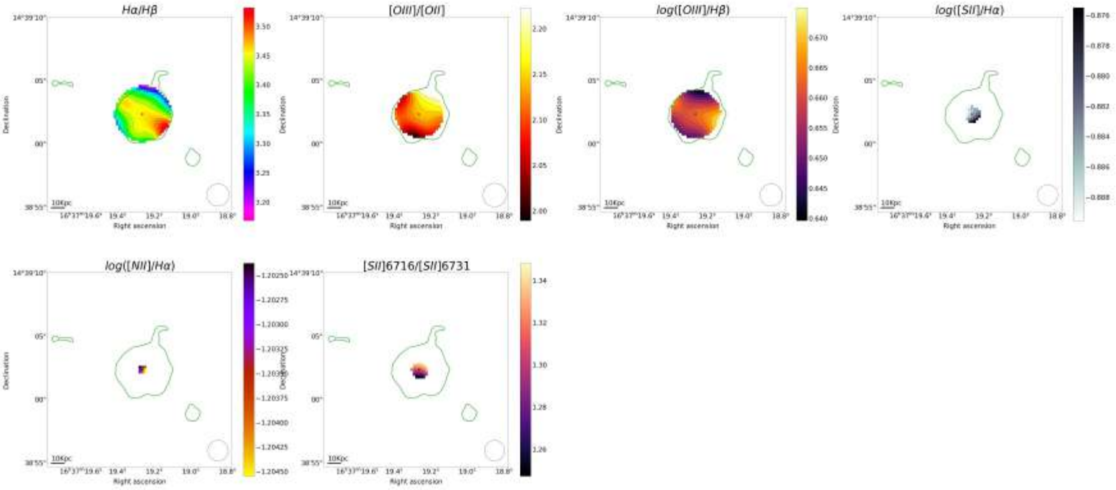

Figure B.44 Line ratio maps for GP21.

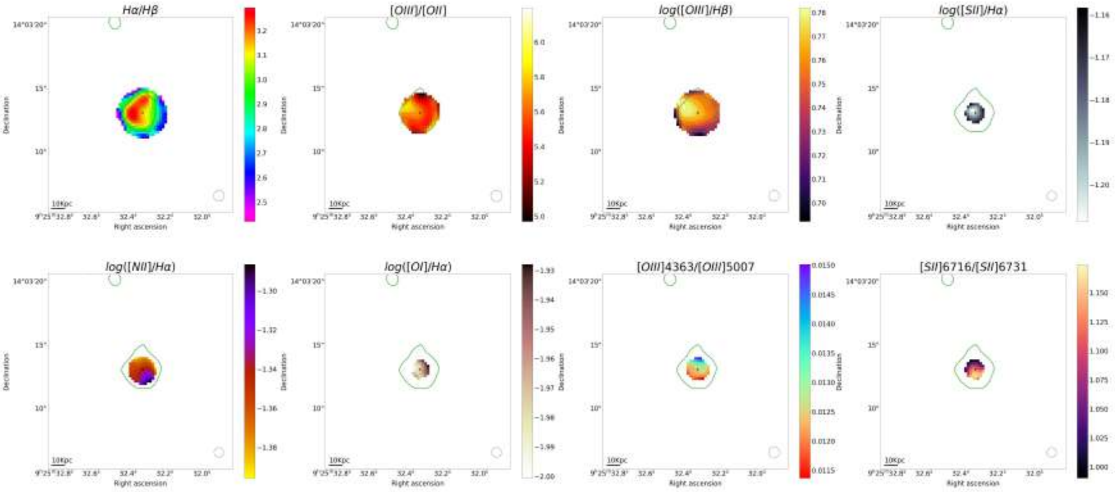

Figure B.45 Line ratio maps for GP22.

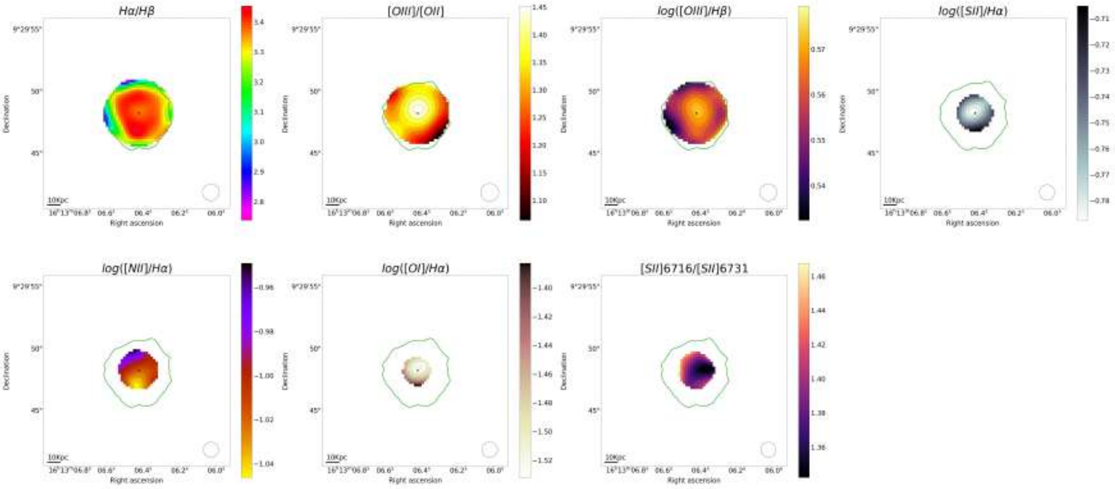

Figure B.46 Line ratio maps for GP23.

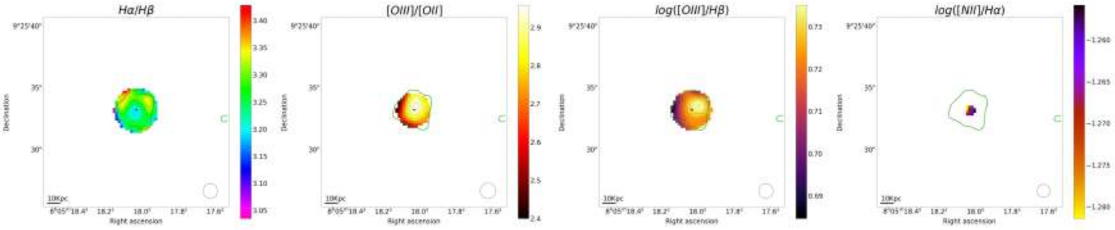

Figure B.47 Line ratio maps for GP24.

B.3 Continuum maps

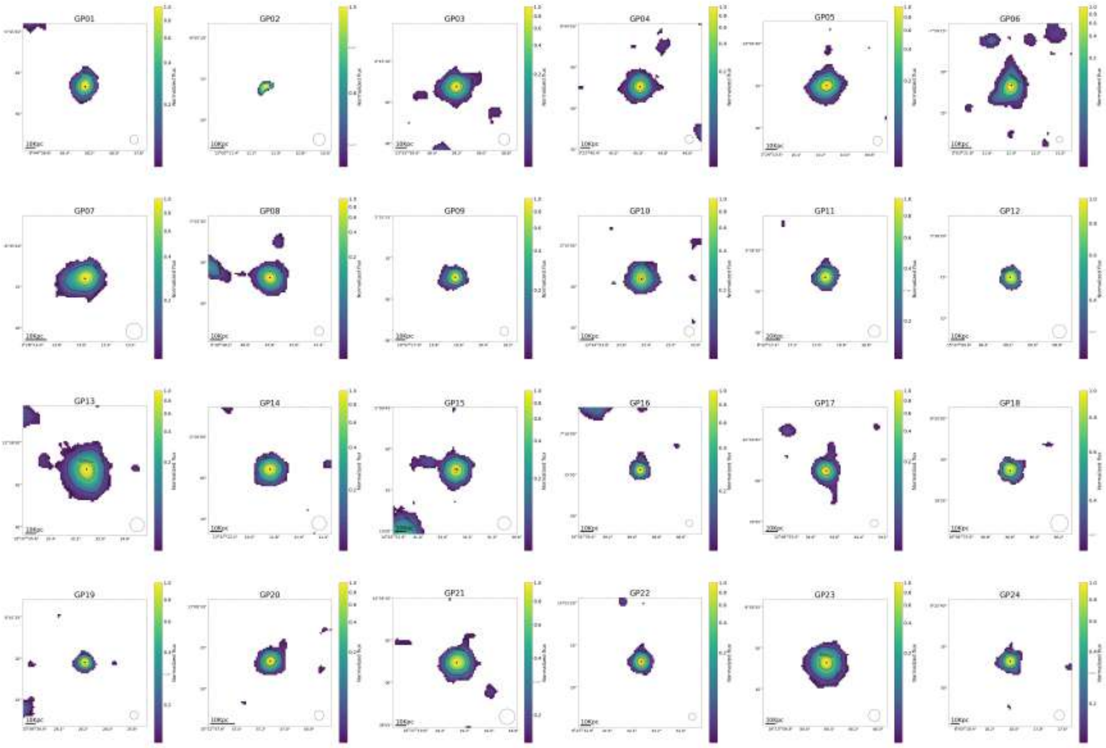

Figure B.48 Continuum maps of all GPs.

B.4 Radial Profiles

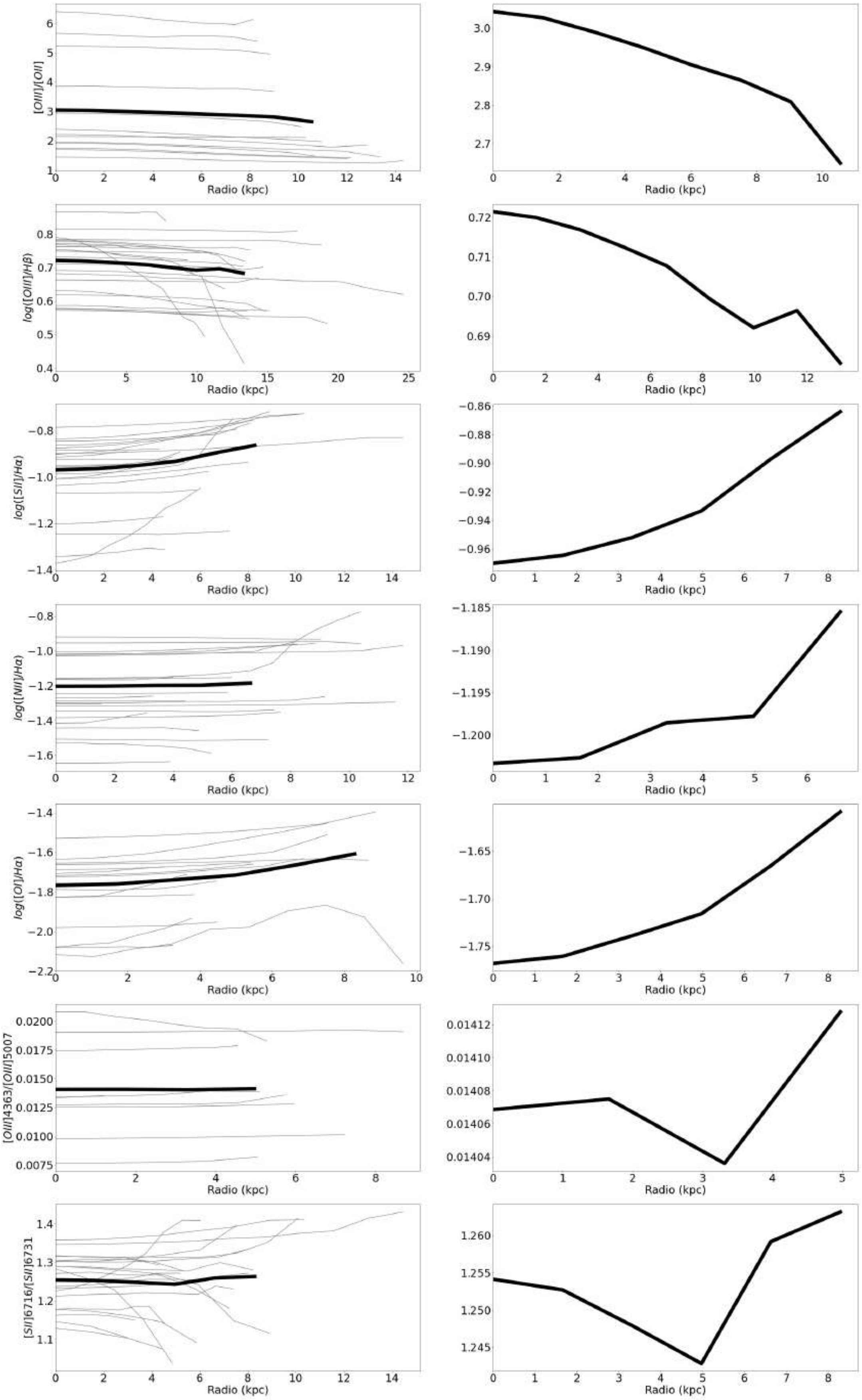

Figure B.49 Radial profiles of the rest of emission line ratios.

B.5 Spectra

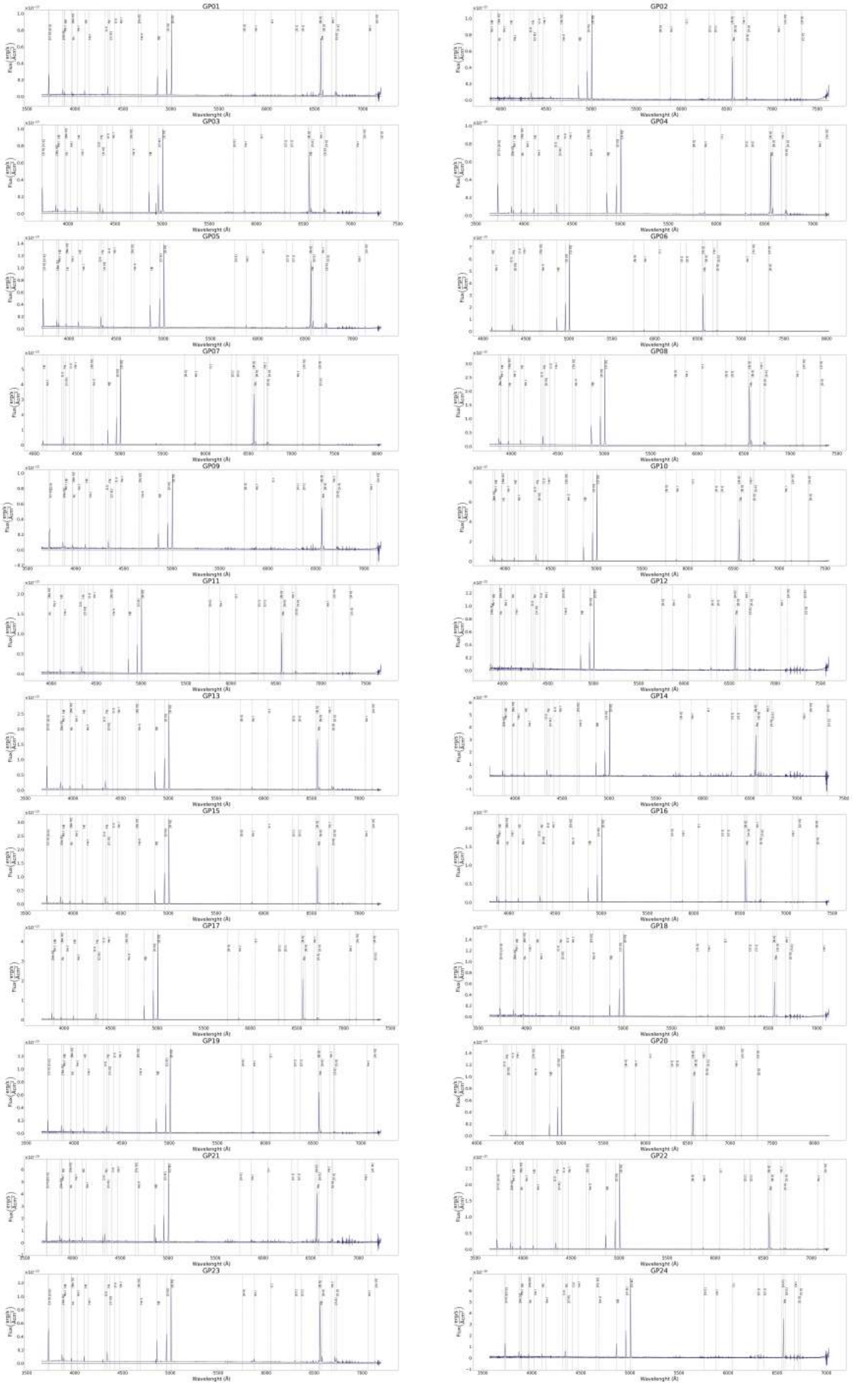

Figure B.50 Integrated spectra.

B.6 Emission line data and properties of the ionized gas

Table B.1 Emission line fluxes, extinction and EW of [OIII] line.

Name (1)	[OII] (2)	[OIII]4363 (3)	[OIII] (4)	[OI] (5)	[NII]6584 (6)	[NII]6716 (7)	[SII]6731 (8)	$C_{H\beta}$ (9)	Hα flux (10)	[OIII] EW (11)
GP01	223.4±1.4		386.0±0.8	4.9±1.2	27.3±1.2	19.9±1.2	14.4±1.3	0.3	265.3±1.6	181.27
GP02	190.3±4.0		555.8±1.5		14.9±0.6	20.0±0.6	14.2±0.6	0.206	92.7±0.4	382.38
GP03	235.3±1.3		416.2±3.3	6.3±0.5	18.6±0.8	20.6±0.7	15.1±0.8	0.239	167.1±0.7	240.11
GP04	219.6±1.1		373.4±0.7	7.2±0.6	29.3±0.5	21.2±0.9	18.9±1.1	0.277	280.4±0.8	204.96
GP05	225.5±1.3		368.2±0.8	6.3±0.4	26.3±0.5	22.8±0.6	18.8±0.6	0.215	285.5±0.9	239.1
GP06	89.2±1.0	11.21±0.12	583.9±0.6	2.8±0.18	6.32±0.23	7.98±0.17	6.6±0.16	0.221	263.6±0.5	682.41
GP07	207.1±1.3		514.1±0.7	5.3±0.5	21.09±0.35	16.7±0.5	14.4±0.5	0.235	231.6±0.5	529.68
GP08	221.2±1.3		407.8±0.6	7.3±0.2	26.78±0.32	23.4±0.3	14.2±0.3	0.252	576.4±1.2	262.73
GP09	203.5±1.6		473.2±1.0	5.1±1.6	17.0±2.1	14.8±2.0	13.4±2.1	0.171	193.8±1.6	253.81
GP10	179.3±1.2	6.5±0.5	590.5±0.7	4.8±0.3	11.82±0.15	14.78±0.18	11.92±0.16	0.181	664.3±0.9	747.48
GP11	187.3±1.2		498.0±1.2	4.5±0.9	11.6±0.5	18.4±0.6	13.5±0.6	0.142	125.5±0.38	352.65
GP12	206.3±2.7		551.6±1.3	4.2±0.9	12.21±0.47	15.3±0.8	11.0±0.9	0.285	170.8±0.5	534.84
GP13	231.4±1.0	8.8±1.2	473.0±0.7	6.4±0.5	13.1±0.9	20.4±1.1	14.5±1.2	0.237	570.3±2.7	340.42
GP14	229.9±1.8		503.3±1.1	6.1±1.0	17.2±1.0	17.8±1.0	14.8±1.0	0.321	132.4±0.7	351.05
GP15	95.2±1.0	11.6±0.5	622.3±0.8	2.2±0.5	6.8±1.0	8.5±1.1	6.8±1.3	0.148	371.9±1.7	945.78
GP16	185.4±2.1		549.3±1.0	10.7±1.0	10.3±1.0	16.9±1.1	14.3±1.1	0.142	155.4±0.8	562.67
GP17	179.5±1.6	8.1±0.3	602.1±0.8	4.4±0.3	11.17±0.28	15.54±0.29	11.3±0.3	0.162	325.8±0.7	703.58
GP18	124.6±2.1		675.7±1.2	4.5±0.9	12.0±0.8	12.9±2.6	10.6±2.5	0.204	320.4±1.5	782.27
GP18	149.5±1.8		573.6±1.0	3.98±0.4	13.28±0.3	12.1±0.7	10.2±0.7	0.201	194.3±0.5	637.66
GP20	80.8±1.1	12.6±0.2	736.8±0.8	2.01±0.16	5.75±0.12	7.1±0.16	5.97±0.16	0.151	209.0±0.3	1999.99
GP21	223.0±2.0		458.1±1.7	6.5±0.7	18.9±1.0	20.9±1.4	16.1±1.6	0.279	176.3±0.9	281.3
GP22	103.8±0.7		590.7±0.7	2.7±0.5	10.4±0.5	9.4±0.5	8.1±0.5	0.123	328.7±1.0	978.47
GP23	277.8±1.3		379.5±1.0	9.5±1.0	28.5±1.2	26.9±2.0	17.9±2.4	0.276	297.0±1.9	179.29
GP24	189.8±2.1		525.8±1.2		13.5±2.0	26.6±2.0	21.2±2.1	0.218	176.8±1.4	412.39

Column (1): Name of the galaxy. Columns (2), (3), (4), (5), (6), (7) and (8): Extinction corrected flux of several lines normalized to Hβ (Hβ flux = 100). Column (9): Extinction coefficient. Column (10): Hα luminosity ($\times 10^{40}$ erg s^{-1}). Column (11): Hα EW (Å).

Table B.1 Continuation of the previous table.

Name (1)	[NeIII]3869 (2)	[FeIII]4658 (3)	[HeII] (4)	[ArIV]4711 (5)	[ArIV]4740 (6)	[HeI]4922 (7)	[ArIII]7136 (8)	[OII]7319 (9)	[ArIII]7751 (10)
GP01	32.4±0.6						7.6±1.5		
GP02							7.6±0.5		
GP03	35.8±0.5						7.44±0.24		
GP04	31.1±0.5								
GP05	29.7±0.5						6.02±0.2		
GP06			1.85±0.06	1.77±0.05			3.92±0.09	1.57±0.21	
GP07							7.44±0.12	2.8±0.3	1.9±0.3
GP08	34.1±0.4						6.55±0.19		
GP09	42.4±0.8								
GP10	44.2±0.4						6.55±0.1	1.9±0.3	
GP11							7.27±0.15	1.6±0.7	
GP12	50.6±2.0						7.4±0.6		
GP13	40.4±0.4						5.84±0.11		
GP14	40.7±0.6						5.7±0.5		
GP15	44.2±0.4		1.34±0.07				6.2±0.17		
GP16	44.5±0.4						7.1±0.5	2.7±0.4	
GP17	48.1±0.3						6.88±0.16	2.11±0.25	
GP18	52.0±1.0								
GP18	51.6±0.8						6.11±0.26		
GP20		0.97±0.06	1.08±0.06	2.18±0.06	1.24±0.05	0.95±0.05	5.06±0.06	1.48±0.2	1.28±0.09
GP21	35.9±1.1						7.1±0.4		
GP22	46.5±0.4						7.0±1.0		
GP23	33.9±0.5						7.0±1.2		
GP24	43.2±0.8								

All columns represent extinction corrected flux of several lines normalized to Hβ (Hβ flux = 100).

Table B.2 Properties of the ionized gas.

Name (1)	O32 (2)	log([OIII]/$H\beta$) (3)	log([NII]/$H\alpha$) (4)	log([SII]/$H\alpha$) (5)	log([OI]/$H\alpha$) (6)	T_e (7)	n_e (8)	12 + log(O/H) (9)	log(N/O) (10)
GP01	1.81±0.02	0.587±0.004	-1.02±0.02	-1.02±0.02	-1.76±0.09		71.0±41.0	8.03±0.03	-0.95±0.06
GP02	2.93±0.06	0.745±0.005	-1.28±0.02	-1.28±0.02	-1.77±0.07		210.0±70.0	8.05±0.04	-1.24±0.03
GP03	1.81±0.02	0.62±0.01	-1.18±0.02	-1.18±0.02	-1.66±0.03		86.0±27.0	8.21±0.05	-1.13±0.02
GP04	1.67±0.01	0.572±0.003	-0.992±0.007	-0.992±0.007	-1.6±0.03		351.0±42.0	8.05±0.02	-1.02±0.03
GP05	1.63±0.01	0.563±0.002	-1.034±0.009	-1.034±0.009	-1.65±0.03		260.0±70.0	8.06±0.02	-1.10±0.04
GP06	6.56±0.08	0.766±0.002	-1.65±0.02	-1.65±0.02	-2.01±0.03	15059.0±21.0	302.0±20.0	7.902±0.008	-1.23±0.04
GP07	2.50±0.02	0.711±0.003	-1.131±0.007	-1.131±0.007	-1.74±0.04		373.0±24.0	8.16±0.02	-1.00±0.03
GP08	1.82±0.02	0.609±0.002	-1.042±0.005	-1.042±0.005	-1.60±0.02		200.0±70.0	8.13±0.06	-1.01±0.01
GP09	2.32±0.02	0.674±0.004	-1.23±0.05	-1.23±0.05	-1.74±0.12		520.0±170.0	8.17±0.02	-1.08±0.07
GP10	3.33±0.03	0.770±0.002	-1.382±0.006	-1.382±0.006	-1.78±0.03	11910.0±90.0	246.0±9.0	8.24±0.01	-1.27±0.03
GP11	2.62±0.02	0.698±0.004	-1.38±0.02	-1.38±0.02	-1.80±0.08		87.0±22.0	8.05±0.03	-1.30±0.05
GP12	2.79±0.04	0.742±0.004	-1.36±0.02	-1.36±0.02	-1.83±0.08		64.0±38.0	8.13±0.04	-1.20±0.05
GP13	2.02±0.01	0.675±0.002	-1.33±0.03	-1.336±0.03	-1.648±0.03	14880.0±260.0	48.0±28.0	7.95±0.02	-1.29±0.05
GP14	2.18±0.02	0.702±0.004	-1.22±0.03	-1.22±0.03	-1.67±0.06		340.0±60.0	8.26±0.03	-1.14±0.05
GP15	6.38±0.07	0.794±0.003	-1.62±0.06	-1.62±0.06	-2.11±0.09	14880.0±70.0	230.0±120.0	7.94±0.01	-1.21±0.07
GP16	2.96±0.03	0.739±0.003	-1.44±0.05	-1.44±0.05	-1.42±0.04		350.0±60.0	8.06±0.02	-1.37±0.05
GP17	3.30±0.03	0.778±0.002	-1.39±0.02	-1.39±0.01	-1.82±0.03	12970.0±39.0	280.0±70.0	8.148±0.009	-1.26±0.02
GP18	5.53±0.10	0.827±0.003	-1.37±0.03	-1.37±0.03	-1.80±0.08		320.0±180.0	8.04±0.05	-1.2±0.1
GP18	3.87±0.05	0.758±0.002	-1.33±0.01	-1.33±0.01	-1.86±0.03		350.0±50.0	8.13±0.03	-1.07±0.06
GP20	8.73±0.12	0.867±0.002	-1.695±0.009	-1.695±0.009	-2.15±0.04	14233.0±26.0	345.0±22.0	8.048±0.004	-1.25±0.02
GP21	2.06±0.02	0.661±0.006	-1.18±0.03	-1.18±0.03	-1.65±0.05		150.0±50.0	8.27±0.03	-1.14±0.05
GP22	5.67±0.05	0.762±0.002	-1.43±0.02	-1.43±0.02	-2.03±0.07		390.0±50.0	7.97±0.04	-1.09±0.05
GP23	1.31±0.01	0.579±0.007	-0.99±0.02	-0.99±0.02	-1.47±0.05		180.0±70.0	8.14±0.02	-1.06±0.06
GP24	2.77±0.04	0.719±0.004	-1.32±0.06	-1.32±0.06	-1.79±0.06		300.0±70.0	8.12±0.03	-1.46±0.08

Column (1): Name of the galaxy. Column (2): Ionization parameter ([OIII]/[OII]). Columns (3), (4), (5) and (6): BPT ratios. Column (7): Electron temperature (K). Column(8): Electron density (cm^{-3}). Column (9): Metallicity. Column (10): N/O abundance in log scale.

B.7 Kinematic analysis

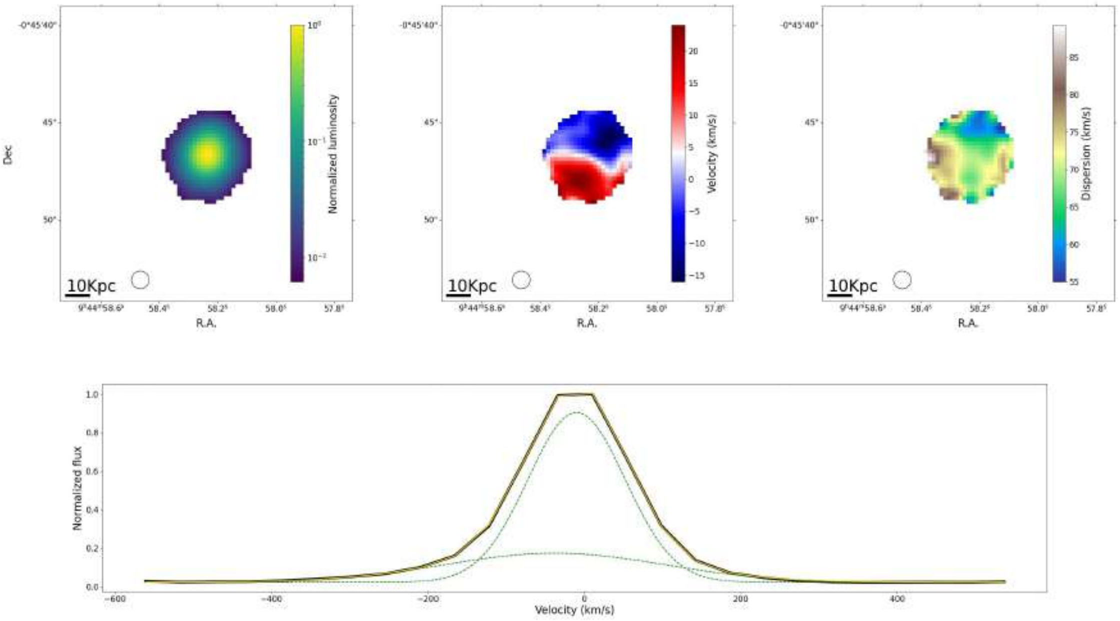

Figure B.51 Kinematic analysis of GP01. Top panels show the luminosity, velocity, and velocity dispersion of Hα for the spaxels with S/N>3. On the bottom it is represented the integrated spectrum using the same spaxels where a multi-Gaussian fit is applied to the profile of the line. For the subsequent figures the same approach is used.

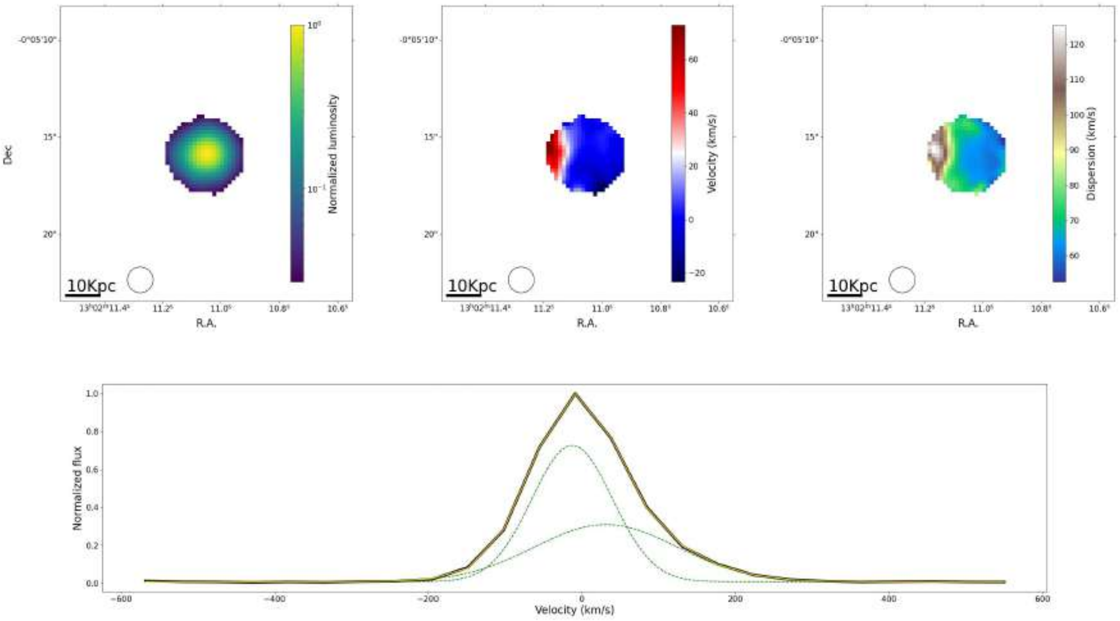

Figure B.52 Kinematic analysis of GP02.

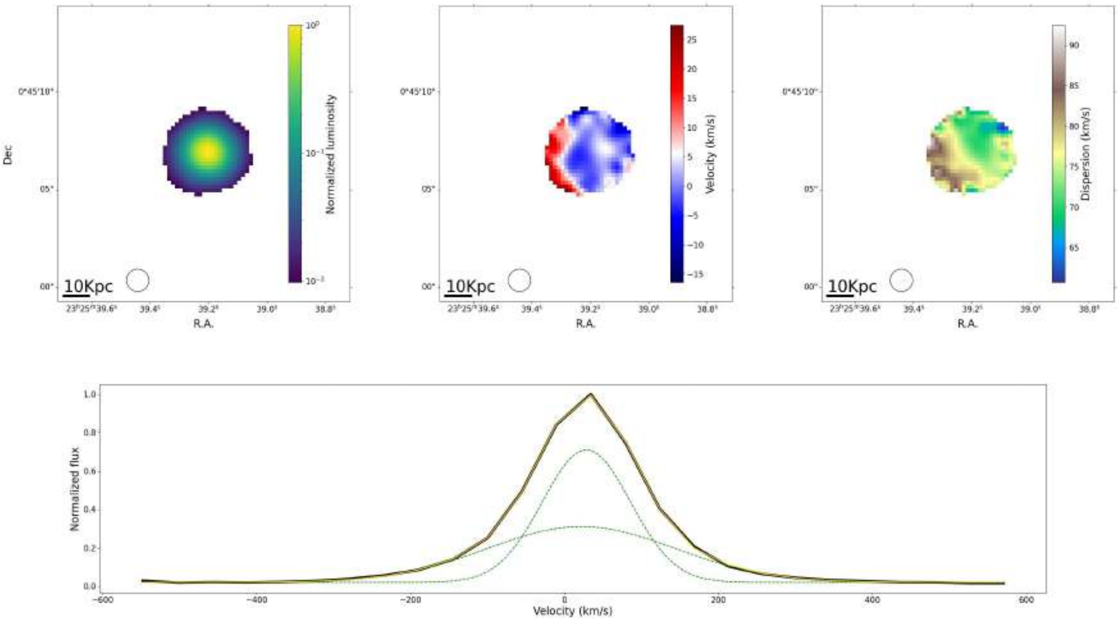

Figure B.53 Kinematic analysis of GP03.

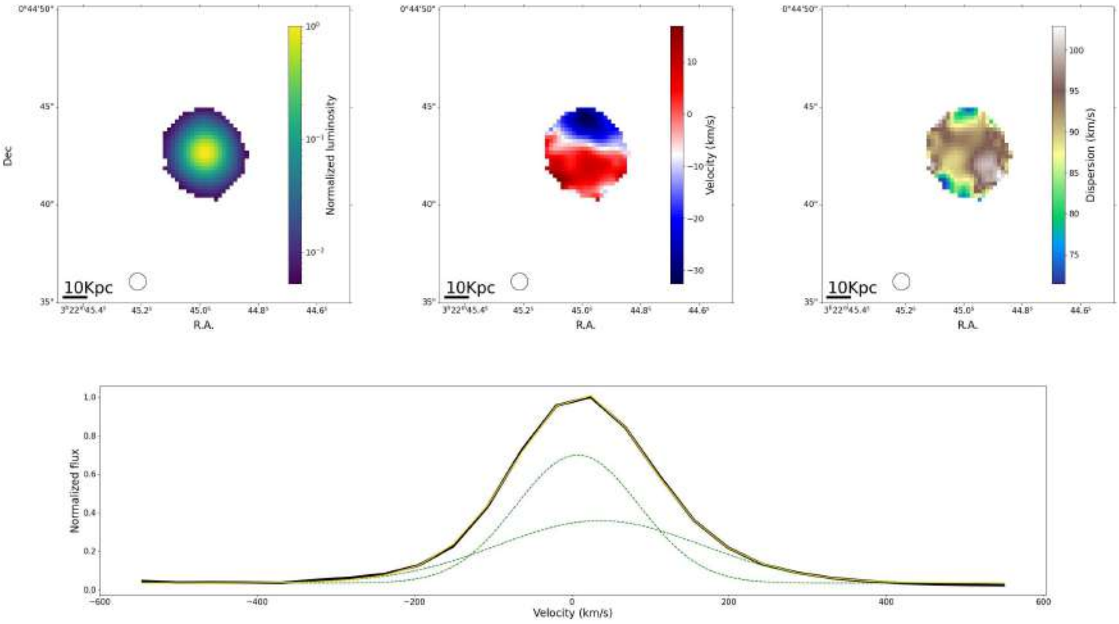

Figure B.54 Kinematic analysis of GP04.

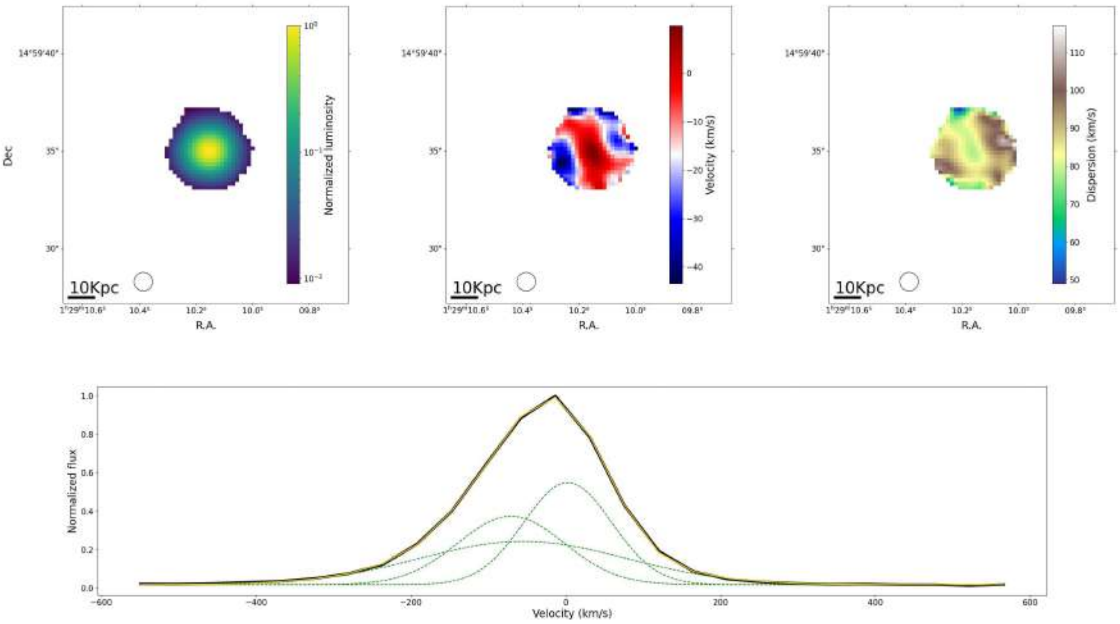

Figure B.55 Kinematic analysis of GP05.

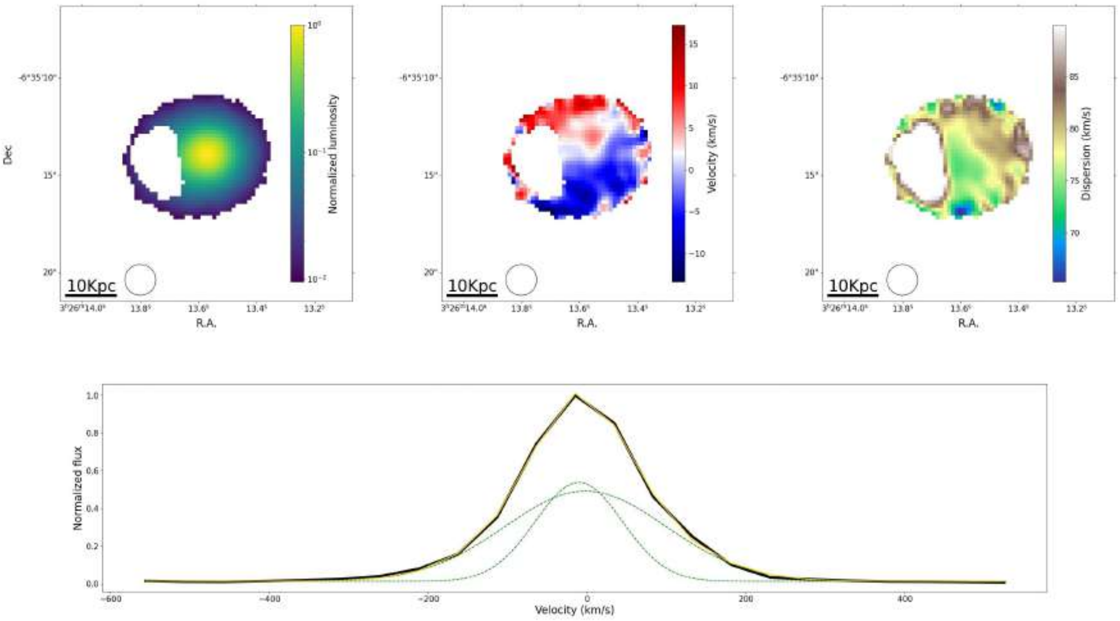

Figure B.56 Kinematic analysis of GP07.

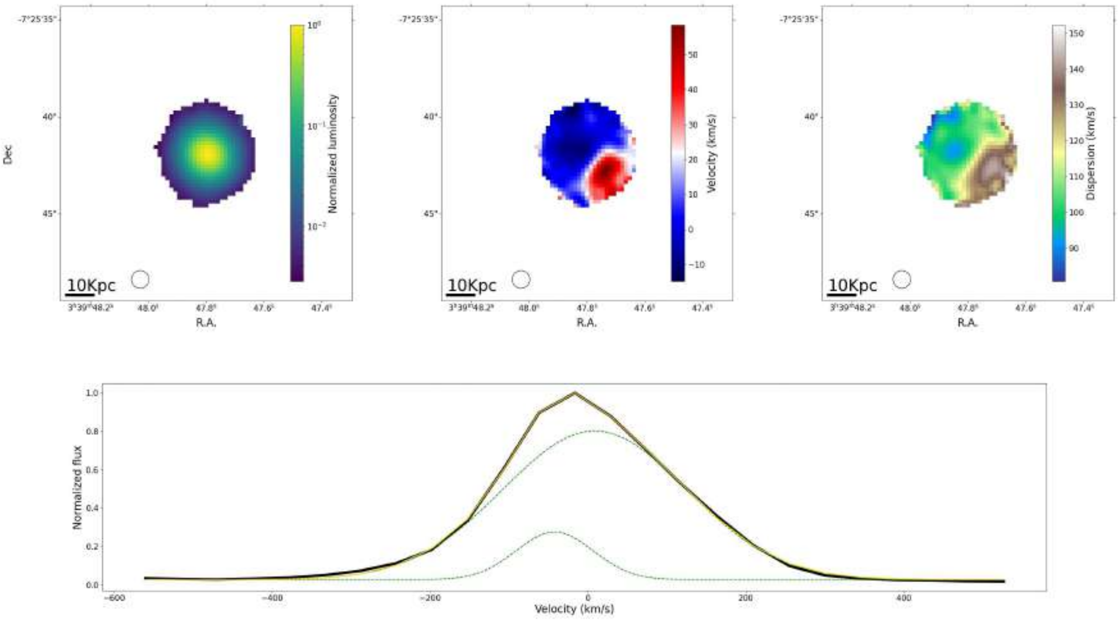

Figure B.57 Kinematic analysis of GP08.

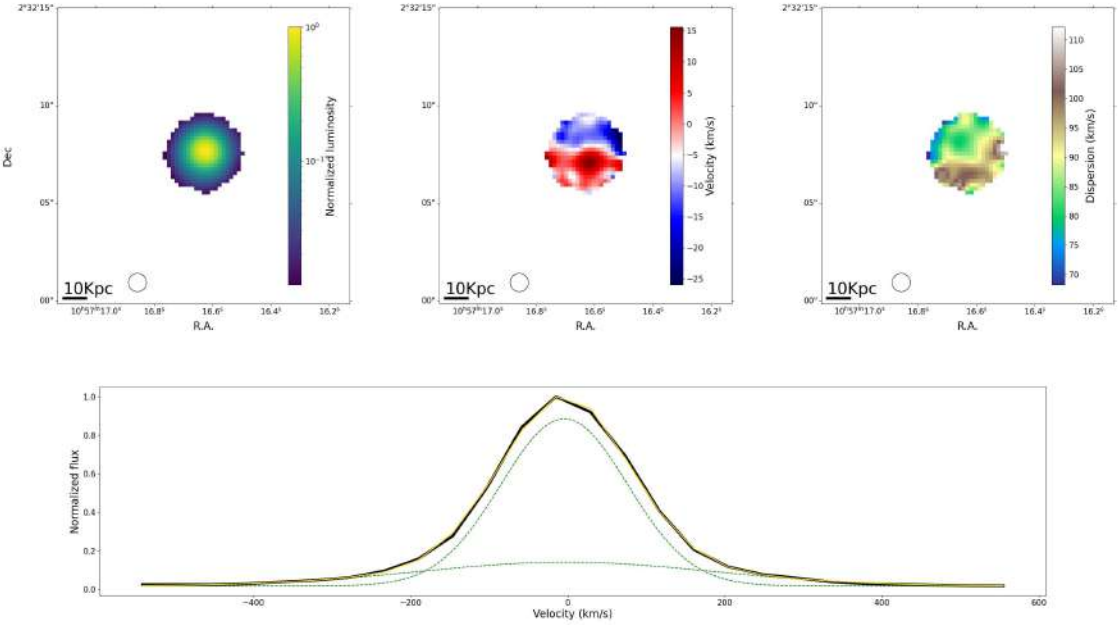

Figure B.58 Kinematic analysis of GP09.

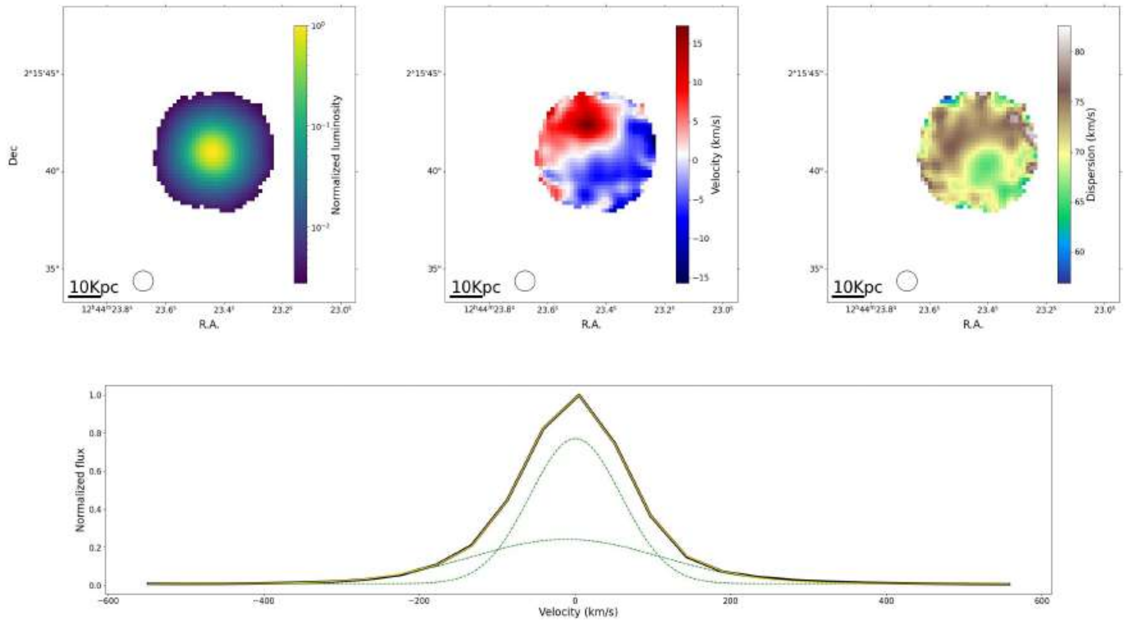

Figure B.59 Kinematic analysis of GP10.

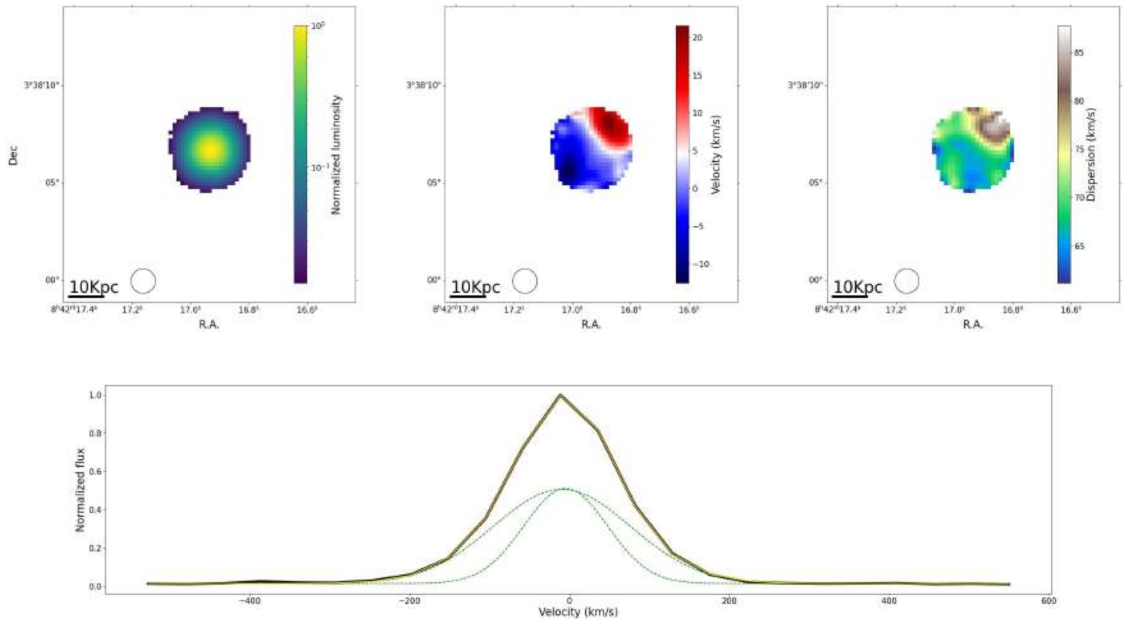

Figure B.60 Kinematic analysis of GP11.

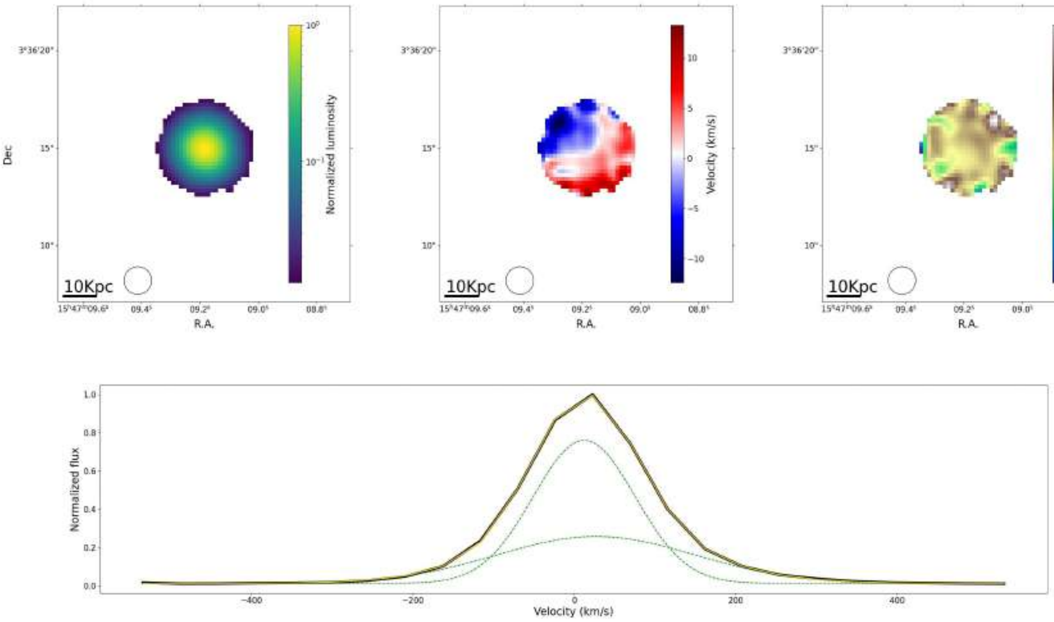

Figure B.61 Kinematic analysis of GP12.

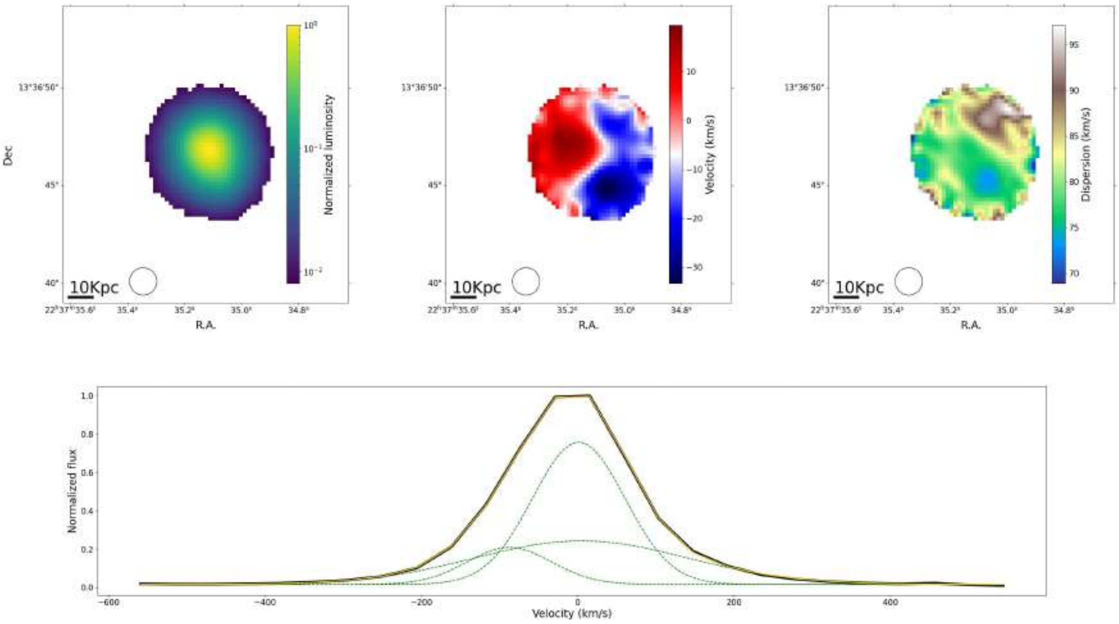

Figure B.62 Kinematic analysis of GP13.

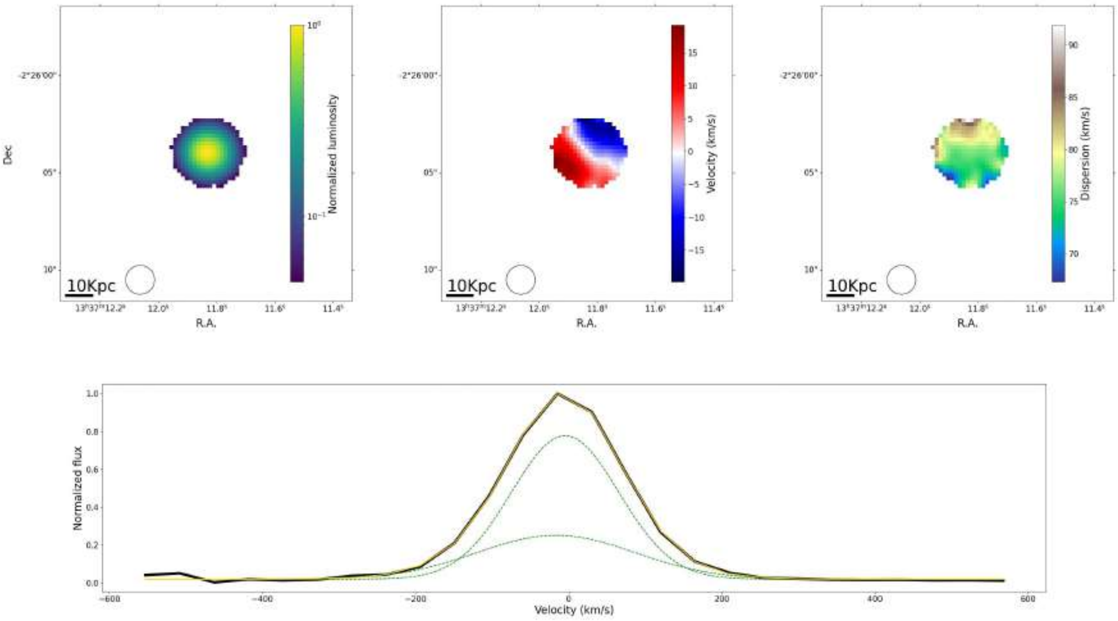

Figure B.63 Kinematic analysis of GP14.

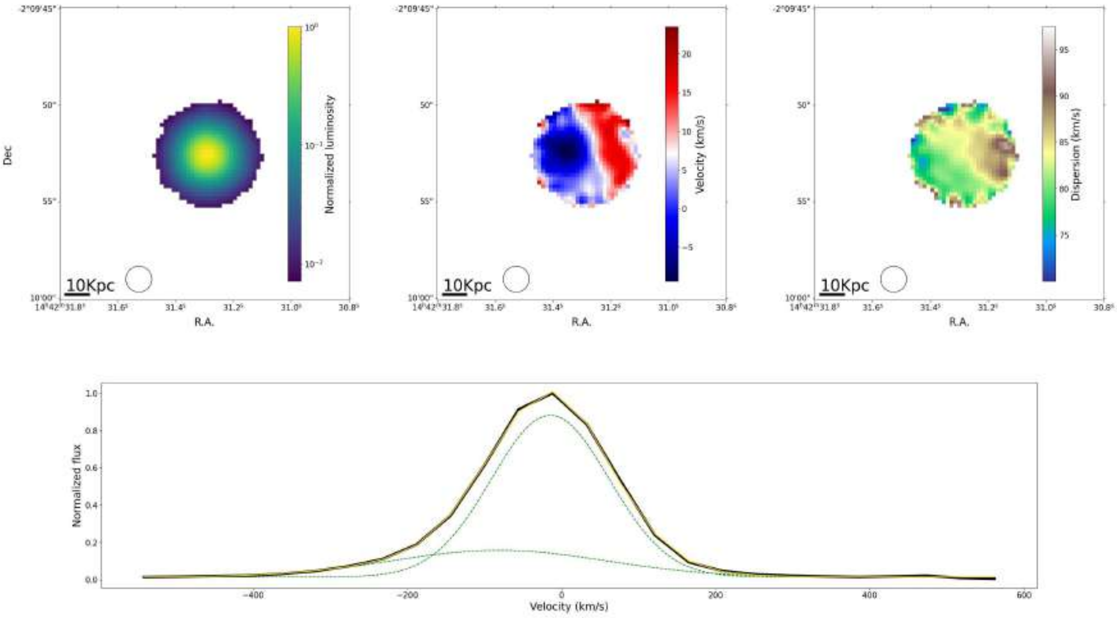

Figure B.64 Kinematic analysis of GP15.

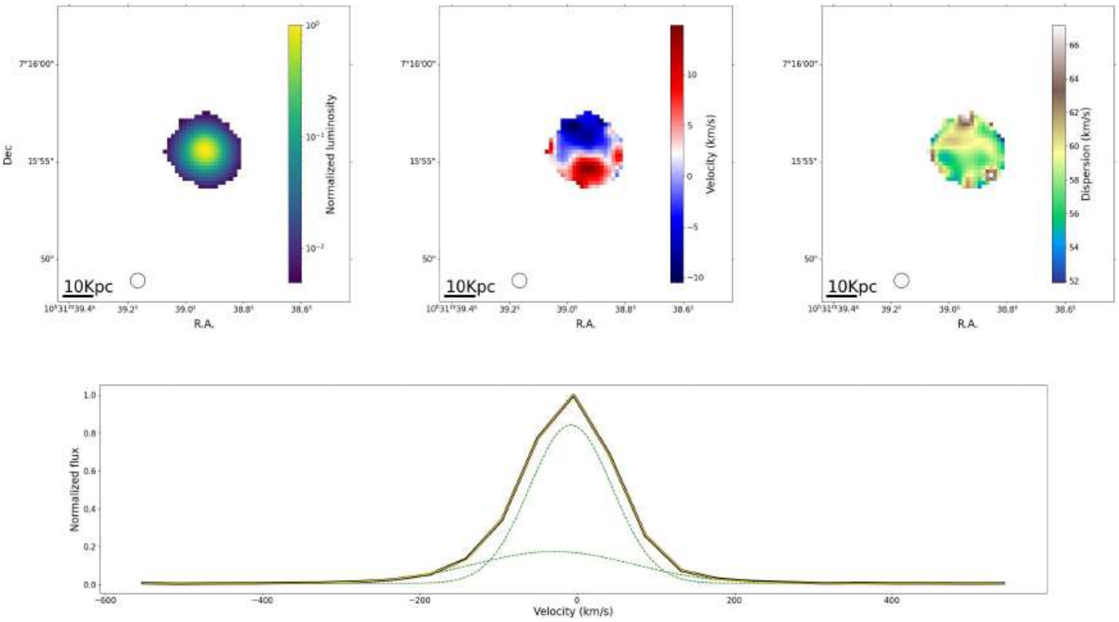

Figure B.65 Kinematic analysis of GP16.

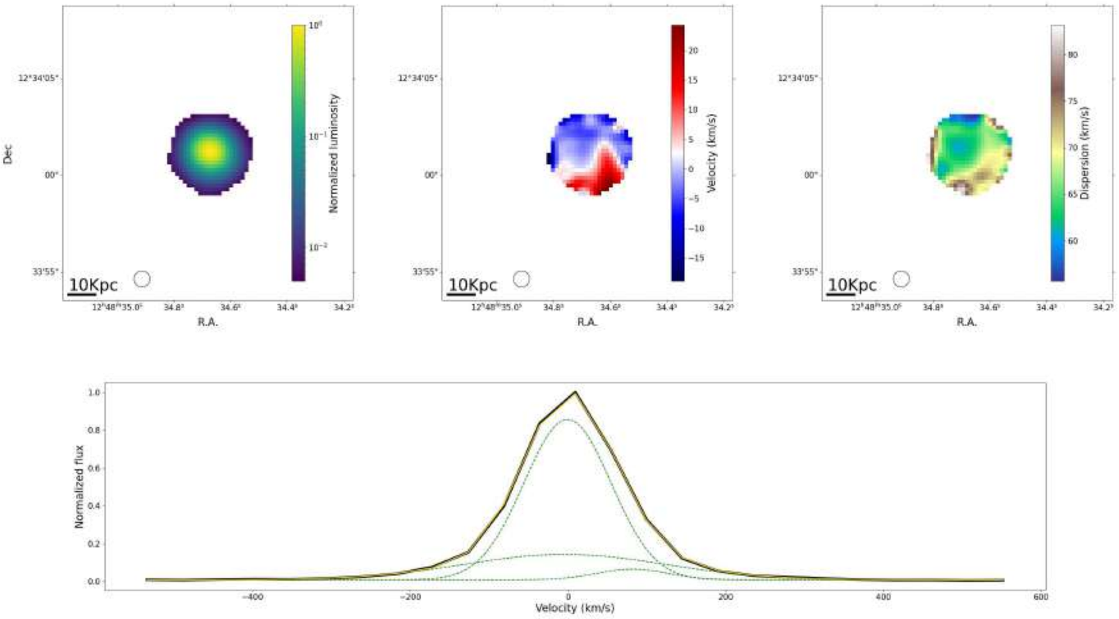

Figure B.66 Kinematic analysis of GP17.

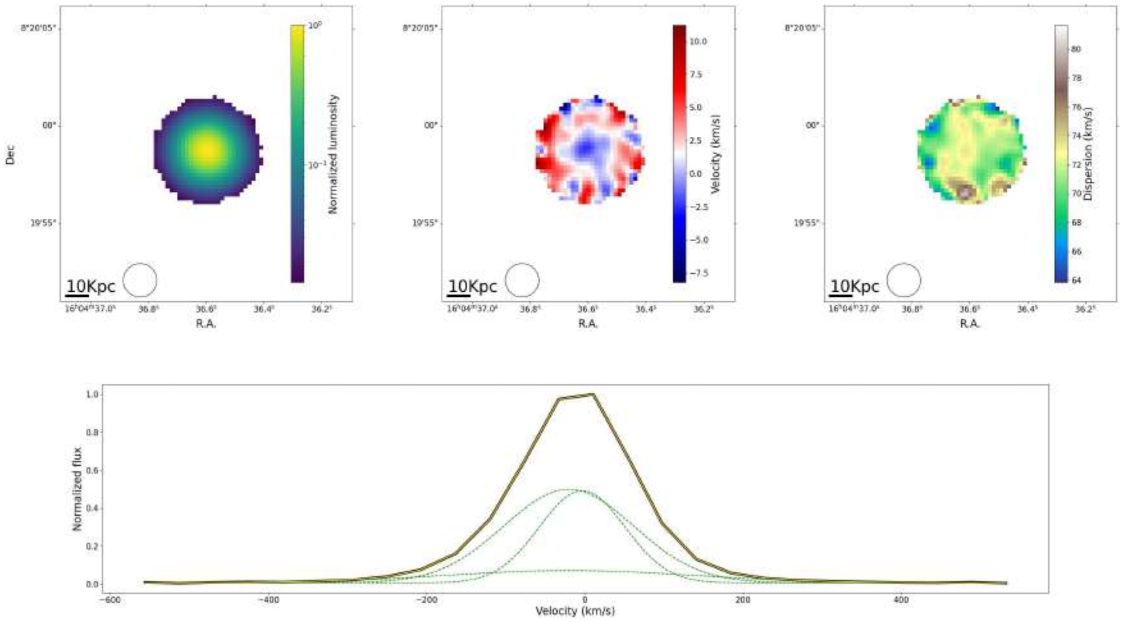

Figure B.67 Kinematic analysis of GP18.

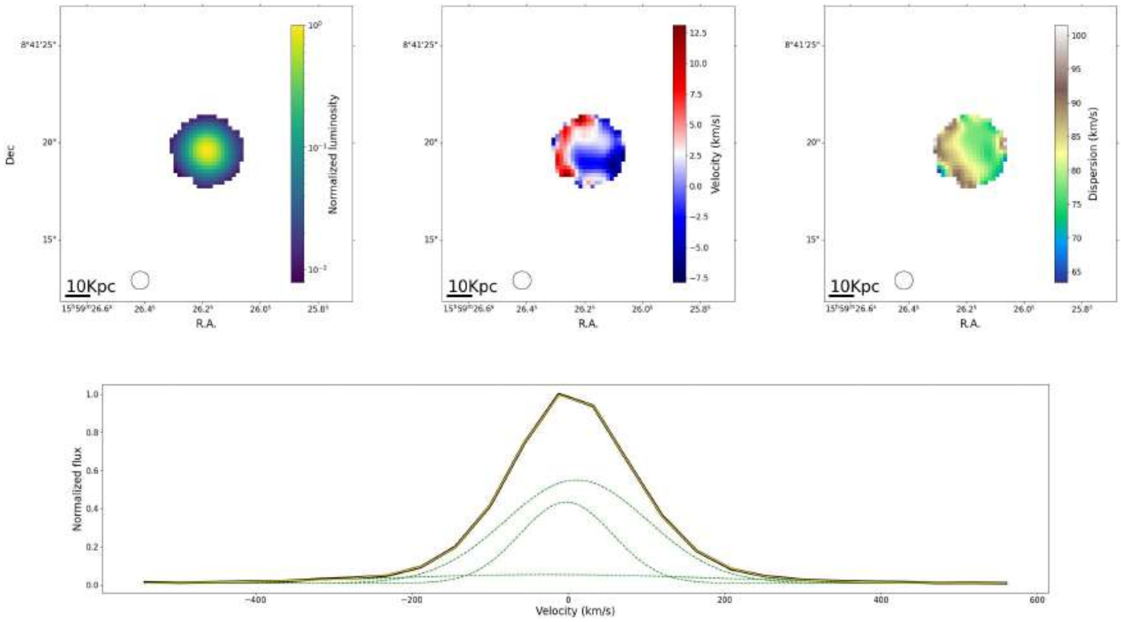

Figure B.68 Kinematic analysis of GP19.

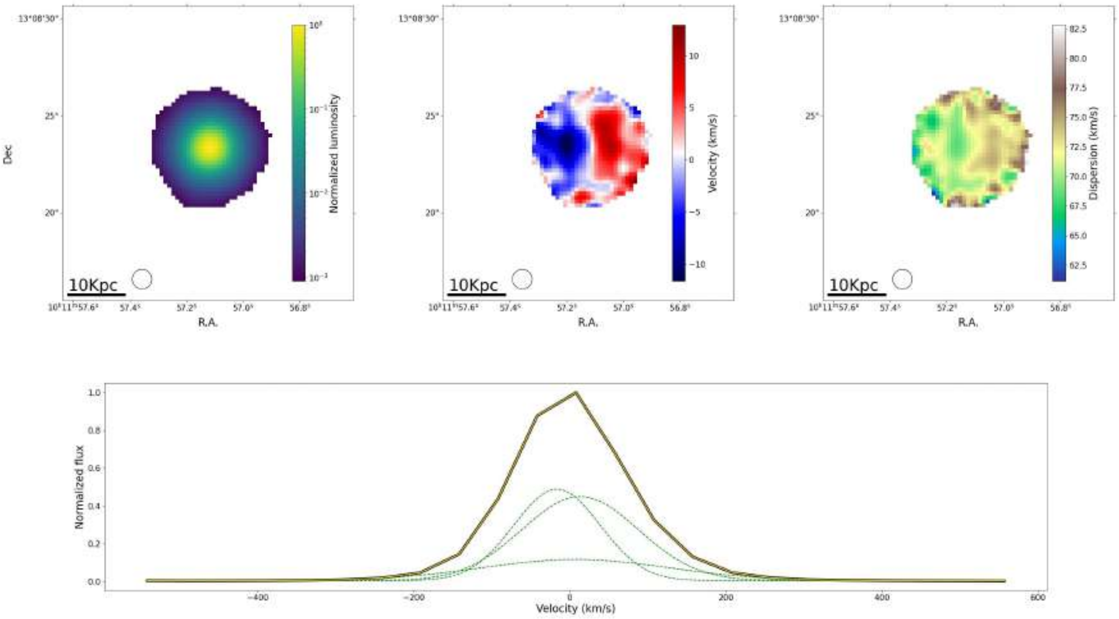

Figure B.69 Kinematic analysis of GP20.

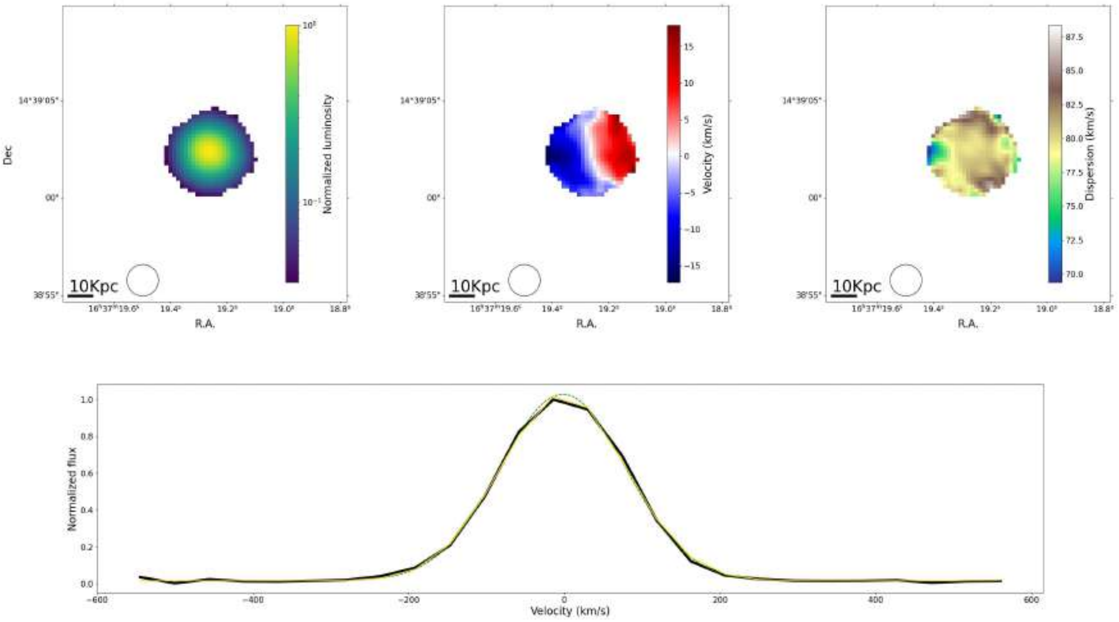

Figure B.70 Kinematic analysis of GP21.

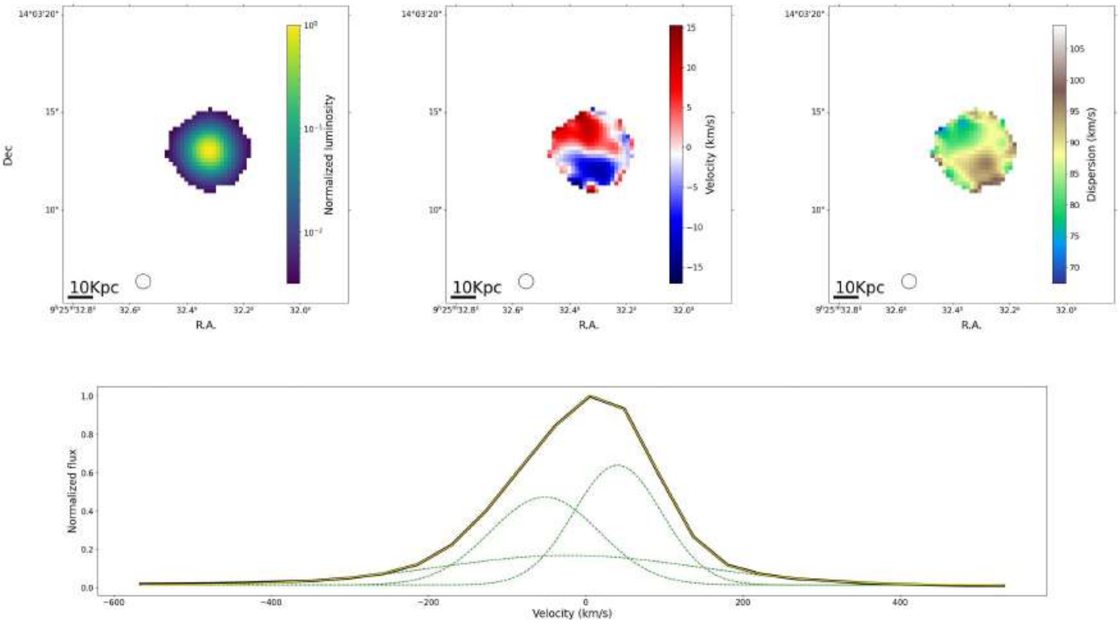

Figure B.71 Kinematic analysis of GP22.

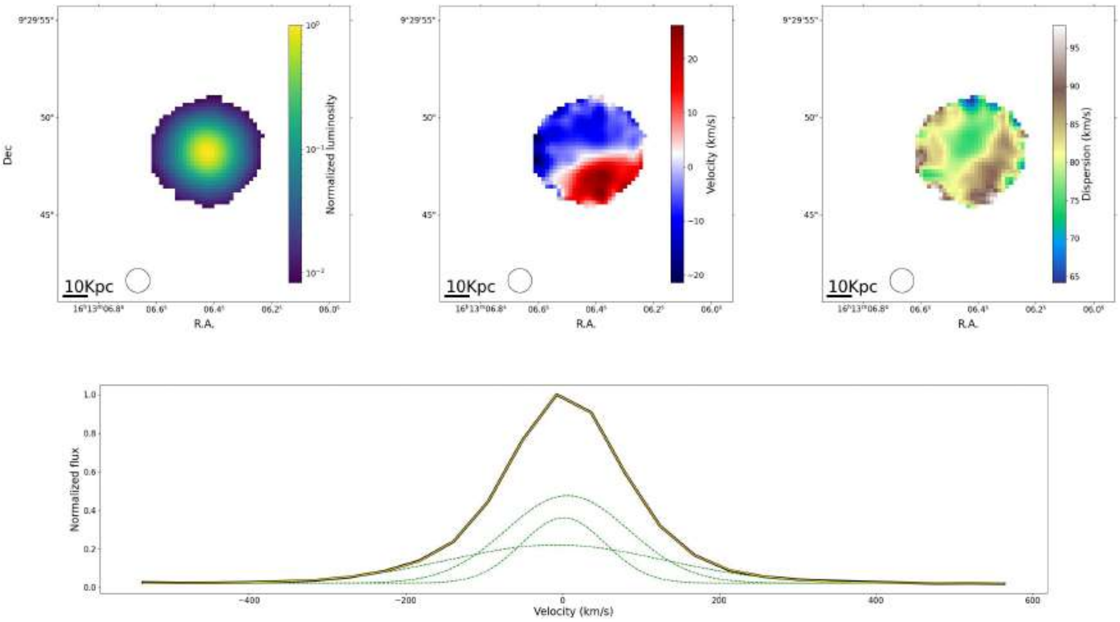

Figure B.72 Kinematic analysis of GP23.

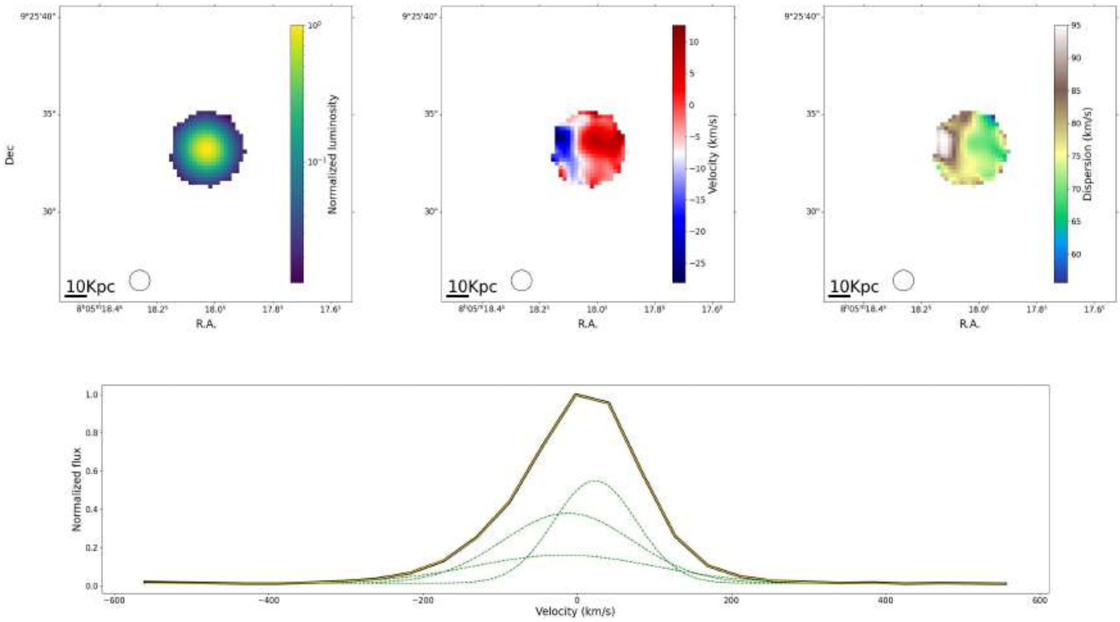

Figure B.73 Kinematic analysis of GP24.

Appendix C

IZw18

C.1 3D kinematical representation

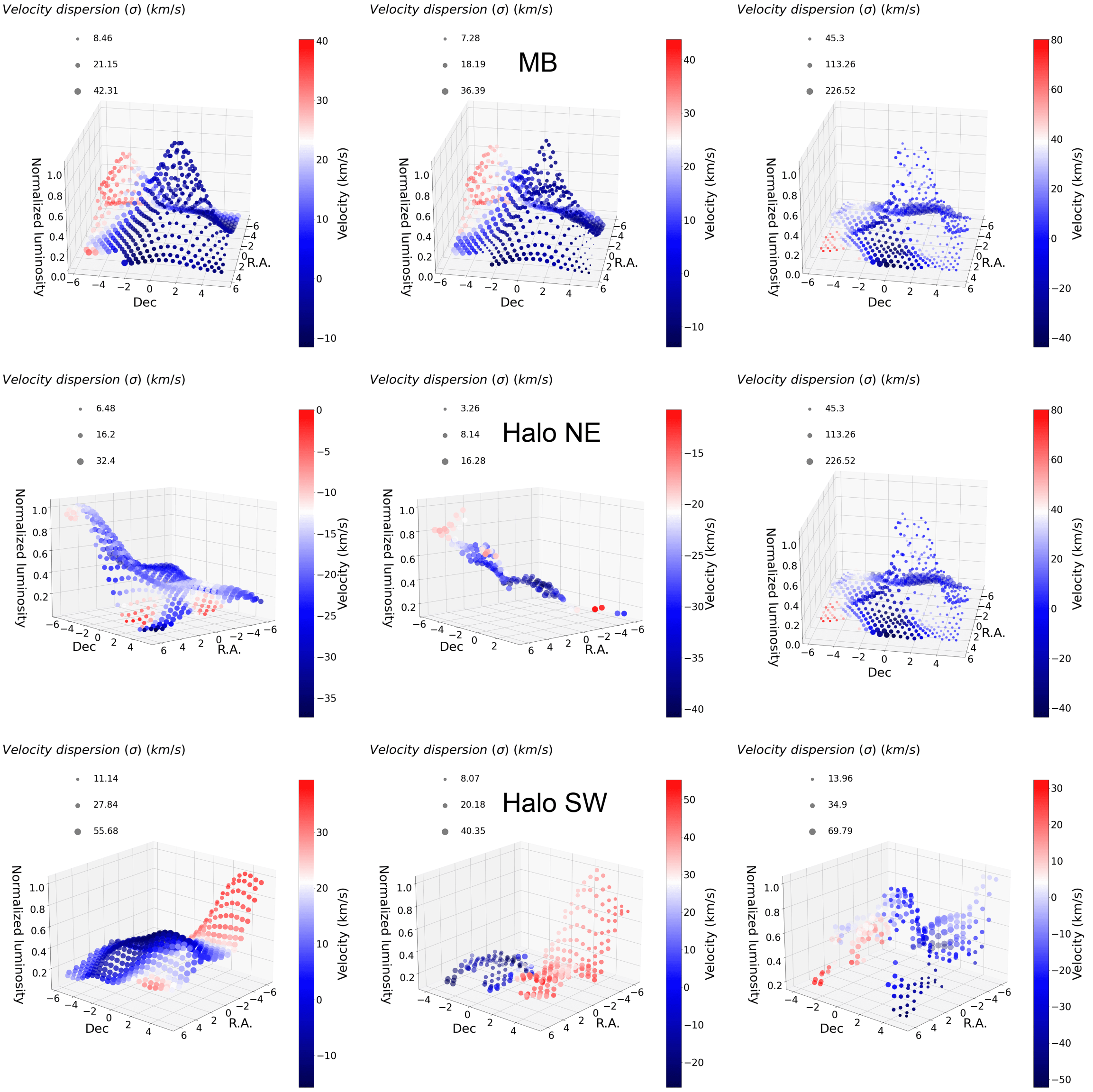

Figure C.1 3D representation of the kinematical data of IZw18. Top row corresponds to the MB, middle row to the Halo NE and bottom row to the Halo SW. In the left column we represent data from the single-component fit. In the middle column it is represented data from the principal double-component fit. The right column correspond to data from the secondary double-component fit. Each 3D figure presents the following features: The x and y axis correspond to R.A. and Dec. in arcseconds from the center of the galaxy. The z axis (vertical axis) represents the normalized luminosity. Colorbars correspond to the velocities, with respect to the systemic velocity of the galaxy. The sizes of the points are related to the velocity dispersion (as indicated in the top left legend in each 3D figure).